Development & Implementation of the Integrated Photonic Spectrograph for Astronomy

By

Nick Cvetojevic

A thesis submitted to Macquarie University
for the degree of
Doctor of Philosophy
Department of Physics and Astronomy
August 2014

MACQUARIE
UNIVERSITY
FACULTY OF SCIENCE

Typeset in LaTeX 2_ε.

Contents

List of Figures

List of Tables

Abstract

The next generation of telescopes currently under construction are vastly larger than any previously built. While their monumental size will allow astronomers to peer deeper into space, a fundamental scaling law means that instrumentation used by astronomers on these telescopes dramatically increases in both size and cost. This imposes an immediate obstacle for the next generation of instrumentation, and in particular spectroscopic instruments which are used extensively in astronomical research. Spectrographs are used in a wide range of fields, from the study of local stars in our galaxy to extra-galactic astronomy, and as such, have become a work-horse instrument on most research observatories around the world. Furthermore, certain key fields in astronomy, such as galactic archaeology or the study of exo-planets, place extreme requirements on spectrograph performance in terms of resolution and stability. Constructing conventional spectrographs in this parameter space has led to spiralling costs and complexity.

In this thesis, we explore the use of recently developed photonic technologies, such as low loss micro-optical circuitry in glass, and evaluate their possible impact on astronomical instrumentation with the aim of creating, testing, and demonstrating an integrated photonic spectrograph (IPS). The integrated photonic spectrograph is a miniaturised, monolithic dispersive device on a silica-on-silicon wafer. These wafer-based components are typically only several square centimetres in size and a few millimetres thick, orders of magnitude smaller than conventional spectrographs. Their size and integrated nature makes them robust against misalignments or flexure due to environmental factors, a property highly sought after for astronomical instrumentation.

To develop this technology, we present in this body of work the experimental characterisation, as well as the theoretical underpinnings, of a series of prototype IPS devices built using arrayed waveguide grating (AWG) photonic circuitry. We demonstrate their initial laboratory performance, alongside enhancements to AWG design which improves IPS performance three-fold. Further, we demonstrate a direct multi-fibre injection method which enables the prototypes to concurrently accept light from several optical fibres, successfully producing multiple independent usable spectra for each individual AWG chip.

We demonstrate and study the feasibility of the prototype IPS with a proof-of-concept test on the 3.9 m Anglo-Australian Telescope at Siding Spring Observatory. We provide the results of the successful test, with detection of carbon-monoxide absorption lines in the spectrum of the star Pi Gru using the IPS. This was, to our knowledge, the first successful capture of a spectrum from a source beyond Earth using a photonic spectrograph. Further, the telescope interface for the IPS, which required the use of

additional astrophotonic technologies (such as the "photonic lantern") is described in detail and its performance and limitations discussed.

Lastly, we present a comprehensive redesign of AWG circuitry to better suit specific astronomical requirements. Two particular designs are discussed, alongside their predicted performance modelled using beam propagation algorithms. The free spectral range of the IPS is increased to encompass an entire NIR atmospheric window (H-band). This allows for the construction of an entirely-photonic platform with a small physical footprint, ideal for space applications, while maintaining broad wavelength coverage. Secondly, we present a new AWG design with a resolving power of 60,000, which was designed specifically for high precision radial velocity studies of planets around M-dwarf stars. This high resolution AWG chip is to be used as part of the PANDORA instrument, collaboratively developed between Macquarie University, the Astrophysical Institute of Potsdam, the Australian Astronomical Observatory, and the Subaru telescope in Hawaii. We highlight the overall instrument concept with its projected performance, and highlight the advantages over a traditional spectrograph design.

Statement of candidate

The use of arrayed waveguides was first recommended by AAO chief scientist Fred Watson. This seeded the Integrated Photonic Spectrograph (IPS) project, which evolved from a collaboration between Joss Bland-Hawthorn at the University of Sydney (UoS), the Australian Astronomical Observatory (AAO) and Macquarie University (MQ), with UoS & AAO procuring the original prototype IPS devices and MQ & AAO being responsible for the characterisation of all the prototype devices and commissioning the IPS instrument on the Anglo-Australian Telescope (AAT). When the project progressed to designing and fabricating new IPS devices for high-resolution exoplanet science, a further collaboration was established between MQ/AAO, the Leibniz Institute for Astrophysics Potsdam (AIP), and the Subaru Telescope (National Astronomical Observatory of Japan). For this phase of the project, the initial IPS design, modelling and lithographic mask layout was split between MQ/AAO and AIP, with Subaru developing and implementing single mode fibre (SMF) injection with an extreme AO chronograph (SCExAO) for the purpose of future testing.
From the start of my PhD I was involved in the laboratory characterisation of all the IPS prototypes. This included the construction of the first laboratory testing systems for Arrayed Waveguide Grating (AWG) photonic spectrograph and the creation of analysis code and procedures. Further, I was responsible for the creation of the on-telescope instrument, which included the precise linking of multiple astrophotonic devices, and the design and integration of much of the optical components. The exceptions were the Integral Field Unit at the Cassegrain focus, which was part of the GNOSIS instrument, and all components within IRIS2. The data reduction of astronomical observations was done with some assistance from Dr Simon Ellis[1]. Much of the design and modelling work for the high resolution AWG was done in close collaboration with Andreas Stoll[2], Dr. Harendra Fernando[3], and Dr. Roger Haynes[4]. Any other components of this thesis represent my original work and contributions.

This thesis is submitted in fulfilment of the requirements of the degree of Doctor of Philosophy at Macquarie University and has not been submitted for a higher degree to any other university or institution. I certify that to the best of my knowledge, all sources used and assistance received in the preparation of this thesis have been acknowledged. This thesis does not contain any material which is defamatory

[1] simon.ellis@aao.gov.au – Australian Astronomical Observatory
[2] astoll@uni-potsdam.de – Leibniz Institute for Astrophysics Potsdam, Germany
[3] hfernando@aip.de – Leibniz Institute for Astrophysics Potsdam, Germany
[4] rhaynes@innofspec-potsdam.de – Leibniz Institute for Astrophysics Potsdam, Germany

of any person, form or corporation and is not in breach of copyright or breach of other rights which shall give rise to any action at Common Law or under Statute.

Nick Cvetojevic

of any person, form or corporation and is not in breach of copyright or breach of other rights which shall give rise to any action at Common Law or under Statute.

Nick Cvetojevic

"I am driven by two main philosophies: know more today about the world than I knew yesterday and lessen the suffering of others. You'd be surprised how far that gets you. "

Neil deGrasse Tyson

Acknowledgements

I would like to express my sincerest gratitude to all the people who have influenced, mentored, and helped me in various ways during my PhD candidature. This thesis would not have been possible without your care and consideration.

Firstly I would like to thank my supervisors; Dr. Jon Lawrence, Dr. Nemanja Jovanovic, and Professor Michael Withford. Their patience, support, direction, and enthusiasm is without equal. Jon, thank you for all your dedication, guidance, and for taking a chance on me all those years ago. You ignited my love of research, encouraged and pushed me to achieve the best possible results in all that I have undertaken. To my mentor and friend Nem, few words can express the gratitude I feel for all the hard work you put in helping and supporting me during my PhD. You wisdom on everything from lab etiquette, to public speaking, to general life and career advice was instrumental in getting me to this point, and is something I will cherish forever. Your dedication and work ethic is something I always hope to emulate. Mick, thank you for all the help and advice over the years. You always made time for me, pushed me to aim higher and take on more responsibility, and preached calm and composure in times of stress. I will always be thankful for the environment you have fostered at MQ CUDOS, which has given to me so much and made my time at Macquarie an absolute joy.

I would also like to thank the other researchers at Macquarie University and the Australian Astronomical Observatory that provided support during my PhD. To my collogue and friend Dr. Graham Marshall, you were an inexhaustible fountain of knowledge and ideas, and were always happy to make time to bounce ideas around. The ingenuity you demonstrated regarding conference lanyard modification is something that still hangs on my wall with pride. I would also like to thank Dr. Simon Gross, thank you for all your advice and guidance with all things lab related (and for introducing me to the finer points of German beer). Dr. Anthony Horton and Dr. Simon Ellis, thank you for your invaluable assistance and support during our time at the telescope.

I would like to acknowledge the contribution and the hard work done by Andreas Stoll, Dr. Harendra Fernando, and Dr. Roger Haynes at the Leibniz Institute for Astrophysics Potsdam. Thank you for the fruitful and productive collaboration, and for making my visit to Potsdam an amazing and productive experience. I would also like to thank all the other members of innoFSPEC I had the pleasure of meeting and working with during my time there.

To my student colleagues Geraldine Marien, Alex Arriola, Izabela Spaleniak, and others, thank you for the amazing times. To G, my astro-buddy, it's been a long, hard journey and I couldn't have done it without you. Thanks so much for everything. Alex, it has been a pleasure writing up along side you, thanks for all the encouragement and

great times. I am sure our paths will cross again, and I eagerly look forward to it.

I would also like to thank all the members of the Physics department at Macquarie University for all the years of support and for creating such a friendly and collegial atmosphere in which to study. I would also like to thank the administrative staff (Carol, Lisa, Laura, Jane, & Amanda) for helping me navigate the treacherous waters that is university bureaucracy. I would like to acknowledge the support of the AAO and its staff, in particular the Anglo-Australian Telescope's observing support staff who made my time at the telescope an amazing experience I will always cherish. The brilliant conversations at AAO morning tea with people like Simon O'Toole and other brilliant astronomers had a huge impact on me.

Finally and most importantly, I wish to thank my family and loved ones, to whom I dedicate this thesis. To my parents Mihailo & Divna Cvetojevic, thank you for all the sacrifices you have made during your life to ensure Iva and I had the opportunity to follow our dreams. Your unshakable strength, unwavering support, boundless love, and ceaseless curiosity inspire me daily. To my sister Iva, thank you for all the support, love, and the occasionally needed kick-in-the-pants. To my aunty Dejana and baka Danica, thank you for the years of support and love. Thank you for always being interested in what I'm working on, but most of all, thank you for being proud of me when I have succeeded at it. I would also like to thank my brilliant friends & house mates for all the good times and binging me back down to earth. Lastly and most importantly I would like to thank my beautiful partner Chloe Braithwaite, who provided limitless support and joy during this time in my life. You were my anchor in times of rough seas, the star that help me navigate the darkness, and the calm wind that carried me to the end of this voyage.

Cheers,
Nick

This work was produced with the assistance of the Australian Research Council under the ARC Centres of Excellence & LIEF programs, and the Macquarie University Research Excellence Scholarship.

"First I shall do some experiments before I proceed further, because my intention is to cite experience first and then, with reasoning, show why such experience is bound to operate in such a way. And this is the true rule by which those who speculate about the effects of nature must proceed."

Leonardo da Vinci

1 Introduction

The term "spectrum" (Latin for "appearance" or "apparition") can be dated back to 1704 in Sir Isaac Newton's seminal work "*Opticks*" [1], used to describe the colours produced when sunlight is dispersed through a prism. In the text, he offers one of the earliest known recordings of a spectrum, along with labelling the colours found therein (Fig. 1.1). At the time Newton was not equipped to study the spectrum in more detail, however later using a telescope and prism Newton viewed the light from Venus, again noting the light contained a continuous spectrum. Newton's work with spectral light was not broadly recognised, and little additional work on the nature of spectra was done in the subsequent 150 years.

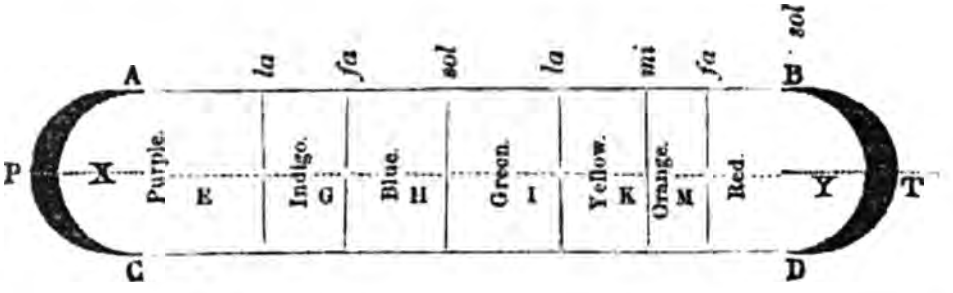

FIGURE 1.1: One of the first illustrations of the optical spectrum made by Sir Isaac Newton. The diagram was made of the spectrum as seen projected on a wall through a prism. Figure courtesy of [2].

The early 19^{th} century saw a number of pivotal breakthroughs on the nature of light and early applications in astronomy. In 1800, William Herschel tested the heating power of the colours of the solar spectrum by placing sensitive thermometers at various locations of the spectrum. Herschel discovered that the maximum heating effect took place beyond the red end of the visible spectrum, widely considered as the first detection of infrared (IR) light. Furthermore, the following year J.W. Ritter tested the effect of the solar spectrum on various chemicals, using a quartz prism and chemically coated paper. Ritter found that silver chloride blackened when placed at a point beyond the violet end of the spectrum, discovering ultraviolet (UV) light.

In 1801, a new demand for high quality glass and lenses arose, driven predominantly by the French military government of the newly conquered Bavaria. The poor quality of the lenses available at the time for surveyor's transits severely limited the survey of Napoleon's new territories, triggering the creation of a glass-making company in a monastery called Benediktbeuern near Munich. By 1814, Joseph von Fraunhofer was in charge of Benediktbeuern's glass production, and in an attempt to measure small differences in the glass composition from one melt to another, he turned to a discovery that had been made in 1802 by English chemist William Hyde Wollaston. Wollaston noted that if sunlight is passed through a prism of sufficiently high quality, a series of dark bands superimposed at regular intervals over the coloured spectrum of light can be observed. At the time, what gave rise to the lines was not understood, nevertheless Fraunhofer measured their position with great accuracy, enabling him to calibrate and measure differences in various glasses manufactured by glassmakers around Europe. During the 1820's, he had made careful measurements of 574 dark lines in the Sun's spectrum, providing a detailed road map for other investigators to follow. Interestingly, it appears Fraunhofer never tried to find out what the lines were or where they came from, but due to his detailed benchmark observations, the dark lines of this type are today referred to as "Fraunhofer lines".

In 1859, Gustav Kirchhoff and Robert Bunsen working at the University of Heidelberg conducted experiments observing the solar spectrum when passed through a sodium flame. To conduct their investigation, they developed what could arguably be called the first spectroscope. Earlier devices used only a prism to refract the light source to a separate viewing scope, making detailed measurements difficult. The spectroscope

that Bunsen and Kirchhoff developed had an integrated slit, prism, and collimator. Debate still exists as to whether the spectral dispersion optics used by Fraunhofer classify as a "spectroscope", and hence credit him with its invention, or whether it was Bunsen & Kirchhoff's improvements to Fraunhofer's design (by adding the slit and collimating optics) that deserve the distinction of being the first spectroscope. Nevertheless, the improvements made to previous designs enabled one of the most important discoveries in astronomy.

It had been known for some time that the light from burning materials, when passed through a prism, splits up into a series of sharp lines called spectral lines, rather than a continuum, as happens with sunlight. Kirchhoff and Bunsen's goal was to look at light from burning materials in a systematic way, cataloguing the positions of various spectral lines. They accurately recorded the spectra of lithium, sodium, potassium, calcium, strontium, and barium salts burned in a flame. Their discovery was a demonstration that the solar absorption lines were the reverse of some of emission lines recorded in the lab. In 1861, Bunsen and Kirchhoff performed experiments that led them to the conclusion that the dark lines in the solar spectrum, observed by Fraunhofer, arise due to the absorption of light by gases in the solar atmosphere that are cooler than those emitting the light. They showed strong evidence for the presence of iron, magnesium, sodium, nickel, and chromium in the atmosphere of the Sun. Further, using this technique, the pair discovered two new elements: caesium and rubidium. Kirchhoff and Bunsen's use of spectral analysis to determine the chemistry of the solar atmosphere is often considered to be the birth of modern astrophysics. The late 19th century saw a series of major astrophysical discoveries enabled by the spectroscope, which at the time was quickly being absorbed into the typical tool set used by astronomers. The amateur astronomer Norman Lockyer used a spectroscope and a six-inch telescope in his back yard to discover the solar chromosphere (by observing hydrogen emission lines) and demonstrated that sunspots were cooler than their surroundings (by noting that the Fraunhofer lines became darker). Perhaps more importantly, in 1868 while studying the solar spectrum, he noticed an absorption line nestled between two bright yellow sodium lines that did not belong to any known element. Lockyer named the element helium, from Helios, the Greek word for "Sun".

The development of early photography in the mid-19th century was also quickly

picked up by astronomers who combined this new technique with the existing spectroscopes, enabling the spectra to be recorded and accurately catalogued, creating the first early spectrographs. Sir William Huggins and his wife Margaret Lindsay Murray were among the early spectrograph pioneers, using their study of spectral features to distinguish the difference between nebulae and galaxies. They were also the first to examine the spectrum of a planetary nebula, record the spectrum of a nova, and identify ethylene in the spectrum taken of a comet. Photography also enabled the Henry Draper (HD) catalogue, which compiled spectra of nearly a quarter of a million stars for study.

Today, the use of spectra to analyse the chemical composition of celestial objects is so widespread that a spectrograph (and often more than one) is a part of nearly every major research observatory in the world. Over the last century, the individual components of the spectrograph have been vastly improved, in particular the dispersion element responsible for splitting the light. Volume Phased Holographic (VPH) gratings, ruled transmission gratings, Echelle gratings, Grisms (a combination of a prism and a grating), as well as others, have provided astronomers with unparalleled resolution, efficiency, and flexibility when building spectrographs. Modern spectrographs are integral to almost every form of astrophysical inquiry, from the study of distant Quasars, to the hunt for extra-solar planets. Their wide use and the ever-present need for more sensitive and accurate measurements, has propelled spectrograph construction and design into something of an art form. The complexity of modern designs, necessitated by the drive to stay competitive, has driven the cost and scale of some spectrographs into the scale of multi-million dollar projects. While modern fabrication techniques in the commercial sector have somewhat slowed the spiralling costs, the instrument costs are steadily rising with the next-generation of large-aperture telescopes being built. Interestingly, while the individual components have advanced spectacularly, the fundamental spectrograph design has not really changed since mid-19th century. Collimating and focusing optics (either refractive or reflective optics), a dispersive element (grating or prism), and a detector, still constitute the majority of spectrographs currently deployed around the world.

Recent developments in photonics provide an entirely new approach to solve the problems faced by the next generation of spectrographs. Photonics centres on the

manipulation, generation, and detection of light on both macro and microscopic scales using new materials and new processes to create photonic circuits. Optical fibres are one such photonic technology, which has already seen extensive use in astronomy and in particular, spectrograph design. Optical fibres are used by observatories around the world to capture light from the telescope focal plane and remap it to a pseudo-slit which feeds the spectrograph. This form of Multi Object Spectroscopy (MOS) not only allows for an arbitrary configuration of the focal plane fibre positions, but also can transport the light efficiently over great distances, and place them arbitrarily in whatever orientation is needed. However, while optical fibres have been widely accepted as standard use in astronomical instruments, the field of photonics has produced other technologies which have not yet been explored in detail for astronomical use.

Since the 1990's, great leaps have been made in the area of integrated photonics, where microscopic waveguides inside glass are used to guide and manipulate light on the fundamental scales. The rapid development of photonic circuitry was largely driven by the rise of the Internet and the ever-growing need for fast and reliable telecommunications. Because all modern high-speed communication is encoded in light, integrated photonic circuitry allowed for passive manipulation of the signal using no moving parts or electronics. Today, the use of photonic circuitry is found in almost every fibre-network, with commercial companies around the world able to reproducibly fabricate complex photonic circuits.

This thesis focuses on exploring the application of emerging photonic technologies for new astronomical spectrograph designs. In particular, we explore light-guiding circuitry in glass as a possible new platform for creating modular, ultra-stable, miniature spectrographs. The light can be manipulated over much smaller baselines than in conventional spectrographs, with the light being dispersed over a region of a few centimetres rather than metres associated with conventional spectrographs. The emergence of astrophotonics, a field that lies at the interface of astronomy and photonics, is timely, as it has the potential to solve a number of outstanding problems in astronomical instrumentation.

In this thesis we outline the concept of the Integrated Photonic Spectrograph (IPS), a 'spectrograph-on-a-chip' for astronomical use. We outline the design, theory, and manufacture of the photonic circuitry used to create prototype devices, as well as

highlight the first successful on-telescope demonstration of a photonic spectrograph, before presenting new designs for the next generation of IPSs currently in construction. We also discuss a few instrument concept ideas which employ IPSs to, in some cases, achieve an improvement in stability over classical designs.

In Chapter 2, we present the fundamental principles that govern the operation of spectrographic devices and derive and explain basic spectrograph terminology which will be used for the rest of the thesis. We also discuss in detail the characteristics of slit spectrometers, which are needed to appropriately compare and contrast with the photonic approach presented in this thesis.

A comprehensive explanation of integrated photonic circuitry is provided in Chapter 3, with a particular focus on the Arrayed Waveguide Grating (AWG) architecture. We provide a basic outline of the design, theory, and manufacture process of the photonic circuitry used to create prototype IPS devices. In Chapter 4, we describe the experimental set-ups used to probe lithographically fabricated AWG-based spectrographs and results obtained from their tests. The techniques used to measure key specrograph performance parameters such as resolving power and throughput are presented, and new injection techniques are highlighted. We characterised two separate AWG designs to compare and contrast design parameters for astronomical use and explain how, with minimal changes to off-the-shelf designs, we were able to obtain a more than three-fold improvement in resolution.

While photonic spectrographs have been characterised in laboratory conditions for their applicability for astronomy, they were not previously demonstrated on a working telescope. This is of particular importance as the interfacing of photonic technologies, particularly diffraction limited (mono-mode) devices to ground based telescopes is a challenge. In Chapter 5, we outline the design, construction, and telescope interface of a prototype IPS instrument tested on the 3.9 m Anglo-Australian Telescope (AAT) at Siding Spring Observatory, Australia. The test resulted in the detection of carbon monoxide molecular absorption lines in the NIR, which are to our knowledge the first astrophysical spectral features detected using a photonic spectrograph of any kind.

The development of IPS prototypes thus far has used AWG designs originally developed for telecommunications purposes. As such, key spectrograph performance parameters of the devices, such as resolution and the free spectral range, were not tailored for

any specific astronomy science case. In Chapter 6, we present how the key parameters can be increased to provide performance above the typical telecommunication requirements and make them comparable, if not superior, to existing astronomical spectrographs. In the chapter we discuss two distinct AWG designs and propose how they can be scientifically advantageous. The first is a large FSR design (few hundred nm) that can enable the realisation of an entirely-photonic spectrograph directly bonded to a detector. The second design explores the high-resolution regime (R ~60k) where the inherent environmental stability of a monolithic on-chip spectrograph is highly sought after. For this application, we provide an expanded science case for exo-planet detection, in particular the exciting prospect of studying earth-like planets in the habitable zone of M-dwarf stars. We present both the designs and beam-propagation modelling results of AWG performance for the two cases. Lastly, we describe the PANDORA technology demonstrator instrument, that is being fabricated at the time of writing, which will employ the High-R AWG chip designed in this thesis and an extreme adaptive optics system at the Subaru telescope. This device can potentially provide unprecedented radial velocity sensitivity in the NIR at a fraction of the cost of comparable non-photonic systems.

Concluding remarks and future outlook are provided in Chapter 7 along with a summary of the key themes and achievements contained in this thesis.

"Light brings us the news of the Universe."

Sir William Bragg

2

Overview of Astronomical Spectrographs

Over the last few hundred years, spectrographs have become one of the most important tools for studying the physics of celestial objects. It is therefore no surprise that spectrographs have seen considerable development from their basic roots in the 1800s. Today a large fraction of telescope time is used to obtain spectral data, with spectrographs becoming work-horse instruments for astronomy. Further, many different configurations of spectrographs are used to service specific science cases.

For a traditional spectrograph setup, detailed spectral information is obtained by passing light through a slit before continuing through a dispersing element, such as a prism or diffraction grating. In this case, a spectrum is obtained for each source whose light passes through the slit. However, in the case of large surveys, this configuration is not ideal, thus various forms of slitless spectroscopy are used. Here, a prism or grating is used to disperse the entire telescope focal plane, producing a small spectrum at the location of every source in the image.

Other spectroscopic configurations used extensively in astronomy are multi-object spectroscopy (MOS), integral field spectroscopy (IFS), and high-resolution Echelle (single object) spectroscopy. Each of these modes can use optical fibres to transfer light from a 2D focal surface of a telescope to a 1D spectrometer slit, combining the advantages of both the slit and slitless techniques. The difference between the modes is the arrangement of the fibres on the 2D focal surface. For MOS, each fibre is set on a single

source within a group of stars or galaxies, while for IFS the fibres are tightly packed in an integral field unit (IFU) in order to get spectra over an area of an extended source (galaxy, nebulae, etc.).

In this chapter, we present an overview of the basic principles that govern the operation of spectrographic devices. The overview provided in this chapter is by no means exhaustive, with entire books dedicated to this subject (in particular, the reader is directed to [3–5]). However, we cover the key topics required to understand terminology, which will be important in later chapters, such as resolution limits, spectral resolving power, and free spectral range. We also discuss in detail the characteristics of slit spectrometers, which are needed to appropriately compare and contrast with the photonic approach presented in this thesis.

2.1 Spectrograph fundamentals and definitions

Each type of spectrometer is denoted by the kind of dispersing element that is used, hence prism, grating or Fabry-Perot spectrometer. The dispersing element is typically located between auxiliary optics that collimate the light beam from the telescope and focus the dispersed beam onto a detector.

One type of spectrometer that does not have a dispersing element is the Fourier transform spectrometer. This instrument is essentially a Michelson interferometer whose output is an interferogram from which spectral information is derived by Fourier analysis. Because the Fourier spectrometer is not a dispersive device, the definitions in the following sections that include dispersion don't apply. While we do not focus on this particular type of spectrograph in the thesis it is worth mentioning as a possible alternative.

2.1.1 Angular and linear dispersion

Each type of dispersing element is characterised by its angular dispersion, defined as $d\beta/d\lambda$, where $d\beta$ is the angular difference between two rays of wavelength difference $d\lambda$ emerging from the disperser. This is shown schematically in Fig 2.1 for a single ray incident on the dispersing element. Further details on specific dispersion elements (transmission & Echelle gratings) are given in later sections.

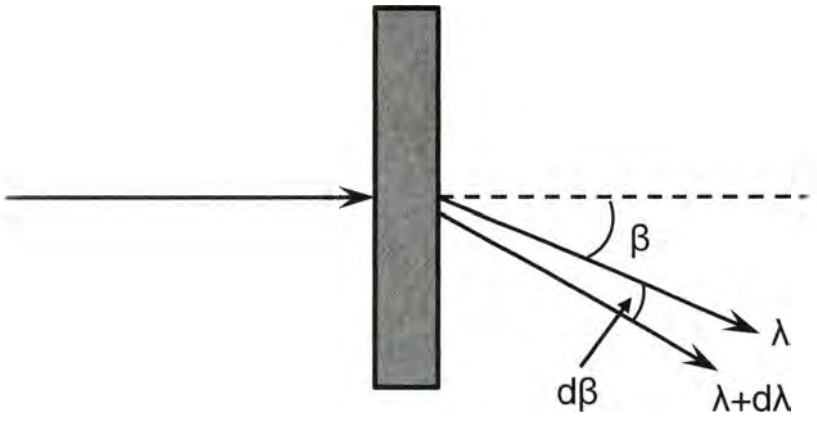

FIGURE 2.1: Schematic of dispersive element.

The angular dispersion is a parameter associated with the dispersing element, independent of the configuration that is used. When the element is part of an optical system, the characteristics of both are combined to define linear dispersion $(dl/d\lambda)$, where dl is the linear separation on a focal surface between two rays of wavelength difference $d\lambda$.

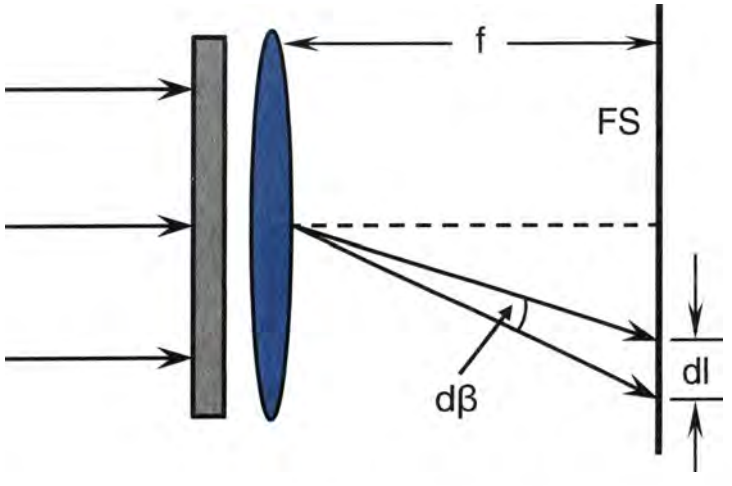

FIGURE 2.2: Schematic of linear dispersion. The spectrum is focused onto the focal surface (FS).

If collimated light is incident on the disperser, then the linear dispersion is given

by:

$$\frac{dl}{d\lambda} = f\,\frac{d\beta}{d\lambda} = fA, \tag{2.1}$$

where f is the focal length of the optics following the dispersing element, and A is the angular dispersion. This is shown in Fig. 2.2.

If a convergent beam of light is incident on the disperser, the linear dispersion is:

$$\frac{dl}{d\lambda} = s\,\frac{d\beta}{d\lambda} = sA, \tag{2.2}$$

where s is the distance from the disperser to the focal surface, as shown in Fig. (2.2).

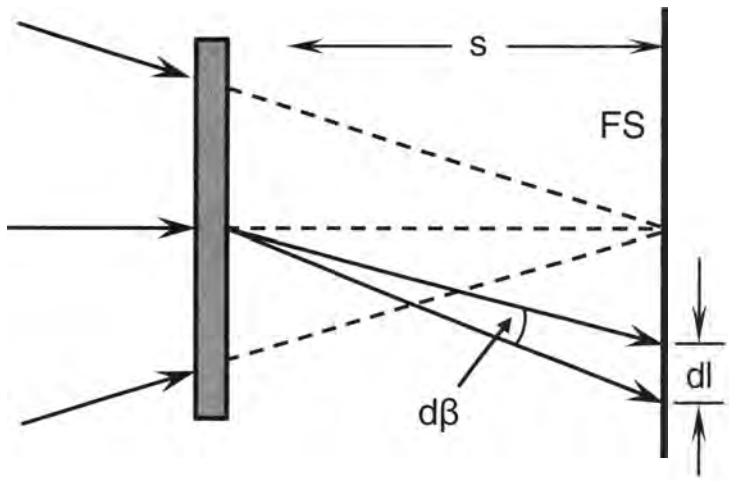

FIGURE 2.3: The spectrum is focused onto the focal surface (FS) with convergent light incident on the disperser.

2.1.2 Spectrometer Modes and Plate factor

Spectrometer configurations to which Eq. (2.1) applies include both slit spectrometers and a slitless mode where a prism or grating is placed in front of a telescope. In the case of a slit spectrometer, a separate collimator provides a collimated beam to the dispersing element and f is the focal length of the focusing optics, traditionally referred to as 'camera optics'. The configurations that Eq. (2.2) applies to include a slitless mode where a disperser (typically a grating or grism) is placed in a converging telescope beam ahead of the focal surface. The grism is a combination of a grating and prism, with the grating as the main dispersive element. The equation also applies to

a Monk-Gillieson spectrometer, in which a mirror preceding the disperser is both the collimator and camera.

For any spectrograph setup, it is important to define P the plate factor, or the reciprocal of the linear dispersion, where:

$$P = (fA)^{-1}, \tag{2.3}$$

with the units usually given as Angstroms ($\AA$) per millimetre, or nanometres per millimetre.

2.1.3 Slit Spectrometers

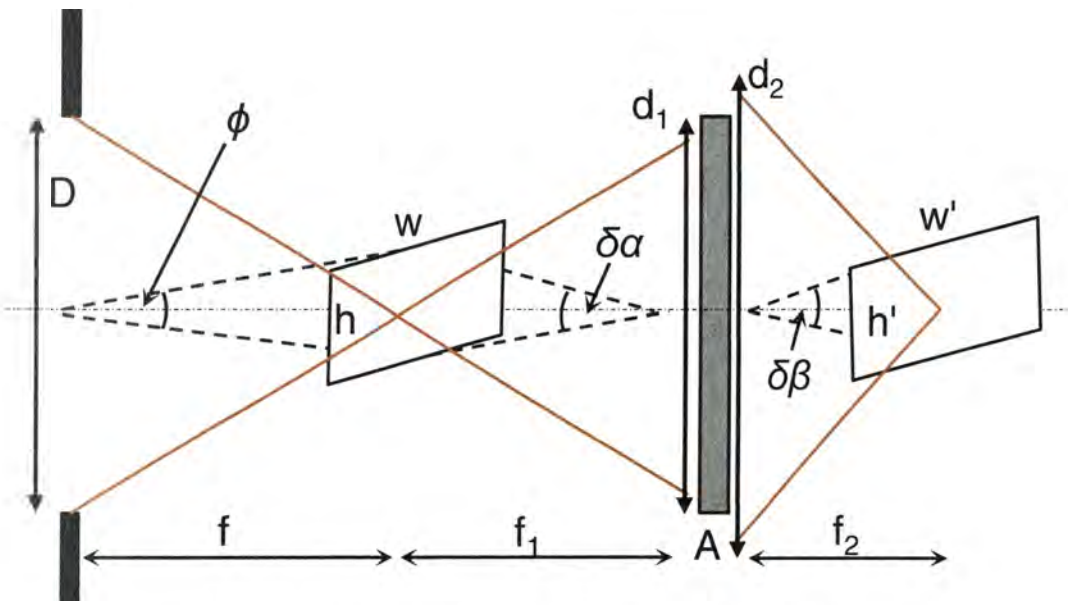

FIGURE 2.4: Schematic layout of a slit spectrograph.

A general layout of a slit spectrometer in the most commonly used arrangement is shown in Fig. 2.4. Elements of the spectrometer include an entrance slit of width w and height h at the telescope focus, collimator and camera optics to reimage the entrance slit, and a disperser with an angular dispersion of A. The focal lengths of the collimator and camera optics are f_1 and f_2 respectively. The reimaged slit has a width of w' and height h' at the camera focus.

The entrance slit subtends angles ϕ and ϕ' on the sky and $\delta\alpha$ and $\delta\alpha'$ at the collimator, where $\phi = w/f$, $\phi' = h/f$, $\delta\alpha = w/f_1$, and $\delta\alpha' = h/f_1$. The collimated

beam incident on the disperser has a diameter d_1, with the direction of dispersion parallel to the slit width.

Typically, for optimal performance, the slit-width (w) is matched to a number of parameters unique to each telescope. In particular, it is changed such that the angle subtended on the sky by the slit (ϕ) matches the typical angle of an unresolved point-source in the sky, usually stars. Apart from a few rare exceptions such as Betelgeuse, the physical size of the star is always unresolved, and so all stars will appear as Point Spread Functions (PSFs) of the smallest resolvable feature by the telescope. There exist two cases; *seeing limited*, where the size of the smallest PSF (and therefore ϕ) is determined by the local atmospheric conditions at the observatory, and therefore not determined by telescope design, and *diffraction limited*, where ϕ is directly determined by the telescope's size and geometry. These cases are discussed in detail in later subsections.

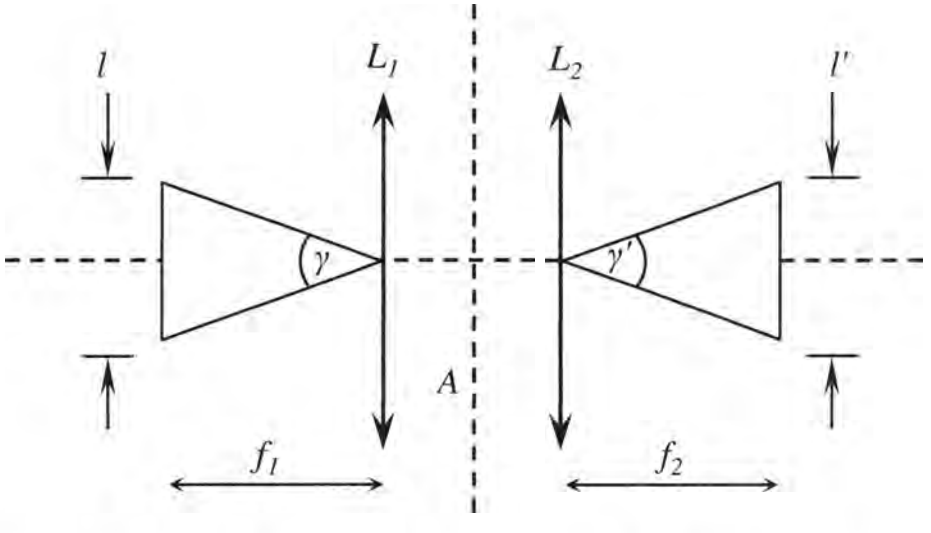

FIGURE 2.5: Layout of anamorphic magnification due to a dispersive element.

The size of the projected slit image depends upon f_1, f_2 and the characteristics of the disperser. Figure 2.5 shows the collimator and camera represented by equivalent thin lenses, with an object of length l subtending an angle γ at the collimator and its image of length l' subtending an angle γ' at the camera. For a system with no dispersing element between the lenses, $\gamma' = \gamma$ and $l' = l(f_2/f_1)$. Because a system without a disperser is rotationally symmetric, these relations are true for any orientation of the object.

If a dispersing element is placed between the lenses, rotational symmetry is broken, and the equality of the subtended angles is not necessarily preserved for different orientations of the object. In the direction perpendicular to the dispersion, the beam remains unchanged, ($\gamma' = \gamma$). This is not the case in the direction along the dispersion, where possible magnification effects of the disperser must be taken into account such that $\gamma' = r\gamma$. In terms of the subtended angles in Fig. 2.4 :

$$r = \frac{d\beta}{d\alpha}. \tag{2.4}$$

The parameter r is called the 'anamorphic factor' or 'anamorphic magnification', and depends on the type and orientation of the dispersing element. The anamorphic factor is essentially the ratio of the beam widths at the collimator and the camera ($r = d_1/d_2$), which for now we simply note but is derived in the next section for grating spectrometers.

Applying these results to the slit dimensions in Fig. 2.4, we obtain

$$w' = rw(f_2/f_1) = r\phi DF_2, \tag{2.5a}$$

$$h' = h(f_2/f_1) = \phi' DF_2, \tag{2.5b}$$

where $F_2 = f_2/d_1$. This definition of the camera focal ratio in terms of the collimator beam diameter is made to ensure that F_2 can be used in a meaningful way when discussing irradiation of detector pixels in the next section.

The relation of Eq. (2.5a) is important in establishing the proper value of F_2 for a detector whose pixel size (Δ) is correctly matched to w', the reimaged slit width. If we match it so that two pixels cover the width ($2\Delta = w'$), then $2\Delta = r\phi DF_2$. If for example we choose $\Delta = 20$ μm, $\phi = 1$ arcsec, and $D = 4$ m, then from Eq.(2.5a) we find that $rF_2 = 2$. This matching between pixel size and projected slit width is based on the Nyquist criterion for discrete sampling. For this chapter, we simply state that the minimum of two samples per resolution element are required for unambiguous separation of images that are just resolved according to the Rayleigh criterion.

2.1.4 Spectral Resolving Power and Resolution Limit

Let us consider a spectrometer entrance slit of width w, illuminated by light from two monochromatic wavelengths, λ and $\lambda + \Delta\lambda$. The slit image at each wavelength has width w' and from Eq. (2.1), the separation between the centres of the images (Δl) is

$$\Delta l = f_2 A \Delta\lambda. \tag{2.6}$$

We define the limit of resolution ($\delta\lambda$) as the wavelength difference for which $\Delta l = w'$. Hence, the spectral images are on the verge of being resolved with a detector satisfying the Nyquist criteria. Placing this condition on Δl into Eq.(2.5a), and using Eqs.(2.1) & (2.3), gives

$$\delta\lambda = (\frac{d\lambda}{dl})\Delta l = Pw' = \frac{r\phi}{A}\frac{D}{d_1}, \tag{2.7}$$

where from Fig. 2.4 it can be seen that $f_1/d_1 = f/D$.

For a given telescope diameter and angle subtended on the sky, it is clear from Eq.(2.7) that the key factors that determine the limit of resolution are the angular dispersion and collimator beam diameter. We also see that placing a given spectrometer on a large telescope, gives a larger $\delta\lambda$ for the same angle on the sky. In order to maintain the same resolution with a given spectrometer on a large telescope it is necessary to keep $\phi D/d_1$ constant, hence a larger spectrograph is required for the same angle on the sky.

2.1.4.1 Spectral Resolving Power

The spectral resolving power (R) is a dimensionless figure of merit of the resolution limit for spectrographs used in astronomy and is defined as $R = \lambda/\Delta\lambda$. Thus,

$$R = \frac{\lambda}{\delta\lambda} = \frac{\lambda A}{r\phi}\frac{d_1}{D}. \tag{2.8}$$

This equation highlights an important and somewhat counter-intuitive fact, that the resolving power of a spectrograph is inversely proportional to the telescope diameter (D). If a spectrograph is taken to a larger telescope, all things being equal, the resolution will drop. This is seemingly unusual as it implies the spectrograph 'knows' about the telescope it is placed on. During the spectrograph design, the value for R

is usually picked to match particular science goals of the instrument, and is therefore fixed. Thus, larger telescopes require a larger beam diameter (d_1) for a given type of disperser if the resolving power is to be kept constant. This gives rise to the telescope-spectrograph size relation (highlighted in the next chapter), where the physical size of the spectrograph instrument scales in size with the size of the telescope it is placed on. This is because as the collimating optics increase in size (to accommodate the larger beam diameter), the camera optics also increase. Faster optics (where the focal length of the lens is smaller for a given beam diameter, in this case d_1) are harder to manufacture without aberrations and are typically more expensive. Therefore, slower optics are used instead which extends the focal length, which when combined with the larger beam diameter, leads to an overall size and volume increase to the instrument.

2.1.5 Diffraction limit

The reason the size relation highlighted above is not evident in many non-astronomical spectrograph designs is because the relation for the limit of resolution does not take into account the limit on the image size set by diffraction. Assuming no atmosphere is present (space telescopes for example), the telescope focuses to the perfect image allowed by diffraction. One important characteristic of a perfect image from a telescope with an circular aperture is the FWHM of the airy ring, given by

$$\phi_{FWHM} = 1.03\frac{\lambda}{D}. \tag{2.9}$$

In this case, the effective width and height of the entrance aperture can be set such that they are equal to the FWHM, so

$$\phi = 1.03\frac{\lambda}{D} \approx \frac{\lambda}{D}. \tag{2.10}$$

By substituting this value for ϕ into the the equation for the resolution limit (Eq. (2.7)), we get

$$\delta\lambda = \frac{r}{A}\frac{D}{d_1}\frac{\lambda}{D} = \frac{r\lambda}{Ad_1}, \tag{2.11}$$

and solving for resolving power R gives

$$R = \frac{\lambda}{\Delta\lambda} = \frac{Ad_1}{r}. \tag{2.12}$$

It is clear that in the diffraction limited case, the telescope diameter term (D) cancels out and spectrograph performance is purely a function of its internal components (angular dispersion and beam size). Hence, for diffraction limited telescopes, the size relation is broken.

2.2 Grating Spectrographs

The diffraction grating is the primary dispersing element in most astronomical spectrographs, where it has an advantage of significantly larger spectral resolving power than a prism of comparable size. A grating is also versatile in the spectral formats it can provide, and can be efficient over a reasonable wavelength range. In this section, we describe the basic relations outlined in the previous section if a grating is used as a primary dispersive element.

2.2.1 The Grating Equation

The starting point for most discussions involving gratings is the well-known grating equation, see for example [3] for a detailed derivation. For the case of a chief ray in the xz-plane, with the grating grooves parallel to the y axis in the yz plane, the grating equation is

$$m\lambda = \sigma(\sin\beta \pm \sin\alpha), \tag{2.13}$$

where m is the grating order, σ is the distance between successive equally spaced grooves on the grating, and α and β are angles of incidence and diffraction respectively, measured from the normal of the grating surface. The plus sign in the equation above applies to a reflection grating and the minus sign to a transmission grating.

The schematic of grating cross-sections are shown in Fig. 2.6 for both a reflection and transmission grating. For a reflection grating, the angles α and β have the same signs if they are on the same side of the grating normal, while for a transmission grating they have the same signs if the diffracted ray crosses the normal at the point of diffraction.

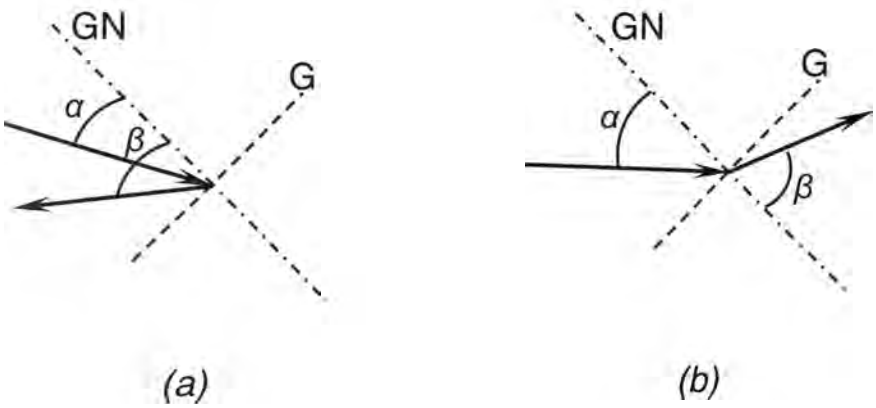

FIGURE 2.6: Schematic showing angles of incidence (α) and diffraction (β) compared to the grating (G) and grating normal (GN), for a reflection grating (a) and a transmission grating (b).

2.2.2 Angular Dispersion

The angular dispersion follows directly from Eq. (2.13) by holding α constant and differentiating with respect to λ, resulting in

$$A = \frac{d\beta}{d\lambda} = \frac{m}{\sigma \cos\beta}, \tag{2.14a}$$

$$A = \frac{\sin\beta + \sin\alpha}{\lambda \cos\beta}, \tag{2.14b}$$

From here on in we will refer to reflection gratings, hence the plus sign in Eq. (2.14b).

From Eq. (2.14a) the angular dispersion in a given order m is a function of σ and β. When looked from this point of view, changing A means choosing a grating with a different groove separation and/or using the grating at a different angle of diffraction. From Eq. (2.14b), we see that A, at a given wavelength, is set entirely by the angles α and β, independent of m and σ. Thus a given angular dispersion can be obtained with many combinations of m and σ, provided the angles at the grating are unchanged and m/σ is constant. Recognition of this fact led to the development of Echelle gratings, coarsely ruled reflection gratings specifically designed to achieve high angular dispersion by making α and β large (typically $\sim 60°$). Echelle gratings

typically have groove densities in the range of 300 to 30 per mm with values of m in the range of 10 to 100 for visible light. Typical first- or second-order gratings have groove densities between 300 and 1200 per mm.

2.2.3 Anamorphic Factor

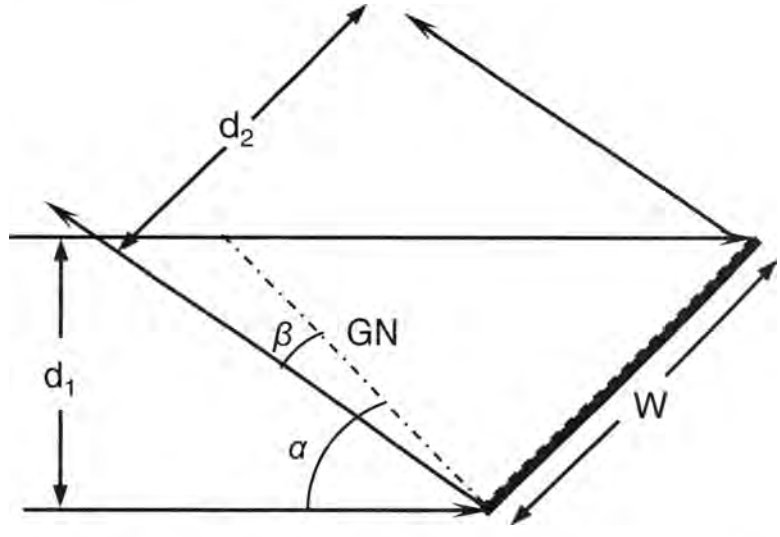

FIGURE 2.7: Change in collimated beam width due to anamorphic magnification from a grating.

The relation for the anamorphic factor is derived from Eq. (2.13) by holding λ constant and finding the change in β for a change in α. The result is $\cos\beta\, d\beta + \cos\alpha\, d\alpha = 0$, and thus it follows that

$$r = \frac{|d\beta|}{|d\alpha|} = \frac{\cos\alpha}{\cos\beta} = \frac{d_1}{d_2}. \tag{2.15}$$

The relation between the beam widths and angles is derived from the geometry shown in Fig. 2.7, with $d_1/\cos\alpha = d_2/\cos\beta$.

Because r is in the denominator of the resolving power given in Eq. (2.8), the choice of $r < 1$, hence $\beta < \alpha$, gives a higher resolution. This condition means that the grating normal is more in the direction of the camera than of the collimator optics. If the grating is to accept all the light from the collimator, it follows that $W = d_1/\cos\alpha$ is required, where W is the width of the grating.

2.2.4 Spectral Resolving Power

Substituting Eq.(2.14a) into Eq. (2.8) we get

$$R = \frac{\lambda}{\delta\lambda} = \frac{\lambda m W}{\sigma \phi D}. \tag{2.16}$$

If we define the number of illuminated grating grooves to be $N = W/\sigma$, we obtain

$$R = \frac{\lambda m N}{\phi D}. \tag{2.17}$$

2.2.4.1 Diffraction Limited Grating Spectrograph

As demonstrated before, if the telescope is diffraction limited $\phi \approx \frac{\lambda}{D}$. Thus, substituting this into Eq. (2.17), we obtain.

$$R = mN. \tag{2.18}$$

This is the common equation used to describe the resolving power of grating spectrographs operating at the diffraction limit. It is exclusively a function of the grating order m and the number of illuminated grooves on the grating N. At this point, it is important to highlight that N is not the total number of grating grooves, but the total number of illuminated groves by the incoming collimated beam, which as part of this derivation we assumed are the same. This is a subtle difference, but it is rare in practice that all the grating teeth are illuminated with even illumination, and one that will become important when discussing diffraction-limited photonic spectrographs in the next chapter.

2.2.5 Free Spectral Range

For a given pair of α and β, the grating equation is satisfied for all wavelengths for which the grating order m is an integer. Thus, there are two wavelengths in successive orders λ and λ', for which we have $m\lambda' = (m+1)\lambda$. The wavelength interval between these two wavelengths is called the Free Spectral Range (FSR), and is defined as

$$FSR = \Delta\lambda = \lambda' - \lambda = \frac{\lambda}{m}. \tag{2.19}$$

Because the two wavelengths are diffracted in the same direction, they will overlap on the camera and will be spatially indistinguishable. There are two solutions to eliminate the wavelength overlap: either the other orders are rejected using a filter prior to

the camera, or the orders are separated using another disperser in the perpendicular direction, referred to as cross-dispersion. Depending on the circumstances either technique can be employed, however it is important to note that if a 2D detector is used to image the camera's focal surface, cross-dispersion will allow multiple orders to be recorded simultaneously, expanding the total wavelength coverage of the spectrograph.

2.3 Conclusion

In this chapter, we derived some key spectrograph parameters such as the resolving power and free spectral range. We also provide a brief overview of the various spectrograph components and their impact on performance. We focused primarily on grating-based slit spectrographs, as they are the clearest analogue to the photonic spectrographs we present in the next chapter.

In addition, we derive the reason for the telescope-spectrograph size relation (Section 2.1.4.1) which exists for spectrographs implemented on seeing-limited telescopes. This scaling law has resulted in spectrographs becoming physically larger as the primary mirror size of modern telescopes increased. With the next generation of extremely large telescopes on the horizon, alternatives to the traditional bulk-optic spectrographs outlined in this chapter are highly sought after.

"Science is a way of thinking much more than it is a body of knowledge."

Carl Sagan

3 Photonic Spectrographs

In the previous, chapter we outlined how conventional bulk optic spectrographs operate, however over the past 20 years there has been considerable development of photonic technologies driven by the telecommunications industry. One such technology is integrated photonic circuitry which may hold the key to fabricate a new type of integrated photonic miniature spectrograph for astronomical use.

Traditionally, prior to the advent of Adaptive Optics (AO) based systems, instruments were designed to match the natural seeing of the site. This means that as the telescope aperture D grows, the size of the instrument grows in proportion to D, and the cost of the instrument increases as D^2 or faster [6].

Scaling from existing concepts, a single spectrograph for an ELT could cost \$50-100M, comparable to the cost of building today's largest telescopes [7]. Given that the astronomical community is now moving towards extremely large telescopes (ELT), the dependence of cost on D poses a major problem to realising practical ELT instruments. Even if cost is ignored, such large spectrographs have inherent difficulties when performing high resolution radial velocity studies, and require complex and expensive engineering to overcome misalignments due to temperature variations or flexure.

Recent developments in photonics provide an entirely new approach to solving this problem. The light can be manipulated over a much smaller footprint than in conventional spectrographs. The light is injected into an integrated photonic circuit,

and dispersed over a region only a few centimetres in size rather than a few metres, as is more commonly the case. The emergence of astrophotonics, a field that lies at the interface of astronomy and photonics, is timely as it has the potential to solve a number of outstanding problems in astronomical instrumentation [6, 8–12].

In this chapter, we outline the concept of the Integrated Photonic Spectrograph (IPS), a 'spectrograph-on-a-chip' for astronomical use. We outline the design, theory, and manufacture of the photonic circuitry used to create prototype devices. Further, we briefly discuss the impact of seeing on successful telescope implementation of photonic devices.

3.1 The case for photonic spectrographs

In certain respects, the concept of an integrated photonic spectrograph already exists within photonics and telecommunication research groups, although in order to achieve a device that is suitable for astronomy, a significant amount of research and development is required. The possibility of exploiting IPSs in astronomy was proposed as early as 1995 [13, 14], however at the time the technology to fabricate the required devices was not yet mature enough. The concept was re-visited in 2006, this time exploiting existing technologies which had been developed in the intervening decade [15].

The early fibre optic networks were based on data transfer at a single laser frequency in single-mode fibres (with multimode fibres finding occasional use in the last stages of the network). By 1995, it was clear that the projected need for much higher data rates would require dense wavelength division multiplexing (WDM), i.e. independent data streams carried by many separate wavelength channels in a single fibre. A key requirement of WDM is the ability to disperse the multi-band signal within a specific input fibre or a set of input fibres into separate output channels, and the ability to switch signals between input and output channels. This has given rise to a remarkable device called the array waveguide grating (AWG), also known as the optical phased array (phasor), phase-array waveguide grating, or the waveguide grating router.

The first such device was invented by M. Smit (1991)[16] in the Netherlands. These are now commercially available in various incarnations. AWGs were actually preceded by another similar technology called photonic Echelle gratings, which as the name implies is an integrated micro-Echelle grating on a photonic chip. However, due to

manufacturing difficulties, the micro-Echelle gratings have not seen the same growth and user adoption as AWGs.

At or near the diffraction limit, the focused spot of a telescope is independent of atmospheric seeing (see Eq. (2.12)), and has a size that is compatible with photonic devices. If the light can be efficiently coupled into the device, it can remain within the device and be manipulated by it, before being imaged at the detector. The light does not need to see an air-glass boundary again. Further, as the light stays confined within the glass chip, effects such as thermal convection are non-existent, relaxing the requirements compared to traditional bulk optic designs. The cross-talk performance of telecommunication-grade commercially available devices already indicates that light scatter, birefringence and polarisation effects can be managed to a high degree, and are indeed less than that of bulk optic designs. Instruments based on integrated circuit technology are cheaper to mass produce, easier to control, and much less susceptible to vibration and flexure.

3.2 Arrayed waveguide grating spectrographs

Arrayed waveguide gratings are a particular design of planar (2D) waveguide circuits created in a thin layer of glass, often on a silicon substrate. This AWG chip, is an all-photonic platform (no bulk optics or moving parts) which can spectrally disperse light using an array of waveguides, and conduct passive multiplexing (routing a particular spectral channel into a particular waveguide/fibre). This has made them highly sought-after in the telecommunications industry as an integrated chip based wavelength demultiplexer. As such, much of the development in AWG technology and design has been directed to these applications.

Sales of arrayed waveguide grating wavelength de/multiplexers, a much more complex device than the simple coupler/splitters typically fabricated, have been increasing significantly since the late 1990s [17]. AWGs are one of the first examples of optical integration living up to the promise of eliminating most of the painstaking hand assembly from optical devices. More recently, even more complex devices, i.e. AWGs with switches and variable optical attenuators (VOAs) to act as multiplexers with channel power control (VMUXs), and reconfigurable optical adddrop multiplexers (ROADMs), have seen success in the market.

In this section, we explain the theoretical underpinnings of AWG devices, as well as highlight particular design aspects that will be important in later chapters. This overview is by no means exhaustive, but does deliver the necessary background knowledge from an astronomical instrumentation perspective. For a detailed overview of AWG technology, the reader is directed to Chapter 9 of "*Fundamentals of Optical Waveguides*" by Katsunari Okamoto (2006) and the corresponding review paper [17].

3.2.1 AWG Overview

The essential components of an AWG are the input and output free propagation regions (FPR), also known as star-couplers, and the waveguide array (see Fig 3.1). The basic concept of the operation of this device is as follows. The input FPR (comparable to the collimator of a conventional spectrograph) is a slab waveguide with a step index which allows the light to diverge in the plane of the chip onto an array of closely spaced single-mode waveguides at the far end. The light is collected by the array of waveguides and propagates independently, in each arm of the array. These in turn feed an output star-coupler (another FPR), which is in most applications identical to the input one. The input and output ends of both FPRs are in fact curved to match the so-called Rowland curvature [18], which is tailored in such a way that the waveguides of the array collect the diverging light in-phase (i.e. along a given wavefront). The ouput beams of the waveguide array interfere in the output FPR, and depending of the phase difference between the waveguides in the array, the constructive interference for a given wavelength would appear at a different spot at the output.

Each waveguide in the array is incrementally longer than the previous one by a constant amount, such that a specific central wavelength is chosen to be focused on the end-surface of the output FPR. The array of waveguides behave analogously to the teeth of a grating, i.e they create multiple point sources that interfere. The light interferes in the second FPR such that a dispersed spectrum is formed at the output end of the FPR. For telecommunication applications, the dispersed light at the output of the second FPR is typically coupled into a series of output waveguides [18].

The waveguides in the array are chosen to have a path length greater than the adjacent waveguide by an integer multiple of the center operating wavelength of the device in the effective medium of the waveguide. Thus, the array has a path length

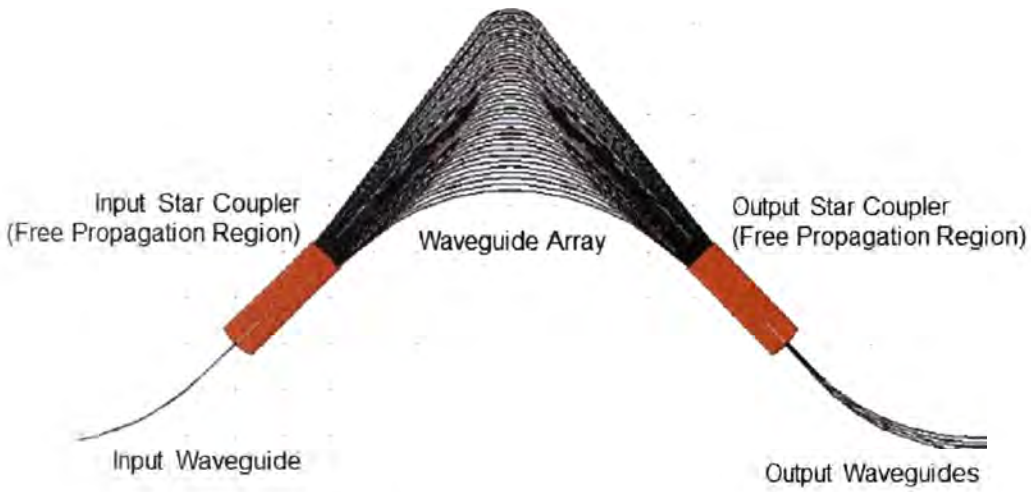

FIGURE 3.1: Typical schematic of an AWG device.

difference between each successive waveguide equal to

$$\Delta L = \frac{m\lambda_0}{n_a}, \tag{3.1}$$

where, m is the diffraction order of the array, λ_0 is the central operating wavelength of the device, and n_a is the effective index of refraction of the waveguide array.

At the center wavelength, the light in each arm of the array will arrive with the same relative phase, producing a mirror image at the output FPR of the field in the input FPR. Thus, when it propagates into the second slab waveguide, it becomes convergent and will be focused into the center of the output side of the second FPR. However, at other wavelengths, as the field propagates along the arrays, the path length differences will cause the overall phase front (the phase front that propagates in the FPRs) to tilt. As a result, these wavelengths will be focused at an angle to the center wavelength. At the output of the second free propagation region, receiver waveguides are typically placed so that these focused fields can be properly confined and guided out.

These free propagation areas are designed in the context of star-couplers. The star couplers in the AWG are based on a Rowland circle geometry and are further discussed in the next section. The geometry of these star couplers is shown in Fig. 3.2.

The central phase matching equation [19] as a result of this system is

$$n_s d \sin(\theta_i) + n_a \Delta L + n_s d \sin(\theta_o) = m\lambda \tag{3.2}$$

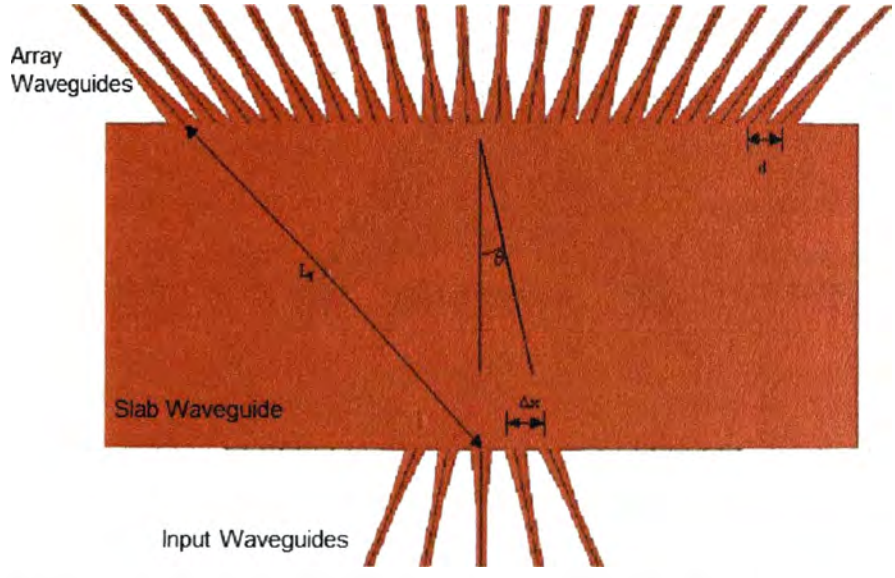

FIGURE 3.2: Typical schematic of a basic star coupler (FPR). The input waveguides enter the slab waveguides at the bottom of the figure. In this case five input waveguides are drawn, but star couplers can have an arbitrary amount of input and output waveguides. The output waveguides are at the top of the figure, with the light in this case propagating from the bottom to top. Important to note is that the star coupler can in fact operate in the reverse direction (light propagating from the top), as will be seen when discussing the output FPR. Parameters used in equations in this section (and elsewhere) are shown with respect to the FPR geometry.

where:

$$\theta_i = i^* \frac{\Delta x}{L_f} \tag{3.3}$$

$$\theta_o = j^* \frac{\Delta x}{L_f} \tag{3.4}$$

where, n_s is the effective index of the slab in the FPR, d is the separation of the inputs and outputs of the waveguide array, i is the number of the input waveguide, j is the number of the output waveguide, Δx is the separation of the input waveguides, and L_f is the focal length of the star coupler.

3.2.1.1 Angular and linear dispersion

To get the angular dispersion of the system, we differentiate Eq. (3.2) with respect to λ, with the assumption that $\theta_i \approx \theta_o \approx 0$, due to the comparatively long length of the FPR compared to d or Δx. Further, we can make the assumption that θ_i is constant,

i.e. only a single input port is used at a time. Thus:

$$m = n_s d\frac{\partial\theta_o}{\partial\lambda} + \frac{\partial n_a}{\partial\lambda}\Delta L \tag{3.5}$$

Substituting ΔL at the centre wavelength λ_0 gives:

$$m = n_s d\frac{\partial\theta_o}{\partial\lambda} + \frac{\partial n_a}{\partial\lambda}\frac{m\lambda}{n_a} \tag{3.6}$$

$$\frac{\partial\theta_o}{\partial\lambda} = \frac{m}{dn_s}\left(1 - \frac{\lambda_0}{n_a}\frac{\partial n_a}{\partial\lambda}\right) \tag{3.7}$$

giving the wavelength dispersion relation:

$$\frac{\partial\theta_o}{\partial\lambda} = \frac{mn_g}{dn_s n_a} \tag{3.8}$$

where n_g is the group refractive index given by:

$$n_g = n_a - \lambda_0\frac{\partial n_a}{\partial\lambda}. \tag{3.9}$$

Rewriting the dispersion relation in terms of frequency:

$$\partial f = \frac{-c^2}{\lambda}\,\partial\lambda \tag{3.10}$$

$$\frac{\partial\theta_o}{\partial f} = \frac{m\lambda^2 n_g}{cdn_s n_a} \tag{3.11}$$

Thus, Eq.'s (3.8) and (3.11) give us the dispersion relation in terms of wavelength and frequency respectively.

We can then solve for the linear dispersion in terms of wavelength and frequency. This is often referred to as the channel spacing and is the spectral shift for a given output waveguide separation (Δx).

$$\Delta\lambda = \frac{\Delta x}{L_f}\frac{\partial\lambda}{\partial\theta_o} = \frac{\Delta x d n_s n_a}{L_f m n_g} \tag{3.12}$$

$$\Delta f = \frac{\Delta x}{L_f}\frac{\partial f}{\partial\theta_o} = \frac{\Delta x c d n_s n_a}{L_f m n_g \lambda^2} \tag{3.13}$$

where L_f is the focal length of the FPR.

3.2.1.2 Free Spectral Range

Much like traditional grating spectrographs described in the previous chapter, AWGs typically operate at multiple orders (m) like Echelle gratings. An additional similarity is that the higher orders are superimposed on top of each other at the output FPR. Hence, when designing AWGs the FSR is often the main determining factor in the allowed number of channels (output waveguides). The free spectral range can be solved for by using Eq. (3.2) for the order $m+1$ channel [16]. Thus, for design purposes, if we make $FSR = \Delta f \times \#\ of\ OutputPorts$, we get:

$$(n_s + \Delta n_s)d\sin\theta_i + (n_c + \Delta n_c)\Delta L + (n_s + \Delta n_s)d\sin\theta_o = (m+1)\frac{c}{f + FSR} \tag{3.14}$$

Next, we find that:

$$\Delta n_c = \frac{\partial n_c}{\partial f}FSR = -\frac{c}{f^2}\frac{\partial n_c}{\partial\lambda}FSR, \tag{3.15a}$$

$$\Delta n_s = \frac{\partial n_s}{\partial f}FSR = -\frac{c}{f^2}\frac{\partial n_s}{\partial\lambda}FSR, \tag{3.15b}$$

Solving Eq. (3.14) by substituting Eq.'s (3.15a), (3.15b), and (3.2), as well as making the assumption that $f(f + FSR) = f^2$ (i.e. the free spectral range is much smaller than the wavelength $FSR << f$, which is typically the case), and that

$$n_g \approx n_s - \lambda\frac{\partial n_s}{\partial\lambda} \quad for \quad \Delta L >> d(\sin\theta_i + \sin\theta_o) \tag{3.16}$$

we get the relation:

$$FSR = \frac{c}{n_g(\Delta L + d\sin\theta_i + d\sin\theta_o)}[Hz] \tag{3.17}$$

For the diagonal ports where $\theta_i + \theta_o = 0$:

$$FSR = \frac{c}{n_g \Delta L}[Hz] \tag{3.18}$$

Using (3.10) we can solve for the FSR in terms of wavelength:

$$FSR = \frac{\lambda}{m}\frac{n_a}{n_g}[m] \tag{3.19}$$

3.2.1.3 Resolving power

$$R = \frac{\lambda}{\Delta\lambda} = \frac{mN}{C} \tag{3.20}$$

where N is the number of waveguides in the waveguide array, and C is a factor that accounts for imperfections in fabrication. This factor C includes things such as not reaching the diffraction limit due to either multimode operation of the device, or when tapered waveguide sections are introduced in the chip design (see section 3.2.4). Further, imperfections introduced in the manufacturing process, i.e., path length errors in the arrayed waveguides, refractive index deviations, or waveguide geometric distortions contribute to C. The test devices that we developed shows that C is approximately ~ 1.6 [20], and this is something we will discuss in detail in later chapters.

3.2.2 Star coupler / Free Propagation Region design

Star couplers have been used in high-speed, multiple-access optical networks, since they distribute the input signal evenly among many waveguide receivers and make possible the interconnection between them. Fundamentally, a star coupler is used so the input power, from any one of N waveguides in an input array, is radiated through a slab or free-space region of constant refractive index, and received by an N-port output array. A star coupler typically consists of a fanout shape, with N input waveguides, N output

waveguides, and a slab region in between. [21, 22]. Figure 3.3 shows the schematic configuration of a $N \times N$ star coupler. In order to get the uniform power distribution into N output waveguides, the radiation pattern at the output side of the slab array interface should be uniform over a sector of N waveguides.

The behaviour of a star coupler is such that when light is injected into a single port at the input end, the light diffracts within the slab waveguide section and is essentially coupled to all the waveguides at the output. Alternatively, when light is injected into multiple ports at the input, and the light is coherent, they interfere with each other as they propagate through the slab waveguide and can be directed into the desired output port by adjusting the phase of the light in the input waveguides.

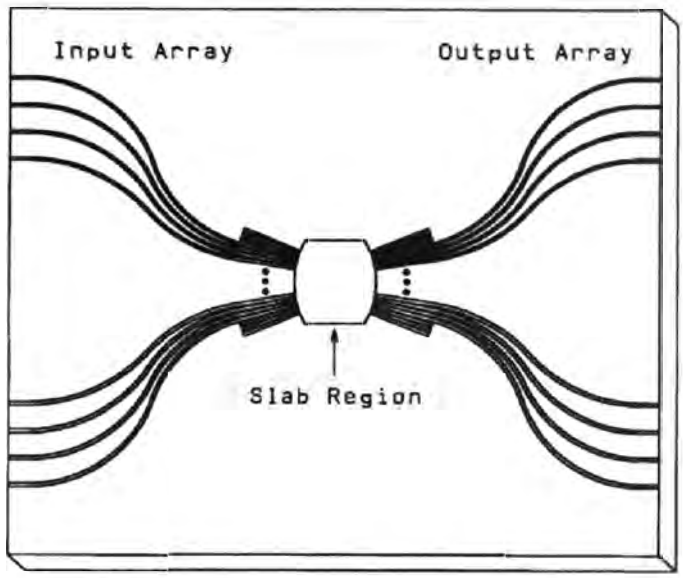

FIGURE 3.3: Schematic layout of an $N \times N$ star coupler, courtesy of [23].

While star couplers have seen numerous uses in planar waveguide devices, in the case of AWGs they have specific design parameters to tailor AWG performance. As such, the FPR found in AWGs have more defined layouts which are outlined in this section. The lens element that constitutes the body of the input FPR is constructed from the geometry shown in Fig. 3.4. The design is essentially identical for the output FPR, except that the light will be incident on the arc swept by R_o rather than by R_i, where $R_i = L_f$.

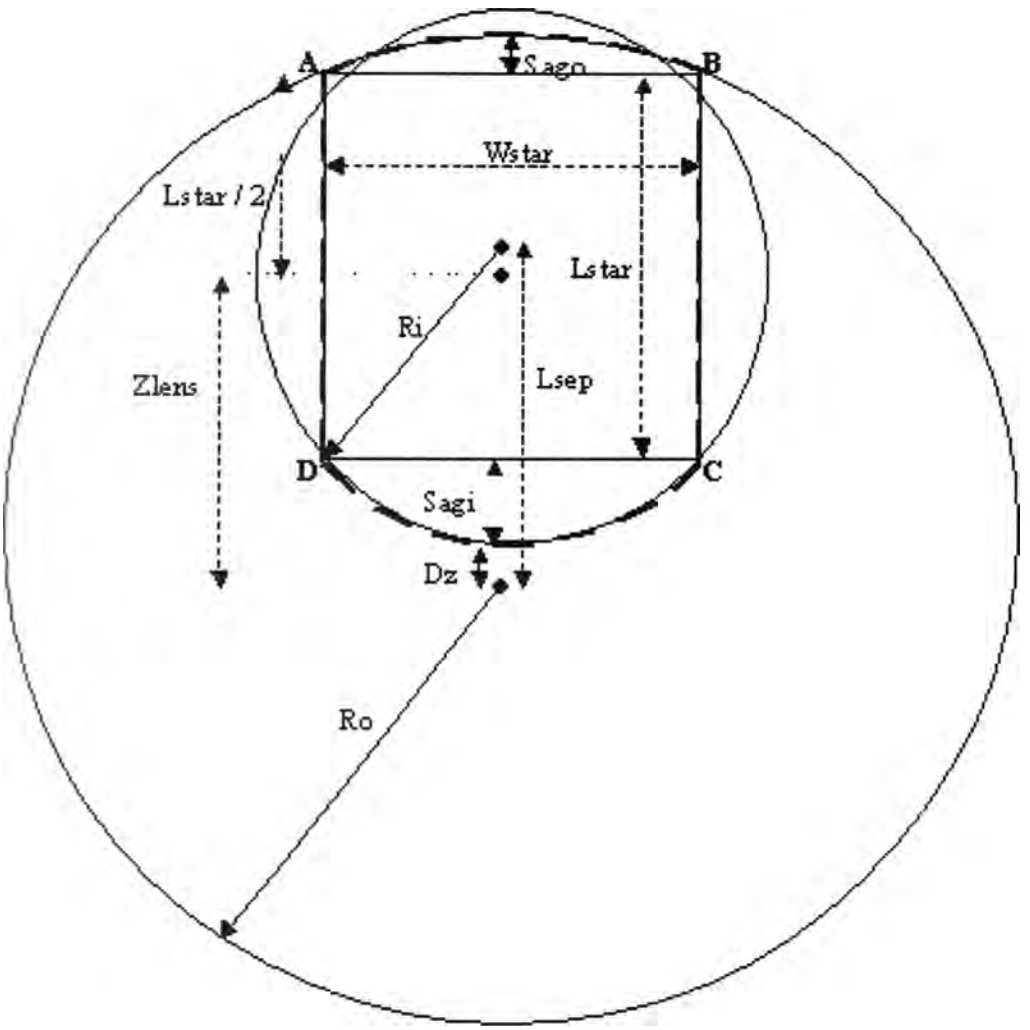

FIGURE 3.4: Rowland circle geometry of the FPR. The body of the FPR is formed between ARC AB, ARC CD, and line Z_{lens} is between the center of the outer Rowland Circle and the center (reference point) of the part of the coupler body. L_{sep} is between the centres of the inner and outer circles. Further parameters such as R_0, R_i, and L_{star}, which are used in the equations in this section are defined in the figure. Note that this figure does not contain parameters described in Fig. 3.2, but in contrast shows how the waveguide design parameters influence the overall FPR geometry, the most important of which are the Rowland curvatures.

In order to design the FPRs, the parameters are set based on the wavelength dispersion Eq. (3.8), however for simplicity we approximate that $n_g \approx n_a$ so that:

$$\frac{\partial \theta_o}{\partial \lambda} = \frac{m}{dn_s}. \tag{3.21}$$

While this approximation is adequate to describe the general design of the FPR, it

must be noted that it breaks down in more complicated designs such as those presented in the final chapter of this thesis.

If we assume the input and output FPRs are identical, then Eq's. (3.3) & (3.4) can be combined to the more general form:

$$\theta = \frac{\Delta x}{L_f} \tag{3.22}$$

and thus the radius of the output Rowland Circle can then be solved:

$$R_o = L_f = \frac{n_s}{m}\frac{\Delta x\ d}{\Delta\lambda} \tag{3.23}$$

Typically in many designs, R_i is set to be $R_i = R_o/2$. The Rowland curvatures determine many of the other geometric parameters of the FPR. For example, the parameters S_{agi} & S_{ago} are defined as:

$$S_{agi} = R_i - \sqrt{R_i^2 - \left(\frac{W_{star}}{2}\right)^2}, \tag{3.24a}$$

$$S_{ago} = R_o - \sqrt{R_o^2 - \left(\frac{W_{star}}{2}\right)^2}, \tag{3.24b}$$

where, W_{star} is the width of the FPR, typically defined by the number of waveguides in the array (N) multiplied by the separation of the waveguides (d).

The physical length of the segments AD and BC (L_{star}) is given by:

$$L_{star} = (R_i + R_o) - (S_{agi} + S_{ago}) - L_{sep} \tag{3.25}$$

with L_{sep} centering the Rowland circles (typically $L_{sep} = R_i$).

3.2.3 Review of terminology

At this point we will summarise certain terms and acronyms we defined in the previous two chapters that are used extensively throughout the remainder of the thesis. The terms are collated below.

Term	Definition
IPS	Integrated Photonic Spectrograph; a miniaturised astronomical spectrograph on a photonics platform..
FSR	Free Spectral Range; the wavelength separation between different grating orders, or alternatively the width in wavelength of a given order.
FPR	Free Propagation Region; the slab waveguide in an AWG where the light is unguided and diffracting.
R	Resolving Power; a dimensionless figure of merit derived from dividing the wavelength of interest by the smallest resolvable spectral element.
PSF	Point Spread Function; the physical shape of the spectrograph's output light given a monochromatic input.
Throughput	The end-to-end efficiency of a device. Typically given as a percentage describing the internal losses.
Tapers	The change in waveguide dimensions to alter the propagation of the light.
Star Coupler	The collection of waveguides and an FPR which maintain coupling between multiple waveguides.
Rowland Radius	The radius of curvature of input and output waveguides in a star coupler to maintain a constant phase-front when coupling.
Diffraction Limit	Typically used to denote the smallest PSF achievable limited only by diffraction of internal optics.
Seeing	or Seeing Limited; typically denotes a PSF which is larger than that of the diffraction limit due to turbulence caused by Earth's atmosphere.

TABLE 3.1: Collection of terminology and acronyms which are used throughout the thesis.

3.2.4 Waveguide tapers

For most applications, the dispersed light is collected at the output FPR end-face using a series of output waveguides. When light is coupled into the collection waveguides, maximum coupling occurs when the injected light has a wavelength that corresponds to that channel, and the further that wavelength is shifted from the channel the more the spot is shifted laterally at the output. As the wavelength of light is varied, the position of where that beam lands on the FPR output changes. Hence, when using the collection waveguide at the output, small offsets in the wavelength will cause a lateral shift, and the light will not couple into the waveguide. Therefore there is a monotonically increasing loss the further away the light is from the centre wavelength of the channel.

This places tight restrictions on the wavelength tolerance of devices when used for telecommunication, and requires accurate temperature control for both AWGs and laser diode sources. Moreover, since optical signals are transmitted through several filters in optical networks employing AWGs, the cumulative passband width of each channel becomes much narrower than that of the single-stage AWG filter. Therefore, flattened and broadened spectral responses were required for AWG devices for telecommunications applications and have become ubiquitous in AWG design. This particular set of techniques aim to induce a physical broadening of the focal spot at the output, without changing its spectral characteristics. As we will see in later chapters, such designs have a negative affect on AWG spectrograph performance, dramatically reducing the resolution. For the time being, it is important to understand the theory of how waveguide tapers work in this context.

Several approaches have been proposed to flatten the pass bands (broaden the focal spot at the output FPR) of AWGs [24–29], which makes it less sensitive to misalignments. One is to create a flat electric field distribution at the input waveguide. Since the AWG is an imaging device, a flat electric field is reproduced at the output plane. The overlap integral of the flat field with the Gaussian local normal mode gives a flat spectral response. Parabolic waveguide tapers (sometimes referred to as parabolic-horn tapers) [25] or 1×2 multimode interference couplers [26] can be used to create a flat electric field distribution at the input waveguide.

A second approach is to engineer the array waveguide design such that it creates a flattened electric field at the output plane while maintaining the Gaussian input field. There are two methods to achieve this. One is to make a sinc-like electric field envelope in the array waveguides by appropriate control of the optical pathlength of each waveguide in the array [24]. Since the focused electric field profile is a Fourier-transformed image of the electric field in the array waveguides, this technique can generate a flattened field distribution at the output plane. The other is to make two focal spots at the output plane [27]. In this case, the light is focused to two focal spots rather than one, which are slightly offset in position laterally. These two peaks overlap to form one broader larger peak.

A third approach is to employ sophisticated operational principles [28, 29] (effectively some form of active mechanical compensation on the chip itself). In these

techniques, the input position of the beam moves synchronously with the wavelength change of the signal. Then, the output beam lies in a fixed position independent of wavelength within one channel span. This type of flat AWG is called synchronous-beam-movement-type AWG.

The remainder of this section will focus on waveguide tapers, as they were the method employed in the AWG devices used in this thesis.

3.2.4.1 Parabolic-horn tapered waveguides

Figure 3.5 shows the enlarged view of the interface between (a) input waveguides with parabola-shaped tapers and (b) normal output waveguides. The width of the parabolic horn along the propagation direction z is given by [30]

$$W(z) = \sqrt{2\alpha\lambda_g z + (2a)^2} \tag{3.26}$$

where α is a constant less then unity, $\lambda_g = \lambda/n_c$ is the wavelength in the guide, and $2a$ is the core width of the waveguide (see inset of Fig. 3.6).

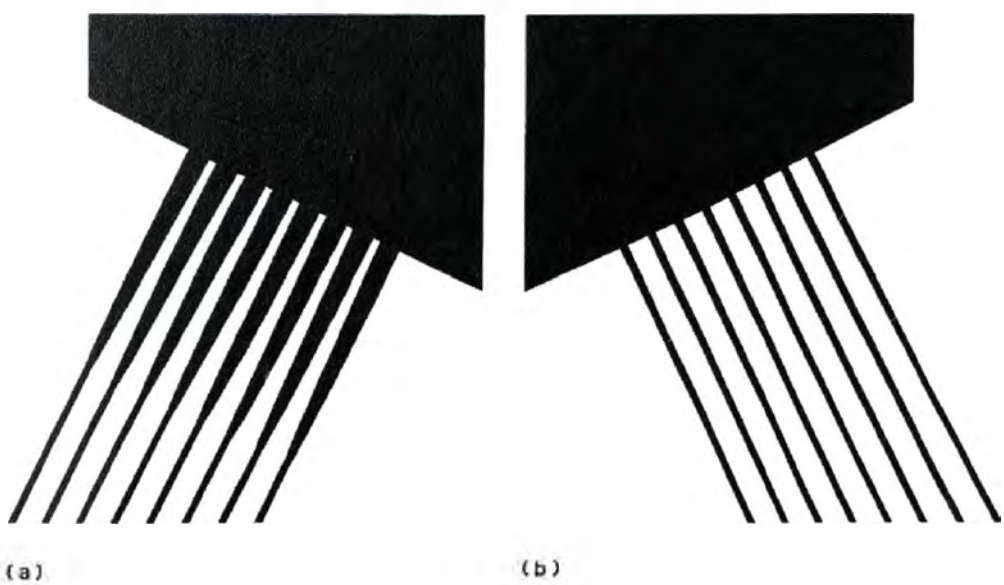

FIGURE 3.5: Schematic of a typical interface between (a) input waveguides and the input FPR and (b) the output FPR and output waveguides.

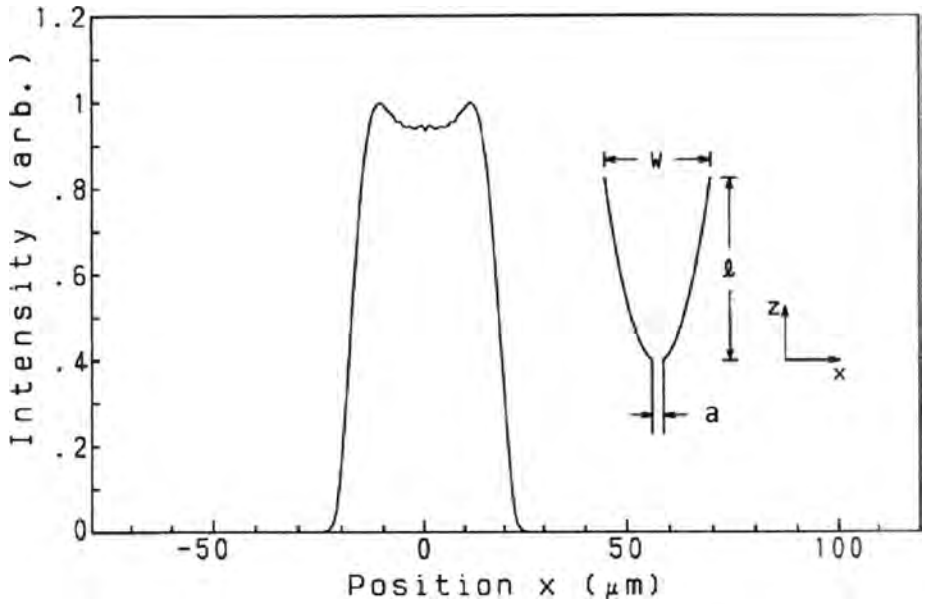

FIGURE 3.6: Simulated intensity profile at the output FPR for a typical AWG with a parabolic horn. Inset shows the schematic configuration of parabolic waveguide horn. [17]

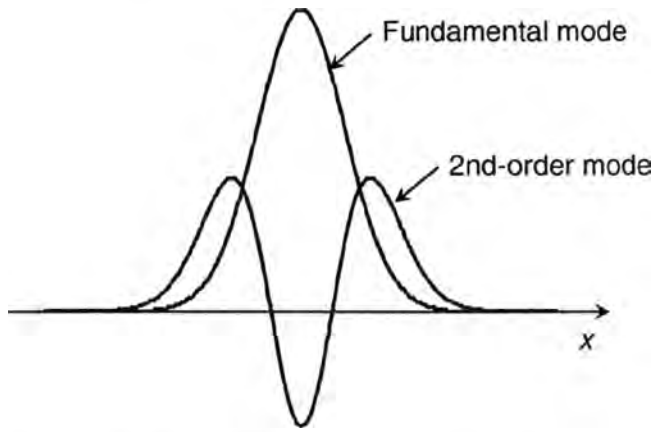

FIGURE 3.7: The electric field amplitude of both the fundamental mode and 2^{nd}-order mode as they occur in a parabolic waveguide horn taper [17]. The x axis corresponds to the spatial axis across the horn end-face.

In a parabola-type flat AWG, a double-peaked electric field distribution is created by the interference of the fundamental mode and the 2^{nd}-order mode as shown in Fig. 3.7. The phase retardation experienced by the fundamental mode propagating throughout the taper is different from the 2^{nd}-order mode. Therefore, the total phase at the end of the parabolic waveguide horn is not a uniform phase. Phase retardations

between the fundamental and 2^{nd}-order modes at the end of the parabolic waveguide horn can be adjusted by adding a straight multimode waveguide [31] as shown in Fig. 3.8. At the appropriate multimode waveguide length, the phase retardation of the fundamental and 2^{nd}-order modes can be equalised.

At the appropriate horn length ($z = \ell$), a slightly double-peaked intensity distribution can be obtained as shown in Fig. 3.6. A broadened and sharp falling optical intensity profile is obtainable by the parabolic waveguide horn, which is quite advantageous for achieving wide passband without deteriorating the nearest neighbour crosstalk characteristics. The broadened and double-peaked field is imaged onto the entrance of an output waveguide having a non-tapered core width (a). The overlap integral of the focused field with the local untapered mode of the output waveguide gives the flattened spectral response of the AWG.

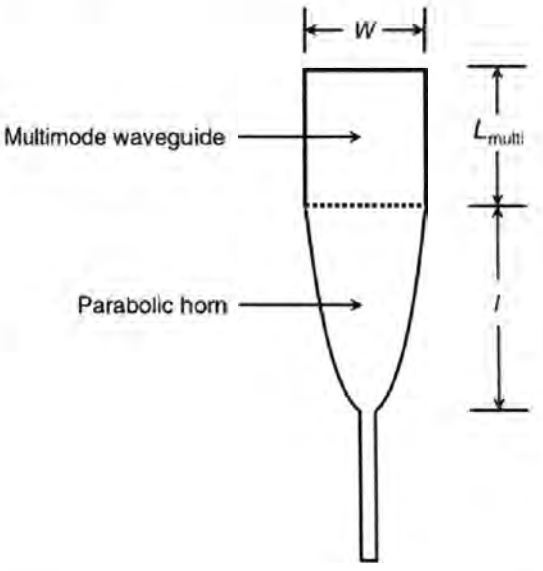

FIGURE 3.8: Parabolic waveguide horn with a straight multimode waveguide of length L_{multi} and width W.

3.2.5 Typical losses in AWGs

Typically, losses in AWGs due to absorption in the glass or scattering loss in the waveguides are very small ($< 1\%$). The dominant cause of loss is due to the imperfect light capture at the FPR - waveguide array interface. There are generally two origins of this

loss. One is a spillover loss in which the peripheral part of the far-field intensity distribution cannot be captured by the array waveguides, since we cannot place infinitely many array waveguides. Hence the Gaussian far-field profile is truncated. Normally, this is taken into account when designing the AWG, and traditionally the waveguides stop at the $1/e^2$ edges of the far-field. It should also be noted that this truncation also contributes to the factor C when determining the AWG resolution we discussed previously. The equation $R = mN$ assumes that the full beam is incident on the array (the entire beam is influenced by all N), but as we can see this is not strictly the case. It is a subtle effect, but one worth noting as it is part of the reason the true resolving power deviates from the equation.

The other loss comes from a mode-profile mismatch between the FPR mode and the array waveguides. The intensity profile at the far-end of the FPR is a broad Gaussian profile. However, the field in the array is confined to each waveguide. Therefore, unless the field in the FPR is adiabatically converted into that of the array waveguide with the use of several tapers, there will be a mismatch of the fields causing imperfect capture and hence loss. Several techniques have been proposed to reduce the imperfect light capture loss at the FPR and array interface [32–35]. Among them, the vertical-taper technique [33] offers the smoothest electric field transition and substantially reduces the field mismatch loss. However, this can be difficult to manufacture, and a simpler technique called segmentation [36] is more commonly utilised to provide the adiabatic taper region.

The adiabatic taper works by reducing the abruptness of the transition from the waveguide array to the FPR. Segmentation is the easiest to implement since it does not require any extra fabrication steps. In the segmentation process, one simply adds sections (15 is a typical number) perpendicular to the waveguides. The section center-to-center spacing is constant, but their widths gradually decrease as their distance from the slab increases, as can be seen in Fig. 3.9. The purpose is to taper the effective refractive index which influences the mode gradually as a function of distance into the array. Because the segments are smaller than the mode, their effect is averaged such that from the mode's perspective the effective refractive index is increasing, slowly constraining the mode. The effect is such that the large Gaussian profile of the slab-mode eventually begins to resemble the acceptance mode-field of the array as close as

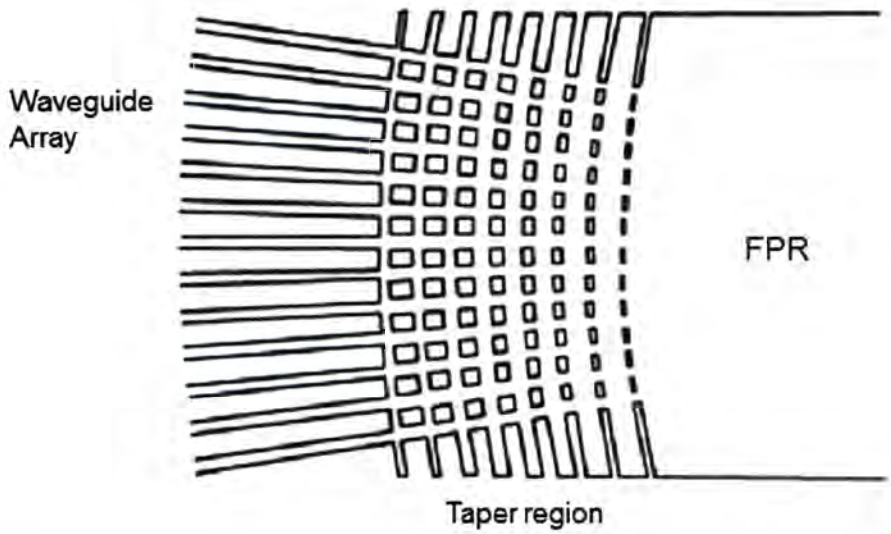

FIGURE 3.9: A schematic of a segmented taper region at the FPR - waveguide array interface.

possible.

3.2.6 Manufacturing process

The manufacturing processes used to create photonic circuitry can vary dramatically depending on the application and wavelength region of interest (the guiding materials used change depending whether the device is to perform in the optical, NIR, or MIR etc.). As such, we will limit the discussion to the most common fabrication processes employed in commercial AWG manufacture, with further focus on the specific methods used create the AWG devices tested in the subsequent chapters.

The planar nature of the AWG architecture, which is to say all the waveguiding structures do not change in height, enables the devices to be manufactured using a micro-fabrication technique called photolithography. In this section an overview of the photolithographic manufacturing process is provided. However, as this fabrication process is integral to the creation of semiconductor circuits, photonic circuits, and other nano-scale structures, the existing body of literature on this topic is vast. The reader is instead directed to Chapter 7 of *"Fundamental Principles of Optical Lithography"* by Chris Mack [37], and the references therein, which expands on the processes outlined in this section. As mentioned previously we limit the scope to processes used to make

the AWG chips used in this thesis.

Fundamentally, photolithography uses light to transfer the desired waveguide pattern from a photomask (often referred to as simply 'the mask') onto a light-sensitive photoresist layer on top of a wafer substrate. This technique can be split into two separate processes; the creation of a lithographic mask, and the printing of the circuits onto a wafer.

A lithographic mask is typically a transparent fused silica (glass) plate covered with an opaque film (normally a chrome metal layer, although other variants exist). The mask is created by covering the chrome layer with a photoresist resin into which the desired circuitry is written using an electron beam (e-beam). The photoresist is developed and etched, transferring the design onto the chrome layer. At this point it is important to note that the chrome layer is a 1:1 image of the desired waveguide layout as the chrome layer will create the areas of higher refractive index later on in the process. Thus, when the mask is finished, it will have the layout of the waveguide circuitry in a thin opaque chrome layer, with the rest of the mask remaining transparent.

The mask is ultimately the deciding factor of how accurate the device can be. Thus, high accuracy tools are used to ensure sharp edges and accurate features. As lithographic masks are an integral component of modern semiconductor manufacture, e-beam technology is well established in commercial foundries and is capable of writing with the precisions required for typical photonic circuitry. Importantly, most of the fabrications cost is in the mask design and fabrication. Once the mask is fabricated, it can be used in the writing process as many times as required, enabling the mass production of the actual photonic chips. Hence, for a single fabrication run including mask creation and wafer imprinting the costs are typically in the order of $\$30,000$ USD, with every chip thereafter closer to $\$5,000$ USD. This form of fabrication is ideal for the telecommunication industry which requires mass-produced components, but unlocks interesting avenues for astronomical spectrographs, as in some cases modular designs may become cheaper than a single monolithic spectrograph. This idea is revisited in Chapter 6.

The lithographic waveguide imprinting process is outlined in Figure 3.10 and starts with a circular wafer substrate. The substrate will never interact with the guided light and is used as blank canvas on top of which the actual guiding layers will be deposited.

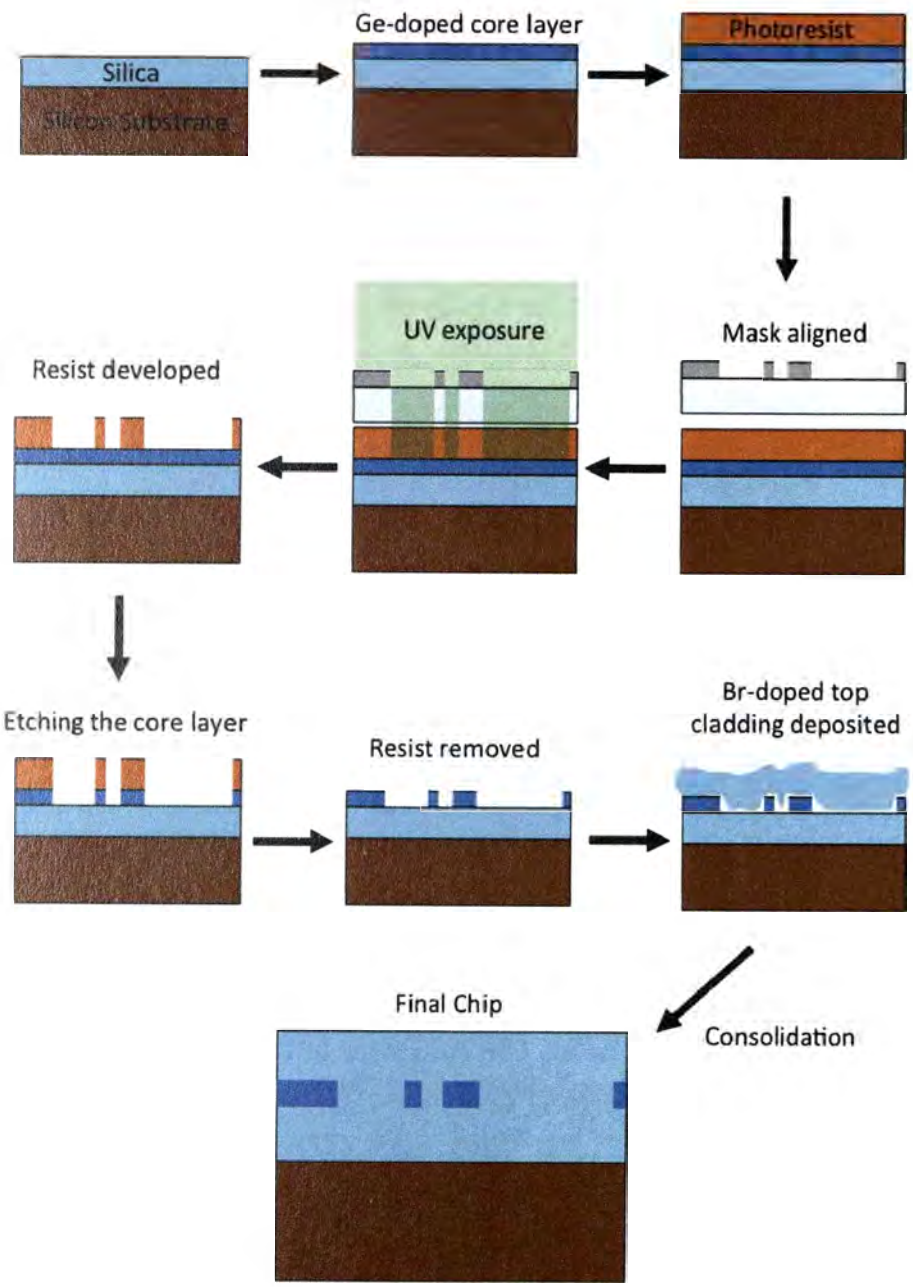

FIGURE 3.10: Typical fabrication processes for planar waveguide circuits.

Because the deposition layers are usually spin coated onto the substrate (to ensure even coverage) the wafers are almost universally circular, with typical sizes ranging from 4" to 8" in diameter. Silicon is traditionally used as a substrate (as it can be produced with minimal surface defects), with silica being occasionally used in specific circumstances (typically when creating photonic circuits for MIR applications).

The next step involves depositing three distinct layers onto the silicon wafer substrate (although more layers can be deposited, three is preferred for when creating AWGs). It is important to note that the choice of material used to create the bottom cladding (sometimes referred to as an under-cladding), waveguide core, and upper cladding (over-cladding), is important in two ways. Firstly, the change in refractive index (Δn) will determine the size of the fundamental mode guided by the waveguides, and its confinement. Thus, higher Δn materials are used to create smaller footprint AWGs, when the size of the device is an issue. Secondly, the materials are chosen to be as transparent as possible at the wavelength range of interest. Commercial AWGs are designed to operate at NIR wavelengths centred at 1.5 μm, hence silica was chosen as the primary material for the guiding layers. An additional reason for choosing silica was to match the Δn of a single-mode fibre, the primary mode of injecting light into an AWG.

For the IPS devices explored in this thesis, a layer of pure silica was deposited as the under-cladding, using flame hydrolysis deposition (FHD). This process produced fine glass particles (with any accompanying dopants) in the oxy-hydrogen flame and deposited them on the substrate. After the under-cladding is complete, a germanium-doped silica layer is deposited in a similar fashion. The germanium dopant increases the refractive index of the glass to obtain the desired Δn, and makes the glass sensitive to the etching process that follows. The core layer is then covered with a photoresist layer, and the photomask is aligned with the wafer. The wafer and mask are then exposed to UV light, the photoresist developed, and the mask removed. This process leaves the photoresist layer with the exact circuitry contained in the mask, with the rest being removed. The wafer (which now contains the substrate, under-cladding, core layer, and photoresist) is then etched using reactive ion etching (RIE) to remove any part of the core layer not covered by the photoresist, thereby imprinting the waveguide circuitry in the core layer. After this step the photoresist is removed.

The final layer to be deposited is the upper-cladding. To obtain symmetric mode confinement the refractive index of the upper-cladding must match that of the under-cladding. Normally, one would deposit another layer of silica as the upper-cladding to ensure the same refractive index, however there is a fabrication subtlety which makes

this non-ideal. When the upper-cladding is deposited, the layer will not uniformly distribute around the (now square) cores of the waveguides, leaving pockets, particularly near sharp edges, and further bulging above the cores themselves. The most common way of removing these effects is to heat the wafer to the glass softening point such that it flows and fills in the pockets, smoothing out the upper-layer. This process is known as consolidation. However, if the same material is used as the under-cladding, the softening temperature would be the same for both layers, with the heating procedure causing the whole circuit to warp. Thus, the upper-cladding is actually doped with elements such as boron, which decreases the glass' softening point while maintaining the same refractive index. With a boron-doped upper-cladding deposited, the heating process only softens the top layer, allowing the cladding to uniformly envelop the cores. It should be mentioned that the exact quantity of dopants varies between foundries and is matched specifically to the exact processes and temperatures used. The dopant ratios are typically formulated by the foundries themselves, often referred to as "recipes", and are normally protected as commercial secrets. The resulting chips are covered in a thin polymer layer to protect the silica against scratches.

3.3 SWIFTS Photonic Spectrographs

In the previous section we have explained the details of AWG operation, design, and manufacture. Even though we exclusively focus on this technology in the thesis, it is important to highlight the advancements made developing an alternate form of integrated photonic spectrographs. Stationary-wave integrated Fourier transform spectrometry (SWIFTS) is an alternate analytical technique used for measuring the distribution of light across an optical spectrum and has been successfully implemented in the creation of miniature on-chip spectrometers [38].

3.3.1 Lippman Spectrograph Concept

In 1894 , Gabriel Lippman published an article on how photographic plates he produced were able to record colour information in the depth of photographic grainless gelatine and how the same plate after processing could restore the original colour image through light reflection. He thus invented interferential colour photography for which he received the Nobel Prize in 1908. Unfortunately, this principle proved to be too

complex for commercial use and the method was abandoned a few years after its creation. Further, at that time any spectroscopic applications of the Lippmann concept were ignored. With recent renewed interest into the miniaturization of spectroscopic equipment (in context of both astronomy and telecommunication) the concept was revisited.

The concept of using a photo-electric device to probe stationary waves for spectroscopic measurements was initially proposed in 1933 by H. Ives [39]. More recently, in 1995 P. Connes proposed to use arising new technology of detectors to make 3D Lippmanns based spectrometry [40]. Following this, a first realisation of a very compact spectrometer based on Micro-Opto-Mechanical System (MOEMS) has been reported by Knipp et al. in 2005 but with a very limited spectral resolution [41]. The SWIFTS concept was brought into the realm of photonics in 2007 by le Coarer et al., demonstrating the concept in a waveguide based architecture and detection of the evanescent field using optical nano-probes [38].

The principle of SWIFTS is shown in Figure 3.11. Two configurations are shown in which a direct near-field detection of confined standing waves are performed: the standing waves are issued either from a guided mode reflection as in G. Lippmanns principle of colour photography (Fig. 3.11a) or from two counterpropagative modes interference (Fig. 3.11b). In the counter propagative architecture the two optical signals are injected at the opposite ends of the waveguide. The evanescent waves propagating within the waveguide are then sampled thanks to optical probes (Fig. 3.11c)), which can either measure the evanescent field directly, or nano-scale material can be deposited which scatters the light to a 2D detector. A mathematical function known as a Lippmann transform, similar to a Fourier transform, is later used to give the spectrum of the light.

3.3.2 Technology Comparison

One of the primary benefits of this technology is the high level of miniaturization that is possible for this type of spectrograph. As in classical Fourier spectrometry, the spectral resolution achieved by SWIFTS is given by the length of the detected interferogram, such that in a single mode waveguide, the spectral resolution is only limited by the optical length of the waveguide. For example, a SWIFTS spectrometer based on an

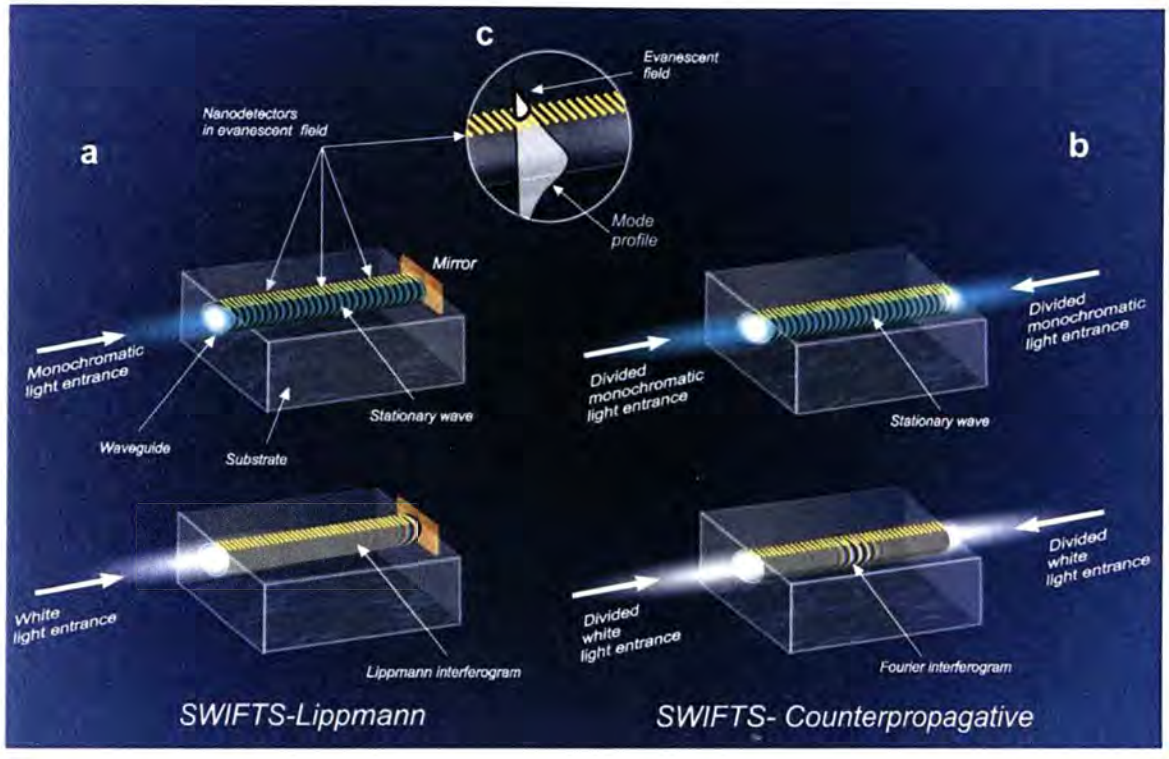

FIGURE 3.11: The standard Lippmann configuration SWIFTS is shown in a), the forward propagating wave coupled in the waveguide is reflected by the mirror at the end, leading to a stationary wave inside the waveguide. If the light is polychromatic, the sum of the stationary waves forms a Lippmann interferogram. For the counterpropagative configuration b), the light is divided prior to entering the waveguide, then injected in both ends. If there is no optical path difference between the two beams, the white fringe of the Fourier interferogram will be located at the waveguide center. This configuration is sensitive to the phase shift. Schematic of the near-field detection of the guided mode using a collection of nanodetctors is shown in the inset c). Image courtesy of [38].

optical waveguide including detectors placed over a length of 1 cm, would allow for a spectral resolution of about R=40,000 (15 pm) at a 600 nm wavelength.

This level of miniaturization does come with its own challenges however, particularly with how the evanescent field of the standing wave is sampled. Due to the sub-wavelength nature of the interferogram fringes, various nano-technologies must be employed to detect the fringes in a passive and compact manner. For example, some SWIFTS prototypes utilize gold nanowires (5 x 5 nm) deposited on top of the waveguide which act as nano-scale scattering centres [38]. The scattered light can then be reimaged onto a detector above the waveguide. Hence, in practice, the limitation on the resolution and wavelength coverage of SWIFTS is how much of the interferogram

can be accurately imaged without fabrication defects or imaging aberrations. Furthermore, as this is an interferometric reconstruction technique, the fringes on the interferogram are sensitive not only to scattering defects, but other pathlength-matching issues common to photonic interferometric devices, such as waveguide/glass dispersion. Furthermore, even though the challenge of coupling telescope light into a single-mode waveguide is common to both AWGs and SWIFTS spectrographs, the waveguides in typical SWIFTS devices support more localized modes, requiring lensed fibres to couple light into the device, and thus making insertion losses higher.

Nevertheless, this technology is a successful demonstration of miniaturizing spectrographs using photonic technologies. It stands to revolutionise many aspects of how spectrographs are implemented for sensing and indeed astronomy.

3.4 Seeing-limited to diffraction-limited conversion

A seeing-limited telescope is one where the fundamental limit to the size of its focal spot is not the telescope diffraction-limit, but rather an atmospherically aberrated spot dependent on the turbulance in the air at the time. While this can be initially thought of as a broadening of the telescope's point-spread function, limiting the angular resolution the telescope can achieve from the ground, for astrophotonic devices there are more subtle aspects of seeing that can affect successful coupling into devices such as the IPS.

3.4.1 Astronomical Seeing

Astronomical seeing refers to the blurring of astronomical objects caused by turbulent mixing in the airmass above the telescope, along the line of sight. Without an atmosphere, a point source object like a star would form an Airy-disk function in the telescope's focal plane, determined by the diffraction of the telescope's geometry (and diameter). However when light enters the Earth's atmosphere, the different temperature layers and convection zones alter the flat stellar wavefronts leading to distortions in the image once focused. The distortions are rapidly varying, typically changing on millisecond time-scales. During astronomical observations, exposure times of seconds or even minutes are used, so the various distortions average out as a seeing disc. The diameter of the seeing disk (FWHM of the PSF), is typically referred to as the seeing

spot-size or seeing-limit. As seeing is a well known and studied phenomena in astronomy, and as it does not impact AWG spectrographs except in the case discussed below, it is unnecessary to go into exhaustive detail and derivations of seeing in this thesis. The reader is directed to Fried's 1965 seminal work on seeing [42] for a more thorough overview.

3.4.2 Impact on photonic devices

The rapidly varying change in the wavefront caused by the atmosphere produces a temporally changing speckle pattern at the focal spot [43]. This can be thought of as a highly multimoded spot, with each mode related to different coherent patches across the primary mirror. When injecting into optical fibres, the number of modes, along with the seeing disk size, can be a source of major losses in coupling if the appropriate fibre geometry is not used. For example, the AWG chip performance severely degrades with the introduction of multiple modes, hence they are designed to only allow the fundamental mode to propagate through the chip. As single-mode fibres (SMF) are used for injection into the AWG chip, trying to couple seeing-limited light directly into an SMF is very impractical and dificult as demonstrated by Shaklan and Roddier [?]. This is primarily because the core size of a single-mode fibre is an order of magnitude smaller than the size of a seeing-limited point spread function (PSF) at focal planes for large astronomical telescopes. Further losses are the result of mode mismatch between the telescope PSF and the Gaussian mode-profile of a SMF. This is why seeing-limited telescopes use the much larger multimode fibres (MMFs) for efficient light collection at the focal plane.

As this is a common predicament faced by most astrophotonic devices, a practical solution using a transitional multi-fibre taper known as a photonic lantern has been demonstrated. The photonic lantern acts as an efficient multimode to single-mode converter allowing for the N-modes of the multimode fibre to be split into N individual single mode cores using adiabatic transitions. Hence, it is able to convert the light fed from a 50 μm core MMF into nineteen separate SMFs.

"An expert is a person who has made all the mistakes that can be made in a very narrow field. "

Niels Bohr

4

Laboratory Characterisation of Arrayed Waveguide Grating Spectrographs

In the previous chapter, the concept of photonic spectrographs and in particular AWG based designs, were introduced and explained. In this chapter we describe the experimental set-ups used to probe lithographically fabricated AWG-based spectrographs and the results obtained from their tests. Section 4.2 and 4.2.4 explain the techniques used to measure key spectrograph performance parameters such as resolving power and throughput, as well as highlighting new injection techniques. Section 4.2.5 describes differential interference contrast microscopy techniques used to measure waveguide dimensions, with Section 4.2.6 outlining the technique of refractive index profilometry. The results of the laboratory characterisation of the AWG chips is presented in Section 4.3.

We characterised two separate AWG designs to compare and contrast design parameters for astronomical use, which we refer to as Chipset A and Chipset B. Chipset A is the AWG format used in the initial IPS prototype described in the section below. Chipset B consisted of three separate but identical AWG chips with the same design as Chipset A, but with the input waveguides removed to allow for direct coupling into the input FPR.

4.1 First IPS prototype

The first IPS prototype was fabricated by the Centre for Integrated Photonics (CIP) using a slightly modified off-the-shelf AWG chip. The chip was characterised and demonstrated for the first time to obtain a continuous sky spectrum. The details of this work can be found in [20]. In this section we provide an overview of the results and technology involved. This work was a foundation for the project and serves as important background.

4.1.1 Prototype properties

Figure 4.1 shows a schematic of the AWG used for the initial testing. The grating had a single input waveguide (of width 8 μm) with $L_f = 22$ mm focal length free-propagation zones and 428 array waveguides (with a length increment $\Delta L = 28$ μm). The device is designed to operate at a centre wavelength $\lambda_0 = 1550$ nm with a 100 GHz output channel separation and 40 output waveguide channels.

Several modifications were made to this commercial AWG to create an IPS that can be used for astronomy. The primary hurdle was that the output consisted of a series of single-mode waveguides, each carrying a wavelength channel. Since we wish to obtain a continuous spectrum at the device output these individual channels are not required. The output waveguide array was removed by slicing the chip near the output of the output FPR, and polishing down towards the output focusing surface, so as to remove any waveguide 'stumps' left by the cleaving process. This AWG configuration is referred to as Chipset A in the thesis.

Flat-field AWGs have been proposed using aberration theory to remove the Rowland curvature, which is inherent to this technology [44]. Our prototype did not have any such correction and is simply polished flat. Thus, we expect the IPS's focal plane to have a radius of curvature of ~ 22 mm, defined by the focal length of the output free-propagation zone. In both the laboratory and on-sky imaging experiments however, the curvature had little measurable effect on the resulting image, as the depth of the focal plane curvature is only ~ 90 μm at the edges of the active region (the region over which the single on-axis input waveguide is dispersed at the focal plane of the output free-propagation zone). If the magnification of the imaging optics is greatly increased,

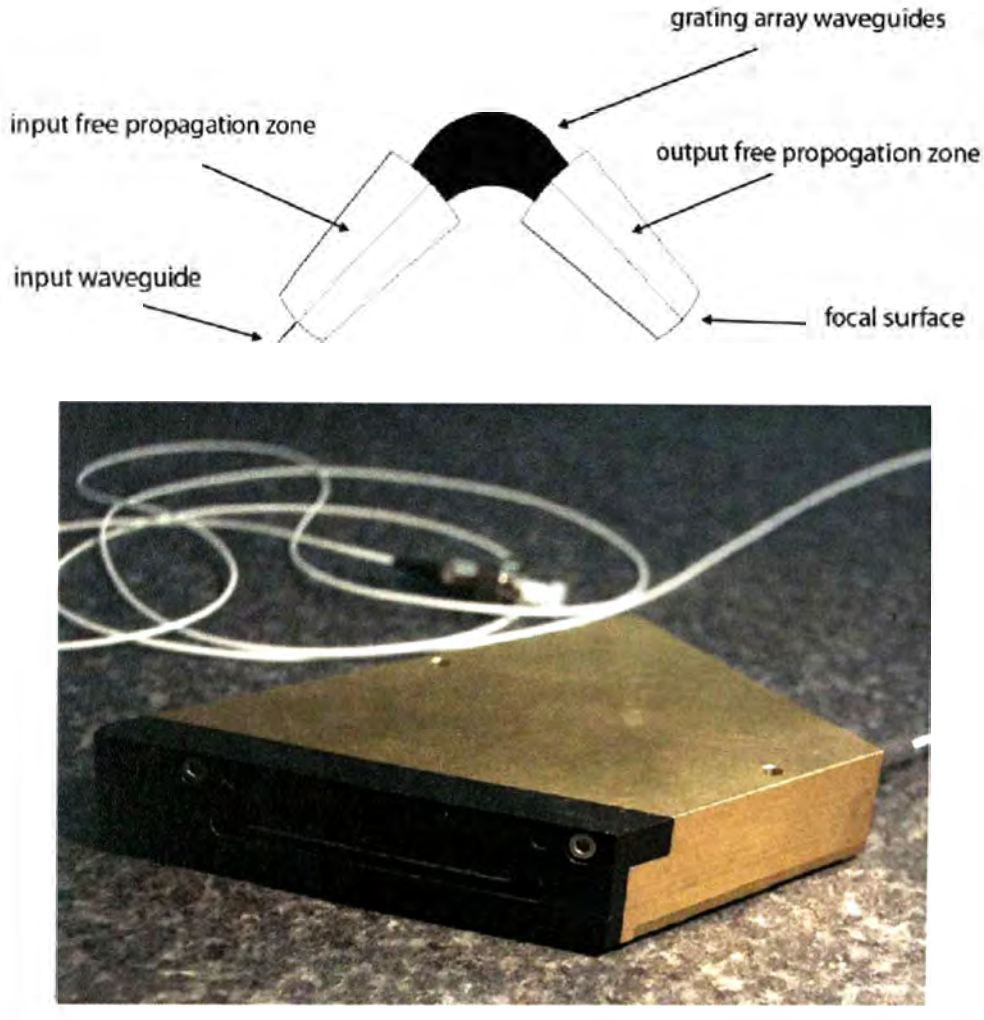

Figure 4.1: Top: schematic of the AWG chip. Bottom: photograph of the IPS prototype. In this prototype device (Chipset A), the output array waveguides (standard in commercial devices) have been removed, the output facet has been polished back to the focal surface, and the chip packaged. The fibre input is at the rear of the image, and the polished flat output facet at the front. The open face of the chip is $\sim$ 38 mm in length. The active area is $\sim$ 3 mm across, and is situated at the centre of the polished face.

a detector array placed directly at the focal surface of the IPS, or if the active length is increased, then the aberrations caused by the curvature may become significant. D. Wang and Tsay [45] previously reported a similarly modified AWG device for use in optical monitoring, with a flat, non fiber-coupled, output. That device was not designed for an imaging system, but utilised a series of photodiodes to derive the channel power information at high diffraction orders. A custom package was constructed so the IPS has one single-mode input fibre and an exposed output facet to allow coupling to an

external lens or imaging array.

4.1.2 IPS performance

The device operates principally in the 26^{th} diffraction order at the central wavelength. It exhibited relatively high efficiency ($50 - 60\%$) over a large fraction of its active area. The spectral resolution FWHM was 0.75 ± 0.05 nm, corresponding to a spatial resolution of 23 ± 1 μm with a linear dispersion of 33 nm/mm, and a resolving power $R = \lambda/\Delta\lambda = 2100 \pm 150$. Furthermore, there was little observed variation in the FWHM of the output spectral PSF across the laser tuning range.

Physically, the total output active area is ~ 2.8 mm. This region contains ~ 1.6 diffraction orders with a free spectral range of 57.4 ± 0.6 nm. Scattering of light (i.e., due to undispersed or redispersed stray light or small-scale wings of the spectral PSF) around the central orders was very low ($< 0.1\%$).

4.2 Experimental procedures

The primary goal of the characterisation set-up presented in this chapter is to reproducibly and accurately measure the spectrograph's PSF and losses as a function of wavelength simultaneously. By measuring both parameters at the same time, we are able to quickly characterise the spectrograph chips in terms of resolving power (R) and throughput.

The PSF is a typical parameter of interest in spectrographs as it directly determines the spectrograph resolving power, which we define as the full-width half-maximum (FWHM) of the PSF profile. The PSF is identical to a mode-field profile commonly measured in photonic devices, hence the terms are used interchangeably. The measurement of the mode-field is performed by taking a near-field 2D image of the spectrograph's output spot. Because the chips were designed to work in the astronomical H-band ($1490 - 1790$ nm), commercial silicon based detectors could not be used for PSF characterisation due to their poor response beyond ~ 1 μm. We therefore used an InGaAs near infrared CMOS array detector to image the NIR PSF, the details of which are found in Section 4.2.1.1.

While there are many methods of accurately measuring the wavelength dependent throughput of AWG chips, the modified arrangement of our prototypes' output makes

such techniques very time consuming. Typically, an unmodified AWG will have output waveguides which are coupled to optical fibres, and in turn taken to a power-meter or optical spectrum analyser (OSA) for analysis of each output port. However, as our AWG prototypes have the output waveguides removed, we opted to measure the throughput across the entire output focal-surface, making injection back into fibres impractical. This is because the focal spot will shift laterally with the changing wavelength and require re-alignment for every data point.

It is important to note that this procedure was used in our original paper [20] when characterising Chipset A. A 50 μm core multimode fibre was used to capture the focal spot and analyse it on a NIR OSA, as a NIR detector was unavailable at the time. The process proved to be incredibly difficult and laborious and was sensitive to misalignments. Furthermore, while we did attempt to account for the coupling losses going into the MMF, it ultimately led to incorrect measurements of the throughputs. In addition, the process was not sensitive enough to detect the true shape of the PSF of the Chipset A AWG, which we show in Section 4.3.2.

Therefore, the InGaAs CMOS detector, which was used to measure the PSF profiles, was flux-calibrated to provide reliable power measurements for each mode profile. A fibre beam-splitter was used that picked off some of the incoming light to a power-meter that was monitored in real time. This procedure allowed for accurate calibration of any temporal power variations of the laser source used for probing. The methodology of the detector and experimental calibration is explained in detail in Section 4.2.2.

Using this technique, we were able to accurately image the mode-profile emanating from the spectrograph chip, as well as its encircled power. Combined with active monitoring of the input light, we obtained precise measurements of throughput at each wavelength increment.

4.2.1 Characterisation set-up

To probe the AWG spectrographs we used a tunable diode laser (Santec TSL-210). The TSL-210 is an external cavity tunable semiconductor laser that can be tuned in wavelength and optical output power.

The laser is capable of scanning between 1500 nm and 1580 nm at increments of 0.01 nm, ideal for characterising the central grating order of the AWGs. The laser's

linewidth is 1 MHz ($\approx$ 0.008 pm), which enables the PSF to be accurately measured because it is far narrower than the expected spectrograph PSF. The output power of the laser was set to 5 mW, more than necessary for the experiments. The laser power during experiments was adjusted with a variable fibre attenuator placed downstream to avoid saturation of the detectors.

The primary characterisation setup used is shown in Fig. 4.2. The laser output was connected to a single-mode fibre (SMF-28), which passed through the variable optical attenuator (VOA1550-FC), and into a 90:10 fibre beam-splitter. The 90:10 splitting ratio was used to account for the different sensitivity and saturation ceiling of the InGaAs camera and NIR power-meter. The power-meter used had a Ge photodiode sensor with a 50 nW - 40 mW power range with a 10 nW resolution (700 nm - 1800 nm wavelength range). Whereas the InGaAs detector was optimised for high-sensitivity, low-noise imaging and saturated at $\sim$ 16000 counts per pixel, and hence required less light to saturate. Therefore, the 90% arm of the beam-splitter was sent to the power-meter where measurements could be made well above the noise floor, with the 10% arm being injected into the AWG spectrograph chips.

Different injection methods were used for the two chipsets. 'Chipset A' had an unmodified input (input waveguides into the FPR) as is typically found in off-the-shelf AWGs, to explore the effect of input waveguide tapers on spectrograph performance. 'Chipset B' had these waveguides removed to investigate the effect of a direct fibre launch into the FPR and multiple off-axis fibre launch. The launch configuration for Chipset A was a butt-coupling of the 10% arm of the beam-splitter with the chip's input fibre. The fibre was a standard FC connectorised SMF-28 fibre, which was already aligned, bonded and packaged to the input waveguide that feeds the FPR, and can be seen in the bottom-right of Fig. 4.3.

Chipset B however, required a direct fibre coupling to the input FPR. For this chipset the input FPR was polished back to the edge of the Rowland curvature providing a flat optical surface with which the fibres were butt-coupled to. For initial testing, a single SMF-28 fibre pigtail was used (connectorised to the 10% arm, cleaved end to chip) to inject the light into the input FPR. The fibre was precisely aligned using a NanoMax 5-axis flexure translation stage which had a 0.5 μm positional accuracy.

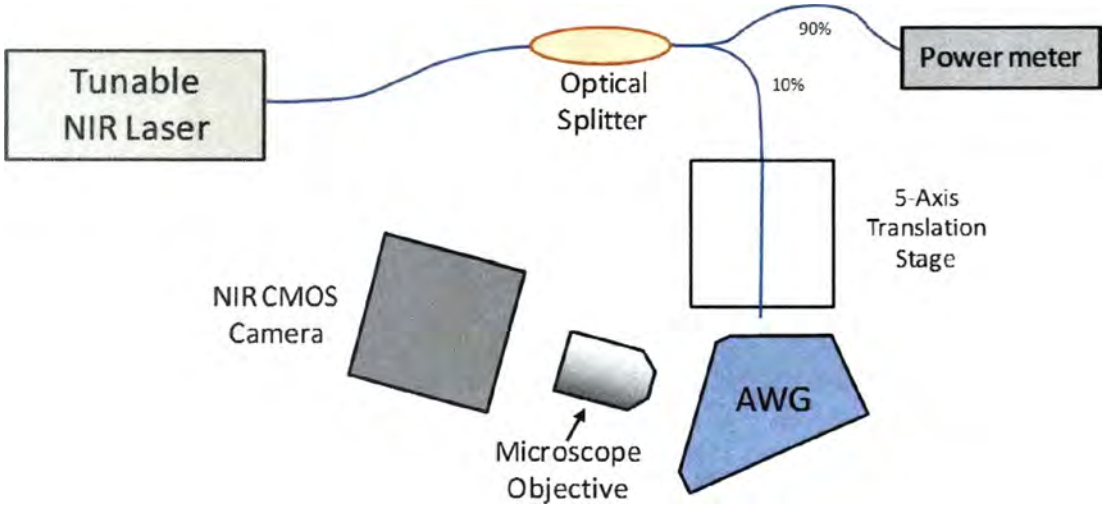

FIGURE 4.2: Experimental setup for the concurrent characterization of the chips' point spread function and throughput efficiency. Light from the tunable laser source is split in a 90-10 ratio, with the majority of the light feeding a power meter for real time calibration and the rest injected into the AWG chip. The injection fibre is aligned to the AWG using a translation stage and the output reimaged onto a 2D NIR InGaAs detector.

The fibre position was maximised using active feedback from the detector imaging the AWG output. The separation of the chip and fibre was assisted by a vision system which magnified and imaged the fibre-chip interface. Fresnel reflection at the interface was minimised with the use of index matching oil.

The AWG output focal plane was re-imaged onto the detector using a 100x, long working distance, Olympus microscope objective. The long working distance of the lens (few millimetres) allowed us to image the AWG output in free space without the need for immersion oil. The objective was attached to the InGaAs camera using a lens tube, which minimised background light falling on the detector. The lens magnification and throughput were calibrated and described in detail in Section 4.2.2.

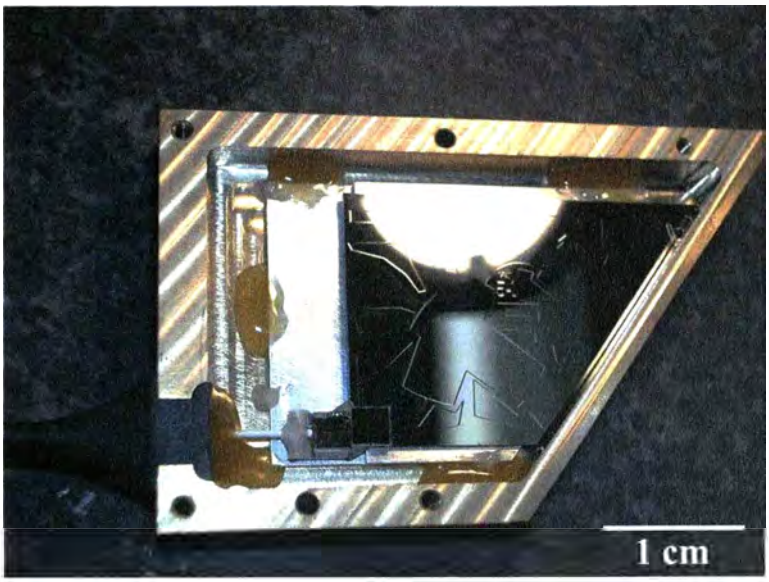

FIGURE 4.3: Image of the IPS prototype for Chipset A. The optical fibre can be seen connecting to the input waveguide in the bottom left of the image. The outline of the AWG circuitry can be seen on the chip itself. The spectrum focal-plane is at an angle in the centre-right of the image.

4.2.1.1 Xenics NIR detector

The main detector used to obtain results is the Xenics Xeva-1.7-640 thermo-electrically cooled InGaAs detector. The detector has 640×480 pixels, with a pixel pitch of 20 μm (no inter-pixel dead-space). The camera's wavelength response is $0.9 - 1.7$ μm, with a typical spectral response shown in Fig. 4.4. The camera was interfaced with a computer using USB 2.0, and operated using proprietary software 'X-Control Advanced', which offered direct access to camera settings such as exposure time and operating temperature. Prior to making measurements, we performed a two-point uniformity correction and bad pixel calibration (correcting for both 'hot' and 'dead' pixels).

4.2.2 Calibration

To minimise uncertainty in our measurements, particularly throughput, we carried out a number of calibrations and normalisations of the experimental equipment. Calibrating for the power drift of the laser diode as a function of wavelength tuning, the wavelength response of the fibre beam-splitter, and the flux calibration of the InGaAs detector was key.

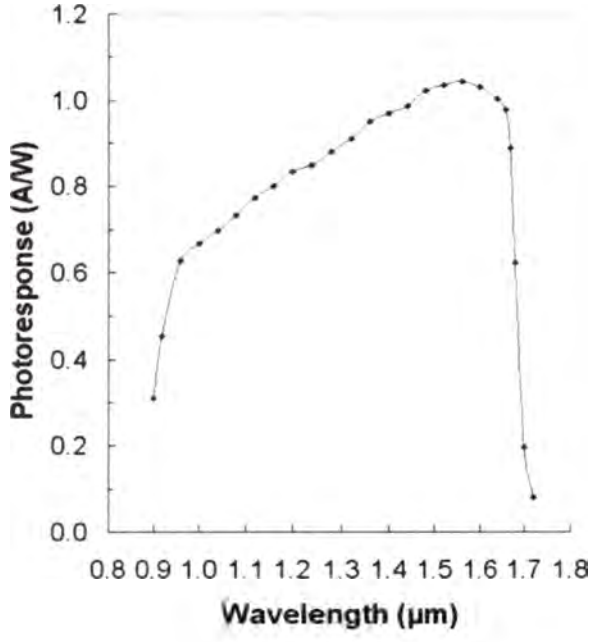

FIGURE 4.4: Typical spectral response of the Xenics 1.7 InGaAs camera [46]. Due to the laser diode used in our experiments, most of our measurements were conducted between 1510-1580 nm, where the camera response remains relatively constant.

4.2.2.1 Laser drift

The tunable laser diode has an internal feedback system in place to stabilise output power, particularly as the lasing wavelength is tuned. However, the accuracy of this power stabilisation is typically $\sim 5\%$. As the laser source was used not only for probing the AWG chips but also for testing the wavelength dependent properties of various experimental components, this error would accumulate and add to the uncertainty of our measurements.

We measured the laser output power as a function of wavelength tuning by connecting the laser output fibre to a power-meter. The laser was tuned in 5 nm increments across its tuning range, and the output power recorded. The results can be seen in Fig. 4.5. The process was repeated by tuning in both directions (from short to longer wavelengths and vice-versa) with similar results observed in both directions to within uncertainty. The laser's wavelength response appeared to be stable over a number of hours. All subsequent calibration measurements of the fibre splitter were normalised

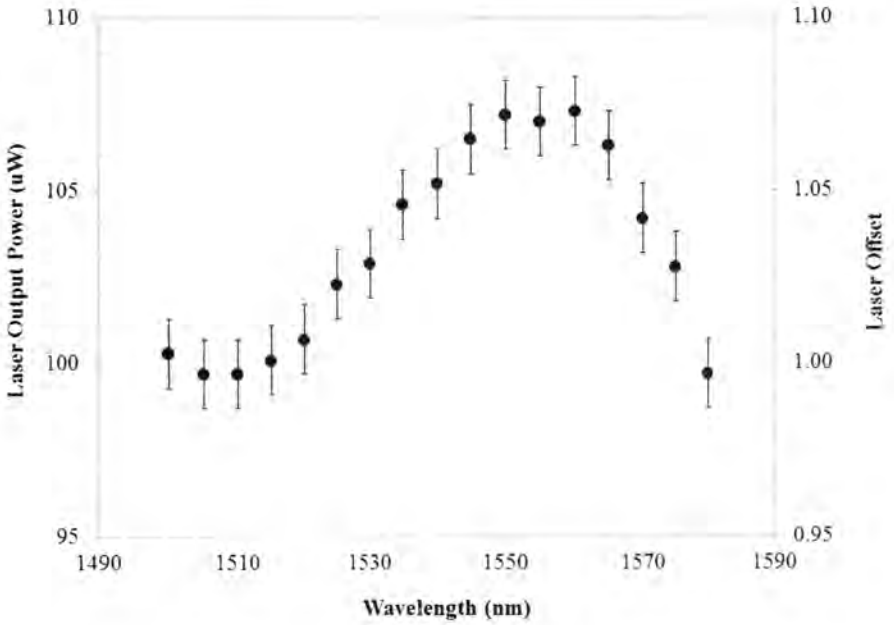

FIGURE 4.5: Laser output power as a function of wavelength tuning was measured to calibrate power fluctuations as the laser is tuned to different wavelengths. The laser was seen to fluctuate by up to 10 % but in a predictable manner which could be calibrated from our final measurement. The error bars denote the accuracy of the power meter measurements. The right axis shows the percentage power offset centred at the output power for 1580 nm.

to the laser's wavelength response.

4.2.2.2 Fibre beam-splitter

As the fibre beam-splitter was used for normalising throughput measurements, it was important to accurately measure the splitter's wavelength response over the probing wavelengths (1500-1580 nm). The beam splitter's input port was connected to the diode laser output, with two separate NIR power-meters measuring output power in both the 90% arm (referred to as 'Port 1') and the 10% arm (Port 2). The laser was scanned between $1500 - 1580$ nm and the output power of both arms recorded at 5 nm intervals. The throughputs were obtained by normalising to the injected power (obtained from the laser output power scan outlined in the section above). The results are presented in Fig. 4.6.

The splitter's wavelength response varied by no more than 1% over the wavelength range tested. These results were used to normalise the throughput measurements of

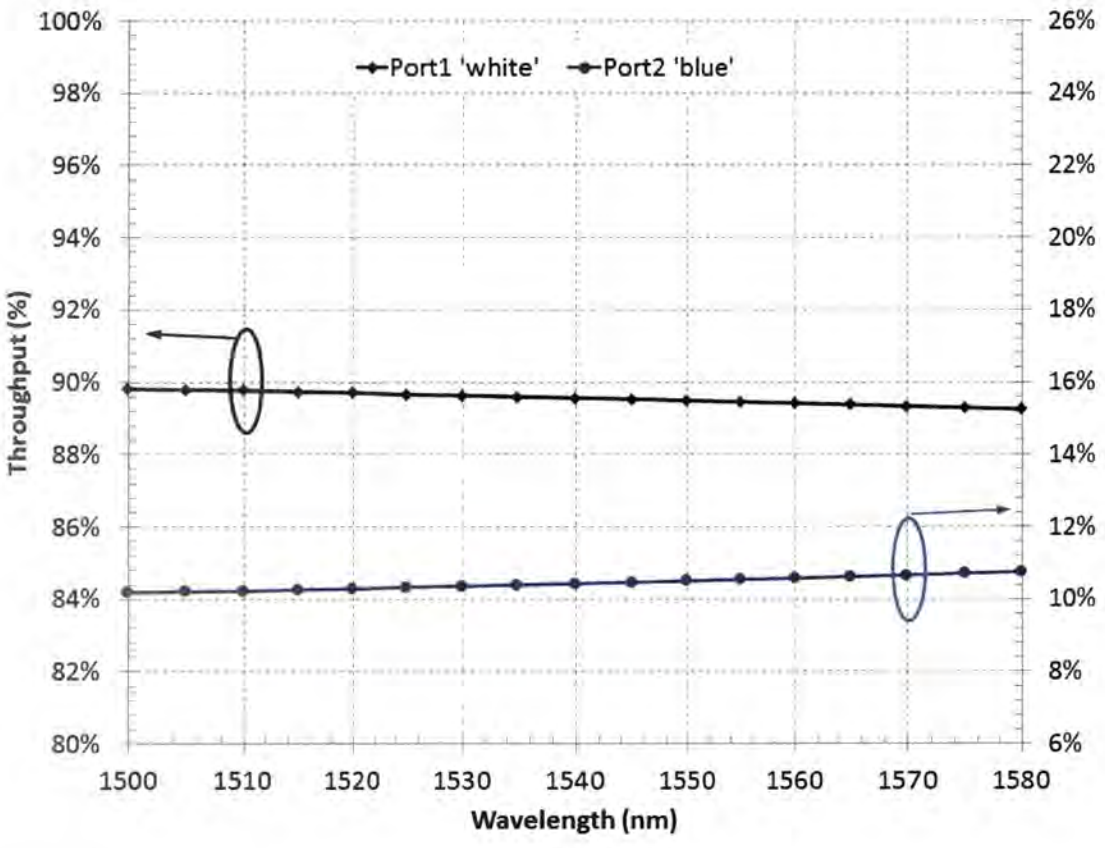

FIGURE 4.6: The wavelength response of the 90:10 fibre beam-splitter for Port 1 (left axis) and Port 2 (right axis).The splitter was characterised to correct any wavelength response the splitter had over the laser tuning range.

the AWG chip. By calibrating both the laser output and fibre splitter, we were able to predict the output power of Port 2 (10% arm), which was used to launch light into the AWG chip, by measuring the output of Port 1 (90% arm). This allowed for active monitoring of injected power to within 5% uncertainty.

4.2.2.3 Detector nonlinearity

To use the Xenics camera to measure the power, the camera was flux-calibrated. This gave us the ability to relate the camera counts (which are proportional to incident photons) to a power value. Further, we checked the camera for nonlinearity.

The camera was flux-calibrated using the set-up in Fig. 4.7. Using the calibrations made thus-far, we are able to accurately predict the power emanating from the fibre

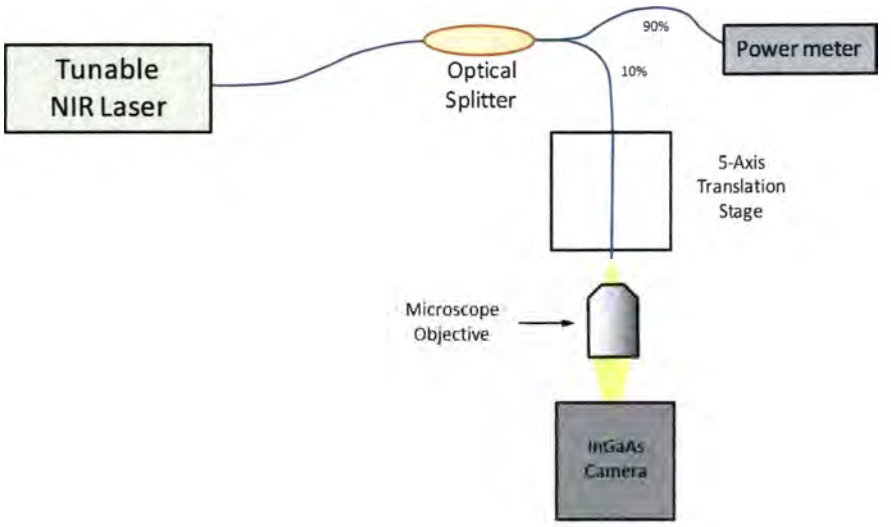

FIGURE 4.7: The experimental set up for camera flux calibration.This setup is similar to the AWG characterisation setup, but here the fibre end face is directly imaged.

pigtail attached to the 10% arm from the beam-splitter. Thus, by imaging the field radiating from the fibre output using the camera at different powers and wavelengths, we were able to record the camera's response. The injection system was identical to the one used to probe the AWG chips, with the camera positioned on a coarse 3-axis translation stage which allowed for initial alignment. Fine focusing onto the fibre end-face was achieved using a NanoMax 5-axis flexure translation stage which the fibre was placed on. The image was determined to be in focus when the fibre mode field appeared to be the smallest. Once the camera was in focus the positions of it and the fibre were locked. The exposure time used was the same as that used in chip probing (200 ms). When an image is taken the power output from the pre-calibrated power-metre is simultaneously recorded, allowing us to calculate the incident power on the detector.

Images obtained by the camera were saved in .csv format, and reduced by a MATLAB script (the script is described in detail in Appendix B, and discussed in Section 4.2.3). The script first subtracts a dark frame to remove the background, then extracts the total encircled counts from the mode profile.

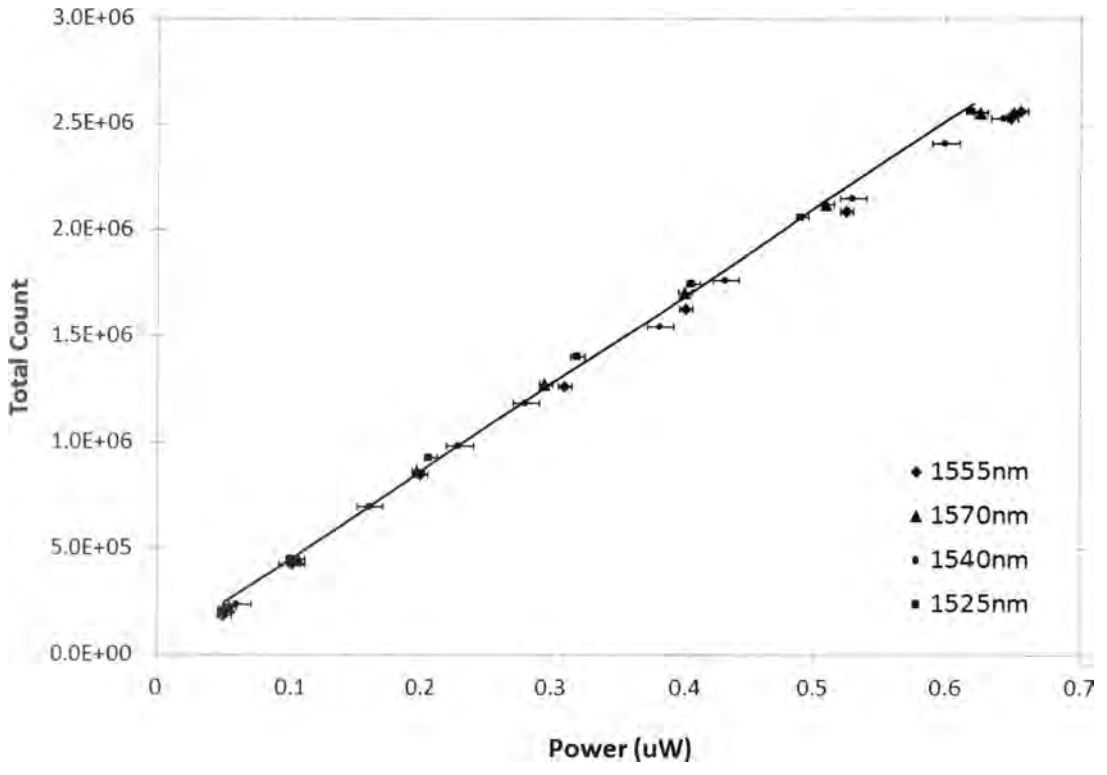

FIGURE 4.8: The detector response to varying incident power for four different wavelengths. The detector response is shown to be linear within experimental uncertainty, with the exception of very low powers where some non-linearity is observed. All experiments were conducted at higher powers to avoid any non-linear effects of the detector. Separate calibration curves were recorded for each microscope objective and exposure time. The values for the horizontal axis were obtained using the low-noise power-meter.

Using a variable optical attenuator we scanned the output power at arbitrary intervals between $100 - 900$ nW. These powers correspond to the camera's background noise floor, and the point where the image begins to saturate respectively. We measured the camera's power response curve for four different wavelengths (1525, 1540, 1555, & 1570 nm) as shown in Fig. 4.8.

With the exception of low powers (< 200 nW), the camera's response is linear within our measurement error. This allows us to accurately extrapolate the relation between total encircled counts and power, provided the imaging system does not change. These calibrations were carried out every time the microscope objective was changed, and

done for a series of different objectives (5×, 40×, 100×), or the exposure time was varied. By flux calibrating the camera, we were able to obtain an accurate measurement of incident power using the same images used for PSF analysis.

4.2.2.4 Magnification of imaging system

The use of microscope objectives for re-imaging was necessary due to the large magnifications required to adequately sample a mode-profile of ~ 8 μm with the detector's 20 μm pixel pitch. The typical imaging distance for the Olympus microscope objectives we used was 160 mm. While they were mounted on a 160 mm lens tube, the tube length itself could vary by up to a few millimetres, hence we felt it prudent to confirm the real magnification of our imaging system.

We used an Echelle grating with a grating pitch of 12.56 μm to confirm the magnification of the system. First, the grating was imaged on a calibrated reflection DIC microscope to measure the grating pitch with an accuracy of ~ 0.5 μm, shown in Fig. 4.9 a). Then, the grating surface was imaged by the camera, using in this case a 40× objective (Fig. 4.9 b)). The grating was illuminated by a diffuse lamp. Using the image from the camera the grating period was measured, and related to the known pixel pitch and dimensions of the detector to determine the obtained magnification. The magnification was then used to scale the measurements of the mode profile sizes, and obtain accurate values for the PSF. This process was repeated for all the objective lenses used in the experiments. Typically, the magnification was accurate to a few percent but was corrected for nonetheless.

4.2.3 Data reduction

The images obtained by the camera were reduced by a MATLAB script, which can be found in Appendix B. In this section, we outline the basics of the reduction code to demonstrate how the throughput values and PSF dimensions were obtained.

First, the code imports the file (typically in .csv format, but also for .tiff), into an array, and calculates basic parameters such as array size, orientation, file name, and maximum value. The code then determines the centre of the mode profile, which were typically Gaussian-like, by searching the array for its maximum value. Note that by this point, the camera was already calibrated for both hot and dead pixels using the

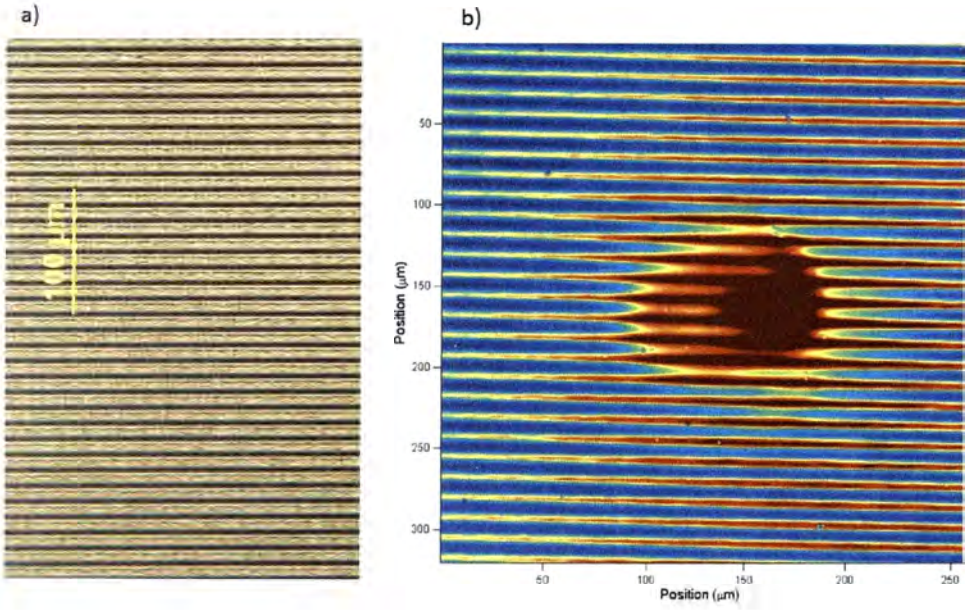

FIGURE 4.9: A) A DIC microscope image of grooves on an Echelle grating used to accurately determine groove spacing. B) Image of the same Echelle grating using the InGaAs detector with a 40x microscope objective. The flare in the middle of the image is an artefact caused by a back-reflection of the non-even illumination source. This has no impact on measurements. The grating pitch was used to calibrate the magnification of the InGaAs imaging system.

camera control software, so in the vast majority of measurements the pixel with the maximum value was the centre of the mode profile. In the rare cases that the automatic process did not work, the user could select it manually.

The code then chooses an area of the image far from the mode profile itself to determine the average background and then subtracts this background from the rest of the image. Much like before, this step can be carried out visually by the user if there are any artefacts or problems. The code then determines an area around the mode-field such that the whole field is included (typically 10% larger than the field itself). It then sums all the pixels into a total number of counts, and converts it to a power value in mW using the extrapolated camera power calibration mentioned above. The code then outputs the power value that is then used in the throughput calculations.

After the total encircled power is calculated and displayed, the code then calculates

and displays the PSF profiles. The previously defined centre of the mode-field is used to determine values important to astronomy; its position relative to the rest of the frame is important for calculating linear wavelength dispersion of the device, the FWHM of the mode (both physically and spectrally) is required to calculate spectrograph resolving power, and the mode-field diameter (MFD) is sometimes required for mode-matching calculations. The FWHM is determined by the code by taking a linear cut through the centre of the mode and searching for the 50% values relative to the centre. Once calculated, it outputs the value in both spectral and physical units. The MFD is calculated much like the FWHM, but instead determines the width to the $1/e^2$ points.

After outputting all the required values, the script prompts the user to select the desired graphing formats (axes, colour, scale, etc.) and then graphs the mode field profile, and produces a .png version of the image. The whole script is automated and allows for quick processing of images from the camera.

4.2.4 Multiple off-axis fibre injection

Ideally, we would like to be able to observe more than one target simultaneously on-sky using an IPS. To do this, we must inject multiple concurrent signals into the AWG, and hence use multiple input fibres simultaneously, and retrieve usable spectra. Therefore, we aimed to investigate if it was possible to inject fibres that are off-axis, where they are no longer aligned to the centre of the input FPR, and assess its impact on spectrograph performance. As Chipset A already has input waveguides, this kind of testing must be done on Chipset B which has its input face polished back to the FPR. Therefore all experiments conducted to test off-axis injection were done using Chipset B.

The first method used was a replication of the direct fibre launch explained in Section 4.2.1. A pigtailed SMF-28 fibre was butt-coupled to the input FPR, and translated across the FPR at 100 μm intervals, with the wavelength maintained at 1540 nm. The PSF size and throughput were recorded for each off-axis position step. The results can be found in Figure 4.23 in Section 4.3.3.1. The fibre was translated using the NanoMax stages a total of 1.8 mm ($\pm$0.9 mm off-centre).

The second method used a linear fibre array (V-groove array), with eight fibres spaced at 127 μm, shown in Fig. 4.10. This allowed for the simultaneous injection of

eight signals into the AWG chip which were directly imaged at the output. The V-groove array was aligned to the input FPR using a NanoMax 5-axis translation stage. The positioning was optimised by monitoring the output power of the on-centre fibre of the V-Groove and the two edge fibres. Unlike the single fibre case, tip-tilt positioning was essential. Index matching oil was used at the V-groove FPR interface to minimize Fresnel reflections and minimize coupling losses.

An eight port fibre splitter was connected to Port 2 (10% arm) and each output port spliced to the eight fibres of the array. Hence all eight fibres injected the laser light simultaneously at varying offset positions, which were imaged at the output using a 20× objective. The laser was scanned from 1500 – 1575 nm at 5 nm intervals. As the complete output spectrum from the AWG did not fit on a single frame due to the magnification used, the camera was translated and multiple images stitched to get the complete AWG output spectrum. The results are found in Figure 4.24 in Section 4.3.3.2.

The testing using the v-groove array could have been conducted instead using the previously mentioned method (translating the input fibre) and would give the same results. However, this does not allow for the injection of light simultaneously into multiple input fibres as only one fibre is used in the translation method. Thus, using the v-groove, one can test all positions simultaneously in any configuration, making data acquisition more efficient. Further, as will be made clear in Chapter 5, for the AWG to be used on-sky, a v-groove was required to inject multiple fibres simultaneously.

4.2.5 Multi-Mode Interference taper analysis

An important part of our experiments was to determine the impact of parabolic horn tapers on AWG spectrograph performance. While the resulting spectrograph output was characterised using procedures outlined in Section 4.2, the physical dimensions of the MMI taper needed to be measured to accurately construct a comparative beam propagation model. Due to the low refractive index difference between the waveguide core and bulk material, the chips were imaged using a differential interference contrast (DIC) microscope, using a beam-shearing interference technique, which is sensitive to very small optical path differences [47].

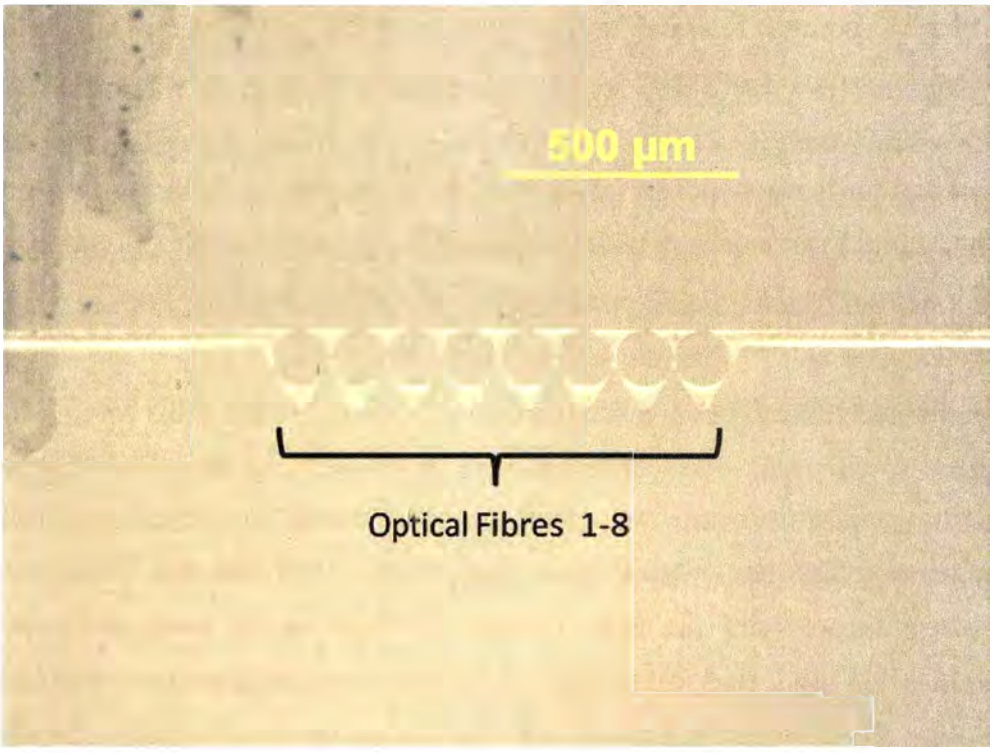

FIGURE 4.10: A) A DIC microscope front-on image of the fibre v-groove array used to launch multiple signals into the AWG chip simultaneously. The eight fibres can be seen sitting in the v-grooves in the centre of the image. The images were taken to characterise the separation of fibres and check their mapping in the v-groove.

The DIC microscope was fitted with a number of objectives (5×, 10×, 20×, 40×, and 100× magnification). The 20×, 40× and 100× objectives are cover slip corrected or feature a collar for adjusting the amount of correction necessary to optimally resolve buried waveguide structures. An Olympus DP72 camera was attached to the side port of the microscope and connected to a computer for capturing digital images. Figure 4.11 shows a DIC image of a series of input waveguides with MMI tapers entering a FPR. Figure 4.11 illustrates the excellent capabilities of the system at resolving low refractive index contrasts (typically $\sim 10^{-3}$).

4.2.6 Refractive index profilometry

The refractive index profilometer (RINCK Elektronik) is based on the refracted near-field (RNF) method, which was initially developed for measuring the transverse refractive index profile of optical fibres [48] and later extended to integrated optical

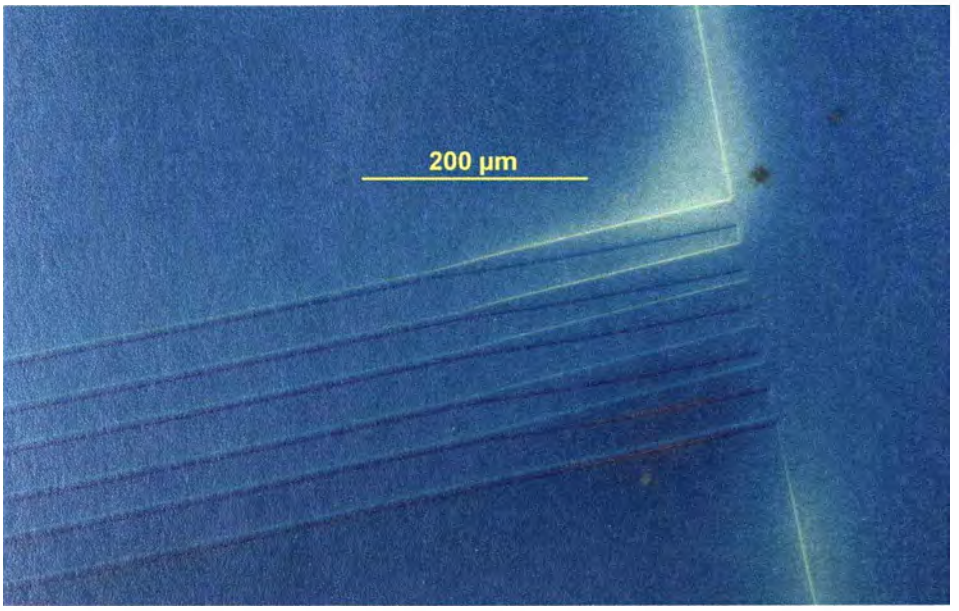

Figure 4.11: Input waveguides entering the FPR of Chipset A, resolved with DIC using the 40× microscope objective. The waveguide along with the taper and FPR slab waveguide are clearly visible.

waveguides [49]. Several variations of the technique and apparatus to measure the refractive index profile of planar or buried waveguides have been reported [50–52]. This technique was used to characterise the refractive index profiles of the waveguides and FPRs of the AWG chips.

The instrument (see Figure 4.12) is equipped with a 635 nm and a 1550 nm laser diode. The spatial resolution is ≈ 0.5 μm at 635 nm with a refractive index resolution of 1×10^{-4}. In order to obtain the specified resolution it was essential to focus the probe laser exactly onto the sample's back surface. The results from this section are shown in Figure 4.14.

4.3 Characterisation results

4.3.1 AWG IPS chipset layout

We characterised the two separate AWG chipsets to compare and contrast design parameters for astronomical use.

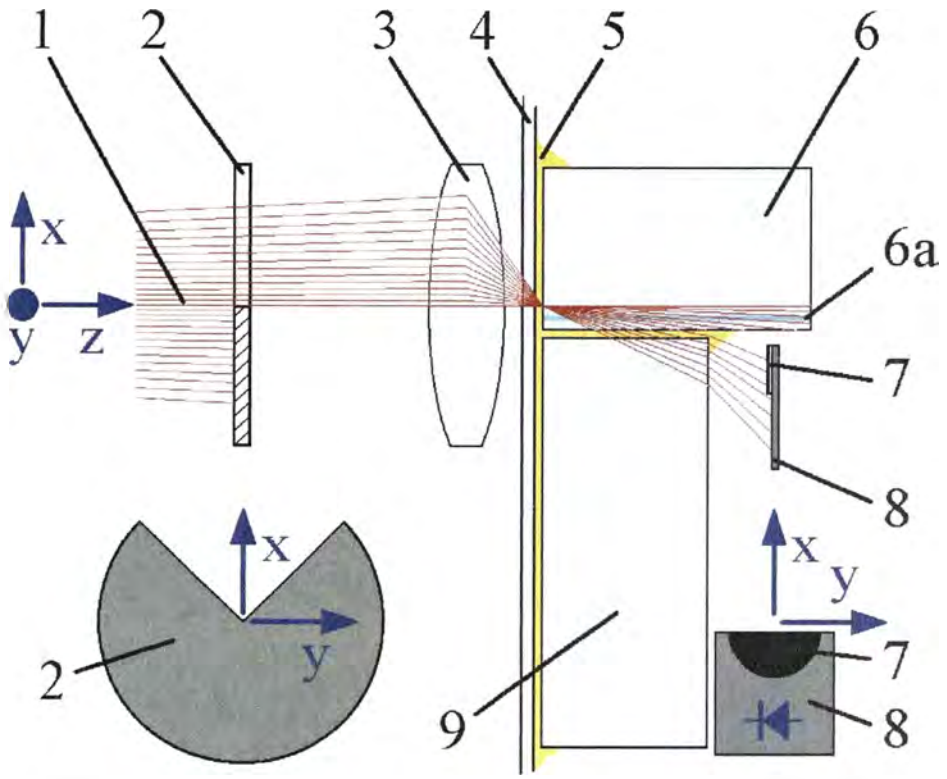

FIGURE 4.12: Schematic of a refracted near-field profilometer (RINCK). The probe laser (1) is obstructed by a sector stop (2) before being focused by a microscope objective (3) onto the back surface of the sample (6). The sample is placed on a carrier cover slip (4) and butted against the reference glass block (9) with the waveguide layer (6a) parallel to it. All gaps between the reference block, carrier cover slip and sample are filled with refractive index oil (5). The refracted light is collected by a detector (8) with partially obstructed aperture (7) in close proximity to the reference glass. (Image is courtesy of Dipl.-Ing. Stephan Rinck)

4.3.1.1 Parameters common to both chipsets

We imaged the chips end-on to measure the thickness of the different layers (Figure 4.13) using a DIC microscope as outlined in Section 4.2.5. Further, using the Refractive Index Profiler (RIP) outlined in Section 4.2.6, we obtained accurate measurements of the refractive index of the individual layers, shown in Figure 4.14.

From the DIC image shown in Fig. 4.13 we can see the various layers that make up the AWG chip. The silicon layer acts as a substrate for the whole device and is approximately 3.8 mm thick. On top of it is a 13.4 ± 0.4 μm thick layer of undoped silica which acts as the bottom waveguide cladding, while the top cladding layer of silica is slightly thicker at 19.3 ± 0.2 μm. Nestled between the cladding layers is a 7.6 ± 0.7 μm

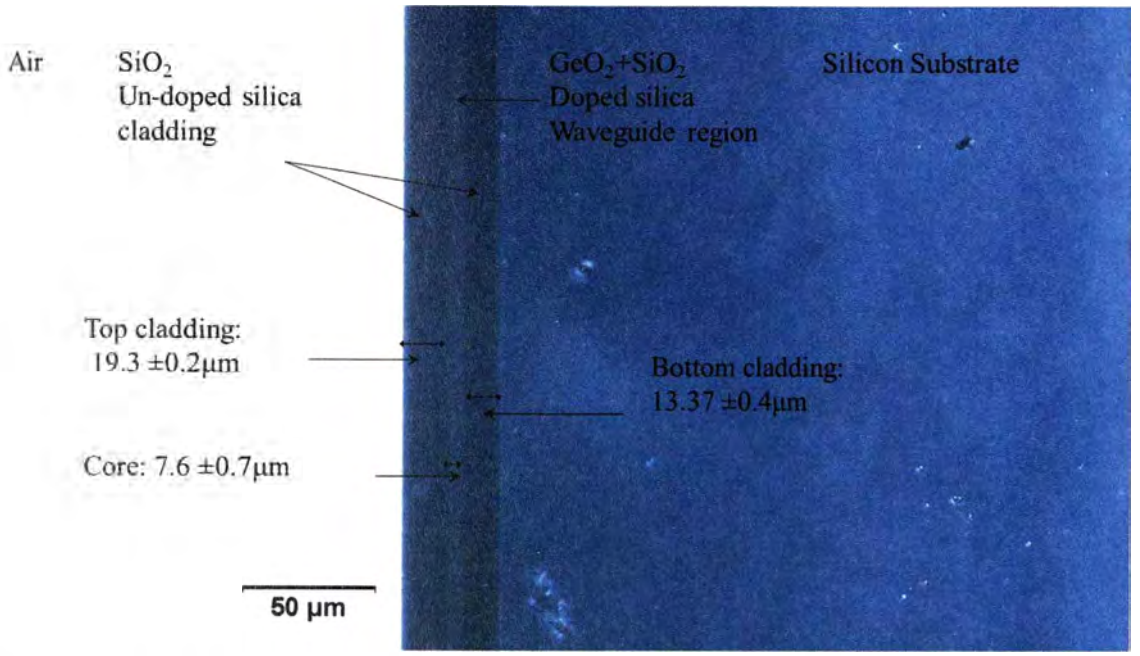

FIGURE 4.13: A DIC image of the AWG chips showing the different layers. A silicon substrate is covered with an undoped silica layer which acts as the bottom cladding. Then a layer of Germanium doped silica is deposited which acts as the waveguide core. After the waveguide circuitry is imprinted it is capped with another layer of silica which acts as the top cladding.

thick waveguide core layer. The core layer is made of germanium doped silica which gives it a slightly higher refractive index than the cladding to allow it to guide light. The dopant also allows waveguide circuitry to be imprinted using the lithographic techniques outlined in Chapter 2. The thickness of the core layer is chosen during the design stage to allow for the propagation of the fundamental mode at the desired wavelength. If the layer is too thick, higher-order modes will begin to propagate.

Figure 4.14 shows the refractive index profile of the AWG along with the reference block and oil. As we outlined in Section 4.2.6, the reference block and oil have a known refractive index value, and thus allow us to calibrate the measurement and obtain values for the AWG layers. The silica cladding layers were found to have a refractive index of 1.4610 ± 0.0001, with the core layer having an index of 1.4718 ± 0.0001. This gives a refractive index contrast (Δn) of $\sim 1 \times 10^{-2}$. The silicon substrate has a refractive index of ~ 3.48.

Another common feature of the two chipsets is that their design parameters are identical. This is an important factor as it allowed for a precise comparison between

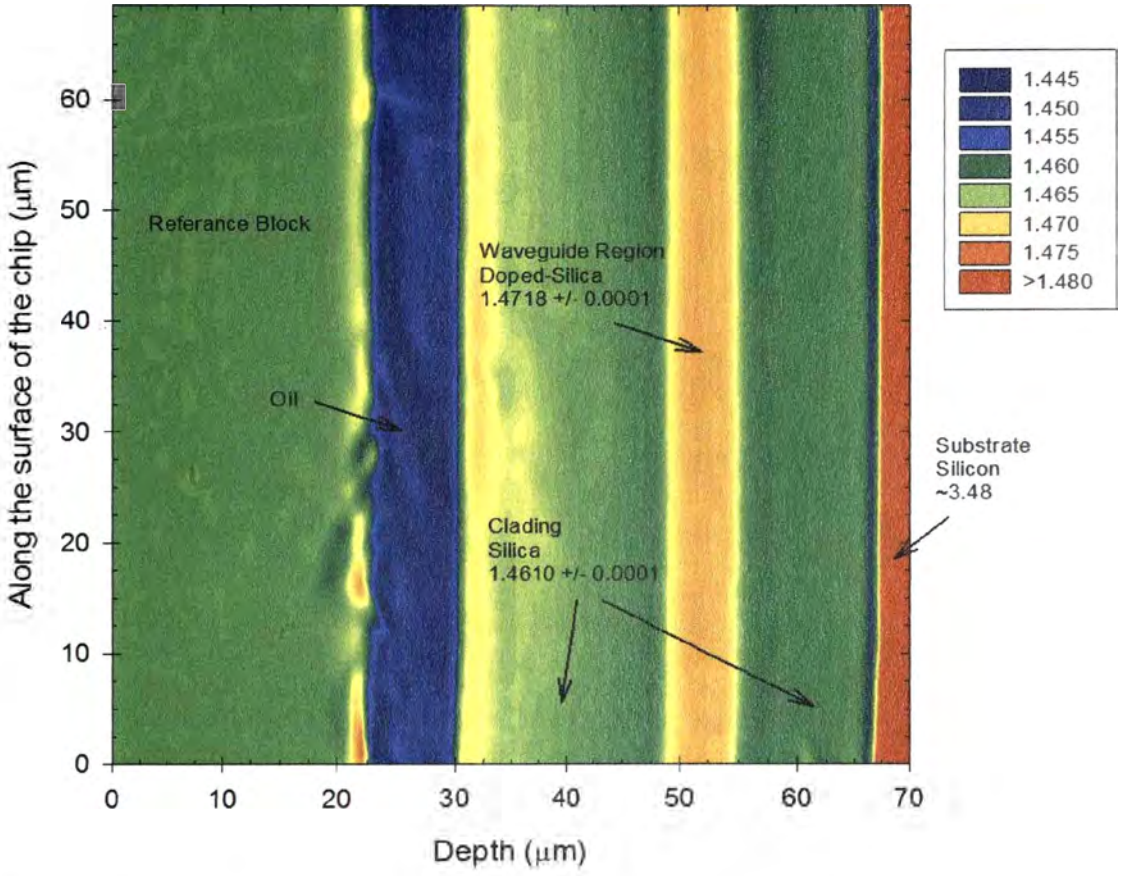

FIGURE 4.14: A refractive index profile of the AWG chip (Chipset A) showing the refractive index of the different layers. The contour plot shows the AWG substrate, cladding, and core layers to the right, along with the calibration oil and reference block to the left.

the tapered, and untapered input. Their central operating wavelength is 1540 nm at the $m = 27$ diffraction order, $\sim$ 22 mm focal length FPRs, and the waveguide array consists of 428 waveguides with a length increment (ΔL) of $\sim$ 28 μm. Both chipsets have had their output waveguides removed and polished to make a flat focal plane. Before the output waveguides were removed, the device was designed to operate with a 100 GHz (0.8 nm) output channel separation, and 40 output waveguide channels.

Figure 4.15 shows the typical AWG IPS layout (in this case Chipset A) with inset DIC images of waveguide circuitry. The overall layout can be seen in Fig. 4.15 c), with the input FPR being at the bottom of the image and the output FPR at the top (and the polished focal plane at the top right). During typical commercial fabrication of AWGs, the manufacturer often superimposes a second mirrored AWG design on top of the original. This is done to maximise the real estate of the lithographic wafer and is

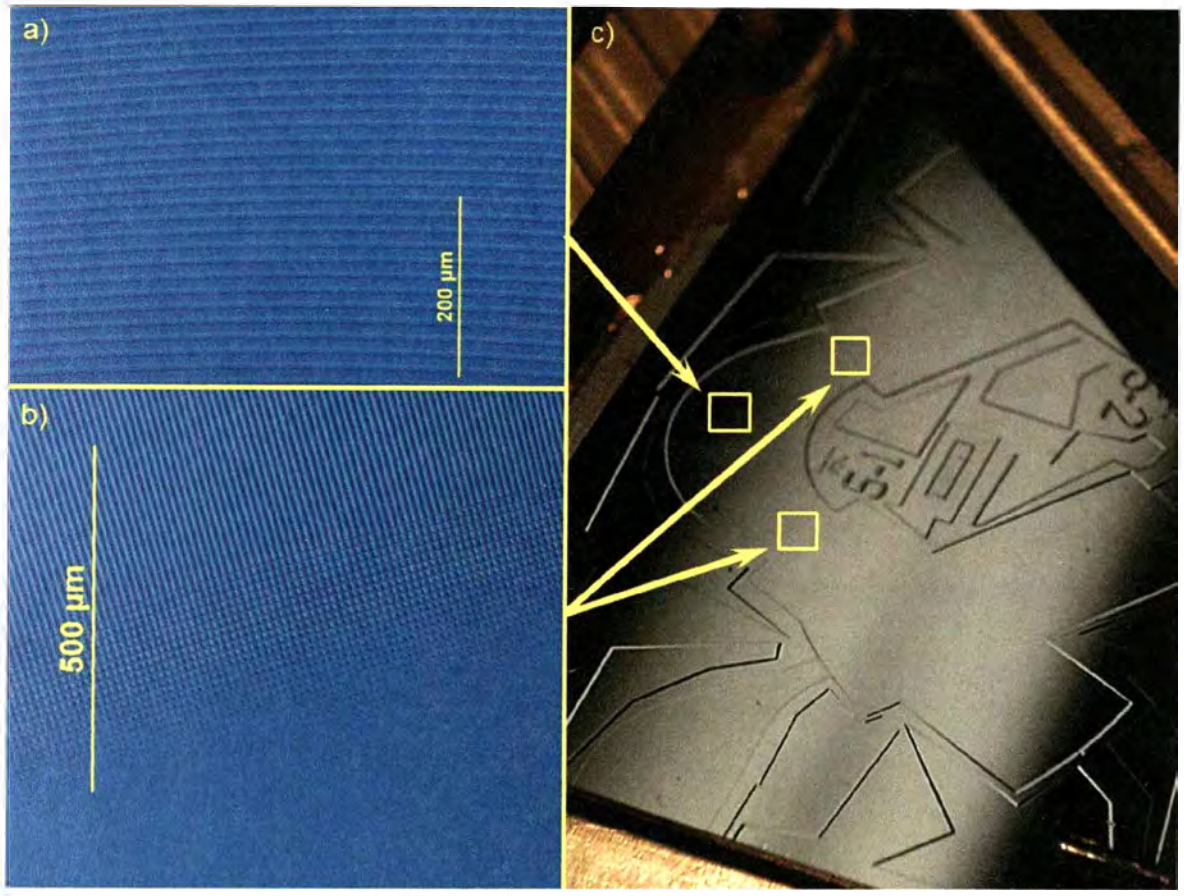

Figure 4.15: Image of a typical AWG IPS layout with inset DIC images of waveguide circuitry. a) DIC image of the waveguides in the array. b) DIC image of the FPR-Array interface showing the segmented taper region. c) Layout of a typical AWG IPS, with the positions of a) and b) shown. The polished output is to the top right of c). While this image is of Chipset A, the circuitry highlighted is common to both Chipsets.

visible in c). It is important to note, however, that while this mirrored AWG is visible in all our AWGs, the second design is not used in any of our Chipsets, and in fact parts of it are removed to achieve the flat focal plane at the output FPR.

Figure 4.15 a) shows the typical layout of waveguides in the waveguide array segment of the AWG. The waveguide cores are ~ 7 μm in width, with their minimum separation ~ 9 μm (at the FPR-Array interface), then expanding as the array bends. The performance of the device reflects that there is no substantial cross-coupling, with the manufacturer specifications placing it typically around -30 dB.

The FPR-Array interface is shown in Figure 4.15 b). Here the waveguide array meets the FPR slab waveguide, employing a segmentation taper (outlined in Chapter 3), which provides low-loss coupling of the light into the individual waveguides of the

array.

4.3.1.2 Chipset A properties

As outlined previously, Chipset A has a parabolic horn taper injection waveguide connected to it. The FPR interface and input waveguides with the parabolic horn tapers can be seen in Fig. 4.16. In the DIC images there are six individual input waveguides on Chipset A. However, as Fig. 4.16 b) demonstrates, the optical fibre is only aligned to one of the input waveguides, so only one input waveguide actually carries any signal. The motivation for using multiple waveguides is to make the fibre-waveguide alignment easier.

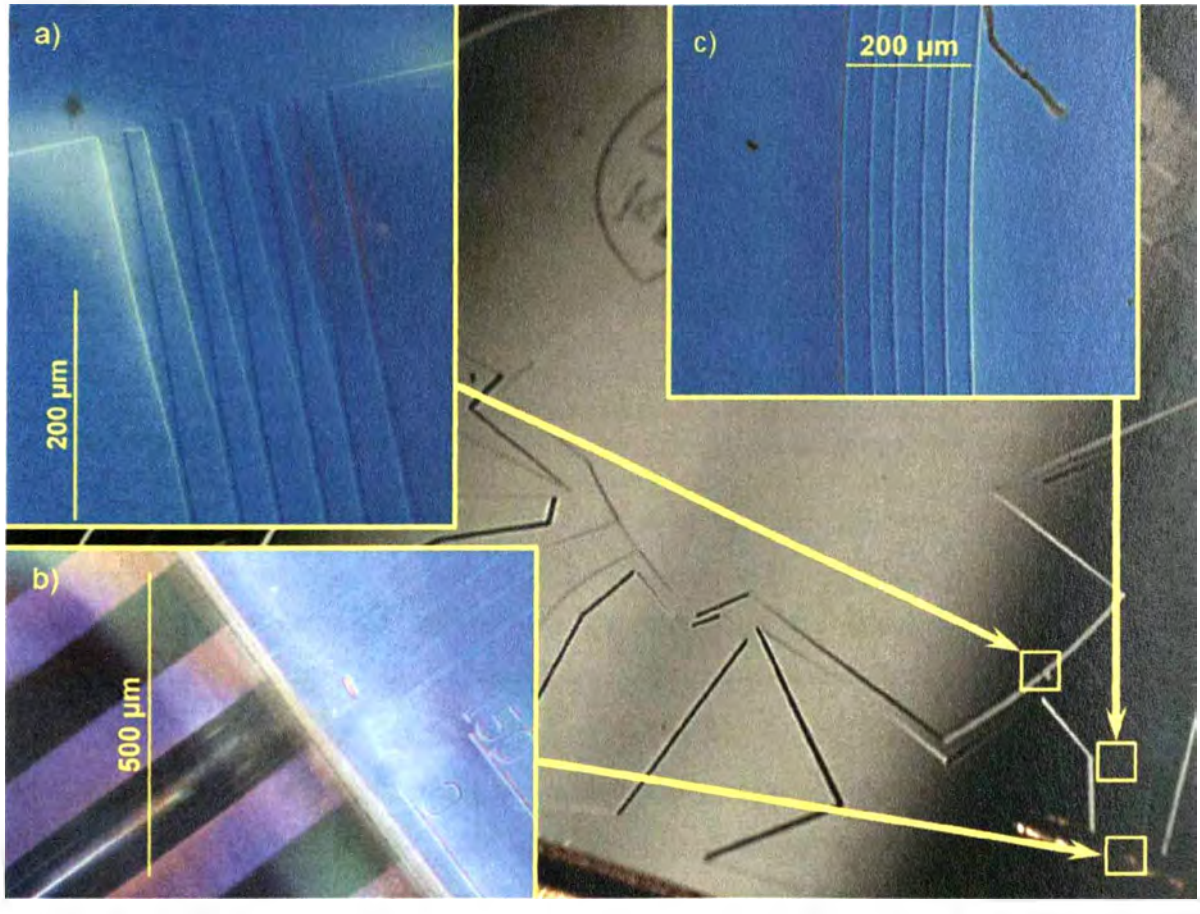

FIGURE 4.16: Image showing the unique circuitry found on Chipset A. a) DIC image of the parabolic-horn tapers at the input waveguide-FPR interface. b) DIC image of the optical fibre-input waveguide interface. c) DIC image of input waveguides.

The reason parabolic-horn tapers are ubiquitous in commercial AWGs is due primarily to the nature of their use in telecommunications. Unmodified AWG-WDMs

focus the spectrally dispersed light into separate waveguides at the output of the chip, thus sampling a continuous spectrum into discrete wavelength channels. If non-tapered waveguides are used for injection and collection of the light, any misalignment between the position of the collecting waveguide and the re-imaged spot will lead to a mode mismatch between the two, and result in a loss in the system. Misalignments can arise from errors in fabrication or temperature changes, but even if the chip itself is stabilised, wavelength instabilities in laser-sources used in telecommunications will cause a mismatch, and result in high losses. To alleviate these restrictions, a parabolic-horn taper is employed where the input waveguides meet the input FPR (Fig. 4.16 a)). As was explained in the previous section, the tapers create interference between the fundamental and 2^{nd} order modes, yielding a double-peaked electric field distribution which is typically two or three times wider than that of a standard single-mode input waveguide. However, when utilising AWGs as spectrographs like in our case, all output waveguides are removed, thus creating a flat output focal plane from which a continuous spectrum can be obtained as desired. Hence, parabolic tapering of input waveguides for loss minimisation is actually redundant, and as will be demonstrated in the next section, is disadvantageous for astronomical applications.

4.3.1.3 Chipset B properties

The chip itself can be seen in Figure 4.17, with a schematic of the waveguide circuitry shown in Figure 4.18. By removing the waveguides, we were able to directly launch light into the input FPR and explore the impact of the parabolic-horn tapers on IPS performance. Further, as the input is not a flat polished plane, we were able to explore the use of multiple input fibres simultaneously, to greatly increase the observation efficiency of the IPS device.

4.3.2 Parabolic-horn taper impact on resolution

The two different AWG chipsets were characterised to explore the effects of parabolic tapers, the first containing parabolic-tapered input waveguides on the chip (Chipset A), and the second having all input waveguides and tapers removed (Chipset B). The

FIGURE 4.17: Image showing the Chipset B AWG. Chipset B has no input waveguide/fibre and no protection housing.

chips were probed using the setup described in Section 4.2.1.

The output mode profile of Chipset A showed the expected distinctly broadened double-peaked profile, as shown in Figure 4.19 a). A wavelength scan was conducted to observe changes in PSF with respect to wavelength, with the results shown in Figure 4.20. The average physical PSF FWHM was 18.7 ± 0.7 μm and the associated spectral FWHM was 0.63 ± 0.02 nm. This translates to a spectrograph resolving power $R = \frac{\lambda}{\Delta\lambda} \sim 2400$.

By contrast, the direct-fibre launched AWG chipset demonstrated a Gaussian profile (Fig. 4.19 b)), with an average physical FWHM of 6.6 ± 0.6 μm, and a spectral FWHM of 0.22 ± 0.02 nm, yielding $R \sim 7000$ (Figure 4.21. It should be made clear that this is solely the result of the smaller physical size of the injection PSF from the single-mode fibre as compared to the parabolic-horn taper rather than the specific shape of the PSF injected. The resulting resolving power is much closer to the theoretical maximum of a diffraction-limited device where for N combining beams, the limiting resolving power is $R = mN \sim 11,600$. Although this is the theoretical resolving power for a flat-top illuminated spectrograph (i.e. equal intensity into every single-mode waveguide), we use it for simplicity to illustrate departures from the ideal case, as in our case there is

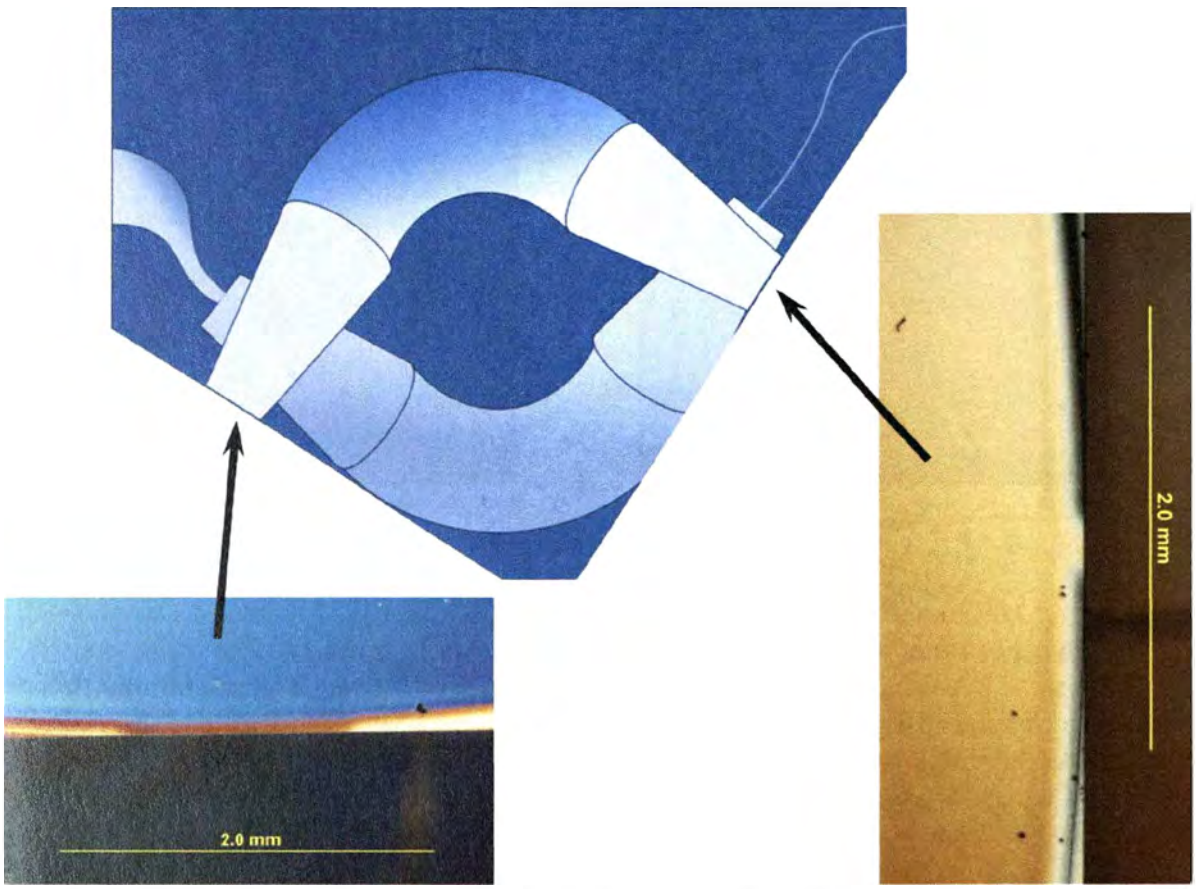

FIGURE 4.18: Schematic showing the layout of the AWG circuitry found on Chipset B. Both the input and output FPRs have been polished back removing all waveguides. The inset DIC images show the polished ends.

a Gaussian illumination profile across the waveguides with some potential truncation.

4.3.2.1 Throughput

The throughput was determined by comparing the injected power, measured at one port of a 90:10 splitter with a power meter, to the total encircled power as measured by the flux-calibrated camera, as described in Section 4.2.1. The two measurements were taken simultaneously to minimise any fluctuations in the power of the probing laser. The peak efficiency was identical for both chip configurations to within our experimental error and is shown inf Figure 4.22.

The average peak throughput was measured to be $\sim 75 \pm 5$ %. As the throughput did not change when comparing Chipset A & B, the direct-fibre launch method of feeding AWG chips is suitable for astronomical use. Indeed, it is preferable as there is a

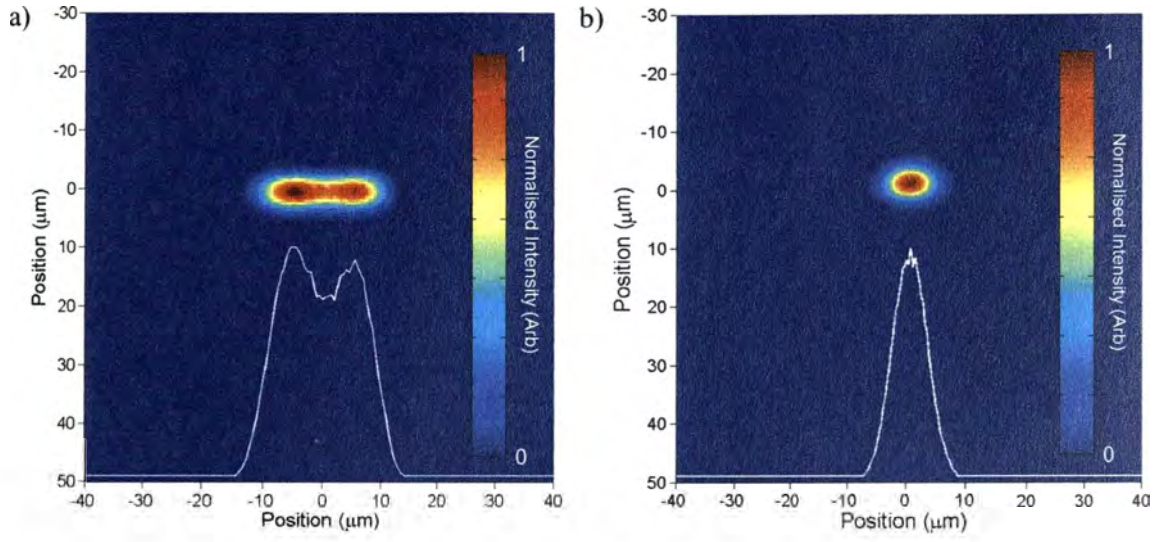

FIGURE 4.19: Image a) is the measured PSF from Chipset A. The figure shows clearly the double peaked mode profile caused by the parabolic-horn taper and has a physical PSF FWHM was 18.7 ± 0.7 μm and the associated spectral FWHM was 0.63 ± 0.02 nm. Image b) is the measured PSF from Chipset B. The figure shows a Gaussian field profile, which is the same as the mode profile that emanates from a single mode optical fibre with a physical FWHM of 6.6 ± 0.6 μm, and a spectral FWHM of 0.22 ± 0.02 nm. The intensity profile for both images is linear in arbitrary units.

three-fold increase in the resolving power associated with the removal of the parabolic-horn tapers. Finally, by redesigning the AWGs, it has been demonstrated that the size and shape of the injection PSF can be tailored to suit a particular application [53], however optical fibres offer the freedom of positioning multiple injection ports at arbitrary positions along the input.

4.3.3 Direct multiple fibre input

As we mentioned in Chapter 2, fibre-fed astronomical instruments typically use multi-mode fibres (usually $\sim 50 - 150$ μm cores) to ensure that the focused light from the telescope is adequately captured and transported down the fibre. This is done as it is difficult to efficiently focus atmospherically perturbed wavefronts into single-mode fibres, even with the aid of adaptive optics [54, 55]. Such large diameter cores result in a highly multimode signal being injected into the spectrographs. These transport fibres are not compatible with AWG technology as any introduction of modes higher than the fundamental mode severely degrades the performance of the devices. Hence,

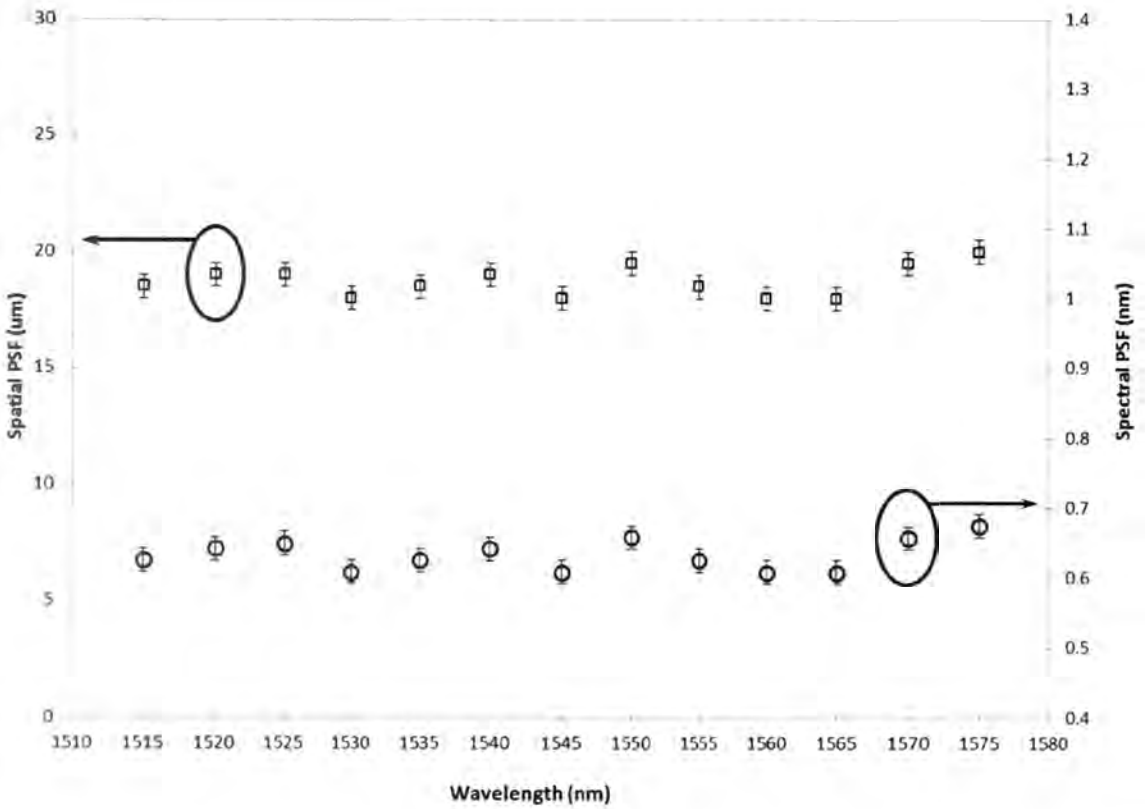

FIGURE 4.20: Results from measurements of Chipset A's PSF as the wavelength is scanned from 1510 nm to 1580 nm. The PSF FWHM is shown in both physical units (left axis) and spectral units (right axis). This shows the PSF is relatively stable across the FSR.

conversion between multimode and single-mode formats using a photonic lantern is necessary. Using photonic lanterns, multimode light captured by the telescope can be efficiently separated into multiple SMFs, enabling devices that only operate in the single mode regime, such as the AWG based spectrograph.

As an example, under seeing-limited conditions, a typical telescope with a 4 m primary mirror diameter, will have a PSF which can support hundreds of modes, scaling up to the ELTs, with mirror sizes greater than 25 m, we potentially face thousands of modes for a single source. Coupled with the fact that for multi-object spectroscopy simultaneous observations of multiple sources is required, this will require thousands of SMFs to interface with our AWG spectrographs. If each AWG chip only takes one SMF input (like Chipset A), thousands of AWG chips would be required for a complete instrument, significantly increasing its total cost and volume, and reducing the inherent

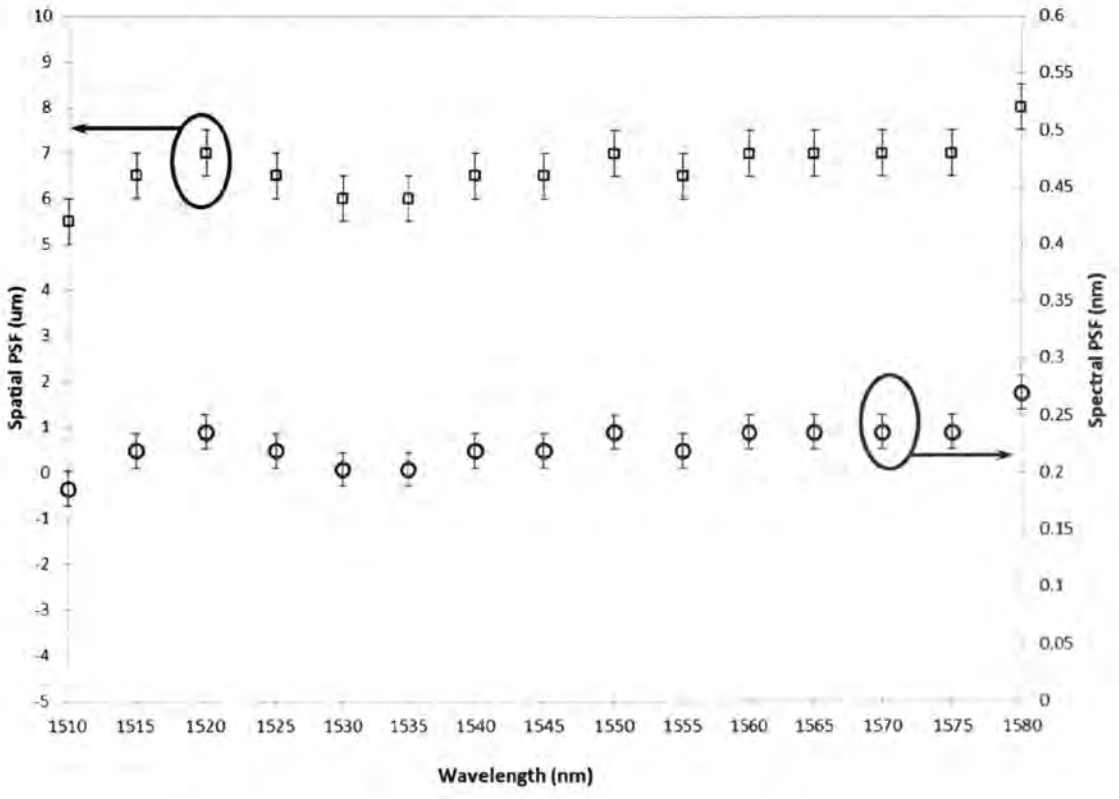

FIGURE 4.21: Results from measurements of Chipset B's PSF as the wavelength is scanned from 1510 nm to 1580 nm. The PSF FWHM is shown in both physical units (left axis) and spectral units (right axis). This shows the PSF is relatively stable across the FSR, much like Chipset A above. Further, both the physical and spectral scale are smaller than Chip A's.

benefits in terms of stability and robustness.

It is therefore desirable to increase the number of SMFs used to inject into the AWGs. By using the direct-fibre launch technique it is possible for an almost arbitrary positioning of the injection fibre along the input FPR, and moreover it enables the possibility to interface multiple fibres with the chip simultaneously. We explored the feasibility of launching multiple single-mode fibres by examining how the throughput efficiency and PSF behave with relation to the input fibre position.

4.3.3.1 PSF aberrations from off-axis launch

The experiments were conducted by translating the injection SMF along the input surface at $100 \sim \mu$m increments, while simultaneously imaging the output and calculating

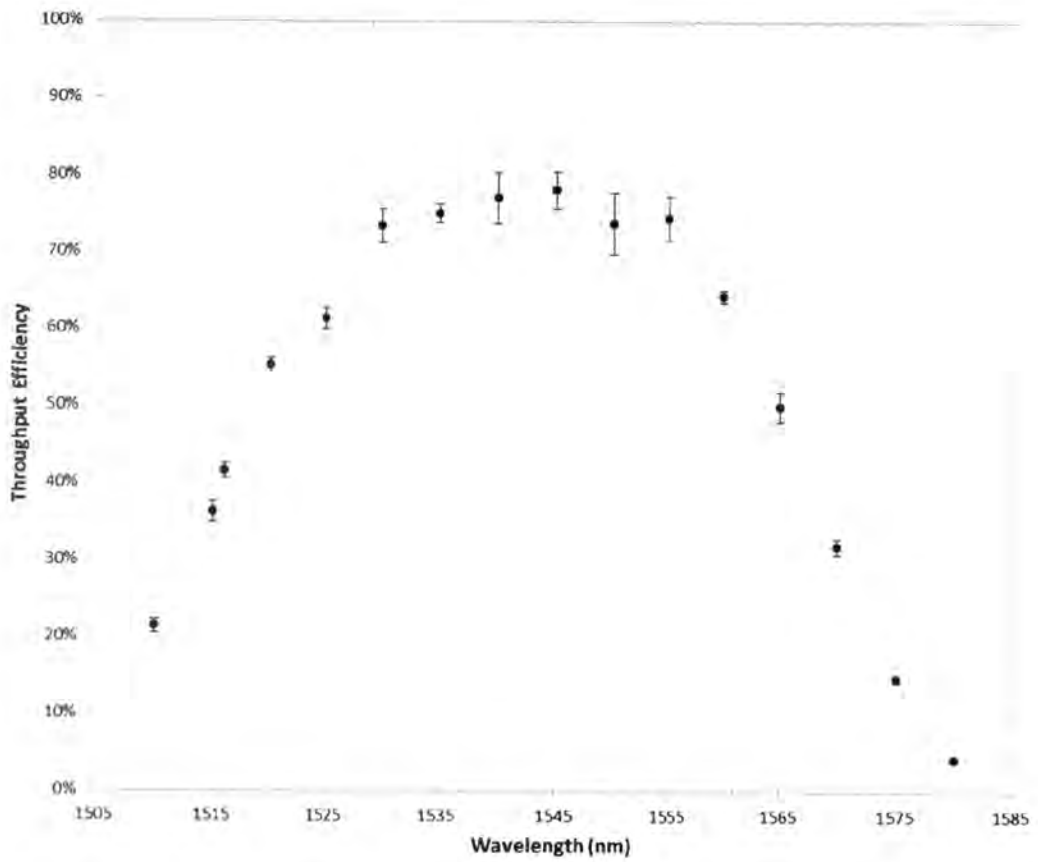

FIGURE 4.22: Graph of throughput as a function of wavelength for Chipset B across a single FSR. Chipset A showed a near identical response.The throughput drops off at the edges as light is coupled into higher and lower orders.

the throughput efficiency, using the same methodology as in the previous section. The results are shown in Figure 4.23.

The throughput efficiency at the central operating wavelength of 1540 nm was measured to be $77 \pm 5\%$ for fibres placed at the centre of the FPR, gradually decreasing as a function of off-centre fibre position (Fig. 4.23 (d)). As shown in Fig. 4.19 b), the PSF has a Gaussian profile for fibres that are launched at the centre of the free propagation zone (also shown in Fig. 4.23 (b)), with a resolving power of $R \sim 7000$ (see Fig. 4.23(d)). However, by injecting fibres with an increasing offset from the centre of the FPR, the PSF becomes increasingly broadened and aberrated as shown in Fig. 4.23 (a) & (c). The broadening of the PSF reduces the R, and indeed, at a position of ± 0.8 mm the resolving power of the spectrograph is $\sim 20\%$ lower.

The angle at which the launch fibre interfaces with the chip was kept consistently

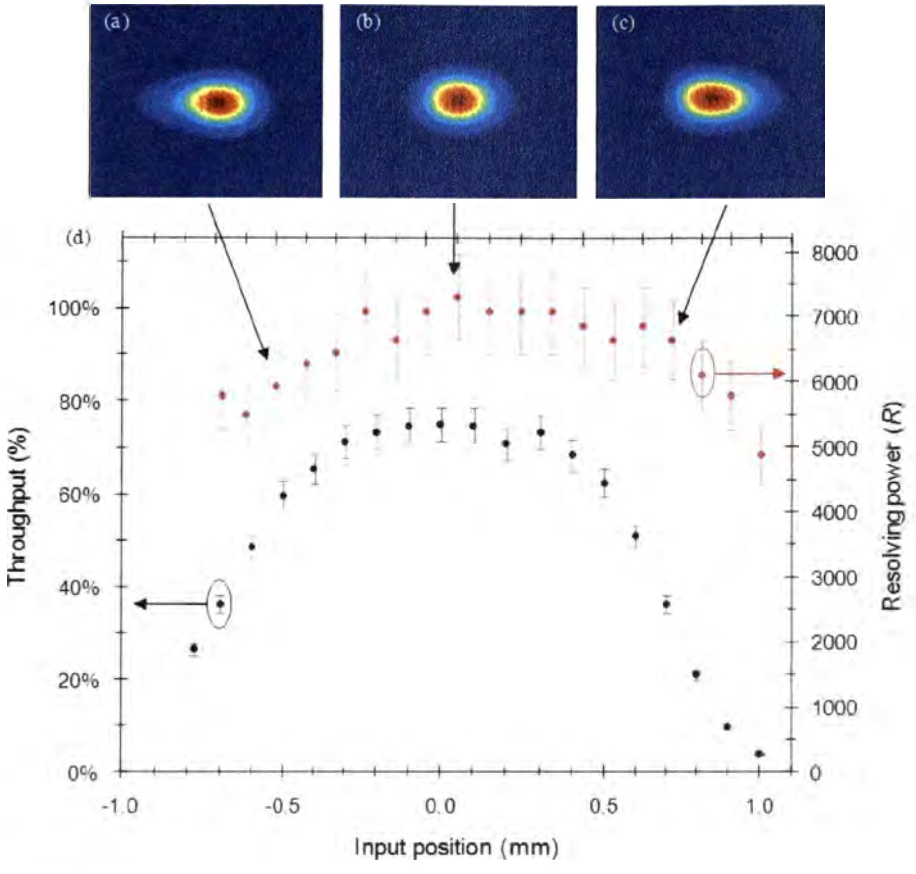

FIGURE 4.23: The resolving power is shown for input fibre positions across the input surface of Chipset B (red). The resolving power drops off for fibres placed further off centre. The throughput as a function of input fibre position is shown in black. The measurements were taken at 1540 nm.

perpendicular to the polished facet. As such, it was not aligned with the Rowland curvature of the input FPR. Therefore, as we moved further from an on-axis launch the angle that the light was injected into the input FPR increased monotonically from normal incidence. This resulted in a mismatch between the wavefronts and the array of waveguides at the far end of the input FPR, which we believe caused the PSF to skew at the output of the device, in the case of the off-axis launch as seen in Fig. 4.23(c). The increasingly skewed nature of the output PSF as a function of increased offset of the injection fiber from the centre was corroborated by using an AWG model constructed in the beam propagation tool 'BeamProp'.

The aberration can in principle be corrected for by matching the input fibre launch angle to the Rowland curvature of the input FPR, and imaging along the Rowland curvature of the output FPR. Nonetheless, it is still possible to use the current device

by first assigning a cutoff for acceptable resolving power and throughput, which in turn will determine the number of fibres which can be used to inject into the AWG chip for that required level of performance. This form of aberration is of course only an issue for AWGs that have had their input waveguides removed (such as in our case), because in typical AWG designs the input waveguides are always made to match the input Rowland curvature. However, the input waveguide separation cannot be altered after manufacture, which places severe limitations on the separation of the resulting spectra at the output (as explained in the following section). By removing the waveguides and injecting directly with fibres we obtained the flexibility to map this parameter space and an adjustable design factor when constructing an on-sky prototype. When constructing a more mature instrument with custom designed AWGs, which take the waveguide separation into account, this problem with PSF aberration is easily and avoided.

4.3.3.2 Central wavelength shift due to off-axis launch

For astronomical observations, the polished focal surface of the AWG chip's output FPR was imaged using a 2D detector array to entirely sample the continuous spectra across the whole FSR. We therefore characterised the efficiency profile for the 27^{th} order by scanning across the full wavelength range of the probing laser (between 1500 and 1580 nm in 5 nm intervals), shown in Fig. 4.24. Multiple fibres were placed at the input using a linear fibre V-groove array with a 127 μm spacing between neighbouring cores. This spacing is the minimum allowable as a result of the physical outer diameter of SMF being 125 μm. While the array comprised 16 fibres, the results presented in Fig. 4.24 are only for a subset of five of the fibres. The first fibre was positioned at the center with the others positioned at 127 μm increments increasingly further off-centre in one direction.

The efficiency curve, while maintaining the same shape, is different for each of the input fibres. The central wavelength of each order shifts to longer wavelengths with respect to the off-axis position of the input fibres. The efficiency curve for a given order will change depending on fibre position, with the central wavelength being shifted by ~ 20 nm for every 500 μm translation of input position as can be seen from Fig. 4.24. However, the profile of the efficiency curve is consistent across the physical output

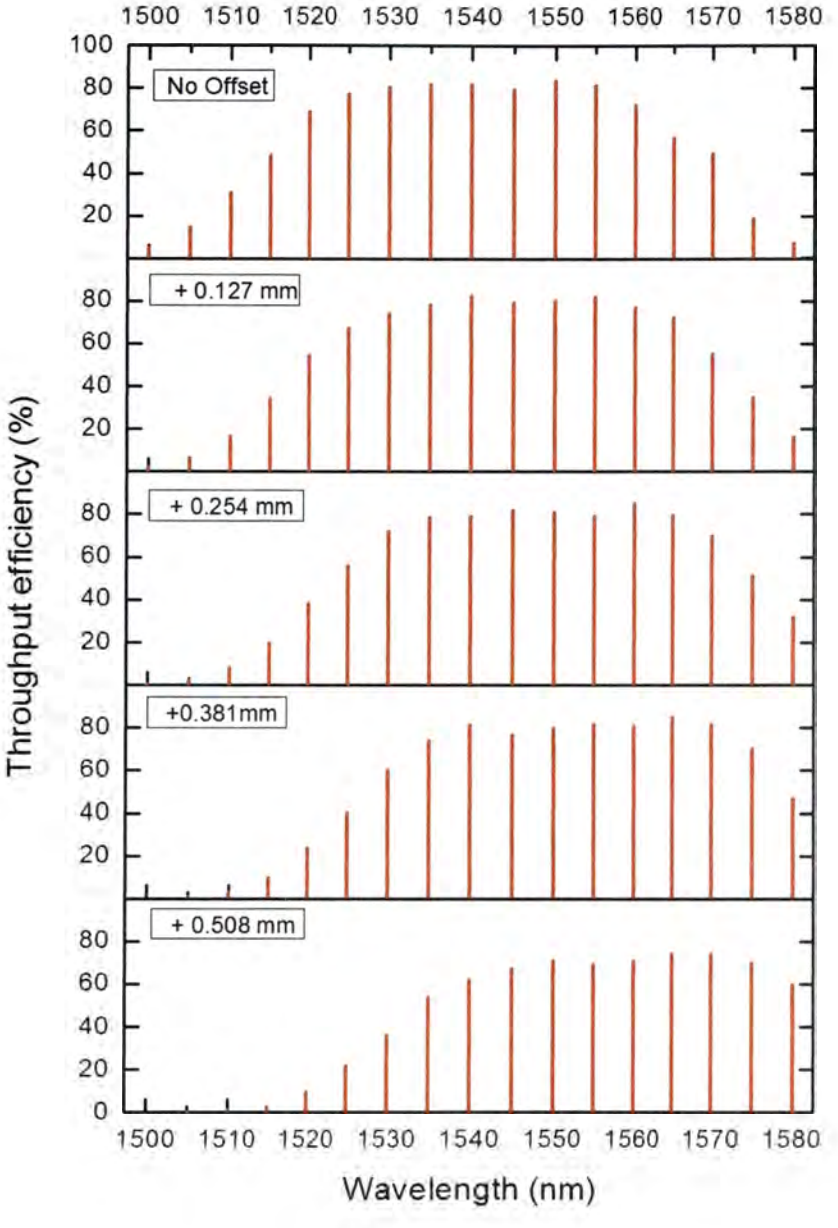

FIGURE 4.24: Efficiency across an 80 nm bandwidth for the 27^{th} order measured in 5 nm wavelength intervals for Chipset B. The experimental uncertainty for all efficiency measurements presented in this plot is 5%. The fibre positioned at the centre of the FPR is shown at the top, with progressively more position offset for subsequent fibres. The central wavelength for the order clearly shifts to longer wavelengths proportionally to off-axis fibre translation.

end-face of the chip for all input fibres, as they are shifted. The impact this has on practically implementing an AWG-based spectrograph with multiple inputs is that the response for each fibre will be different based on its input position, and hence needs

to be characterised before implementation. Furthermore, despite the slight off-axis injection there is still significant overlap with the on-axis output spectrum, hence cross-dispersion in the orthogonal direction is required to obtain a meaningful measurement.

The shift of the central wavelength as a function of the input fibre position imposes a limit to the number of fibres that can be used in total. This is because for a sufficiently large offset in injection position from the center, the peak wavelength of the AWG free-spectral range overlaps with the neighbouring order of the on-axis fibre, which is spectrally indistinguishable. In this case, it would not be possible to separate these two spectra with cross-dispersion. For our AWGs, with a free-spectral range of $\sim$ 60 nm, and a fibre spacing of 127 μm, this would occur at the 13^{th} off-axis fibre. Hence, a maximum of 12 fibres would ensure straightforward distinguishability between neighbouring orders.

4.4 Conclusion

By characterising the direct launch of multiple fibres simultaneously, we have shown that it is possible to increase the number of spectra detected by an AWG-based spectrograph. This can increase observational efficiency in the case of a telescope aided by adaptive optics (where light is directly coupled into SMFs) by allowing multiple sources to be observed per chip. For the seeing limited case, which requires a photonic lantern device to couple into SMFs, we are able to use one chip per source, which is still more efficient than the tens of chips that would be required if a single SMF is injected per chip.

The limitation is that this technique requires cross-dispersion optics and a 2D detector, which adds extra complexity to the system. Alternatively, one can conceive of forgoing multiple fibre injection in favour of using cheaper 1D detector arrays, which in certain circumstances might be favourable, however this will require many more AWG chips to be used. These two approaches would need to be balanced to compare their respective economic viability, as at the moment it is unclear. For the on-telescope testing of an IPS instrument, which we present in the next chapter, the choice of observatory limited us to the seeing limited case and the use of a photonic lantern. Hence, multiple off-axis direct fibre injection was the only practical way to interface the IPS to the telescope.

The conventional practice of using parabolic-horn tapers for increased throughput efficiency is shown to be redundant and detrimental for astronomical applications. By removing the tapers and using a direct-fibre launch we increased the resolving power from 2400 ± 200 (Chipset A) to 7000 ± 700 (Chipset B) while maintaining the same efficiency of $77 \pm 5\%$.

Simultaneous off-axis launch of multiple fibres has its drawbacks, with fibres placed up to 0.8 mm off-centre showing a 20% decrease in resolving power due to mismatch between the fibre launch angle and the Rowland curvature of the FPR. Further, the efficiency curve for a given order will change depending on fibre position, with the central wavelength being shifted by $\sim$ 20 nm for every 500 μm translation of input position.

With this characterisation, we demonstrated that commercially available AWG chips can be modified to simultaneously image spectra that come from multiple input fibres. This can potentially increase the observational efficiency of an AWG based spectrograph for astronomy, and indeed other applications where such spectrographs can be used. With the ability to image multiple spectra, one can now have control fibres to monitor background noise, as well as greatly increasing the number of sources that can be monitored per chip, potentially reducing the number of chips that need to be used, and hence the cost.

"Never memorize something that you can look up."
Albert Einstein

5

First Astronomical Results using the Integrated Photonic Spectrograph

While photonic spectrographs have been characterised in laboratory conditions for their applicability for astronomy, they were not previously demonstrated on a working telescope. This is of particular importance, as the interfacing of photonic technologies, particulary diffraction limited (mono-mode) devices to ground based telescopes is a challenge. In this chapter we outline the design, construction, telescope interface, the science goals, and the results of a prototype IPS instrument tested on the 3.9 m Anglo-Australian Telescope (AAT) at Siding Spring Observatory, Australia.

5.1 Initial on-site testing of the Chipset A IPS

The aim of the initial tests involving the IPS was to acquire a spectrum of a sky source to confirm and demonstrate that the AWG chips can be used in such a manner. We believed it was prudent to do a coarse test of the IPS prior to proceeding with on-telescope tests. The chosen method was to use the IPS to observe the atmosphere's telluric emission spectrum, as it provides a series of sharp lines across most of the H-band, ideal for confirming the laboratory measurements of the IPSs resolving power over a wide wavelength range. The light was coupled from the sky into the IPS using a SMF at the side of the observatory building. At this point, the SMF was simply

pointed at the night sky with no further optics, as we were observing the atmosphere's emission (emanating from the entire sky) not an astrophysical point source. To perform the cross-dispersion and detection of the IPS output we used the IRIS2 imaging spectrograph, which had both the desired spectral coverage for cross-dispersion and a low-noise NIR detector.

5.1.1 Results

On-sky data was obtained with the prototype IPS at Siding Spring observatory during observing runs from the 17^{th} to 21^{st} of June, 2009 (using the IRIS2 near-infrared imager and spectrograph as the cross-disperser and low-noise detector). The IRIS2 instrument [56] employed a 1024 $\times$ 1024 pixel HAWAII-1 HgCdTe infrared detector array, which was illuminated by an $f/8$ to $f/2.2$ focal reducer. A range of standard astronomical filters for imaging were installed inside the instrument dewar, as was a slit wheel and a sapphire grism for spectroscopy. The spatial scale of the IRIS2 detector was 0.45 arcsec/pixel. The 1" slit for spectroscopy projects to 2.2 pixels on the detector, providing a resolution of $R = 2400$.

The IPS input fibre was stabilised, and viewed the night sky at a $\sim 45^{\circ}$ zenith angle. We used a relay optics assembly to re-image the IPS output focal plane onto the IRIS2 slit [20]. This assembly gives a magnification of 3.5, resulting in a final plate scale of 1.2 pixels per IPS resolution element. Due to the lack of strong atmospheric emission lines within the narrowband (i.e. smaller than the IPS free spectral range) IRIS2 filters we used a broadband H filter (1440 – 1820 nm) and a sapphire grism to cross-disperse the IPS output spectrum. In this mode, the multiple orders of the IPS which are superimposed on the instrument entrance slit were spread out in a series of bands across the detector array.

Using a series of 15 minute exposures over a period of 12 hours, the IPS was able to detect the atmospheric emission spectrum as shown in Fig. 5.1. In this case, the PSF obtained was a convolution of the IRIS2 PSF with the IPS PSF. This was the first continuous sky spectrum to be imaged using an arrayed-waveguide grating spectrometer.

The spectrum in Fig. 5.1 shows the detection of upwards of 27 atmospheric OH emission lines across the 380 nm filter bandwidth. If we project the dispersed spectrum

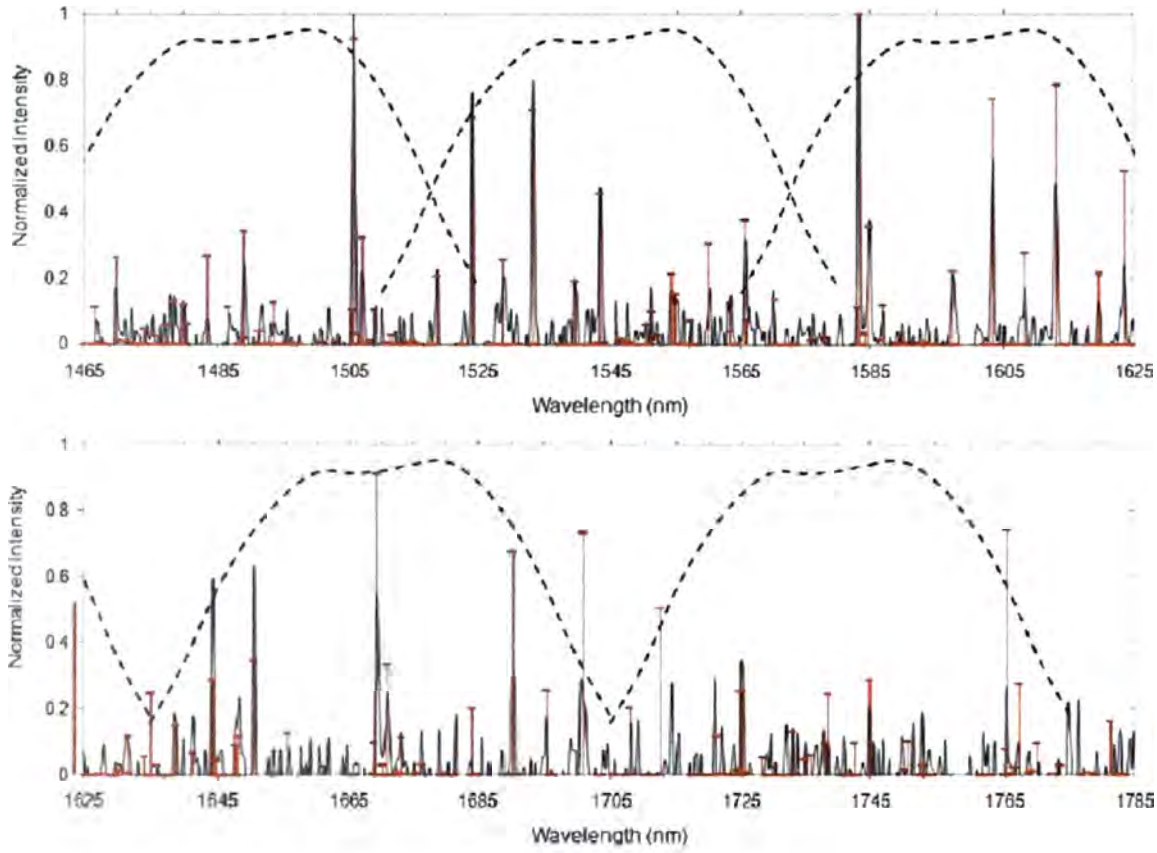

FIGURE 5.1: The night-sky OH spectrum (solid black lines) using the IRIS2 instrument as a cross-disperser for the IPS, superimposed with the theoretical [57] positions and strengths of the OH lines (red), and the diffraction efficiency envelop of the IPS for each order (dashed lines). The AWG grating order is calculated from the known AWG parameters, with the 23rd order starting in the top left, which progresses to 27th order in the bottom right of the graph.

across the IRIS2 slit axis (i.e., giving the IPS spectral resolution), then the average FWHM across the 27 measured sky lines is consistent with the resolution, within experimental error, as measured by laboratory tests. The intrinsic variation in the magnitude of the atmospheric OH emission lines combined with the long exposure times required (due to the small fiber etendue) precludes a determination of the IPS spectral efficiency via the on-sky test.

5.1.2 Limitations of the prototype

While this work demonstrated the possibility of using an IPS device for astronomy, there was still a significant gap between this prototype device and a future astronomical

instrument based on this technology. This prototype employed a single-mode fiber as the input source; this leads to very low coupling efficiencies for astronomical telescopes unless they are operating at close to the diffraction limit. As such, telescope light was not focused into the fibre, with the fibre exposed to the sky directly. In the case of observing the atmospheric emission, this technique is adequate, but not for astronomical sources.

5.2 Instrument Design

Now that we have shown that the IPS has the potential to be used for astronomical research, we proceed by outlining the design and development of an IPS interface for a telescope. We chose the AAT as we were provided access to this telescope. The AAT has a 3.9 m equatorially mounted primary mirror, and is located at the Siding Spring Observatory. The AAT does not employ any form of wavefront control, hence it operates at natural seeing, which at the observatory site, has a median seeing of 1.2-1.6 arcsec.

The IPS was interfaced to the telescope using an integral field unit located at the Cassegrain focus, which coupled light into a MMF. The fibre relayed the light to the IPS testbed at the base of the telescope. The incoming multimode light was separated into a series of single modes using a photonic lantern, then injected into the AWG chip. Much like the test presented in the previous section, we used IRIS2 as the cross-disperser and detector.

5.2.1 Overall system design

The overall system setup is shown in Figure 5.2. The light was coupled from the AAT into the AWG using the IRIS2 imaging spectrograph as a cross-disperser and detector.

An IFU consisting of an array of seven lenslets coupled the telescope light at the telescope's Cassegrain focus into 7 MMFs with 50 μm cores (discussed in detail in section 5.3). For the on-sky results presented here, only one lenslet, and hence one MMF, was utilised. The light was transported to a photonic lantern which converted the multimoded signal to a series of single modes, now in multiple SMFs. These were then simultaneously interfaced to the AWG chip using a 1D fibre array. The AWG Chip outputs the spectrally dispersed signal from all 12 input SMFs on its output face,

which was aligned such that it could be reimaged onto the slit of IRIS2. The Sapphire Grism inside IRIS 2 spectrally dispersed the light perpendicular to the AWG's initial dispersion direction, separating the spectra from the multiple input fibres along with the different orders of the AWG.

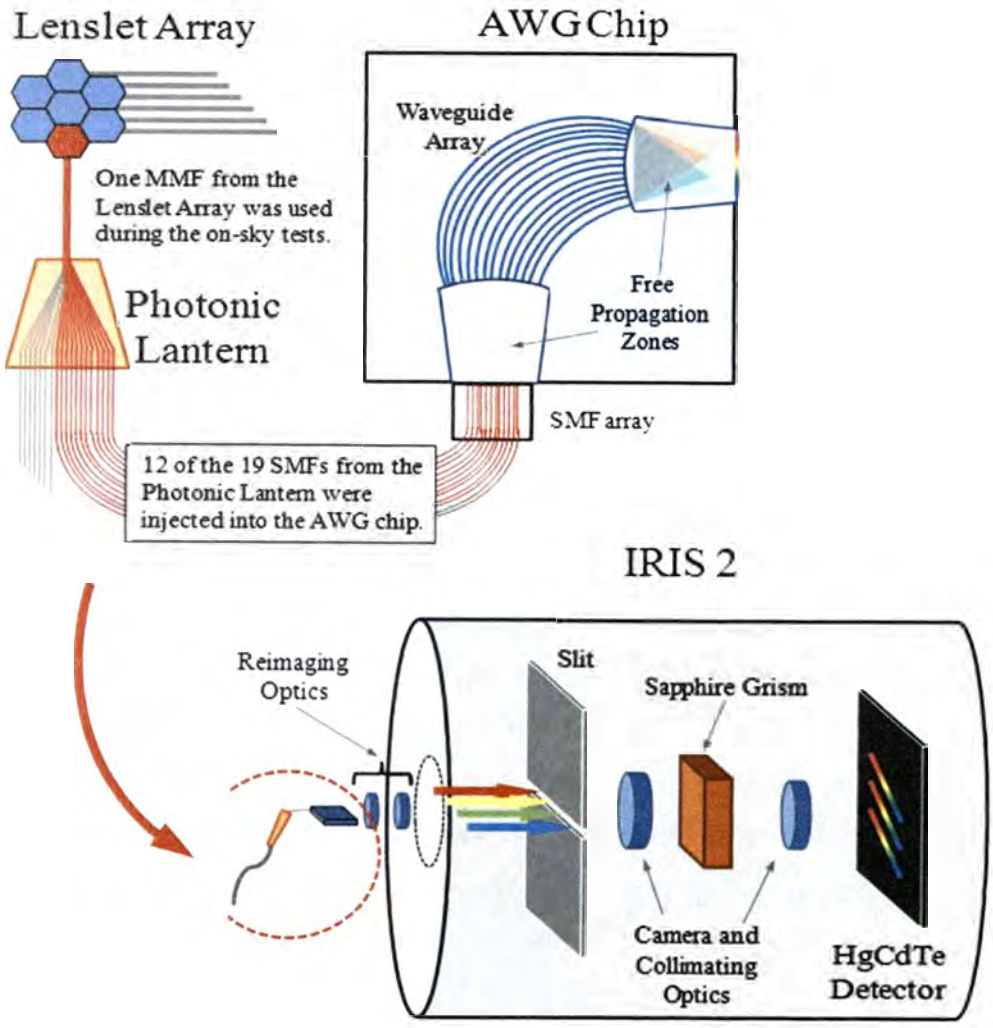

Figure 5.2: A schematic of the IPS on-sky prototype instrument.

5.2.2 Wavelength coverage

The H-band is an astronomical wavelength band in the near-infrared part of the electromagnetic spectrum, centred at 1640 nm with a span of ~ 300 nm ($1490 - 1790$ nm). This particular wavelength region has a number of exciting astronomical targets which

are ideally suited for testing our prototype instrument. Firstly, cool stars such as red giants or Mira variable stars, are the brightest in the H-band and therefore provide a population of bright targets for observation. Second, to test the spectrograph performance, we needed to observe spectral features of the stars, and in most of these red giant stars, the strongest spectral features in the H band are a set of strong absorption bands due to the CO molecule. Such prominent features on the brightest stars in this wavelength range provides a number of targets which could be used to test the IPS prototype.

5.2.3 AWG Chipset-B parameters

Design Chipset B was used for on-sky testing. Of primary concern for the instrument design was the spectral profile at the output face of the chip, as it constrained most of the downstream optics. The performance characteristics of the chips in isolation were presented in detail in Section 4.3, with the important parameters summarised below.

The free spectral range of Chipset B was 57 nm for the central grating diffraction order ($m = 27$). The measured linear dispersion of the chip was 32.9 $\pm$ 0.5 nm/mm, with the spectrum dispersed over 1.73 mm at the output face. The typical PSF was a Gaussian profile with a FWHM of 6.2 μm, providing $\sim$ 200 PSFs per FSR. The chip was highly transmissive ($\sim$ 80%) over the entire H-band. As the single-mode cut-off wavelength of the waveguides was $\sim$ 1250 nm, the AWGs maintained diffraction-limited performance across the entire wavelength range of interest.

5.3 Telescope interface

The IPS prototype was interfaced with the AAT using a fore-optics unit that was mounted at the AAT's Cassegrain focus. The main function of the fore-optics unit was to re-image the central region of the AAT focal plane onto a small Integral Field Unit (IFU) which would couple light to optical fibres to be taken to a gravitationally invariant platform, where the IPS prototype was based.

The telescope interface unit was part of (and initially designed for) the GNOSIS instrument at the AAT [58] and was utilised during commissioning for this instrument.

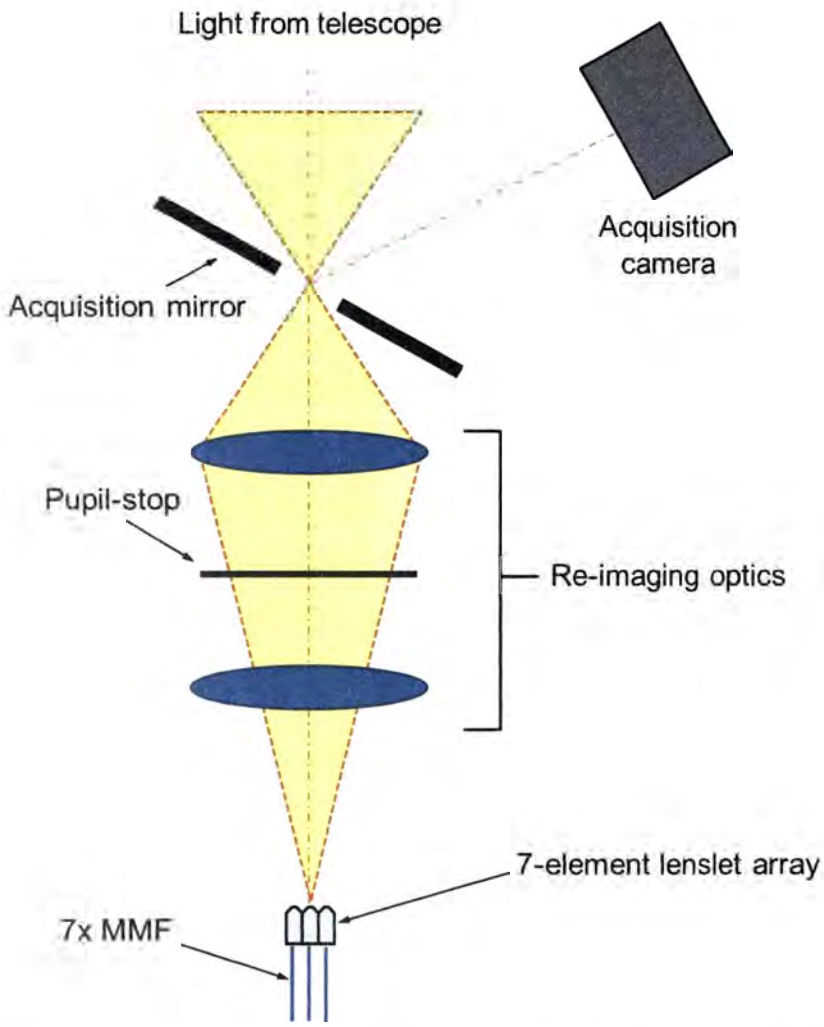

FIGURE 5.3: Schematic of the fore-optic fibre-interface unit used for IPS on-sky testing. The acquisition mirror picked off light not passing through the aperture onto an acquisition/guiding camera. The light was re-imaged and magnified onto a 7-element IFU lenslet array, which coupled the light into 7 multimode fibres.

5.3.1 Fore-optics

The first optical element encountered by the $F/8$ telecentric beam coming from the telescope was an acquisition pick-off mirror. The acquisition mirror was a circular mirror with a central aperture, allowing the central portion of the beam to pass through the aperture and continue to the IFU. The rest of the beam was diverted to a camera, which allowed for object acquisition. The portion of the beam that passed through the acquisition mirror was then magnified to a $F/265$ beam by an optical relay consisting of a magnifying achromatic doublet lens and a doublet field-flattening lens. A pupil

stop was positioned in the telescope pupil plane between the two lenses. Each lens had an AR coating with a reflectance $< 1\%$ over the waveband from $1.0 - 1.7$ μm. The beam was then focused onto the IFU. The overall schematic of the fibre interface fore-optics is shown in Fig. 5.3.

5.3.2 Lenslet Array

The IFU used to couple the starlight into optical multimode fibres consisted of a hexagonal array of seven hexagonal lenslets. The lenslets were made of fused silica. The front face of each lenslet was polished and AR-coated to minimise losses. The lenslets were bonded onto a fused silica substrate using an index-matching UV-curing epoxy (Norland Optical Adhesive 61), which was fixed in a mount attached to the optical relay assembly. Each lenslet had dimensions of 2 mm flat-to-flat end.

Due to the magnification of the optical relay in the fore-optics, the plate scale at the lenslet surface was $0.2''$ mm^{-1}. Therefore, each lenslet subtended 0.4 arcsec on the sky, with a field of view of 0.14 arcsec^2. The entire lenslet array subtended $1.2''$ of sky, with a field of view of 0.97 arcsec^2. This was designed to match the median seeing in the H-band at the AAT (which was ~ 1.2 arcsec).

Each lenslet couples a $F/6.5$ beam into a 50 μm core diameter multimode fibre positioned at the lenslet focus at the back of the substrate. The fibres were placed inside a glass ferrule and attached to the substrate using the same UV curing adhesive used to bond the lenslets.

5.3.3 Multimode fibre feed from Cassegrain focus to IPS

The multimode fibres were approximately 15 m in length and were used to transport the light from the telescope's Cassegrain cage (where the IFU and fore-optics were housed) to a gravitationally invariant platform at the base of the telescope where the rest of the instrument was located. The fibres were jacketed, reinforced, and bundled together in an armoured sleeve as they made their way down the telescope.

5.3.4 Coupling efficiency of telescope interface

The throughput of the fore-optics unit was measured both during assembly and installation at the AAT. The measured throughput of the fore-optics (including the acquisition

Sky Position	Fibre #	Throughput (%)
N	1	79
WNW	2	73
WSW	3	85
C	4	75
ENE	5	75
ESE	6	55
S	7	61
Average:		72

TABLE 5.1: Throughput of individual IFU fibres.

mirror, relay optics, and pupil-stop) was 86.5 $\pm$ 0.5 %. The IFU average coupling efficiency for each element was 83 $\pm$ 1.2%. Thus, the overall average throughput of the telescope-fibre interface unit (fore-optics, lenslet array, and multimode fibres) was $\approx$ 72%. The individual throughput breakdown of each telescope-fibre interface output fibre is listed in Table 5.1.

5.3.5 Photonic lantern

As was alluded to in previous sections, a photonic lantern is a passive photonic device which allows for the conversion from the multimode to single-mode regime [59, 60]. This is an optical fibre device that couples light from a multimode fibre (MMF) to single-mode fibres (SMFs) or single-mode cores, and vice versa. The lantern comprises an array of isolated identical SMF cores as a degenerate multimode system, in which the near-diffraction limited spatial modes are the supermodes of the array. The number of degenerate supermodes is equal to the number of cores, and their propagation constants equal that of the mode of a single core in isolation. Light can couple between the array of SMFs and a MMF via a gradual taper transition. If the transition is adiabatic, then the supermodes of the SMF array evolve into the modes of the MMF core, and vice versa. The second law of thermodynamics (brightness theorem) does not allow lossless coupling of light from an arbitrarily excited MMF into one SMF, but if the effectively multimode system to be coupled to (i.e SMF array) has the same number of degrees of freedom, then lossless coupling becomes possible. Hence, a low-loss adiabatic transition between a MMF with M modes and an array of M SMFs is theoretically possible. Such transitions would couple light from an array of SMFs with M degenerate supermodes

to a MMF core with M modes, and vice versa. A robust mathematical treatment of electromagnetic propagation in this transition can be found in Leon-Saval et al. [61].

Photonic lanterns to date have been manufactured and demonstrated by two different techniques, in both cases the single-mode cores are reduced in size so as to become ineffective waveguides, and the light at the MMF end becomes confined by a second, outer cladding. The first multimode transition with single-mode performance [60] was demonstrated by interfacing SMFs to photonic crystal fibres (PCFs) [62]. A more recent approach was demonstrated by Noordegraaf et al [59], where an all solid standard optical fibre splitter/combiner technique was used. A bundle of SMFs was inserted into a low index glass capillary tube which was then fused and tapered down to form an all solid MMF at the other end.

The IPS feed used one 1×19 photonic lantern to provide the necessary conversion from the multimode fibre line from the IFU to a bundle of single-mode fibres, which could be injected directly into the IPS with no loss in performance. The photonic lanterns were manufactured by NKT Photonics and consisted of a 50 μm core MM port (matched to the IFU fibre feed) on the input, and an array of 19 SMFs at the output (again, matched to the SMF-28 AWG input fibres). Between the two, a taper transition was enclosed in a protective metal case. The MM port of the photonic lantern was spliced to a 1 m MM patch-cord which had one end FC/PC connectorised. The IFU fibre feed was fibre butt-coupled to the MM patch-cord. The SMF end of the photonic lantern was spliced with a SMF-28 linear 1D array in the form of a v-groove array, which was directly bonded with the AWG.

The photonic lanterns are designed to efficiently convert the modes of the MM port into the supermodes of the SMF array. The SMF array only supports N supermodes independent of wavelength, where N is equal to the number of SMFs. Thus, for maximum efficiency the MM port was designed to support M = N modes (19 in our case). However, it is important to note that the number of modes supported by the MM port is wavelength dependent ($M \propto \lambda^{-2}$), which translates into transition losses at shorter wavelengths. At the design wavelength (1550 nm), the number of modes supported by the MMF exactly matches the number of supermodes of the SMF array resulting in minimum loss in the taper transition. Across the H-band, the number of modes will change from 21 on the short wavelength edge, to 15 at the long wavelength cut-off.

The throughput is lower at the blue end because there are more modes in the MMF than there are output SMFs.

The MM to SM throughput was measured by injecting a beam with a NA of 0.086 ($F/5.8$) from an amplified spontaneous emission source (which provides broadband spatially coherent light) centred at 1.53 μm into the delivery fibre and collecting the power from all 19 SMFs. The MM to SM throughput for the photonic lantern used was measured to be 59 $\pm$ 1%. The throughput of the photonic lantern was only measured near the design wavelength, but as the number of modes supported by the MM fibre depends on wavelength, in turn the throughput of the photonic lantern has a wavelength dependency.

5.3.6 AWG input array

A 32-fibre linear v-groove array was used to couple light into the AWG chip. It consisted of 32 SMF-28 single-mode fibres, equally spaced by 127 μm bonded between two silica layers. Using the 6-axis Nanomax stage and the procedure outlined previously for bonding the v-groove aray, we managed to also align to an angular precision of 0.01°. The array was aligned by maximising throughput at the chip output while simultaneously monitoring the central fibre (for translation) and two edge fibres (for rotation angle).

After the array was aligned to the chip, the array was bonded to the chip using index-matching UV curing epoxy. Due to the silicon substrate of the AWG chips not being transparent to UV light, the UV lamp used for curing the epoxy did not evenly illuminate both the top and bottom of the chip (and array). If the epoxy on the top of the chip cured faster than the bottom, the fibre array would begin to shear and misalign vertically with respect to the chip. Hence the chip's output was monitored in real-time as the epoxy was setting to check for misalignment. If any were detected, the epoxy was removed with ethanol and the process repeated. Once the array was bonded to the chip, the photonic lantern SMFs were spliced with the fibre array. As the array had 32 and the lantern 19 fibres, the edges of the array were left unspliced.

During on-sky testing, only 12 of the 19 output fibres were used. As mentioned previously, but is worth highlighting again, this was because the output FSR was dispersed over 1.73 mm on the chip output (Section 5.2.3), and the AWG reimages

1-to-1, if fibres are placed more then 1.73 mm apart, their spectra will overlap even when cross-dispersion is used.

5.4 Cross-disperser and detector

Both higher and lower diffraction orders were spatially overlaid at the output face of the AWG chips, akin to Echelle gratings that operate at a similarly high order. However, as the throughput of the different orders remained high, we utilised them to expand the wavelength coverage of the prototype. Furthermore, as the AWG output was 1D, any off-axis fibres that were injected overlapped with each other at the output. Hence, as mentioned previously, cross-dispersion (a secondary wavelength dispersion in a plane perpendicular to the AWG's primary dispersion) was used to separate the orders to obtain a larger wavelength coverage, and uncouple the spectra from multiple off-axis fibres. More than just separating the spectra from each fibre for individual extraction, the cross-dispersion avoids smearing that would otherwise occur due to the wavelength shift caused by the off axis-injection (Fig. 4.24). Thus by individually extracting each spectra we are able to correct for this offset prior to collapsing them together, making sure there is no degradation of the resolving power.

5.4.1 Need for low-noise detector

We measured the expected throughput of the overall system from the telescope to AWG chip output to be 14% $\pm$ 3% when adding up the signals from the 12 input SMFs. This took into account the fore-optics, splicing losses in the fibres, photonic lantern, and the SMF array to AWG chip coupling losses. Since the IPS used 12 of the 19 available fibre outputs, the light in the remaining seven SMFs was lost, increasing the system's overall loss. However, it is important to note that the power split ratio between the 19 fibres in the lantern varied during observations due to environmental perturbations (temperature, stress/strain) as well as atmospheric turbulence, on time-scales commensurate with the atmospheric coherence time (ms), and is hence difficult to quantify. Nevertheless, the average telescope-to-AWG efficiency for each SMF was measured using a standard source to be 1.0 $\pm$ 0.3%, with a fibre-to-fibre variation due to the atmosphere of 30%.

It was therefore necessary to use a low-noise NIR detector to image the AWG

outputs. While the Xenics NIR detector (4.2.1.1) was adequate to use in chip characterisation, the long exposure times required during observations of faint stellar targets made it a non-ideal candidate. The IRIS2 imaging spectrograph at the AAT provided a perfect test bed as it had a cooled HAWAII-1 HgCdTe detector, and a reconfigurable grism capable of wavelength dispersion in the H-band.

5.4.2 The IRIS 2 instrument

5.4.2.1 Overview

The IRIS2 instrument is a near-infrared ($0.9 - 2.5$ μm) imager and spectrograph designed and manufactured by the Anglo-Australian Observatory (AAO) for use on the AAT [63]. It was commissioned between October 2001 and July 2002, and has been used for wide field NIR imaging, long-slit spectroscopy, and multi-object spectroscopy.

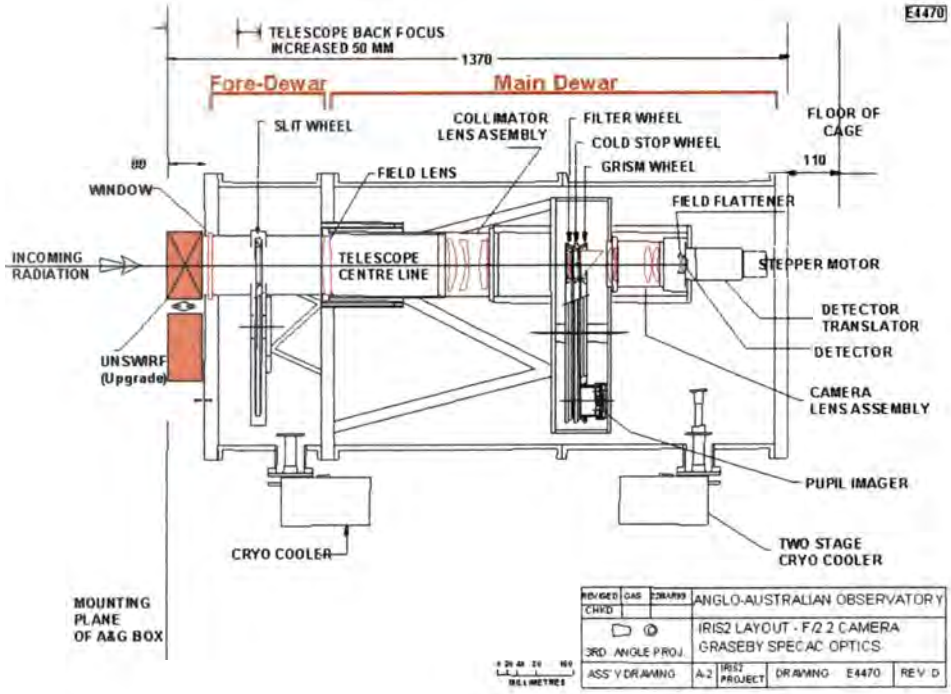

FIGURE 5.4: Diagram of the IRIS2 instrument. Image courtesy of [63].

The instrument is kept cooled using two Cryodyne closed-cycle refrigerators. In order to ensure minimal thermal cycling of the detector, the instrument has two separate dewars, the fore-dewar, and main dewar. The main dewar contains the detector, the collimator and camera optics, and the pupil, filter and grism wheels. The fore-dewar contains the aperture wheel, and was designed to be warmed up and cooled back down on a short (2-3 day) time-scale, to enable the use of custom multi-slit masks or filters.

5.4.2.2 Disperser optics

The optical train contains a total of ten refractive elements, including a window, a 4 element collimator, and a five element camera (Fig. 5.4). All elements were AR coated and had $< 2\%$ reflectivity per element. There are a further four adjustable wheels in the instrument; a slit wheel, a filter wheel, a cold stop, and a grism wheel. There is also a detector focus mechanism, which adjusts the spacing between the detector and the optical train.

For spectroscopy, a slit wheel inserts a 1" wide slit (or multi-slit masks), and a secondary wheel inserts a grism into the collimated beam. These grisms use ~50 mm 45-degree prisms of sapphire to deviate the beam and feed replica transmission gratings applied to their surfaces. A filter is also inserted to select the wavelength cut-offs. For the entirety of our experiments the filter was the H-band spectroscopic filter (1485 – 1781 nm), with a peak throughput of 85% $\pm$ 5%.

The grism used for cross-disspersion was the SAPPHIRE-316 grism which gave a linear dispersion of 0.341 nm/pixel. The slit projected to 2.2 pixels on the detector, providing a resolution R=2400 in the cross dispersed direction.

5.4.2.3 HAWAII-1 detector

The detector was a 1024x1024 Rockwell HAWAII-1 HgCdTe with 18.5 μm pixel pitch, which was configured for use in two read modes; Double Read Mode (DRM) and Multiple Read Mode (MRM). For DRM, the array is reset and a reading taken, followed by a second reading at the end of the exposure. The image delivered is the difference between the two reads. This is the mode used for most broad-band imaging applications (also known as 'Double Correlated' Sampling). For MRM the array is reset and then non-destructively read repeatedly throughout the specified exposure time. The image delivered is a least-squares fit through the non-destructive reads. This mode was used

for all our tests. In MRM, the detector read noise is minimized to ≈ 8 e^- with the detector dark current ≈ 0.0015 e^-s^{-1}. The quantum efficiency (QE) of the detector was measured to be $\approx 65\%$ across the H-band.

5.4.3 Overall IRIS2 throughput

The total throughput of the IRIS2 imaging spectrograph is 11.6 % $\pm$ 1%. This is predominantly due to the large number of refractive optics in the optical pathway, and also because of the low throughput of the Sapphire grism used for cross-dispersion ($\approx 40\%$).

5.4.4 Injection optics

The output of the AWG chip was re-imaged by two 1" achromatic doublet lenses onto the IRIS2 slit. The injection optics magnified the AWG output by 5 so the AWG PSF (6.2 μm) could be Nyquist sampled by the detector's 18.5 μm pixel pitch. The chip was mounted and held in place on a 3-axis translation stage, which was in turn bolted to a breadboard, along with the mounts used to hold the injection optics. The breadboard that held the AWG chip and injection optics was mounted onto IRIS2. Alignment and focusing was carried out by translating the chip's position with respect to the injection optics.

5.5 On-Sky results

5.5.1 Astronomical sources

On-sky testing of the IPS prototype began on the night of 18^{th} May 2011, with the data presented below acquired on the 19^{th}. Due to the IPS being a previously untested prototype we directed the observations to bright stellar sources: α Sco (Antares), α Ara & π Gru. Antares and α Ara were primarily used for final on-sky alignment of the telescope interface optics and calibration of the terrestrial atmospheric features respectively.

5.5.1.1 α Ara

Despite what it name suggests, Alpha Arae (α Ara) is actually the second brightest star in the southern constellation of Ara, with an apparent visual magnitude of 2.93 (β

Ara being slightly brighter at 2.8), and is $\sim$ 270 light-years (83 parsecs) away. It is a massive B-type main sequence star, with a stellar classification of B2 Vne. While such stars have typically featureless and flat spectra in the H-band (with the exception of possible ionised Hydrogen emission lines), they are an ideal bright candidate to use to correct for atmospheric absorption affects.

5.5.1.2 Antares (α Sco)

Antares (α Sco) is a red supergiant star with a stellar classification of M1.5 Iab -b. It is the brightest star in the constellation Scorpius with a visual magnitude of 1.0, and a H-band magnitude of -3.6. This star was chosen primarily due to its high brightness in the H-band, and due to its location on sky during observing (close to zenith). Antares was ideal for testing the instrument throughput and alignment.

5.5.1.3 π Gru

π Gru is a S-type Mira variable star in the Grus constellation with a H-band magnitude of -1.9. S-type stars are late-type giant stars, similar to class K5M. They are an intermediate stage in which asymptotic giant stars (AGB stars) transform from ordinary M class giants to carbon stars of class C-N. Such stars have an abundance of carbon monoxide in their atmosphere, which creates visible molecular absorption bands in the H-band part of the spectrum [64]. Due to their strong spectral features in the H-band, and their high brightness this was the ideal candidate for obtaining spectral lines using the IPS prototype.

5.5.2 Reduction of on-sky data

The data collected during observations were reduced using a custom Matlab script, the steps of which we outline in this section.

5.5.2.1 Raw data

A typical unreduced readout frame from the IPS is shown in Fig. 5.5. Figure 5.6 shows the same frame recoloured and contrasted to demonstrate positions of the individual spectra in the frame. The AWG dispersion was in the vertical direction, with the cross-disperser further dispersing the light in the horizontal direction, hence the spectra appear tilted diagonally. This permits the decoupling of the multiple input signals, as

well as the higher AWG diffraction orders. The twelve individual fibre spectra are thin diagonal lines with a small gap separating the higher diffraction orders. The horizontal features running through the entire frame are caused by surface imperfections (such as dust, flakes and chips) on the AWGs output facet, that cause scattering and a localised decrease in throughput. Such features were removed by dividing by the instrument flat fields, with the procedure detailed later in this chapter.

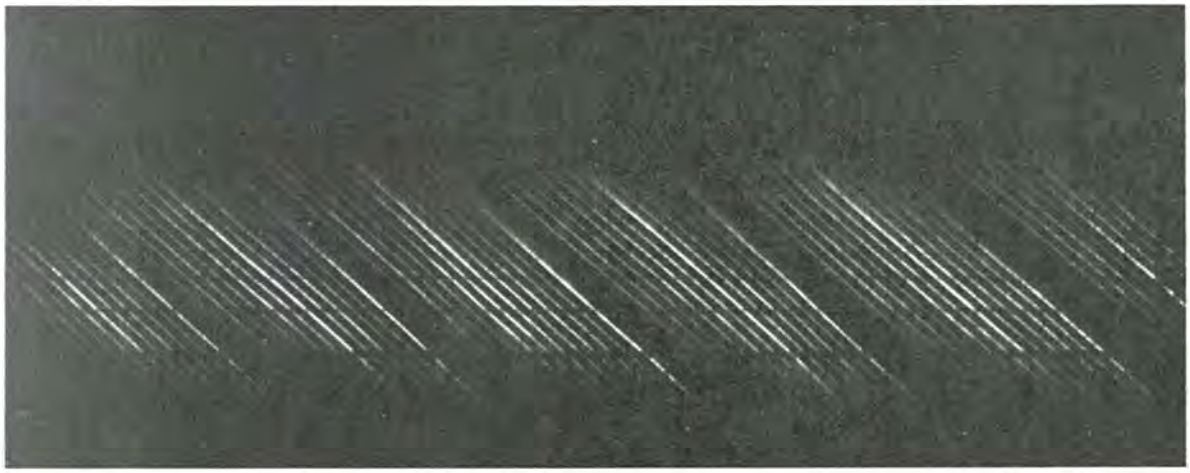

Figure 5.5: A typical raw frame from IRIS2 of Antares.

5.5.2.2 Dark frames

A number of dark frames were taken during observing with different exposure times. The exposure times of the darks matched the astronomical exposures used to acquire the science frames. The darks were subtracted from each frame prior to any further processing. This removed most of the hot and dead pixels from the detector, as well as removing the noise due to the dark current and detector readout.

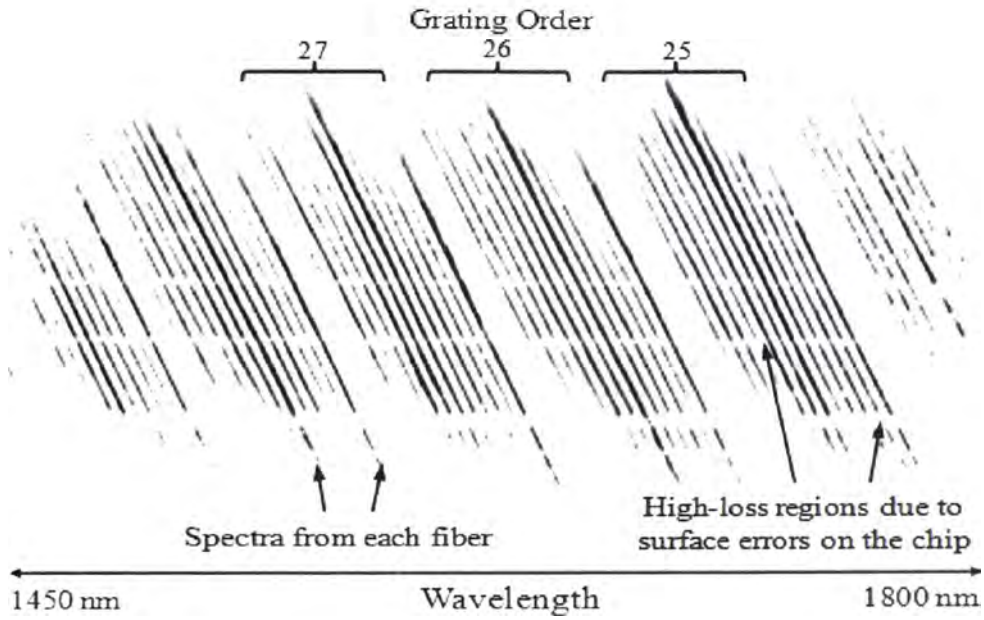

Figure 5.6: Unreduced readout frame from the IPS of Antares, colour inverted and contrasted to demonstrate positions of the spectra and the effects of chip imperfections.

Figure 5.7: Typical flat-field frame from the IPS.

5.5.2.3 Flat-field frames

A series of flat-field frames were taken by projecting broadband light onto a screen in front of the telescope, with a typical frame shown in Fig. 5.7. The flat-field frame shown

in the figure does at first glance appear far noisier than the science frame of Antares shown above. This is because the flat fielding lamp had exceptionally poor coupling to the IPS, requiring longer exposure times. This increased the prevalence of cosmic-ray events and the thermal background. As the light has a flat spectral response across the H-band, any features in this frame are attributed to the IPS instrument itself and the telescope. Thus these frames can correct for any instrument response including fibre-to-fibre throughput variations, surface imperfections on the AWG chip, and telescope coupling, as well as detector biases and thermal noise.

5.5.2.4 Arc frames

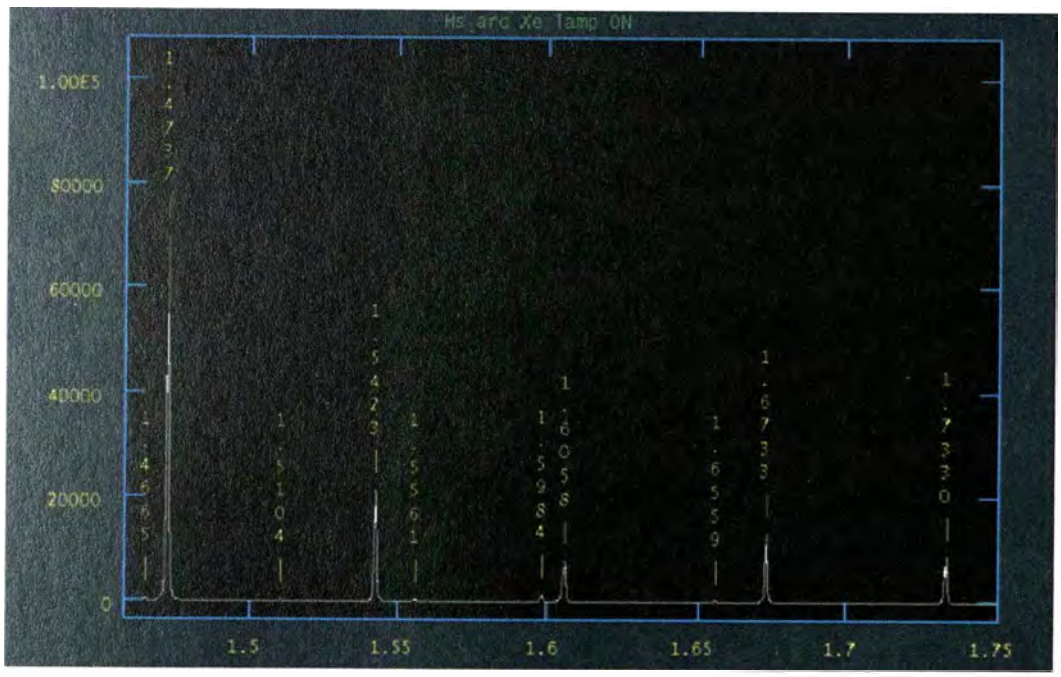

Figure 5.8: The emission spectrum of the Xenon spectral lamp used for wavelength calibration. Courtesy of the AAO [65].

A Xenon lamp integrated with the telescope optics was used as a wavelength calibration source for the IPS instrument. The spectrum of the lamp across the H-band is shown in Figure 5.8, with a typical arc frame shown in Fig. 5.9.

The light from the lamp was reflected off the telescope's secondary mirror into the fore-optics unit and coupled into the MMF. Because of this, the spectra from each fibre had the same calibration light and allowed for the accurate wavelength calibration of

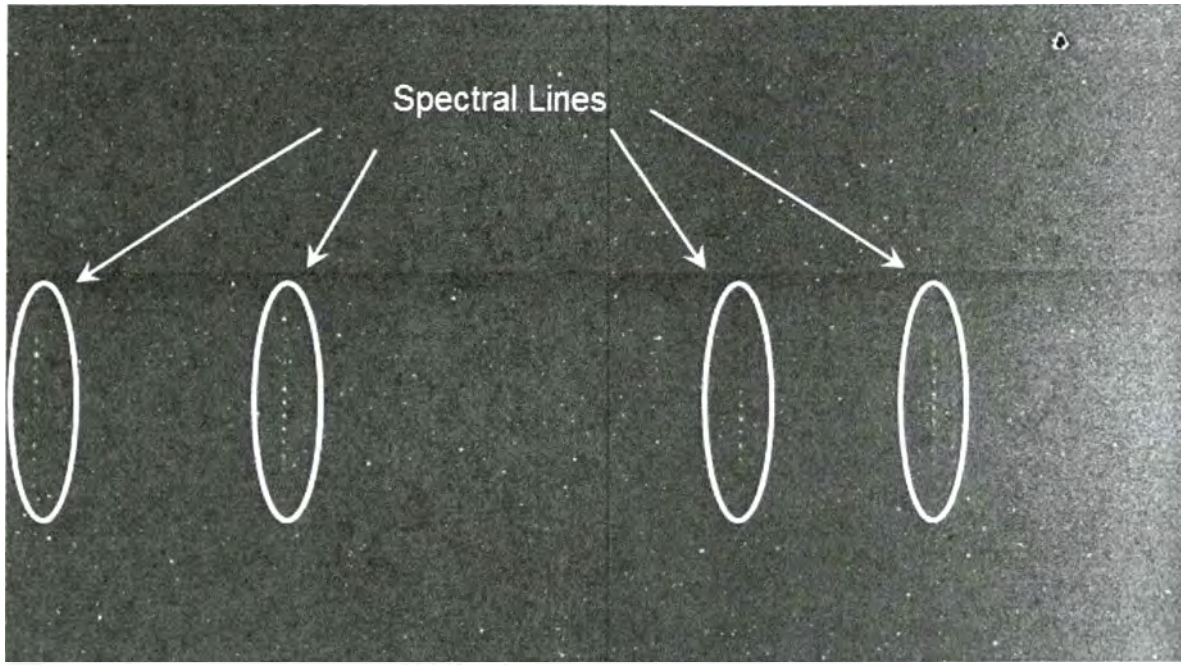

FIGURE 5.9: An unreduced frame from the IPS of the Xe lamp used in wavelength calibration.

each spectrum across the whole wavelength range.

5.5.2.5 Spectra extraction

The signal from the multiple fibres across the many orders of the IPS was extracted, calibrated, and combined to form a single complete H-band spectrum using the Matlab script in Appendix A. Prior to extraction however, we had to rotate each frame using a rotate-interpolate function. The rotation was done to make the co-ordinate system simple for the array-based Matlab script, and speed up extraction. Because a rotation by itself would also rotate the pixel orientation, we used an interpolate function such that we maintained square pixels regardless of the image rotation. This rotation-interpolation function is a standard technique used to extract spectra which are angled on the detector, and was designed to mimic those used in other programming languages (Python, IRAF, IDL etc.). A typical rotated image is shown in Figure 5.10.

Each individual partial spectra was cropped using a rectangular field, shown in Figure 5.11. The cropping-box maintained the same dimensions for all the spectra and was offset by using the 'dip' as a reference. The dip was caused by surface imperfections

Figure 5.10: A typical frame that has been rotated using a rotate-interpolate function.

(such as dust, flakes and chips) on the AWG's output facet, that caused scattering and a localised decrease in throughput. Because this was due to a feature on the AWG output focal plane, it is common to each partial spectra, and is a great reference for the physical x-y coordinates. After being cropped, the script collapses each partial spectra vertically into a 1D array.

5.5.2.6 Wavelength calibration

After each of the 61 partial spectra have been extracted and collapsed, the script uses the Xenon spectral lines to precisely align them in wavelength space. A typical alignment array is shown in Figure 5.12. As the Xe emission peaks are common to each fibre, the script locates the maximum in each partial spectrum and aligns them accordingly. Once aligned, the array is collapsed vertically to form a 1D array, forming

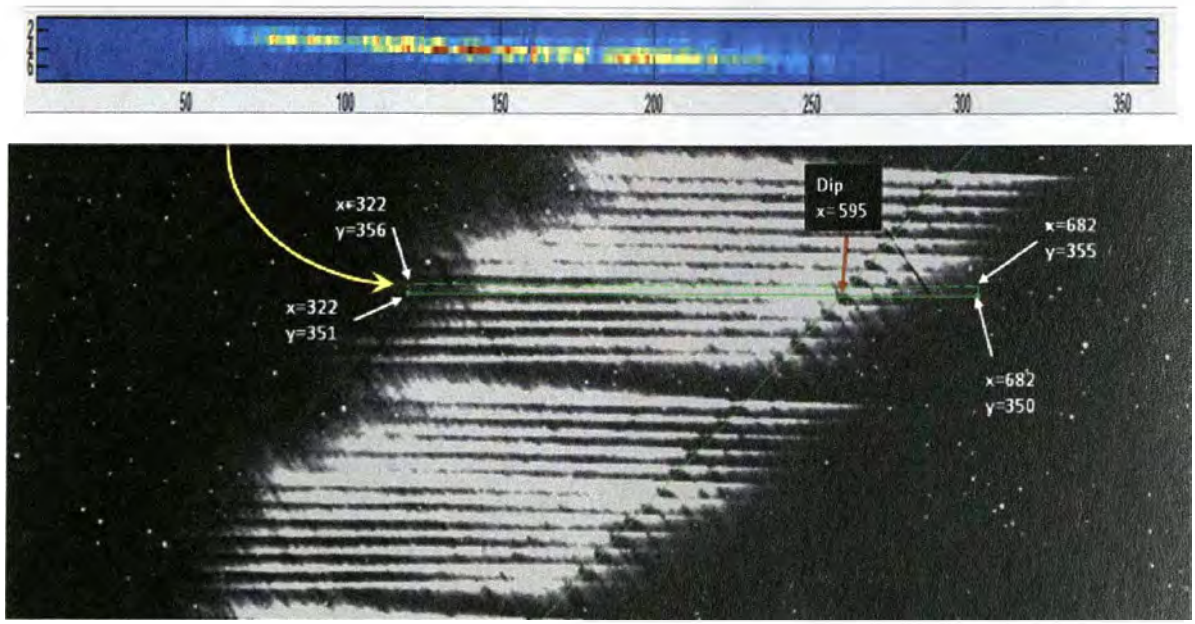

Figure 5.11: The individual partial spectra were cropped and extracted from the original frame in the Matlab script. Each spectrum was isolated using a rectangular cut using the chip imperfections (dip) as a reference.

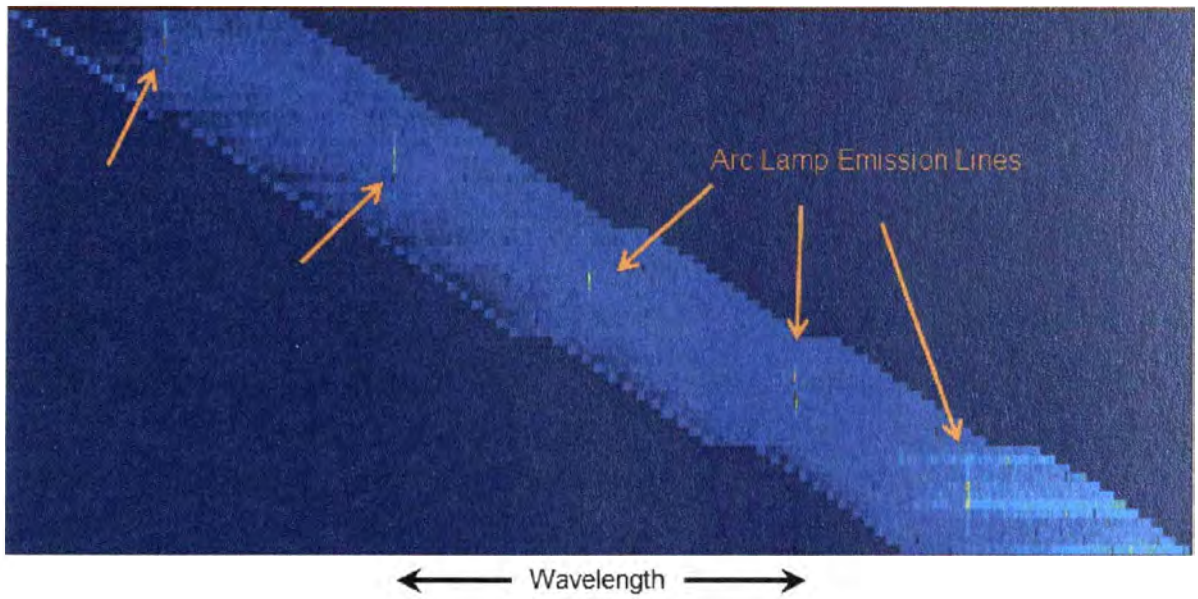

Figure 5.12: Each of the 61 extracted partial spectra were aligned in wavelength using the Xenon arc-lamp spectra.

the complete spectrum across the H-band.

5.5.2.7 Thresholding

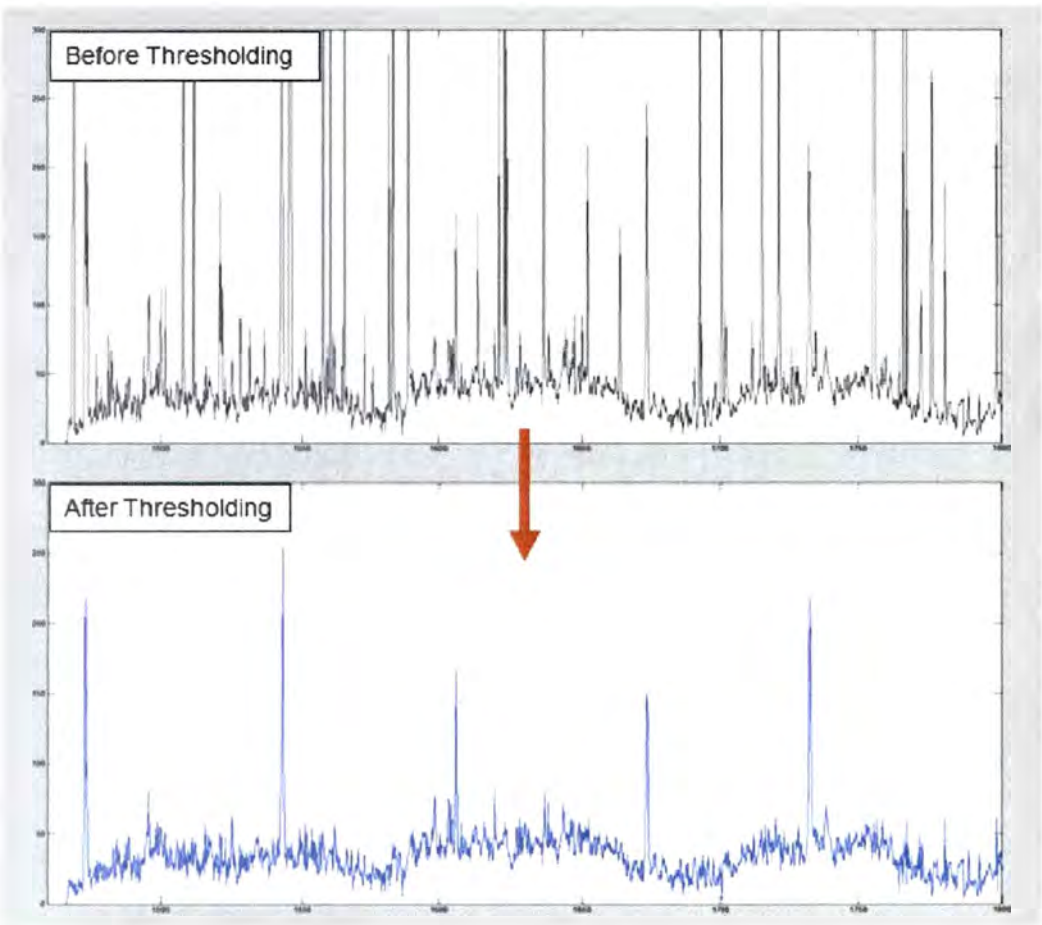

Figure 5.13: By applying a sigma-cut averaging function, we remove most cosmic rays from the frame, as well as any hot pixels not removed in the dark subtract. The non-thresholded spectrum of the Xe arc-lamp (top) is drastically improved, with the Xe emission lines now clearly visible (bottom).

Just before the arrays are collapsed to form a single spectrum, we perform a sigma-cut function to all the partial spectra. This function in the script identifies individual pixels that have counts an order of magnitude higher than the average spectrum count, and replaces them with an average of the surrounding pixels. This is done to remove cosmic rays and remaining hot pixels. Because a cosmic ray or hot pixel typically cause extremely large counts in a single pixel, when the array is collapsed they add noise to the resulting spectrum (Fig. 5.13 (top)). By setting a threshold value for the sigma-cut (typically ~ 300 counts, but varies depending on exposure time), we replace the unwanted pixels with the mean value of the two adjacent pixels (perpendicular to

the spectral direction), which resulted in a much cleaner overall spectrum (Fig. 5.13 (bottom)).

5.5.2.8 Flat-fielding

Once the script could accurately output a complete 1D spectra, we repeated the process for all the science frames, as well as the flat-field frames. The science frames were then divided by a flat-field spectrum to remove any wavelength effects from the instrument.

5.5.3 Stellar spectra

5.5.3.1 α Ara

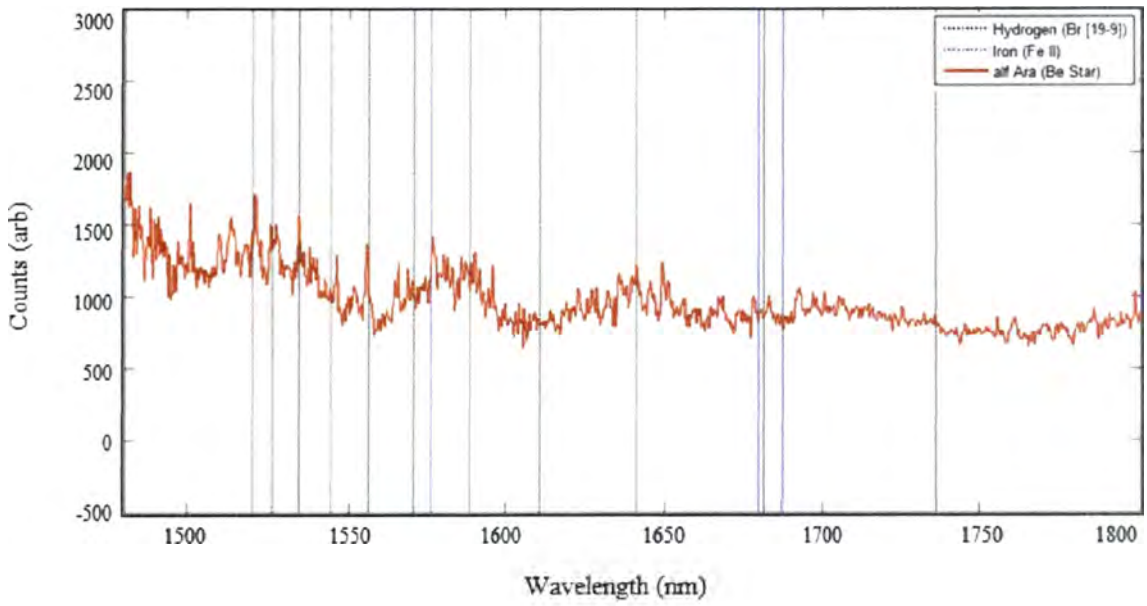

Figure 5.14: The spectrum of α Ara. While the spectrum is relatively featureless, the expected emission features of Be stars (Hydrogen, Iron) have been added for reference.

The spectrum of α Ara is shown in Figure 5.14. As mentioned in section 5.5.1.1, α Ara was chosen for calibration purposes, and hence we don't expect many spectral features in the H-band. However, we do observe small emission features from the Hydrogen Br [19-9] bands.

The spectrum was smoothed by an averaging script and used to remove atmospheric effects from the subsequent spectra.

5.5.3.2 α Sco (Antares)

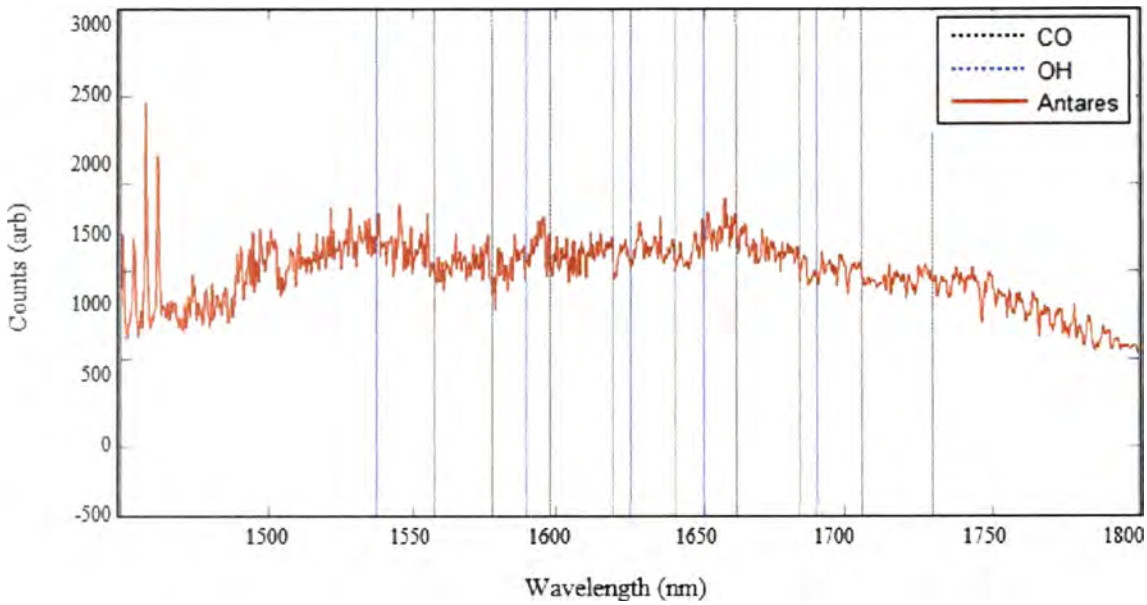

Figure 5.15: The spectrum of Antares. The spectrum does not contain any spectral features expected from red giants. However, broad absorption at the wings of the H-band is indicative of H_2O absorption.

The spectrum of Antares is shown in Figure 5.15. Antares was chosen primarily to aid in initial tests for source acquisition, and for throughput calculations, due to its high brightness in the H-band. As such, we don't expect any spectral features in its spectrum. However, broad absorption at the wings of the H-band is observed (due to H_2O absorption) which is typical for red giant stars.

5.5.3.3 π Gru

We observed the type-S star (π Gru), whose spectrum is shown in Fig. 5.16. π Gru is a variable, late-type star, which is known to contain carbon monoxide (12CO) molecular absorption features in the H-band [64, 66]. The CO molecular bands manifest as a sharp band-edge followed by a forest of vibrational modes decreasing in absorption. Because the vibrational lines are unresolved with the IPS, the CO molecular absorption band appears as a sharp absorption feature followed by a decreasing 'tail'. The results were obtained using an exposure time of 30 minutes, with atmospheric transmission

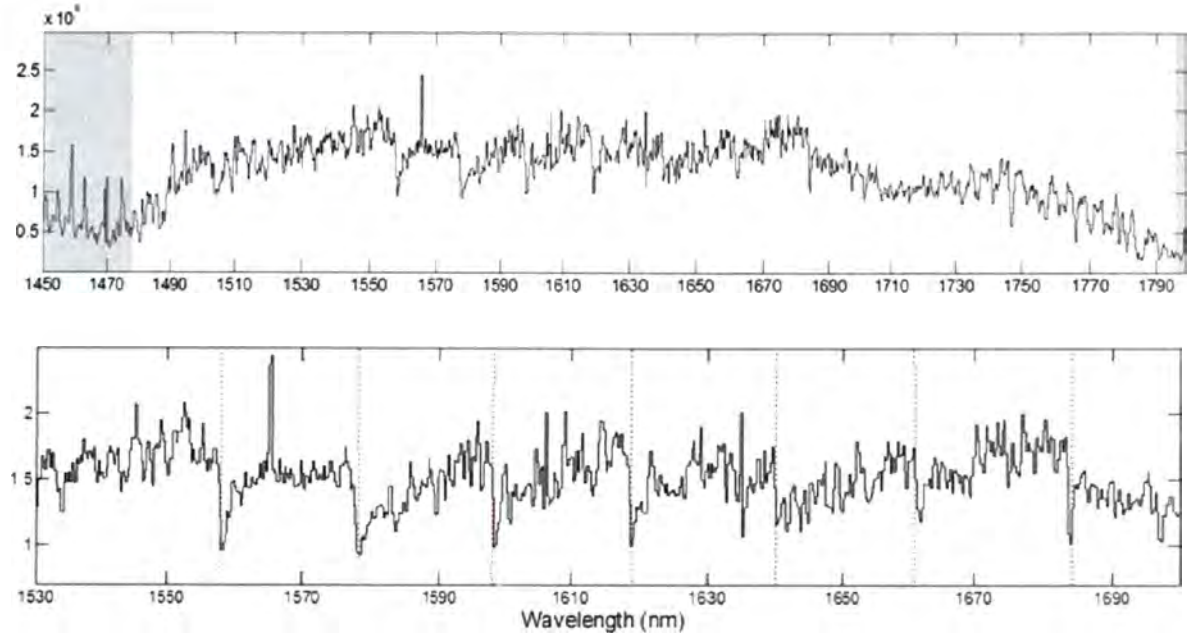

FIGURE 5.16: The complete H-band spectrum of π Gru (top) with gray areas indicating the parts of the spectrum contaminated with atmospheric OH absorption, and a cut showing the CO lines in more detail (bottom). The dotted red lines indicate the wavelengths of the CO (3-0) to (9-6) band-heads taken from [64].

corrected for using α Ara as outlined above. Furthermore, the overall shape of the continuum in the H-band is typical of luminous cool stars like π Gru, due to H_2O absorption in the star's atmosphere [67].

5.5.4 Achieved resolution

While the AWG chip has a native resolving power of 7000 $\pm$ 700 (0.22 $\pm$ 0.02 nm), when used in tandem with the cross-dispersion optics the on-sky resolving power was reduced to 2500 $\pm$ 200 ($\sim$ 0.6 nm resolution). This was due in part to aberrations from the cross-disperser optics, but more significantly because the pixel pitch of the detector was not matched to, and hence under sampled, the chip's PSF. The resolving power was calculated using a xenon arc-lamp spectrum, taken during the observations for wavelength calibrations, with a typical PSF shown in Fig 5.17.

It is not possible to extract detailed information regarding the shape and wings of the PSF from this plot as the PSF was initially under-sampled, and artificially broadened by our extraction algorithm which used a rotation and interpolation function.

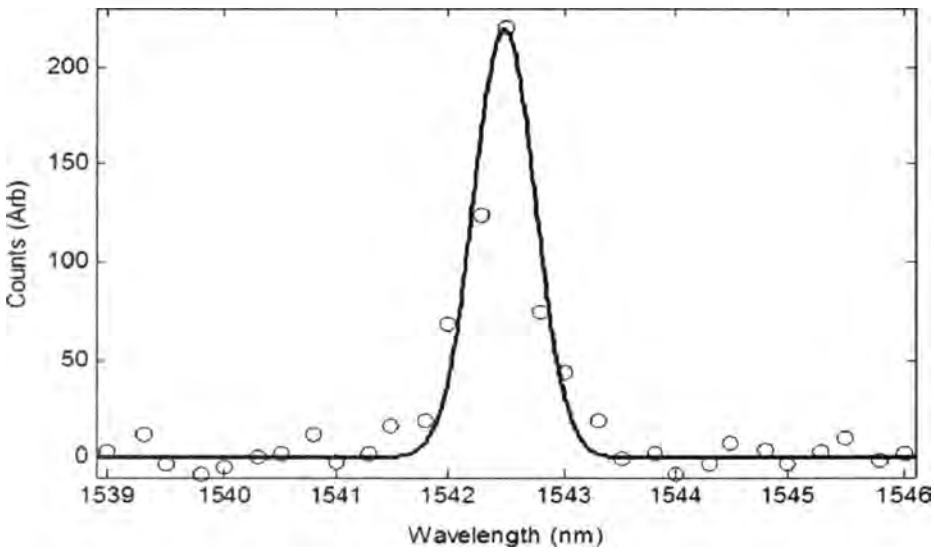

Figure 5.17: A PSF of the IPS instrument obtained using a Xe arc-lamp emission line. The FWHM of the Gaussian fit is 0.62 $\pm$ 0.05 nm

However, details of the raw PSF from the AWG IPS can be found in the previous chapter.

5.5.5 On-Sky efficiency

The telescope interface used to test the IPS on-sky was unoptimised, but was sufficient in coupling enough light to obtain a spectrum using the device. In particular, we used a configuration where a single MMF (and hence one lenslet) of the seven available was used. This setup under-sampled the seeing-limited PSF, which resulted in substantial losses. We measured the efficiency achieved, taking into account the fore-optics, splicing losses in the fibres, photonic lantern, and the SMF array to AWG chip interface to be 14 $\pm$3% when adding up the signals from the 12 input SMFs. Since the IPS used 12 of the 19 available photonic lantern fibre outputs, the light in the remaining seven SMFs was lost, increasing the system's loss. However, it is important to note that the power split ratio between the 19 fibres in the lantern varied due to environmental perturbations (temperature, stress/strain) as well as turbulence, on time-scales commensurate with the atmospheric coherence time (ms) and is hence difficult to quantify.

Nevertheless, the average MMF to AWG efficiency for each SMF was measured using a standard source to be $1 \pm 0.3\%$, with a fibre-to fibre variation of 30%.

5.6 Conclusions

These results are to our knowledge the first spectral features from an astronomical source detected using a photonic spectrograph of any kind. The on-sky tests conducted of the IPS demonstrate the potential of the technology in creating miniature and robust photonic spectrographs for specific astronomical applications.

We have demonstrated that it is possible to interface a diffraction-limited photonic spectrograph to a major seeing-limited research telescope and obtain meaningful astronomical spectra. The overall throughput of this early IPS prototype is poor when compared to modern spectrographs, which was due to the unoptimised nature of the interface optics and also due to the inherent difficulty in coupling a seeing-limited telescope PSF into a photonic spectrograph. Fortunately, these problems could be overcome with a more optimised telescope interface design. Furthermore, as the majority of telescopes in use (or under construction) employ (or plan to employ) an adaptive optics system, a near diffraction-limited PSF will be available allowing for efficient coupling directly into a SMF, albeit currently over a very small field-of-view. Hence, an AO assisted IPS system could potentially be used without the need for a photonic lantern with throughputs and resolving powers competitive with modern spectrographs, while maintaining the inherent benefits of an all-photonic platform. We explore this in the following chapter.

It is the mark of an educated mind to be able to entertain a thought without accepting it.

Aristotle

6

Optimisation of Arrayed Waveguide Grating Designs for Enhanced Astronomical Performance

The development of IPS prototypes thus far was based on AWG designs originally created for telecommunications purposes. As such, both resolution and the free spectral range of the devices were not tailored for any specific astronomy science case. However, as was discussed in Chapter 3, the FSR and R can be modified to provide optimised performance for astronomical use, making them comparable, and in a few specific cases superior, to existing bulk-optic spectrographs.

In this chapter, we discuss two avenues in AWG design, and outline how they can be scientifically advantageous. The first is a large FSR design (few hundred nm) which can enable the realisation of an entirely-photonic spectrograph directly bonded to a detector. The second design explores the high-resolution regime (R ~60k) where the inherent environmental stability of a monolithic on-chip spectrograph is highly sought after. For this application we provide an expanded science case for exo-planet detection, in particular the exciting prospect of studying earth-like planets in the habitable zone of M-dwarf stars. We present both the designs and beam-propagation modelling results of AWG performance for the two cases. Lastly, we describe the PANDORA technology demonstrator instrument, that is being fabricated at the time of writing, which will

employ the High-R AWG chip designed in this thesis and an extreme adaptive optics system at the Subaru telescope, which can potentially provide unprecedented radial velocity sensitivity in the NIR at a fraction of the cost of comparable non-photonic systems.

6.1 Modelling of AWG performance

Before presenting and discussing the different AWG designs created for astronomical applications, it is important to understand the technique we used for generating the designs, as well as the modelling algorithm used to test their performance. The designs were created using a Computer Aided Design (CAD) package which allows accurate AWG circuitry to be generated using a series of geometric parameters. By defining a limited set of specific design parameters (such as desired PSF size and shape, FSR, number of array waveguides etc.) and relating them to a series of geometric parameters internal to the CAD package, which it uses to define position, length, and curvature of the waveguides in the circuit, the package can generate the full AWG layout automatically. Further, as only a handful of these parameters are defined by the user (with the rest related via equations), it is straightforward to modify the design (even drastically) without having to actively modify each component of the circuit. The Rsoft CAD package was used for generating the full AWG layouts, which are necessary for the creation of lithographic masks used in the manufacturing process.

After the creation of the designs we used the BeamPROP simulation engine, a part of the Rsoft package, to simulate the performance of our new designs. In this section, we outline how BeamPROP conducts the simulation, drawing particular attention to the limitations of the algorithm and its subtleties which must be considered to accurately model AWGs. We then discuss the procedure used to model the designs.

6.1.1 BeamPROP

The BeamPROP simulation engine is a part of the RSoft Photonics Suite software, and is based on advanced finite-difference beam propagation (BPM) techniques. It is fully integrated with a CAD environment which allowed us to define the material properties and structural geometry of the device to be simulated. The software is ideal for the design and modelling of photonic devices and photonic integrated circuits, and

has seen extensive use in both photonics research and industry.

The computational core of the program is based on a finite difference beam propagation method (a rigorous description of which can be found in [68–88] and references therein). This technique uses finite difference methods to solve the well-known parabolic or paraxial approximation of the Helmholtz equation. The fundamental physical limitation of the approach results from the parabolic approximation to the Helmholtz equation, which implies a paraxiality condition on the primary direction of propagation. Simply put the BPM approach described in the references can not account for backward reflections since the one-way wave equation, on which it is based, does not allow both positive and negative travelling waves. Thus, in general use, it is limited to simulating propagation in one direction.

These limitations can be reduced using more accurate approximations to the Helmholtz equation (as outlined in [89]), which the software has the capability of simulating. The bidirectional BPM algorithm [90] can consider coupled forward and backward travelling waves, and can account for reflections, including resonant effects as found in grating structures or ring cavities. However, this approach increases the computational time by a few orders of magnitude, and is unnecessary for the simulation of AWG circuitry because of the lack of any reflective components or surfaces, and thus there is no need to simulate backwards propagating light. Nevertheless, this limitation must be highlighted as it can begin to impact how AWGs are simulated if the bends in the AWG become too large. Typically from our experience the simulation begins to break down if the waveguide being simulated bends more than $\sim 15°$ from the direction of propagation. Thus, because the overall bend in the waveguide array of the AWG (which depending on the design can be $> 45°$) the simulation can not easily simulate the full AWG in a single step, in a practical and timely manner. This leads to a more complicated method, outlined in the next subsection, of simulating AWGs.

For the simulation to solve physical propagation problems, it requires two key pieces of information: the refractive index distribution of the circuit $n(x, y, z)$, and the input wave field $u(x, y, z = 0)$. From these initial parameters the software calculates the wave field throughout the rest of the domain $u(x, y, z > 0)$, where z is the direction of propagation.

The solution algorithm requires additional numerical simulation parameters (typically defined by the user) such as a finite computational domain ($\{x \in (x_{min}, x_{max})\}$, $\{y \in (y_{min}, y_{max})\}$, and $\{z \in (z_{min}, z_{max})\}$), the transverse grid sizes (Δx and Δy), and the longitudinal simulation step size (Δz).

6.1.1.1 The Beam Propagation Method

BPM [68, 91, 92] is the most widely used propagation technique for modelling integrated and fibre optic photonic devices, and most commercial software for such modelling is based on it. There are several reasons for the popularity of BPM, perhaps the most significant being that it is conceptually straightforward, allowing rapid implementation of the basic technique. In addition to its relative simplicity, BPM is generally a very efficient method, and has the characteristic that its computational complexity can, in most cases, be optimal, that is to say the computational effort is directly proportional to the number of grid points used in the numerical simulation. Another characteristic of BPM is that the approach is readily applied to complex geometries without having to develop specialised versions of the method. Furthermore, the approach automatically includes the effects of both guided and radiating fields as well as mode coupling and conversion. Finally, the BPM technique is very flexible and extensible, allowing inclusion of most effects of interest (e.g. polarisation, birefringence, coupling losses, bend losses, nonlinearities) by extensions of the basic method that fit within the same overall framework.

BPM is essentially a particular approach for approximating the exact wave equation for monochromatic waves and solving the resulting equations numerically. The basic approach is illustrated by formulating the problem under the restrictions of a scalar field (i.e. neglecting polarization effects) and paraxiality (i.e. propagation restricted to a narrow range of angles).

The scalar field assumption allows the wave equation to be written in the form of the well-known Helmholtz equation for monochromatic waves:

$$\frac{\partial^2 \phi}{\partial x^2} + \frac{\partial^2 \phi}{\partial y^2} + \frac{\partial^2 \phi}{\partial z^2} + k(x, y, z)^2 \phi = 0 \tag{6.1}$$

Here the scalar electric field has been written as $E(x, y, z, t) = \phi(x, y, z)e^{-i\omega t}$ and the notation $k(x, y, z) = k_0 n(x, y, z)$ has been introduced for the spatially dependent wavenumber, with $k_0 = 2\pi\lambda$ being the wavenumber in free space. The geometry of the problem is defined entirely by the refractive index distribution $n(x, y, z)$.

Aside from the scalar assumption, the above equation is exact. Considering that in typical guided-wave problems the most rapid variation in the field ϕ is the phase variation due to propagation along the guiding axis, and assuming that the axis is predominantly along the z direction, it is beneficial to factor this rapid variation out of the problem by introducing a so-called slowly varying field u via:

$$\phi(x, y, z) = u(x, y, z)e^{i\overline{k}z} \tag{6.2}$$

Here $\overline{k}$ is a constant number to be chosen to represent the average phase variation of the field ϕ , and is referred to as the reference wavenumber. Introducing the above expression into the Helmholtz equation yields the following equation for the slowly varying field:

$$\frac{\partial^2 u}{\partial z^2} + 2i\overline{k}\frac{\partial u}{\partial z} + \frac{\partial^2 u}{\partial x^2} + \frac{\partial^2 u}{\partial y^2} + (k^2 - \overline{k}^2)u = 0 \tag{6.3}$$

At this point the above equation is completely equivalent to the exact Helmholtz equation, except that it is expressed in terms of u. It is now assumed that the variation of u with z is sufficiently slow so that the first term above can be neglected with respect to the second; this is the familiar slowly varying envelope approximation and in this context it is also referred to as the paraxial or parabolic approximation. With this assumption and after slight rearrangement, the above equation reduces to:

$$\frac{\partial u}{\partial z} = \frac{i}{2\overline{k}}\left(\frac{\partial^2 u}{\partial x^2} + \frac{\partial^2 u}{\partial y^2} + (k^2 - \overline{k}^2)u\right) \tag{6.4}$$

This is the basic BPM equation in three dimensions (3D). A simplification to two dimensions (2D) is obtained by omitting any dependence on y. Because, the AWGs we simulate are a 2D platform (the circuitry at no point changes in y) we use the 2D version of the above equation. Given an input field, $u(x, y, z = 0)$ (i.e. a Gaussian input field from an SMF for example), the above equation determines the evolution of the field in the space $z > 0$.

It is important to recognise what has been gained and lost in the above approach. First, the factoring of the rapid phase variation allows the slowly varying field to be represented numerically on a longitudinal grid (i.e. along z) that can be much coarser than the wavelength for many problems, allowing for a much faster simulation. Second, the elimination of the second derivative term in z reduces the problem from a second order boundary value problem, requiring iteration or eigenvalue analysis, to a first order initial value problem that can be solved by simple integration of the above equation. This is a major factor in determining the efficiency of BPM, implying a time reduction by a factor of at least of the order of Nz (the number of longitudinal grid points) compared to full numerical solution of the Helmholtz equation.

This increase in simulation speed also has some drawbacks. The slowly varying envelope approximation limits consideration to fields that propagate primarily along the z axis (i.e. paraxiality), and also places restrictions on the index contrast (more precisely, the rate of change of index with z, which is a combination of index contrast and propagation angle). In the case of simulating AWGs, there are no rapid changes of refractive index in the propagation direction, and thus these limitations do not apply in most cases. However, it remains to be said that for more complex AWG designs, in particular designs which employ rapid tapers, or designs in other materials with high index contrasts (silicon-on-insulator for example), this limitation must be taken into account.

A more subtle limitation is that fields which have a complicated superposition of phase variation, such as those found in more complex multimode devices, may not be accurately modelled if the phase variation is critical to device behaviour. This limitation does not apply to most AWG designs, but as before, if complex MMI tapers (similar to the parabolic-horn tapers discussed in previous chapters) are used in the design, the discrepancy between the simulation and the true performance becomes

non-negligible.

The key issue beyond the above restrictions on the variation of u is that the elimination of the second derivative also eliminates the possibility for backward travelling wave solutions; thus devices for which reflection is significant will not be accurately modelled. As mentioned before, while this limitation at first glance does not appear to affect AWG simulation as there are no reflective surfaces, the typical AWG layout has angles in the waveguide array which exceed the tolerances in this approximation. Hence, a modified modelling procedure must be used (explained in the next section). As we will see, this is especially true for the high resolution design presented in Section 6.3 due to its layout.

Boundary conditions: Equation (6.4) is a parabolic partial differential equation that can be forward integrated by a number of standard numerical techniques. Most early BPM's employed a technique known as the split-step Fourier method [91]. Later work demonstrated that for most problems of interest in integrated optics, an implicit finite-difference approach based on the Crank-Nicholson scheme was superior [86–88]. This approach and its derivatives have become the standard, and is frequently denoted FD-BPM in the literature, but will be referred to in the following as simply BPM.

In the finite-difference approach, the field in the transverse $(x - y)$ plane is represented only at discrete points on a grid, and at discrete planes along the longitudinal or propagation direction (z). Given the field at one particular value of z, we derive numerical equations that determine the field at the next, z plane. This propagation step is then repeated to determine the field throughout the circuit. For simplicity, the approach is illustrated for a scalar field in 2D (x & z). We omit the extension to 3D, as it is not necessary for our simulations, but can be found in the literature [93].

Let u_i^n denote the field at transverse grid point i, and longitudinal plane n, and assume the grid points and planes are equally spaced by Δx and Δz apart, respectively. In the Crank-Nicholson method Eq. (6.4) is represented at the mid-plane between the known plane n and the unknown plane $n + 1$:

$$\frac{u_i^{n+1} - u_i^n}{\Delta z} = \frac{i}{2\overline{k}} \left(\frac{\delta^2}{\Delta x^2} + \left(k\left(x_i, z_{n+1/2}\right)^2 - \overline{k}^2 \right) \right) \frac{u_i^{n+1} + u_i^n}{2} \tag{6.5}$$

Here δ^2 represents the standard second order difference operator: $\delta^2 u_i = (u_{i+1} + u_{i-1} - 2u_i)$, and $z_{n+1/2} \equiv z_n + \Delta z/2$. The above equation can be rearranged into the form of a standard tridiagonal matrix equation for the unknown field u_i^{n+1} in terms of known quantities, resulting in:

$$a_i u_{i-1}^{n+1} + b_i u_i^{n+1} + c_i u_{i+1}^{n+1} = d_i \tag{6.6}$$

Expressions for the coefficients (a, b, c, and d) are readily derived and can be found in [88]. The tridiagonal nature of Eq. 6.6 allows rapid solution in order $O(N)$ operations, where N is the number of grid points in x.

Since the field can only be represented on a finite computational domain, when the above equation is applied at the boundary points $i = 1$ and N it refers to unknown quantities outside the domain. For these points, the above equation must be replaced by appropriate boundary conditions which complete the system of equations. Proper choice of these conditions is critical, since a poor choice can lead to artificial reflection of light incident on the boundary (e.g. radiation) back into the computational domain. For example, simply requiring the field to vanish on the boundary is insufficient since it is equivalent to placing perfectly reflecting walls at the edge of the domain. A commonly used boundary condition, and one which we use is the so-called transparent boundary condition (or TBC) [94]. The basic approach is to assume that near the boundary the field behaves as an outgoing plane wave, with characteristics (amplitude, direction) that are dynamically determined via some heuristic algorithm. The plane wave assumption allows the field at the boundary point to be related to the adjacent interior point, thus completing the set of equations. The TBC is generally very effective in allowing radiation to freely escape the computational domain in case of light leakage outside the AWG, and thus does not impact or interfere with the simulation.

6.1.2 Generation of CAD layouts and modelling procedure

While it is possible to design an AWG circuit by manually defining each individual component of the design, such an approach is incredibly inefficient due to the large number

of parameters required. For example, typically AWGs have hundreds of waveguides in the array, with each waveguide requiring precise positioning on the FPR, precise definition of the arcs and radius of curvature, all the while maintaining a predefined pathlength over a few centimetres. It is far more ideal to use a generating script which calculates and defines these geometric values using only a handful of key parameters defined by the user. Such scripts are commonly available as part of various photonic CAD packages. We used a script called "STARGEN" to create the AWG layouts.

6.1.2.1 Generating AWG layouts

To start, we define a number of important parameters required for the script to generate the layout. These parameters are: the core-cladding refractive index contrast, the number of input waveguides into the AWG, the number of output waveguides of the AWG, the number of PSFs across the output of the chip, the number of waveguides in the array, the center operating wavelength, and the desired PSF size at output (in the spectral domain). These are the key parameters needed to generate the AWG. In our case, the number of output waveguides was always set to 0. This is because astronomical applications require the output FPR to be polished back, hence we do not require any output waveguides in any design. The other two key parameters are the PSF size, and the number of PSFs at the output. These are the most important parameters when designing the FPRs. The PSF size here is defined in the spectral dimension, i.e. how many nanometres in wavelength is the PSF's FWHM. This directly translates into the AWG's resolving power (as $R = \frac{\lambda}{\Delta\lambda}$). The number of PSFs at the output then simply translates to the FSR of the device. These two parameters together determine the focal length (and hence the size) of the FPR, and as we will see become the main trade-off during fabrication. Finally, the number of waveguides in the array directly impacts the resolving power, and the overall device throughput. At this point it is important to note that the waveguide size itself need not be defined (although it can be if needed). If, like in our case, the AWG is set to propagate a mode at a predetermined and fixed size, for example a mode size matched to the output mode of an SMF which we use to launch the light into the AWG, then the script will increase or decrease the waveguide size depending on the refractive index contrast such that the mode remains the same.

There is also a secondary set of values that the user can define for greater control

of the final layout. Firstly, the separation of waveguides in the array at the FPR interface is a key parameter that needs to be controlled. This is often set as twice the waveguide size ($\sim$ 18 μm), to prevent cross-talk between the waveguides. This can be an important parameter, particularly when the array has a large amount of waveguides. This is because the radii of the Rowland curvatures are set to match the curvature of the far-field distribution of the light diffracting from the waveguide so maximum coupling is obtained. If the separation is increased, the FPR is modified so the waveguides still capture all the light, which results in a larger Rowland radius, and thus a larger FPR.

Secondly, the user can define the minimum radius of curvature for the waveguide array. For typical refractive index contrasts in silica-on-silicon devices, this is set to $\sim$ 5 mm, which is enough to avoid any bend losses. However, if the refractive index contrast is decreased, this value should be increased to avoid losses. Conversely, if the refractive index contrast is higher (using silicon nitrite-on-silicon), it enables tighter bends and a more compact device.

Thirdly, the user can define the overall shape of the arc that the array makes. In the script, this is often thought of as the angle between the two FPRs on the final layout. As mentioned previously, this is typically around 45°, however is freely changeable. This parameter has no impact on the AWG performance (assuming the angle is not too high to cause overly tight bends), but is used to change the overall layout of the chip on the wafer. This parameter is often changed prior to manufacture to maximise the wafer real estate and fit as many circuits on a single wafer as possible. There are two main constraints for the angle allowed, the minimum radius of curvature in the waveguide array govern how high the angle can be, and the length increment ΔL which determines how low it can be as the array must accumulate enough path-length across the bend.

Lastly, the user can apply tapers (such as the parabolic-horn tapers) on the input waveguides, as well as define the taper region between the FPR and the array. The input waveguide tapers, as we showed in Chapter 4, are detrimental to spectrograph resolution and so are not found in our designs. However, if they are added, the script will modify the layout to try and preserve the predefined PSF FWHM.

Once the parameters are set, the script will generate the full AWG layout file. An

example of what a typical CAD layout looks like can be seen in figure 6.1. From within the CAD software, the user is still free to modify the parameters with the layout file recalculated and redrawn efter every change in real time. While changes to parameters that effect the AWG performance can not be seen without running the simulation, changes to overall layout are immediately evident. Thus, we were able to change the layout (in particular the angle of the array, radius of curvature, and waveguide separation) to maximise wafer real estate.

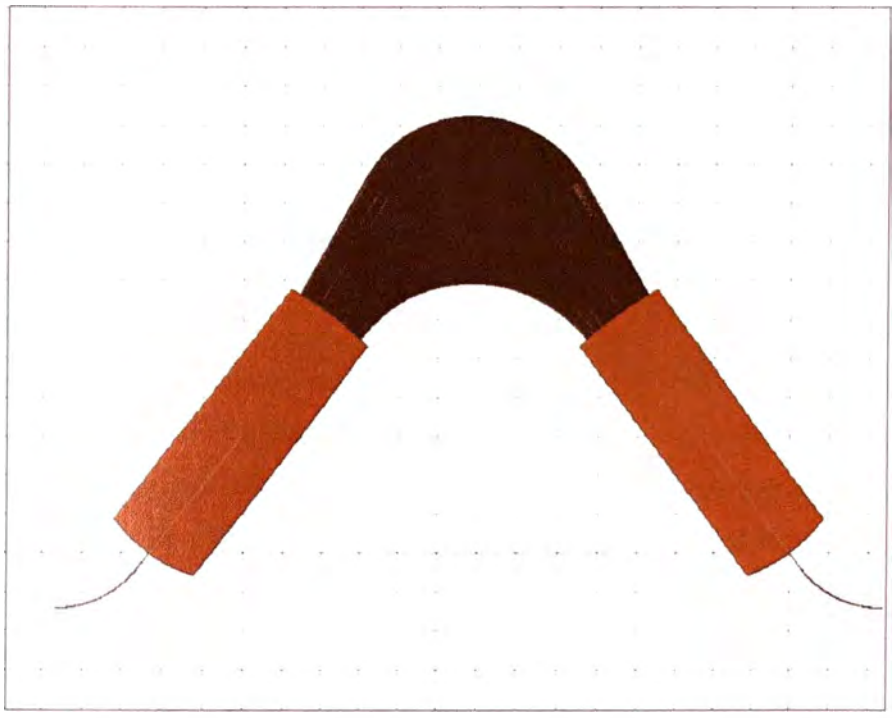

FIGURE 6.1: An example of a typical full-layout CAD design file of an AWG. This particular design was made using the same design parameters as Chipset A & B presented in Chapter 4. This was used to confirm the accuracy of our modelling by comparing it to experimental results found in the same chapter.

When it comes to simulating the AWG, the BPM algorithm cannot simulate the whole AWG in one go, due to the large angles in the array, as we explained in the previous section. Thus, the script also generates two extra design files to make the simulation possible. The two files generated are of the input FPR and output FPR respectively, and can be seen in figure 6.2. The input FPR file contains the input waveguides, the FPR itself and the beginning segments of the waveguide array. The

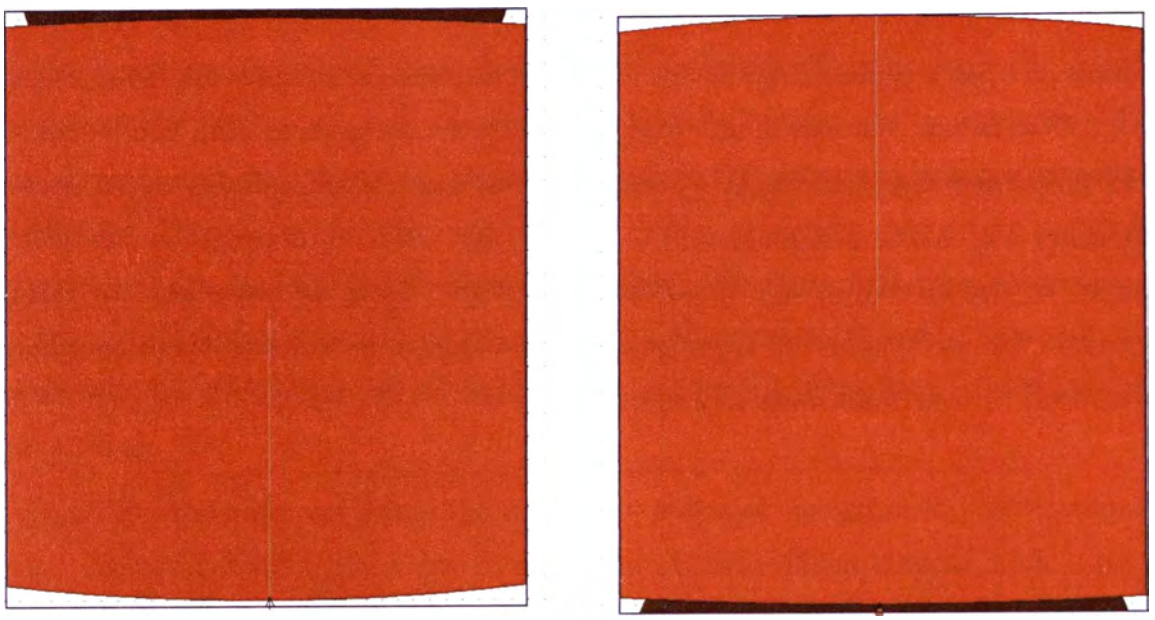

FIGURE 6.2: An example of a typical input (left) and output (right) FPR CAD layouts used in BPM simulations.

output FPR file similarly contains the waveguide array and the output FPR. From the two files we can see that it is easier for the BMP algorithm to simulate the fields (in this case from bottom ($z = 0$) to top ($z > 0$)) as there are no bends. While the individual FPRs can be simulated this way, the whole AWG requires a few additional steps.

6.1.2.2 Simulating the AWG

The simulation is done in several steps. First, the simulation inputs a predefined field at a single wavelength into the input waveguide in the input FPR (in our case an SMF mode, which the program has on file). The algorithm then simulates the input FPR (Fig. 6.3 a)), stopping just after the light enters the waveguide array. It then outputs a "mode" file, which contains the information about the light distribution at the greatest z (i.e. furthest point away from the input) of the input FPR. As the light is already confined in the array by this point, the mode profile is a series of discrete single modes.

The model then runs a script called PHASECOR, which takes each single mode in the output mode file and applies a phase shift to each individually. The shift is determined by the ΔL parameter set in the CAD layout. PHASECOR applies

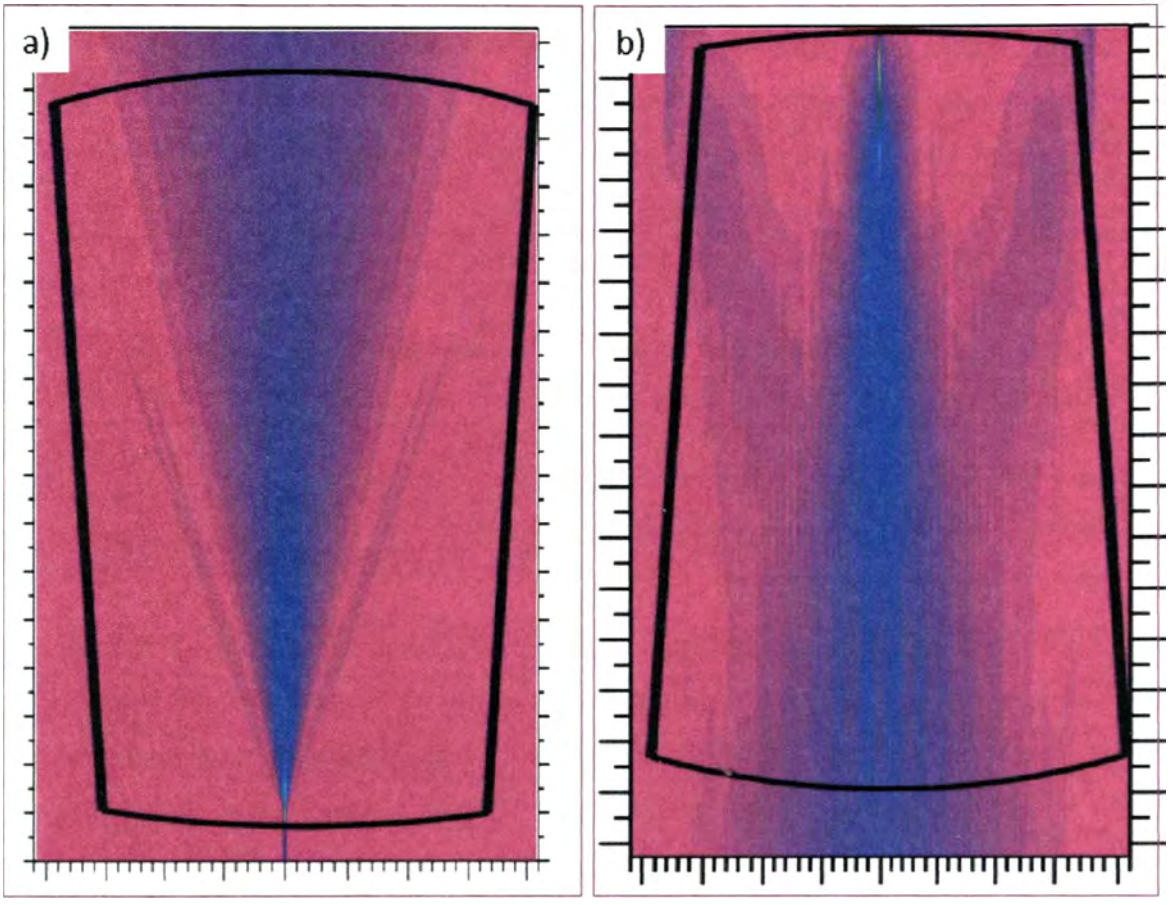

Figure 6.3: Top view of the FPR showing the beam propagation simulation as a function of length for a) the input FPR, and b) the output FPR. The light is propagated from bottom to top of the page.

the appropriate phase delay introduced by the array without needing to do the full propagation of the light. It is important to note at this point that because the light isn't simulated in the full array, losses that can occur due to bend losses are not simulated. However, for a step-index waveguide the bend radius losses have a sharp cut-off (not gradual) [95], thus the bend losses are negligible (and stay negligible) for the bends we have in our AWG designs. The phase corrected file is then re-converted back into a launch field file using a script called FIELDGEN. The new field is launched into the input of the output FPR (Fig. 6.3 b)), and simulated.

The simulation output is the intensity profile of the light field at the uppermost part of the output FPR, which is the output focal plane of the AWG. The field is taken as a cut across x at the final z position, and is shown in Figure 6.4. At this point, it is important to point out that the z-cut does not conform to the Rowland curvature at

the output, but is in fact tangential to the Rowland curvature which is consistent with how our previous chips were polished. The power is normalised to the original input SMF mode at the start of the simulation. From this output we are able to measure the simulated throughput of the AWG (with the exclusion of bend losses in the array), the PSF FWHM and hence the predicted resolving power, and the FSR.

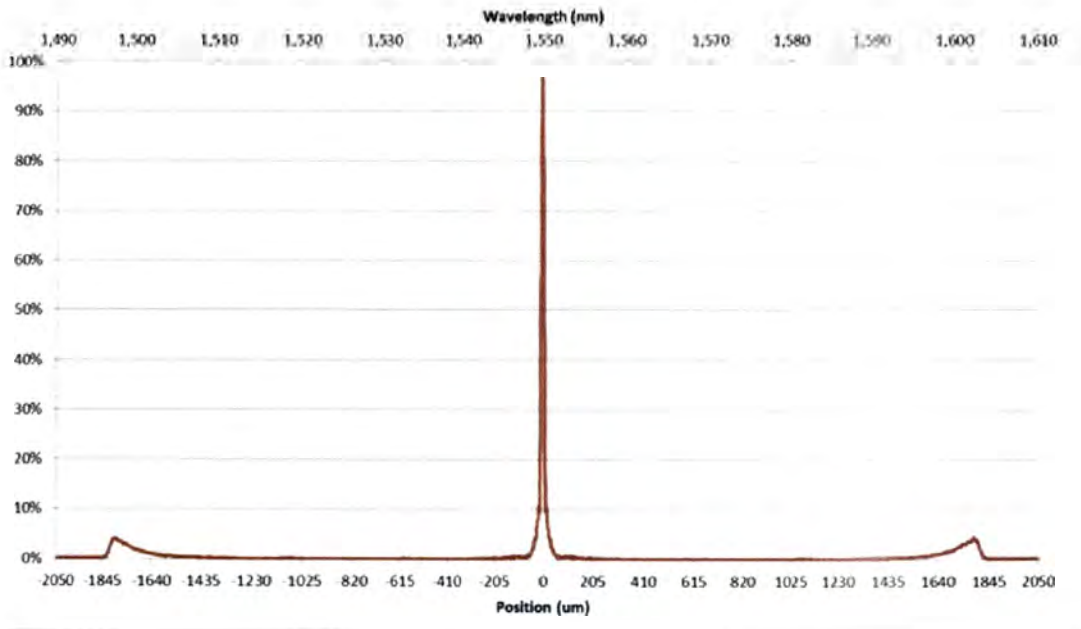

FIGURE 6.4: AWG simulation output for the layout shown in Fig 6.1. This particular layout is the same as the circuitry found in Chipset A and B. The graph shows the light intensity across the AWG output for monochrome 1550 nm signal, and the corresponding spectral scale. The efficiency is normalised to the input SMF mode launched into the input FPR.

The process is then repeated for every subsequent wavelength of interest, one at a time. However, because the simulation is split into two parts, a short-cut can be taken to minimise computation time. The light field in the input FPR does not change measurably with respect to wavelength over a narrow wavelength range (few 10's of nm's). This is because the light is simply diffracting from the launch fibre into the array, so only the inherent dispersion in the glass will have an effect when the wavelength is changed. Thus, the model doesn't re-simulate the input FPR for wavelengths which are within $\sim$ 50 nm of each other and starts the simulation from PHASECOR onwards. This cuts the computation time required in half. However, as material dispersion does have an effect, when simulating the AWG over a broad wavelength range (over the

whole H-band for example), the input FPR is included in the simulation for each wavelength.

By using this method, we can quickly and reliably simulate new AWG designs to asses their theoretical performance. As the simulation takes into account everything except bend losses (which are typically negligible, but are easily simulated separately) and errors due to manufacturing (glass impurities, wall roughness, refractive index non-uniformity etc.), the model provides us with a close approximation to how a real fabricated device would perform and allows us to reliably test new AWG designs for astronomy.

6.2 Wide bandwidth IPS

Thus far, our work in realising an IPS device was limited to the commercially available AWG chipsets. While they were modified by removing the output waveguides to obtain a continuous output spectrum, and removing the input waveguide tapers in Chipset B to increase their resolving power, the fundamental design parameters of the AWG circuitry remained the same as that of the commercial telecommunication-grade chips. In this and the subsequent section, we explore new AWG designs which can unlock the full potential of this platform for astronomical use.

In this section, we explore the motivation of designing circuitry capable of a much larger FSR than that found in the existing chipsets, as well as highlight early instrument concepts which can demonstrate the advantages should such a device be realised. Lastly, we present our High-FSR design for astronomy and present its modelled performance, and include limitations placed on the designs from fabrication considerations.

6.2.1 Motivation

The current chipsets that we explored have a narrower FSR than that of commonly used low resolution spectrographs. Typically, modern NIR spectrographs ($R \sim$ few thousand) will encompass an entire atmospheric band. The H-band for example is roughly 300 nm wide, $\sim$ 6 times wider than the FSR of the AWG chipsets. This limited wavelength coverage can be circumvented by making use of the different grating orders by cross-dispersing the AWG output, as we demonstrated in our on-sky prototype described in the previous chapter. While this technique is straight-forward

to employ and allows an AWG spectrograph to have a similar wavelength coverage, cross-dispersion has a few important drawbacks.

By using a bulk-optic cross-dispersion system, we negate many of the benefits of moving to a photonic platform. While the chip itself is still robust against environmental factors, the cross-dispersion optics will likely not be as robust. Further, much like our on-sky prototype, the cross-disperser will inherently be orders of magnitude larger than the AWG chip, and depending on the application may require a larger dewar which adds complexity and expense to the overall instrument.

Another factor that must be considered when using cross-dispersion is that because the spectra will now be dispersed both horizontally and vertically on the detector, the detector real estate will place a limit on the number of AWGs that can be used simultaneously. This will of course depend entirely on the detector sampling and configuration, but using our on-sky setup as an example, we could not image more than 2-3 AWG chips simultaneously on the detector. This imposes limitations to the type of astronomy that can be pursued. For example, seeing-limited multi-object spectroscopy (MOS) using this configuration of chips and cross-dispersion will not be very efficient and likely uncompetitive with more traditional bulk-optic spectrographs. Three AWG chips per detector will only allow for three MMFs at the telescope focal plane, which is much lower than what is currently achievable [96] and that planned for ELTs [97].

By increasing the FSR from ~ 50 nm to $200 - 300$ nm while maintaining a similar resolving power, we will be able to encompass the entirety of (or a substantial portion of) the H-band in a single order. As other orders are no longer required for extra wavelength coverage, the cross-dispersion optics can be removed and the chip's output directly imaged by a detector (assuming there is a H-band filter upstream of the chip). This opens up greater flexibility when it comes to arranging AWGs on the detector as there is no longer any dispersion vertically, and each chip will produce a single horizontal spectrum on the detector. Even if cross-dispersion is required for a multiple fibre launch / photonic lantern setup, the constraints on the cross-disperser optics are relaxed, as we will demonstrate. Further, configurations such as chip-stacking, where a series of AWGs are stacked on-top of each other and re-imaged onto the detector simultaneously, become feasible. We propose how these improvements in FSR coverage

of the IPS chips could be utilised for three different applications; a seeing-limited MOS, an AO-fed all-photonic IFU, and a space-based (or high-altitude) platform.

6.2.2 Device concepts

6.2.2.1 Seeing-limited MOS

In this concept we describe how an AWG chip with an $R = 7500$ and a $FSR = 200$ nm (design presented at the end of this section) could be used in a seeing-limited MOS configuration. The concept is outlined in more detail in Fig. 6.5.

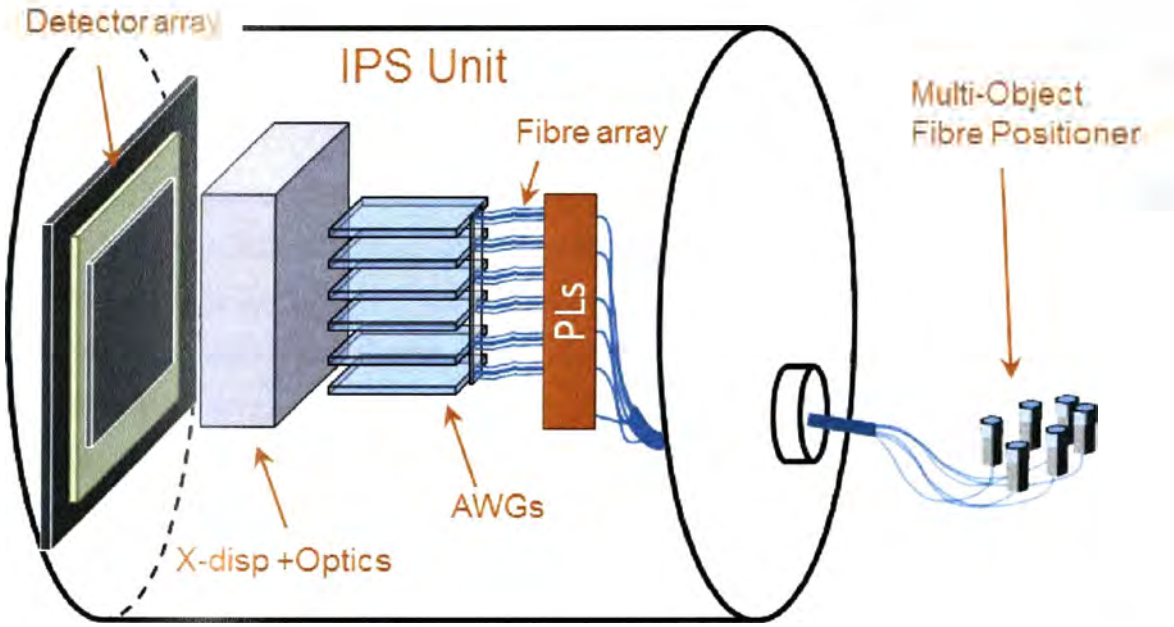

FIGURE 6.5: Illustration showing one possible concept of a photonic multi-object spectrograph instrument. A fibre positioner places multimode or few-mode fibres at the telescope plane, which carry the light to the IPS unit. The MMFs are fed to a set of photonic lanterns, which split the light into a series of SMF arrays. Each AWG chip takes one fibre array (one MMF) and spectrally disperses it. A low-R cross disperser separates the spectra from multiple fibres, with anamorphic optics focusing the light onto a detector.

First, a series of MMFs would be placed at the telescope focal plane to capture the light from individual objects, one per MMF. Reconfigurable fibre positioners have been demonstrated in many existing (and planned) MOS designs, either using a robotic arm to position each fibre individually (such as the 2df fibre positioner [96]) or using micro-mechanical steppers on each fibre itself to reconfigure the field in parallel and more rapidly (as seen in the Starbugs/MANIFEST instrument [98]). These forms of

fibre positioning are seen as the most efficient way to reconfigure fibre-based MOS instruments. The fibres for this example are MMF with a 50 μm core, capable of coupling seeing-limited light. This of course is highly dependent on the median seeing at the telescope, the telescope diameter, and the $F\#$ at a given focus.

The MMFs would carry the light into the IPS unit, whereupon each MMF would enter a photonic lantern. We chose the 50 μm core MMFs as the 50 μm MMF-to-SMF photonic lanterns are the same as those used on our on-sky demonstrator, and those used on the GNOSIS instrument [63], so are well characterised and their performance well understood. In this case the MMFs would each be split into 19 SMFs, which would be coupled into the AWG chips.

At this point it would be prudent to discuss the two different approaches to the photonic lantern MM-SM converter. The traditional approach, and one already demonstrated, can convert the signal with $\sim 80\%$ efficiency. However, it has a sizeable footprint of a few cm per lantern due to the length of the adiabatic taper region. As we will have multiple MMF inputs, a number of lanterns are required and the footprint will increase. This is not that big of an issue for the overall device size, however, if we choose to add fibre Bragg grating (FBG) based OH-suppression (another exciting astrophotonic technology) it increases the size by an order of magnitude. OH-suppression is ideal for removing the atmospheric OH emission lines found in the H-band, allowing for enhanced measurements of high red-shift galaxies. The suppression is done by a complex (multi-notch) Bragg grating inside each SMF, which creates narrow and sharp spectral notch filters which only remove the OH lines, allowing the remaining spectrum to pass through. Spectral lines of astronomical sources (such as galaxies whose spectral features are red-shifted into the NIR) which fall in between the OH lines pass through without atmospheric contamination. Each OH suppression FBG is a few 10's of cm in length and is required for each of the SMF outputs of the lantern, and since FBGs are thermally sensitive must be athermally packaged which further increases their size. For GNOSIS as an example, the FBG unit for 7 MMFs measures roughly $80 \times 50 \times 50$ cm.

Recent developments in 3D laser direct-written waveguides offer an exciting opportunity for dramatic miniaturisation of both OH-suppression and photonic lantern devices. An integrated on-chip photonic lantern (IPL) was first demonstrated by Thomson et. al. [99] at Heriot-Watt, with follow up devices showing $> 90\%$) conversion

efficiency between a 50 μm core waveguide to SM waveguides [100]. The SM waveguides are re-mapped onto a 2D plane with arbitrary user-defined positioning, ideally suited for launching into planar photonic technologies, such as AWG chips. Further, an IPL with Bragg grating notch filters has recently been fabricated [101]. IPLs have a physical footprint of a few square mm's and, as an integrated photonic platform, are robust to temperature changes and do not require sizeable thermal packaging.

Whether IPLs or their fibre alternatives are used, the SM waveguides/fibres are butt-coupled to the AWG chip. The chip's output has to be cross-dispersed before it is focused onto the detector due to the overlapping of the spectra from the different fibres at the chips' output (as explained in previous chapters). In this part of the concept; the detector real estate, the cross-disperser optics, and the fibre separation at the AWG input, are interrelated and must be considered together.

Firstly, an IPS with an $R = 7500$ and an $FSR = 200$ nm has ~ 922 PSFs/FSR. With the PSF being 6.6 μm physically, the entire output spectrum is 6.083 mm in width at the chip's output face. If we assume the detector is akin to a HAWAII 2RG detector (2040×2040 pixels, with a 18 μm pixel pitch), the detector would be 36.72 mm horizontally. Since we need to Nyquist sample the PSF to maintain the resolving power (~ 2 pixels/PSF) we must magnify the AWG output by a factor of $5.5\times$. This makes the entire FSR ~ 33.18 mm wide when re-imaged on to the detector, allowing us to fit the entire output spectrum with some space left over. This matching to detector real estate played a major part in AWG design considerations as we will see later.

With the chips' outputs fitting horizontally onto the detector, we now consider the vertical axis, which is more complex. To start out with, the spacing of the input fibres/waveguides into the AWG chip can be chosen arbitrarily, but as we point out in previous chapters is chiefly limited by the FSR of the chip. The reader may recall that our on-sky demonstrator had 12 input fibres for the 50 nm FSR chip. In that case, we placed the fibres as close together as physically possible (127 μm) but were ultimately limited to 12 of the 19 fibres available from the lantern. As each off-centre fibre causes a wavelength offset at the output, the accumulated shift from the far-left to far-right fibre could not exceed the 50 nm FSR, otherwise they would have overlaped on the detector regardless of the cross-dispersion. However, in this case our FSR is 200 nm allowing many more fibres to be placed. This is because unlike our previous

chips where we had to fit the off-axis fibres within the 50 μm FSR to ensure no overlap between the orders, the larger FSR of this design provides four times more space. While it is entirely possible to place four times more fibres at the original spacing, the photonic lantern output we chose for this example has a limit of 19 fibre outputs, thus for this design the input fibres are spread out further than in the original chips. By interfacing all 19 lantern outputs with even spacing at the AWG input ($\sim$ 320 μm separation), we see that the wavelength offset for each off-centre fibre is $\sim$ 10.5 nm, compared to the $\sim$ 3.6 nm offset for the on-sky demonstrator. If we provide a 1 pixel gap between the spectra from each fibre vertically on the detector (which is adequate in the low cross-dispersion regime), we find that the necessary linear dispersion needed for cross-dispersion is 291 nm/mm (and a $R \approx 77$), easily achievable using off-the-shelf components (preferably a prism to maintain high throughput at low R). With all the spectra from each fibre separated, over the 200 nm FSR, each AWG chip would take up $\sim$ 0.68 mm of detector space vertically.

The second thing we must consider is how closely the chips can be stacked on top of each other. For this design we maintained the silica-on-silicon technology, and therefore the same core and cladding sizes, as the chips we worked with experimentally. Thus from the top of the upper cladding to the substrate below the total thickness is $\sim$ 40 μm. This marks the absolute minimum separation of the two light-guiding layers if they were on top of one another. However, this ignores the silicon substrate of the chips. While it is possible to make chips with multiple guiding layers on one substrate (i.e. substrate→cladding→core→cladding→core→cladding etc.) this has major fabrication drawbacks and is not commonly done. The main reason is that with each subsequent deposition and etching of the chip, the uniformity and accuracy becomes difficult to control. Furthermore, multiple layering can result in a decreased robustness. As it stands, with current fabrication techniques it is likely that the AWG chips will consist of only one guiding layer per chip. When the substrate is included, the chip thickness is 3 mm, and is the closest the guiding layers can be brought together. Ideally, to maximise the detector real estate the chips should be placed at a separation of $\sim$ 1.2 mm. That way, the spectra do not overlap and no empty space is left between the chips vertically on the detector. Since we require bulk optics as part of the cross-disperser, and to achieve the 5.5× magnification necessary for Nyquist sampling, we

can conceive of using anamorphic optics (different magnification for the vertical and horizontal axis) of the chips' output prior to entering the cross disperser. This demagnification of the vertical axis need only be 2.5×, and once more is achievable using off-the-shelf components. If this is done, we can fit 51 AWG chips vertically on the detector's 36.72 mm vertical extent. If anamorphic optics are not used, the number is closer to 20 AWGs.

The whole unit would be able to simultaneously image the diffraction-limited spectra from 51 AWG chips, hence 51 MMFs can be placed at the telescope focal plane. If we assume a 80% photonic lantern conversion efficiency, 80% AWG throughput, $\sim 60\%$ cross-disperser and optics throughput, the whole IPS unit would have an estimated throughput of $\sim 40\%$, then divided by a factor of 19 due to the splitting of the lantern. The signal can be recombined while reducing the data, but it is important to note that due to the specific readout noise, the SNR will increase as a factor of $\sqrt{N}$, where N is the number of spectra (19 in our case). However, this would be neglecting the coupling efficiency from the telescope to the MMF. This varies drastically depending on the seeing conditions, but for moderate-to-low 1.2" seeing, the coupling would be low (in the order of $10 - 20\%$). However, on a site with excellent seeing, or by using a smaller telescope, this would be higher. This is due to the MMF being able to support only a limited number of modes, but also the photonic lantern only being able to convert 19 modes. It is clear that the concept we propose is fluid in this regard, as a higher-mode photonic lantern could be used to support more modes, and increase coupling efficiency. However, this will increase the number of fibres input into the AWG, hence decreasing their spacing at the input, hence requiring stronger cross dispersion, and ultimately resulting in less chips that can fit on the detector simultaneously. Alternatively, depending on the telescope, a ground layer AO system could increase the coupling without the need for bigger lanterns.

It is important however to reiterate the fact that in this configuration, each mode is sampled separately, and thus provides no improvement to SNR over traditional spectrographs. In practise, it is hard to make a case for an IPS to be used in this regime in terms of signal improvement. However, the primary benefit in this regime is one of cost. As we have shown, the size of the IPS spectrograph allows both the dewar and the cross dispersion optics to be far smaller, and therefore cheaper. Furthermore,

as AWGs are mass fabricated, there is little additional cost incurred in fabricating multiple AWG chips.

6.2.2.2 Diffraction-Limited AO-fed IFU

Having discussed the likely configuration for a wide-FSR IPS on seeing-limited telescopes, we now explore the possibility of an instrument that is fed using a Multi Conjugate Adaptive Optics (MCAO) system [102], which provides an improvement in the image across a wide field of view, allowing for superior coupling into SMF. Such a unit is closer to the ultimate aim of creating an entirely-photonic system, where the light will have no glass-air interfaces from the time it is captured by the fibre, until it falls on the detector.

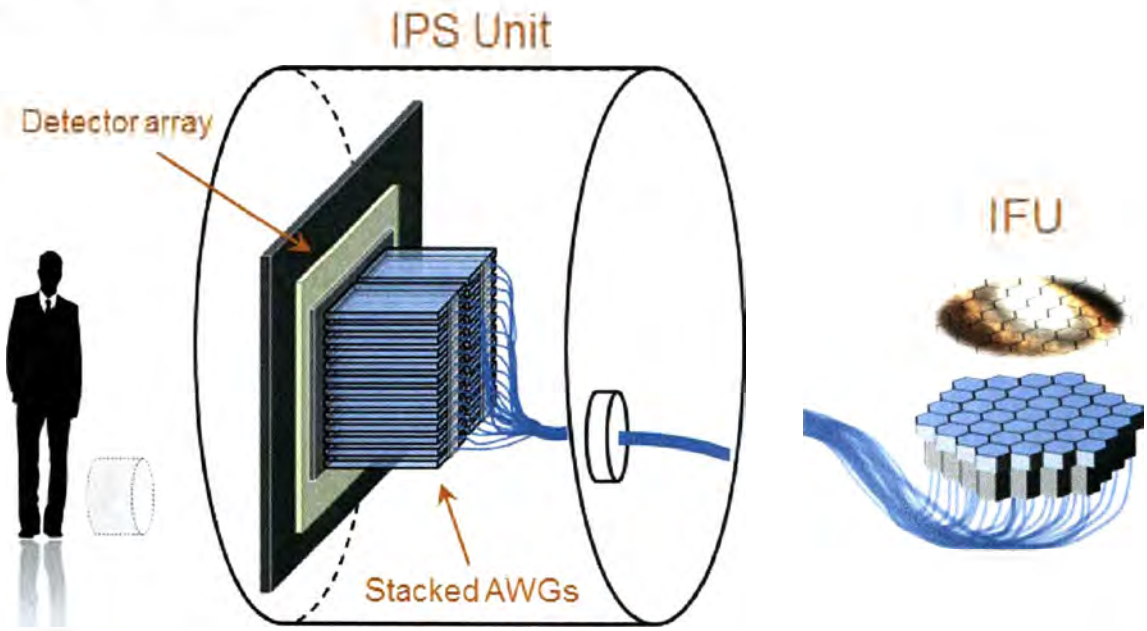

FIGURE 6.6: Illustration showing one possible concept of an all-photonic spectrograph device. An IFU couples AO corrected light from the telescope focal plane into SMFs, which then take the light into the IPS unit. Each fibre is directly coupled to an AWG with no need for a photonic lantern. Such a device would have a very small physical footprint as the entire AWG package would be several tens of cm across.

The ideal configuration of large-FSR AWGs would be to directly bond (or butt-couple) the output face of the AWGs to a detector (a concept is shown in Fig. 6.6). Directly bonding the AWGs removes the need for any optics in the system and provides a truly all-photonic platform. This can be done in a number of ways including directly

bonding a series of stacked AWGs to a 2D CMOS/CCD array, or by bonding a 1D linear array independently to each chip. Both options, however, are limited by detector technology, especially in the NIR. The bonding offers two further benefits. Firstly, extracting data from railway tracks that are straight and not curved on the detector is far simpler. Secondly, as the spectrograph is directly bonded to the detector the spectra do not drift in position with respect to the pixels, providing increased stability.

The typical PSF FWHM for AWGs is ~ 6 μm, but mainstream NIR detector arrays (such as the HAWAII 2RG CMOS detector) have a pixel pitch of ~ 18 μm. When we consider that the PSF should be Nyquist sampled (and hence cover ~ 2 pixels) it is clear that there is a drastic mismatch between AWG PSF spot size and the pixel pitch of the current generation of NIR detectors. Normally, one would simply magnify the AWG output on the detector, but this introduces bulk-optics into the system which we would ideally like to avoid.

Another possible solution is to increase the size of the mode (and therefore PSF) inside the AWG chip itself to better match the detector pixel pitch. This can be achieved by designing a different refractive index contrast in the core, and by changing the wave-guide size; or by introducing complicated 3D waveguide tapers. However, because the PSF-pixel size mismatch is a factor of 3, such designs are incredibly complicated, physically large, and push the limit of manufacturing reproducibly.

As we will show in Section 6.3, it is possible and feasible to create AWGs with an FSR of 200 nm, so the main technology hurdle to realise this IPS configuration is in NIR detectors. It should be said, however, that CCD arrays for the visible part of the spectrum suffer no such technological limitations and can readily achieve pixel sizes small enough to be used by a visible-light AWG. Unfortunately, manufacturing errors make it difficult to make AWGs that work as well in the visible as they do in the NIR, although with recent improvements in fabrication processes visible-light AWGs are starting to be manufactured and tested [103]. Even as visible-light AWGs become commercially available, the primary hurdle for a IFU all-photonic setup is integrating the diffraction limited IPS to a ground based telescope. In the visible, atmospheric turbulence creates a far more multimoded spot at the telescope focal plane than in the NIR [3], requiring state-of-the-art AO systems. While adaptive optics systems are making great strides in the visible regime [104], the field correction necessary for an

IFU is still in its infancy.

This particular concept would couple light from a AO corrected focal plane directly into SMFs, which for a traditional AO system is limited to around a 82% coupling efficiency [105]. This limit arises from the mode mismatch between the Airy spot produced by the primary mirror and the Gaussian acceptance mode of the SMF. The coupling can be further increased to $> 90\%$ with the use of phased-induced amplitude apodisation (PIAA) lenses, which convert the Airy spot into a Gaussian, and are used in the next-generation extreme AO systems [106].

The light is then taken into the IPS unit where each AWG is fed by a single SMF (removing the need for photonic lanterns). Thus, each AWG can now form a single spectrum over the H-band without the need for cross-dispersion. As we mentioned before, at this point there are three likely alternatives. If we use existing technology, which is to say an existing HAWAII 2RG detector, then it is most effective to use a set of anamorphic camera optics to re-image the AWG output onto the detector and maximise real estate. Like in the previous concept, the chips will require a $5.5\times$ magnification in the horizontal plane to match the pixel pitch of the detector. However, as no cross-dispersion is necessary, the chips can create a single horizontal spectrum. Unfortunately, the stacking limitations of 3 mm are still present and will require a de-magnification of $50\times - 33\times$ if the spacing is to be maximised on the detector. This is non-trivial to achieve, but if done can allow for between $1020 - 680$ AWGs to be imaged simultaneously, depending on the anamorphic de-magnification respectively.

Alternatively, a more appealing prospect is to directly bond the chips onto a 2D detector or more likely a 1D detector array. To achieve this, the detector's pixel pitch must be in the order of 3 μm, which is currently unachievable in commercially available NIR detectors. Nevertheless, none of the shortcomings discussed are insurmountable. As detector technology improves and pixel sizes shrink, particularly for low-noise NIR detectors, it is foreseeable that this all-photonic configuration can become practical.

6.2.2.3 Space-Based IPS

The most exciting application of a broadband all-photonic spectrograph would in fact be for space-based (or high-altitude) instrumentation. Without an atmosphere the telescopes do not suffer from seeing, performing at (or very close to) the diffraction limit, and are able to couple efficiently into SMF directly. This acts as an upper limit

as the overlap of the Airy spot at the focal plane does not perfectly overlap with the SMF's Gaussian acceptance field. This can be improved, if not overcome entirely, with the use of PIAA lenses.

Direct and efficient coupling into SMFs removes the need for photonic lanterns, decreasing the number of required AWG chips per object. Further, as the chips are a monolithic device with no moving parts and highly resistant to flexure or mechanical stresses, they would be ideal for space environments. The decrease in physical footprint and weight of an all-photonic approach is highly advantageous in this area as size and weight are often at a premium on space missions.

One potential drawback is the presence of high energy cosmic particles if the device is not properly shielded. Cerenkov radiation can be problematic for light guiding devices, as it adds a layer of random noise as the Cerenkov light is guided throughout the AWG and fibres.

6.2.3 Design and Modelling

Using the methodology outlined in Section 6.1, we designed and modelled the performance of a large-FSR AWG layout for the instrument concepts outlined above. To begin, the FSR for AWGs is determined by:

$$FSR = \frac{\lambda_c}{m} \frac{n_c}{n_g} \tag{6.7}$$

To obtain a large enough FSR we can see from the above equation that the grating order (m) must be reduced compared to the previous chipset, as we are still in the same wavelength, and the refractive indexes are the same. We chose to keep the refractive index contrast the same for two reasons. First, the manufacturing technique is already established and well characterised. Second, and more important, is that the refractive index contrast closely matches that of a SMF, allowing for easy and low-loss coupling of a SMF directly into the input FPR. If the contrast is increased without taking it into account, the mode which propagates in the AWG will be smaller, and cause a coupling loss between the SMF and AWG.

By decreasing the grating order to obtain a larger FSR, we know from Chapter 3

that this often comes with a trade-off in the resolving power (R), as:

$$R = \frac{mN}{C} \tag{6.8}$$

However, as we wish to maintain a similar R to that of the existing chipsets, we must now overcome this by increasing the number of waveguides in the array (N), and hence decreasing ΔL. This has the added effect of increasing the length of the input and output FPRs, where the focal length of these regions can be expressed in terms of the resolution and FSR as:

$$L_f = n_s d \Delta x(R)(FSR)\frac{1}{\lambda^2} \tag{6.9}$$

Δx is the physical PSF FWHM at the chip output, which as we mentioned before is set by the input mode profile which is $\sim$ 6.6 μm. The separation between the waveguides in the array (d) was set to 12 μm to ensure no cross-coupling between the array waveguides. From this equation, it is clear that to increase FSR while maintaining a resolving power of 7500, the length of the FPR must increase.

This is the primary limiting factor in this particular design. The practical limit for the size of the FPR is dictated by the size of the overall wafer onto which the circuit is to be fabricated. Typically, the wafers are constrained to 6 inches in diameter, with some manufacturers offering up to 8 inch wafers. While some flexibility is given by changing the array angle, the overall size of the AWG circuit must be constrained so it can be manufactured. We therefore imposed an upper limit to the overall design size to 15 $\times$ 15 cm. However, as the industry moves to larger 12" wafers, it will be possible to fabricate larger devices.

By imposing a limit on L_f we implicitly apply a limit to the FSR coverage if we are to maintain the necessary R. However, it is important to note that these two parameters can be traded for different scientific needs. For example, if a R of 7500 is not required and can be lower, than a larger FSR coverage can be obtained using the same sized layout. While the physical restrictions do apply an upper limit to our obtainable FSR,

the primary limitation we imposed on the design is of a more practical nature. Because existing large format, low-noise, NIR detectors have an array consisting of usually no more than 2040×2040 pixels, we must consider how the AWG output is to be sampled in a real-world application. In particular, as we need to Nyquist sample the output PSF, we are limited to no more than ~ 1000 PSFs per line on the detector (which in this case is our FSR). Hence, even though the wafer allows for a higher value, we set our FSR to be 200 nm wide, thus obtaining ~ 922 PSFs/FSR at the given resolution.

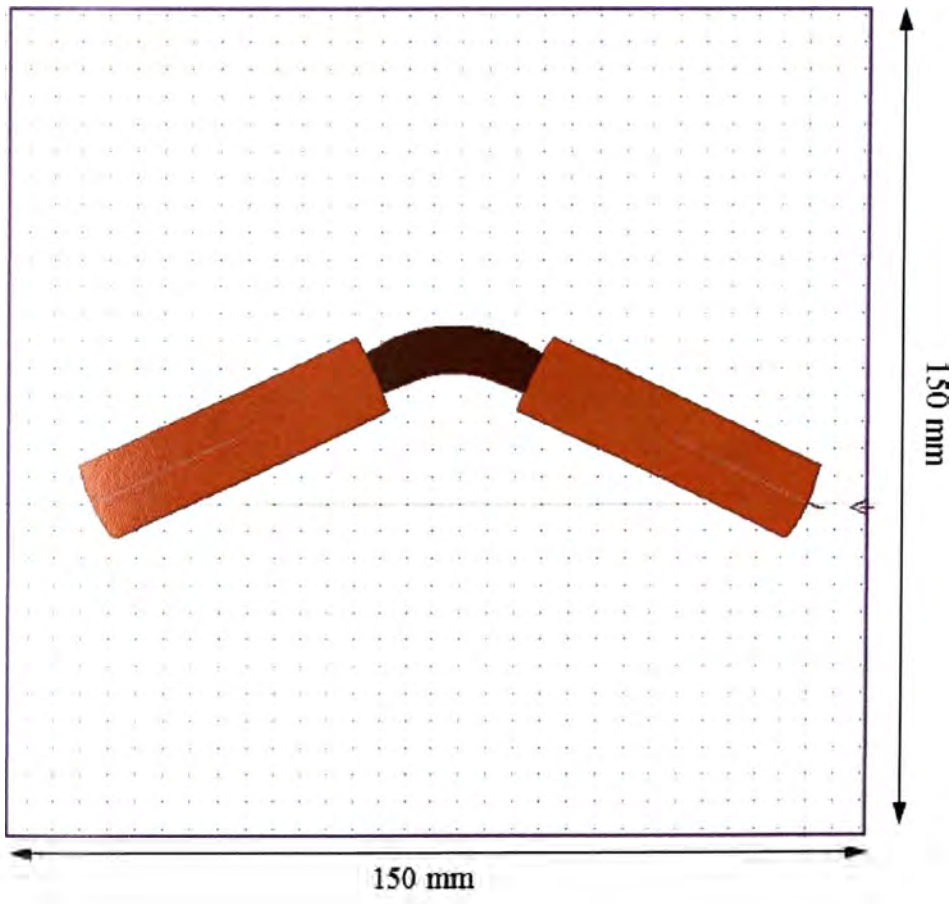

FIGURE 6.7: A complete schematic of an arrayed-waveguide grating spectrograph design used to fabricate lithographic masks. The design shows both the FPRs and the waveguide array. The angle in orientation between the FPRs is chosen to minimise the length of the waveguide array.

The AWG layout was generated using the parameters outlined above, with the full layout shown in Figure 6.7. Additional parameters of interest include the central operating wavelength $\lambda_c = 1550$ nm, the number of waveguides in the array $N = 875$,

and the array length increment $\Delta L = 8.54$ μm. The grating order was set to $m = 8$. This resulted in the FPR length being $L_f = 55.7$ mm. As we can see the total circuit measures $\sim 15 \times 5$ cm, which fits on a 6" wafer.

It can be seen in Fig. 6.7 that the overall layout of the design, and in particular the angle of the waveguide array (angle between the FPRs), is substantially different from the layout of the existing chipsets. As we outlined in the previous section, the angle can be arbitrarily chosen by the user, however there are geometric constraints which do limit the possible angles. In this particular case, the ΔL (which is less than half the size than that in the existing chipsets) imposes an upper bound to the allowable angle. As the path lengths must be maintained, a steep angle will induce an extra pathlength, thus the angle in this design is 12°, far shallower than the typical 45°.

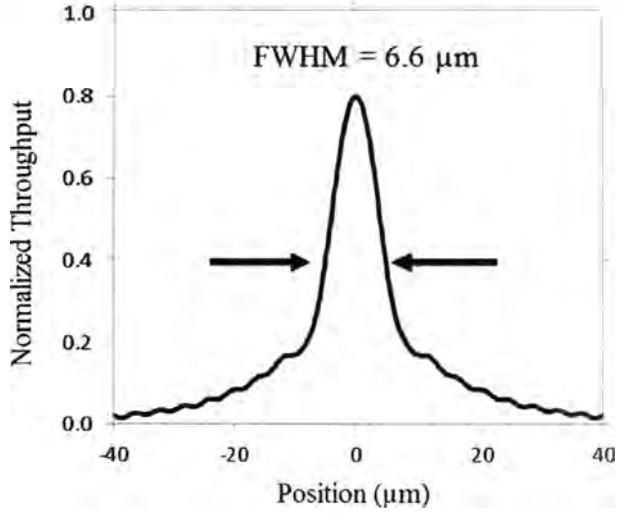

FIGURE 6.8: The simulated output PSF of the device at the central operating wavelength of 1550 nm. The physical FWHM is 6.6 μm with the spectral FWHM of 0.22 nm.

The layout was modelled using the BPM algorithm and scripts outlined in Section 6.1, to assess its performance. Figure 6.8 shows the typical simulated PSF. It has a physical FWHM of 6.6 μm, and a spectral FWHM of 0.22 nm, hence achieving the desired resolving power. From this, we also calculate that the predicted throughput is 80% for the central operating wavelength of 1550 nm.

We performed a wavelength scan over the FSR to observe the efficiency envelope across the entire FSR with the results shown in Figure 6.9. The wavelength scan was

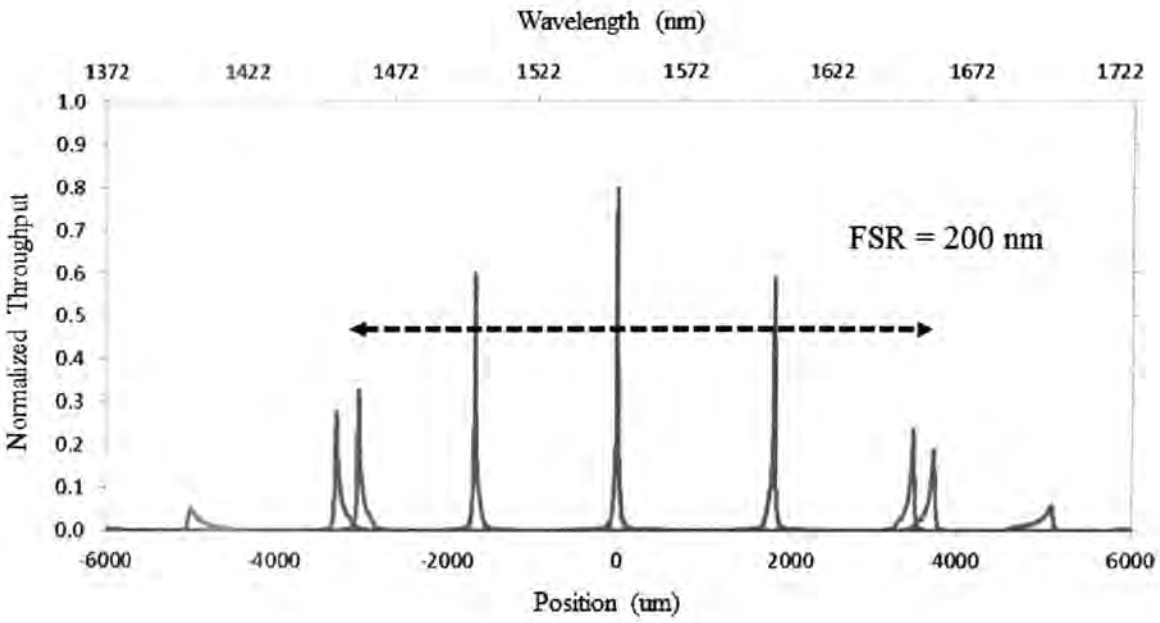

FIGURE 6.9: Several wavelengths from a detailed scan of the AWG output profile.

conducted at 13 nm steps, with the whole AWG simulated each time (taking about 30 minutes per wavelength). From the scan we can see that the overall throughput drops to 35% at the edges of the FSR. This is not a loss in the device, but rather the light being split between the central grating order and the $m + 1$'th and $m - 1$'th order. This is the same effect as experimentally observed in the existing chipsets. The PSF was measured at each wavelength step, remaining unchanged at $FWHM = 6.6$ μm across the FSR. The PSF does degrade sharply however outside the FSR edges.

We have successfully designed an AWG circuit that is capable of being used in the various concepts outlined in this section. The design was made as realistic as possible taking into account both fabrication limitations and factors arising from its possible use as part of an overall instrument.

6.3 High-Resolution IPS

We identify high-resolution spectroscopy as a key area of astronomy where new AWG designs can make a high impact for a number of reasons. Firstly, many scientifically exciting and rapidly growing areas of astronomy utilise high-resolution spectrographs:

FIGURE 6.10: A series of images taken during the construction of the HARPS high resolution spectrograph (top left and top right), with a CAD image showing the overall size of the spectrograph (bottom). These images illustrate the relative scale of the spectrograph itself, the large Echelle grating based on a mosaic construction, and the vacuum chamber. Images courtesy of Lovis *et al.* [107].

chemical tagging for galactic archaeology, temporal evolution of spectral lines for stellar seismology, and high precision radial velocity Doppler measurements for exoplanet science, just to name a few. Secondly, high-R spectrographs are more sensitive to the telescope-spectrograph size relation, which was explained in Section 2.1.4.1. Because high-R spectrographs on large research telescopes typically operate at R's of tens of thousands, the internal collimated beam diameter is very large (10s of centimetres). These spectrographs require large, often custom made optics, very large Echelle or Volume Phase Holographic (VPH) gratings, and are often enclosed in very large and complex vacuum chambers. This trend is especially true for planet-hunting spectrographs that require not only high resolution but exquisite stability and precision over

extended periods of time. Spectrographs like HARPS (at La Silla Observatory in Chile, see Fig. 6.10) are immensely powerful at detecting the minute planet-induced Doppler shifts in the spectral lines of a star [107], but are also tremendously large, and thus notoriously difficult to stabilise, not to mention the massive cost required for construction and upkeep.

This particular subset of spectrographs are ideally suited for possible photonic solutions. By identifying the key spectrograph parameters required for high resolution radial velocity studies, we aim to establish if, through clever design, AWGs can compete with traditional bulk-optic high resolution spectrographs. The results of which we present in Section 6.3.6.

6.3.1 Motivation

6.3.1.1 Exoplanet science

Extra-Solar planets, or exoplanets, refers to planets found outside of our own Solar system. One of the first methods used to detect these planets was the Radial Velocity (RV) technique. This requires astronomers to precisely determine minute Doppler shifts in a star's spectrum, which are due to the fact that both the host star, and its planet orbit a common centre of mass. However, because the mass of the planet is often many orders of magnitude less than the mass of the star, the effective reflex velocity (speed at which the star appears to move away or towards the observer) is in the order of a few m/s to a few km/s.

Another common way of detecting exoplanets is an imaging technique, where a star is observed photometrically with great finesse to detect an overall dimming of the starlight as the planet passes in front of the star, called the transiting method. This powerful method is responsible for most of the $\sim$ 2800 total planetary candidates due in part to the Keplar space mission [108]. However, this technique has a drawback in that it is only capable of detecting planets that pass in front of the star, i.e the system is edge-on to Earth. Nevertheless, the RV technique is still necessary for confirmation of transiting detections. Since high-R spectrographs are only used in the RV technique, we will focus primarily on this method.

The search for extrasolar planets with the radial velocity (RV) technique has led to close to 400 confirmations of planets around stars. Fourteen years after the seminal

discovery of 51 Peg b by Mayor & Queloz (1995) [109], the RV technique is still the most important technique to discover planetary systems.

The holy grail of exoplanet research, however, is to find a habitable Earth-like planet. Earth-like in this context typically refers to a planet that is similar to Earth in size, mass, and composition (i.e. rocky planet). The question of habitability is still debated, but a well accepted hypothesis is that planets that orbit inside the "habitable zone" (HZ) have the highest probability to perhaps sustain life. The HZ is a boundary of orbits where the star's flux incident on the planet is sufficient to allow for liquid water on the planets surface, but not so much so as to boil away the oceans.

6.3.1.2 Calculating radial velocity recoil of star

Both the star and planetary satellite orbit a common centre of mass. It is therefore simple to calculate the expected RV of a star for a given planet at a particular orbit (Fig. 6.11).

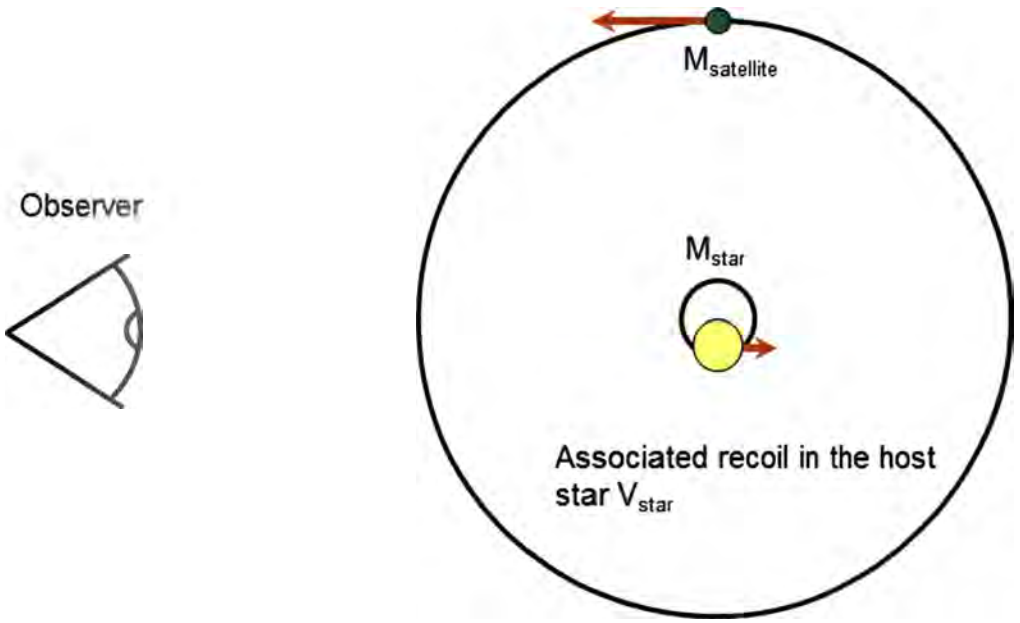

FIGURE 6.11: Illustration demonstrating the typical parameters required to calculate the star's RV induced by an orbiting body. The largest radial velocity in the direction of line of sight of observer occurs at this point and its opposite.

We can determine the orbital radius (r) (in metres) of a satellite from the period P_{orbit} (given in s)

$$r^3 = \frac{GM_{star}P_{orbit}^2}{4\pi^2}, \tag{6.10}$$

where G is the gravitational constant and M_{star} is the mass of the host star. This particular equation assumes no ellipticity in the orbit.

From the radius of the orbit it is possible to calculate the orbital velocity of the satellite ($V_{satellite}$)

$$V_{satellite} = \sqrt{\frac{GM_{star}}{r}}, \tag{6.11}$$

From this it is possible to determine the velocity of the star

$$V_{star} = \frac{M_{satellite} V_{satellite}}{M_{star}}, \tag{6.12}$$

where $M_{satellite}$ is the mass of the satellite.

The final step is to account for the fact that that the orbital plane may not be edge-on.

$$K = V_{star} \sin i, \tag{6.13}$$

where i is the inclination of the orbital plane from the viewer's line of sight.

6.3.1.3 M-Dwarfs and the habitable zone

To date, the majority of planets that have been found are approximately as massive as Jupiter that occupy close orbits around the star. This is due to an instrumentational limitation as that particular combination of mass and orbit produces large RVs which are easier to detect, and are not indicative of typical solar system dynamics. In order to find Earth-mass planets in orbit around a sun-like star, the RV technique either has to achieve a precision on the order of 0.1 m/s, or one has to search around less massive stars as there would be a greater effect due to the gravitational influence from the companion. As such, astronomers started targeting low-mass stars, called M-dwarfs, to observe ever smaller planets.

Low-mass M dwarfs are a natural target for the search for Earth-mass planets with the RV technique. The reflex velocity induced by an Earth-like planet is as much as an order of magnitude higher than around Sun-like stars, and their HZ is closer to the M-dwarf due to its low luminosity (see Fig. 6.12) and thus will require less observation epochs for detection. In addition, there seems to be no general argument against the possibility of life on planets that are in close orbit around an M-dwarf (inside the

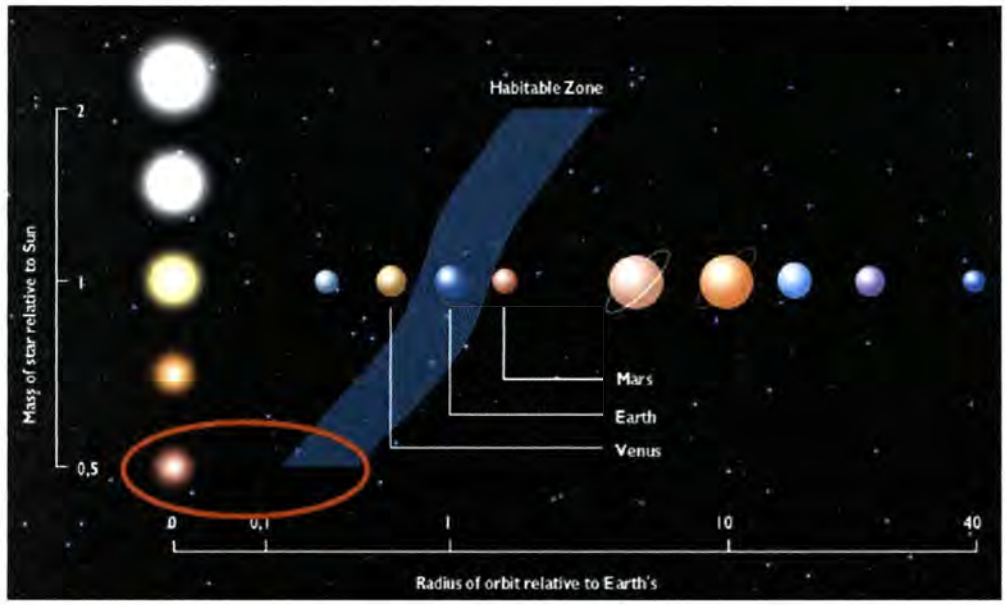

FIGURE 6.12: Graph showing the relative positions of the habitable zone for different star types. The M-dwarfs sit towards the bottom of the graph, circled in red. Image courtesy of NASA

habitable zone [110, 111]). So these stars are becoming primary targets for the search for habitable planets.

So far, only a dozen M dwarfs are confirmed to harbour one or more planets [112, 113]. However, it is important to note that recent Kepler data suggests that the true abundance of Earth-like and Super-Earth sized planets is actually closer to $15 - 25\%$ [108] (see Fig. 6.13). The problem with the detection of RV variations in M-dwarfs is that although they make up more than 70% of the Galaxy, including our nearest neighbours, they are also intrinsically so faint that the required data quality cannot usually be obtained in a reasonable amount of time at which most conventional high-resolution spectrographs operate. M-dwarfs have effective temperatures of 4000 K or less, and they emit the bulk of their spectral energy at NIR wavelengths. The flux emitted by a M5 dwarf at a wavelength of ~ 600 nm is about a factor of 3.5 lower than the flux emitted at ~ 1000 nm [114]. Furthermore, due to their low surface temperature M-dwarfs have abundant and narrow spectral features (typically molecular lines [114]) the majority being in the Y, J, and H-bands. Thus, NIR spectroscopy is much more efficient in measuring radial velocities of low-mass stars.

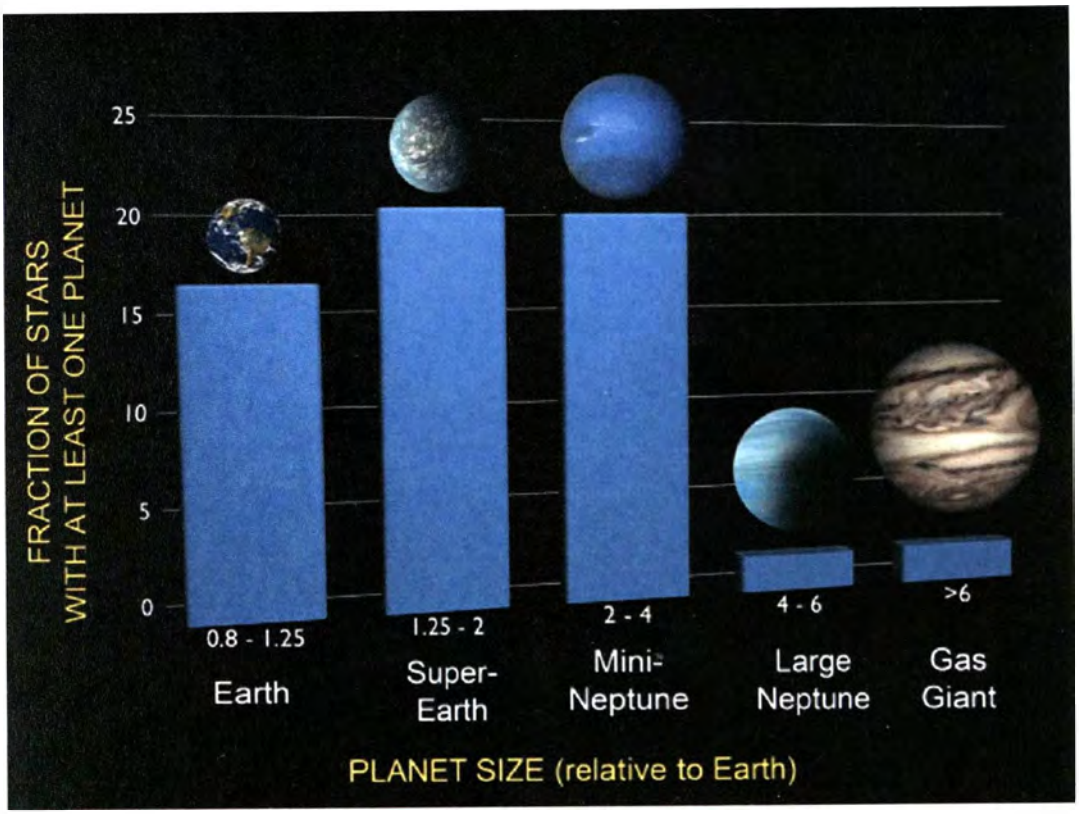

FIGURE 6.13: Graph from Kepler mission showing the estimated abundances of exoplanets. Image courtesy of [108]

6.3.1.4 Parameters required for exoplanet detection

To detect an Earth-like planet in the habitable zone around an M-dwarf star, there are three important parameters we must consider. Firstly, the resolving power of the spectrograph must be high enough to completely resolve the individual absorption lines in the star's atmosphere. This is important as the Doppler shift due to the stars reflex velocity is likely to be very small (few m/s for an Earth or Super-Earth sized planet). This shift is actually a fraction of the PSF, thus the line's shape must be completely resolved so as to allow an accurate determination of the line's centre. Typically for M-dwarfs, the minimum resolving power necessary to do this is between 30,000 and 60,000 in the H-band [115].

Secondly, by substituting known M-dwarf masses into Equation (6.12), we can calculate the expected reflex velocity (hence Doppler shift) by a planet on an M-dwarf. The RV expected from an Earth-like planet is ~ 1 m/s, with Super-Earth companions inducing an RV of ~ 10 m/s. This means that the spectrograph must be wavelength

calibrated to this or better in order to detect such a small shift. While this doesn't directly impose a design parameter when designing high-R AWG chips, it does imply that the chip should be as robust as possible against temperature fluctuations, misalignment, and mechanical flexure, as well as requiring a wavelength reference accurate at least to within 1 m/s.

Lastly, signal-to-noise (SNR) plays a part in determining the ultimate sensitivity of the spectrograph. The more noise that is in the final recorded spectrum, the more uncertainty in measured position of the spectral lines. The uncertainty must be kept under 1 m/s otherwise a detection is impossible. Therefore, we would require as much signal per pixel as possible, hence the system throughput should be as high as possible.

6.3.2 PANDORA Concept

6.3.3 Overview

PANDORA is a technology demonstrator instrument in the early stages of development, which employs our high resolution AWG chip outlined in the following section, and an extreme adaptive optics system to achieve competitive performance for a relatively modest cost. PANDORA is a collaborative project between Macquarie University, innoFSPEC at the Astrophysical Institute of Potsdam, the Australian Astronomical Observatory, and Subaru Telescope in Hawaii.

The fundamental concept of PANDORA is to demonstrate two technologies new to astronomy simultaneously. Firstly, the device will demonstrate the use of a single mode (diffraction-limited) IPS for planet-hunting, characterise its performance, and compare to state-of-the-art systems (such as the IRD high resolution spectrograph [115]). Secondly, the project will demonstrate the use of an extreme adaptive optics system to couple light into a single mode fibre with high Strehl ratio, and high coupling efficiency.

PANDORA has three main parts (see Fig. 6.14): the high resolution spectrograph, photonic wavelength calibration, and extreme adaptive optics fibre injection. The high resolution AWG chip acts as a primary wavelength disperser. The chip's output is passed through a low resolution cross-disperser to separate the orders, and is re-imaged onto a detector (HAWAII 2RG). Based on the detector real estate, we can fit $70 - 100$ orders from the AWG, giving us a wavelength coverage of Y, J, and H bands. While not

stated explicitly in the figure, the cross disperser optics may include a field-flattening lens to correct for the FPZs Rowland curvature at its output plane. The entire system would be enclosed in a temperature-stabilised vacuum chamber.

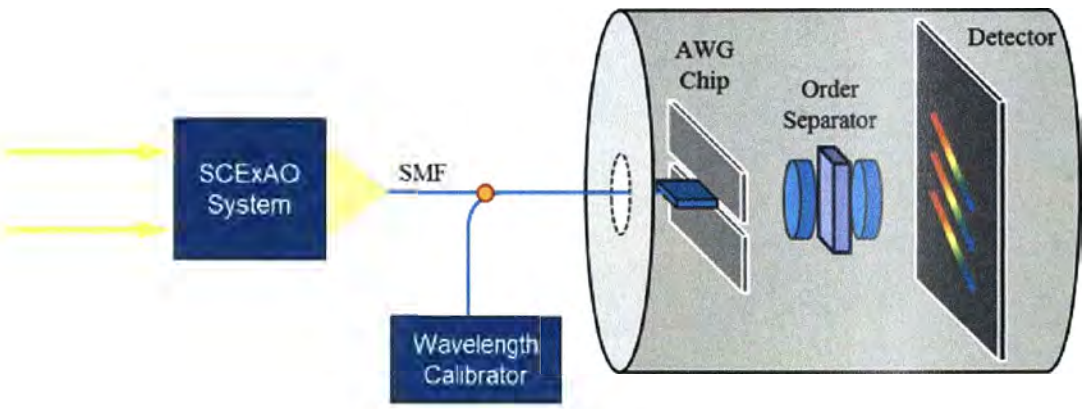

FIGURE 6.14: Schematic showing the overall concept of the PANDORA instrument.

6.3.4 SCExAO

The AWG is fed by one single mode fibre. Light is injected into the fibre using the SCExAO system [116]. SCExAO is an extreme adaptive optics system and chronagraph, developed primarily for directly imaging exoplanets. Extreme adaptive optics systems have demonstrated high Strehl ratios [116], which are required to obtain good coupling into a SMF. Moreover, SCExAO uses PIAA lenses to convert the telescopes pupil from a top-hat beam into a Gaussian as part of the SCExAO coronograph [116]. Thus the spot at the focus is a Gaussian, which has a greater overlap integral with the SMF's acceptance profile than the traditional Airy disk, allowing for coupling efficiencies $> 90\%$.

Launching into an SMF has the added benefit of removing modal noise. Modal noise is one of the leading contributors in limiting the precision to which a spectrograph can be calibrated. Modal noise causes an unpredictable temporal change in the PSF shape

due to a change in the amount of light propagating in each mode of the MMF. The light can easily couple from one mode to another if the fibre has any strain or temperature effects placed upon it from the environment. This is often the case as the fibres run typically from the telescope's focal plane to the spectrograph. Due to the unpredictable nature of modal noise, this effect is notoriously difficult to calibrate out. Because SMFs only allow the fundamental mode to propagate, there is no possibility of modal noise. Of course, if the AO system is not working well, this simply results in poor coupling into the fibre rather than a changing PSF. The guiding properties of a SMF ensure a stable non-temporally evolving PSF. This is a great advantage as this is what limits the accuracy of many similar instruments that use MMFs like HARPS.

6.3.5 Calibration

Because the fibre feed from the AO system to the AWG chip is single-moded, new photonic technologies can be used to cheaply and reliably provide the necessary wavelength calibration. Of particular interest is a commercially available Tunable Fibre Fabry Perot interferometer device. These devices are relatively inexpensive, small, and easy to stabilise. Recent literature suggests that these devices can be stabilised to a precision of 1 m/s [117], the same stability needed by PANDORA. Further, because the light from the calibration source and the star light are not coherent with each other, they can be combined into a single input SMF using fibre couplers, sending the calibration source down the same route as the stellar signal. This allows for it to be imprinted over the top of the stellar spectrum. Such a calibration technique is important as it allows for in situ monitoring of the spectrograph drift, minimising errors.

6.3.6 Design and modelling

In this section we describe a new high resolution AWG design with a resolving power of $\sim 65,000$ in the H-band. The chip was designed specifically for the use in M-dwarf exoplanet detection.

6.3.6.1 Design parameters

The chip was designed to operate at a central wavelength $\lambda_c = 1630$ nm (centre of the H-band) at a central order of $m = 101$. The resolution of the chip was set at $65,200$

which translates to a PSF spectral FWHM of 0.025 nm. The free spectral range was set at $FSR = 16$ nm, which gives 640 PSFs per FSR for the 101^{st} order. This was deliberately chosen because the output of the chip will likely be imaged by a HAWAII 2RG NIR detector which has a detector area of 2048 $\times$ 2048 pixels. Therefore, to Nyquist sample the chip's output we can have no more than $\sim$ 1000 PSFs across the FSR. We opted for a slightly smaller amount because (as we explain in the next section) we plan to cross disperse the output and use the chip over a broad wavelength range (J & H bands), and the FSR changes over the many orders. Because of the evolving FSR across the orders, and the fact that we want to maintain correct sampling which provides more precise fitting, we opted for 640 PSFs

One major difference between this chip design and the ones used in previous chapter is that we used a higher refractive index contrast between the waveguide core and slab ($\Delta n = 0.01535$, compared to $\Delta n = 0.006$). Because this index contrast is higher, the mode is more tightly confined (smaller) in the waveguide. This allows us to manufacture devices with a much smaller physical footprint, and utilise the wafer area more economically. However, the optical fibre that will be used to launch light into the chip has a much smaller Δn and hence a bigger mode profile. If we do not account for this, the mode mismatch between the fibre and the input waveguide would cause extensive coupling loss. To avoid this, we reduced the size of our input waveguides in the AWG from $\sim$ 7 μm to 3.5 μm. This expands the mode profile of our input waveguides so that it matches the injection fibre and our coupling losses are minimised.

While only one input waveguide will be used to launch light into the FPR (because we are injecting with only one fibre), the design has 25 input waveguides. This was done simply as a form of redundancy against manufacturing error, and to provide added flexibility in choosing where on the input FPR the light will be injected.

The FPR has a focal length $L_f = 50$ mm, and feeds an array of 956 waveguides. The array length increment was $\Delta L = 113\mu$m. The waveguides in the array are separated by 15 μm to avoid cross-coupling.

The full layout of the AWG chip is shown in Figure 6.15. The chip area is 88.5 $\times$ 54.5 mm a similar size to Chipset A & B. The AWG layout shown in the figure is a departure from standard practice and that of our previous chipsets. This 'ribbon' configuration is used primarily because of the large ΔL ($\sim$ 10 times larger than

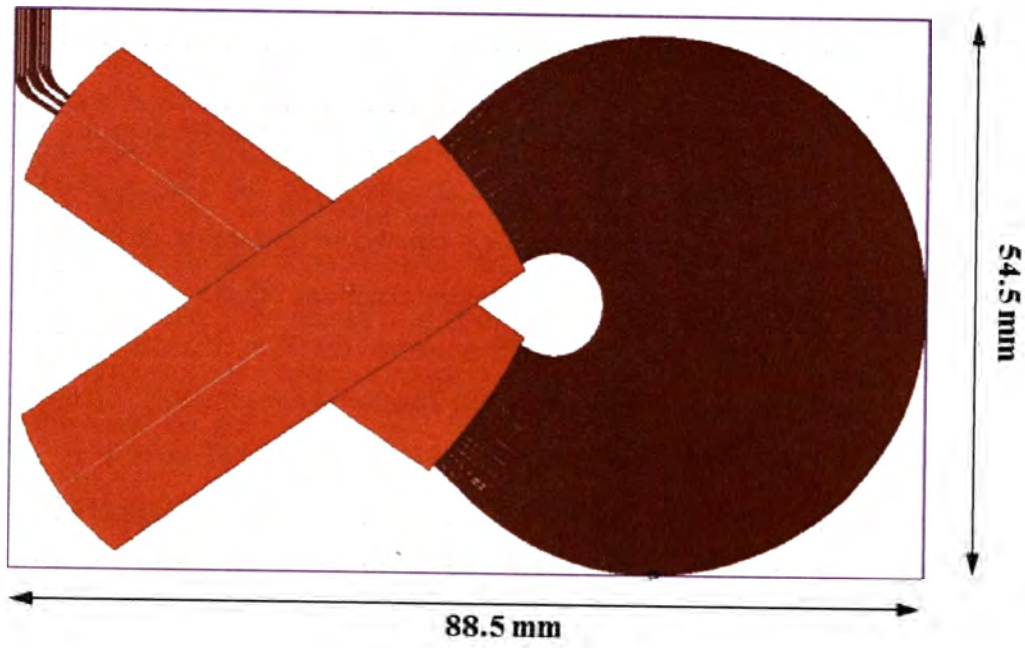

FIGURE 6.15: A schematic of the high resolution AWG design. The chip dimensions (purple box) are 88.5 mm × 54.5 mm

Chipset A & B) required to operate at such a high order, and is a consequence of operating at high resolution. This is further compounded by the fact that we have a large number of waveguides in the array, and accumulate a larger than normal path-length between the 1^{st} and 956^{th} waveguide.

It is important to note that the two FPRs are not on top of one another, but are in fact in the same plane. This layout is not detrimental to the AWG's performance as the FPRs do not confine the mode laterally, and the diffracting light from the input (or the interfering light at the output) do not ever touch the sides of the FPR. Hence an overlap of the FPRs is unnoticed by the propagating light and does not lead to any increase in scattering or other losses. While this particular layout is relatively uncommon for commercially available devices, overlapping FPRs between adjacent AWGs is commonly used to maximise wafer real estate.

While not directly shown on the figure, the chip will be cut and polished tangential to the output FPR's focal plane.

6.3.6.2 Modelling performance

We used the beam propagation algorithm outlined in previous sections to model the AWG performance. Of primary concern was the shape of the PSF at the output of the device as any perturbations, which can be caused by a number of factors, such as cross-talk in the waveguide array, could have detrimental effects for this design's use for exoplanet science (which is particularly sensitive to PSF changes). We modelled the PSF across multiple wavelengths with the results shown inf Fig. 6.16. The PSF remained stable across multiple wavelengths demonstrating that there is no cross-talk in our design. Further, the PSF FWHM behaved as expected, reimaging the mode-field of the injection waveguide. The slight broadening of the PSF's FWHM at longer wavelengths is not due to errors in design, but rather the result of the input waveguide mode-field increasing in size at longer wavelengths. From the modelling results we calculated a resolving power $R = 65,000$, with a $C = 1.48$.

The throughput of the AWG was simulated to be $70 - 80\%$ for the primary peak, with the remaining light being diffracted into a higher and lower order, and no losses due to scattering. If we combine the throughput across the multiple orders the simulated throughput is $90 - 96\%$.

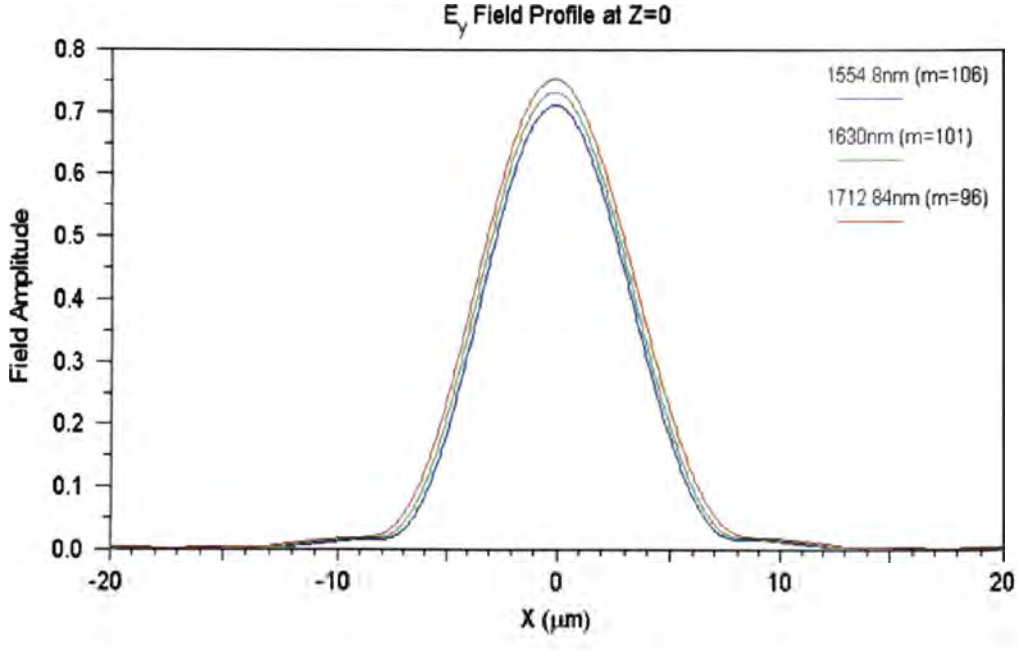

FIGURE 6.16: Simulation results showing the PSF at three different wavelengths.

We also conducted simulations to analyse the affect of misaligning the injection fibre relative to the input waveguide. This was done primarily to quantify the tolerances when aligning and bonding the fibre. The results are shown in Fig. 6.17.

From the figure we can see that an alignment precision of ~ 0.5 μm is adequate to minimize coupling losses. This is easily achievable using off-the-shelf precision translation stages. Further, we see that a separation of a few microns between the fibre tip and chip does not decrease the coupling drastically, giving us more flexibility when bonding the fibre using epoxy.

6.4 Conclusion

In this chapter we showed in detail how new non-commercial AWG designs can be created for specific astronomical goals. We also described how the performance of AWGs can be precisely modelled using Beam Propagation software. We used these tools to create two separate AWG designs, and describe how they can be used in an overall instrument. Lastly, we presented the modelling results for both the large-FSR and high-R AWG designs.

We are collaborating with the innoFSPEC group at the Astrophysical Institute of Potsdam to fabricate the high resolution AWG design outlined above, as part of the overall PANDORA collaborative project, which includes the Subaru Telescope in Hawaii and the Australian Astronomical Observatory. As of writing, the mask designs have been sent to a commercial lithographic foundry and have been fabricated. The vendor is currently in the process of fabricating the initial prototypes of said chips. Because we are aiming to fabricate an AWG with unprecedented resolution, it places tight tolerances on fabrication processes and quality control, so the fabrication and testing lead time for our design is longer than that of typical commercial designs. The laboratory characterisation of the resulting chips will commence mid-2014.

We will begin testing the SMF injection on SCExAO around mid-2014, with the initial chip prototypes commencing on-sky testing towards late-2014, early-2015.

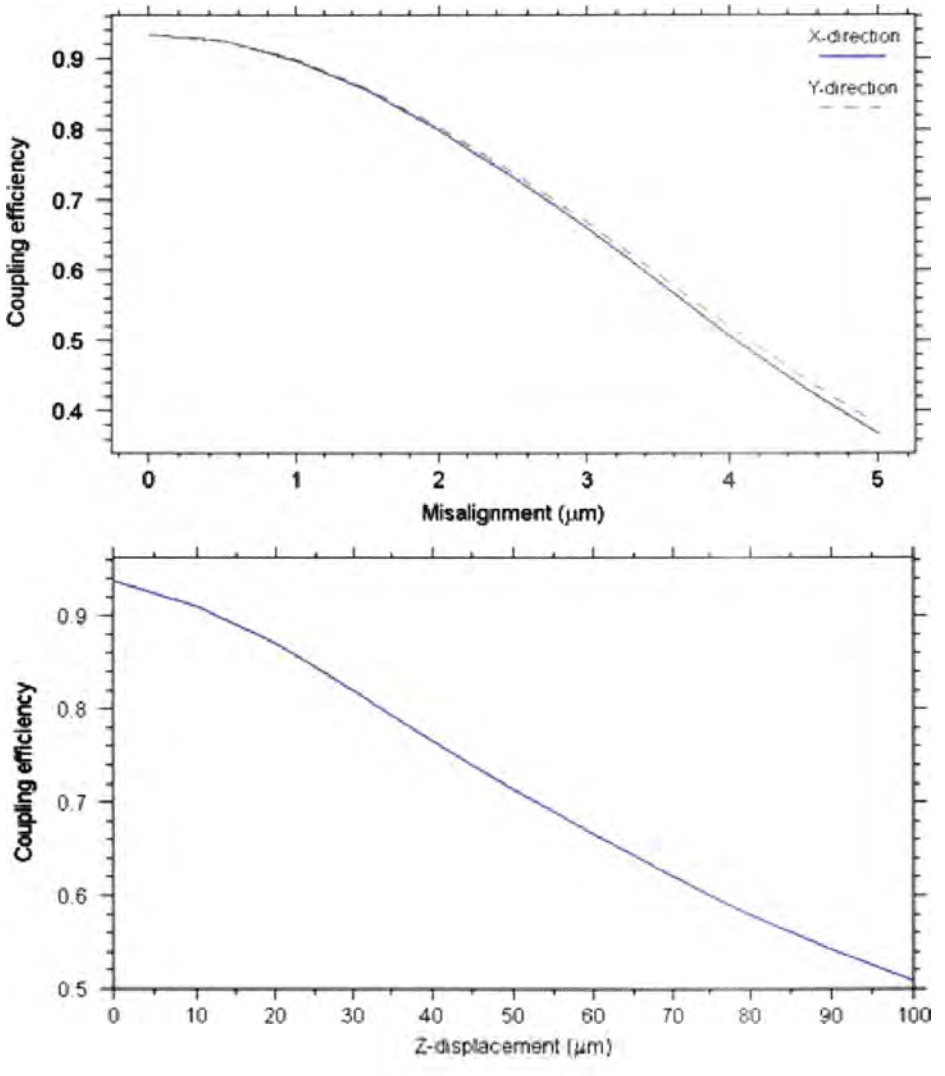

FIGURE 6.17: Simulation results showing the effect of misaligning the injection fibre with respect to the input waveguide. The top graph shows the results from misaligning the fibre laterally with respect to the input waveguide while maintaining butt-coupling. The bottom graph shows the effect of not connecting directly to the chip, and having an air gap between the fibre and input waveguide.

"There are three stages in scientific discovery. First, people deny that it is true, then they deny that it is important; finally they credit the wrong person."

Bill Bryson, *A Short History of Nearly Everything*

7

Conclusions and future work

In this thesis, we explored the use of recently developed low-loss micro optical photonic circuitry in glass to create a new type of photonic spectrograph for astronomical use. After conducting a brief overview of conventional bulk-optic spectrograph designs in Chapter 2, we provided a detailed description of how arrayed waveguide gratings, determined to be the most promising and practical type of photonic circuitry for photonic spectrograph construction, are designed and manufactured in Chapter 3. In that chapter we outlined the processes used to create the Integrated Photonic Spectrograph, a miniaturised, monolithic dispersive device on a silica-on-silicon wafer. These photonic chip-based components were typically only several square centimetres in size and a few millimetres thick, orders of magnitude smaller than conventional spectrographs. Their size and integrated nature makes them robust against misalignments or flexure due to environmental factors, a property highly sought after for modern spectrographs.

To develop this technology, we presented in Chapter 4 the experimental laboratory characterisation conducted of two separate AWG chipsets. We showed the performance of the initial IPS prototype which was based on an off-the-shelf commercial design, that resulted in a spectral resolving power of 2400 at 1600 μm. We found that the resolving power for this particular design was limited by parabolic-horn waveguide tapers at the input waveguides. By removing said waveguides and launching light directly into the FPR using a SMF, we were able to show a three-fold increase in resolving power with no

measurable detriment to other performance parameters. The subsequent AWG chips had no input tapers and a resolving power of 7000 at 1600 μm. Both the chipsets had an end-to-end throughput of $75 \pm 5\%$.

With the input waveguides removed, we performed tests to determine the viability of injecting multiple off-axis fibres simultaneously into the AWGs to allow for multiple spectra to be acquired using a single chip. We demonstrated that 12 fibres could be injected simultaneously limited by the FSR and quantified the impact of this method on resolving power and throughput.

We used the improved AWGs to create a prototype on-sky demonstrator instrument and conducted a proof-of-concept test on the 3.9 m Anglo-Australian Telescope at Siding Spring Observatory. We provided the results of the successful test, with detection of carbon-monoxide absorption lines in the spectrum of the star Pi Gru using the IPS in Chapter 5. This was, to our knowledge, the first successful capture of a spectrum from a source beyond Earth using a photonic spectrograph. Further, we outlined the required telescope interface for the IPS, which required the use of additional astrophotonic technologies (such as the photonic lantern). We described in detail the IPSs performance and limitations.

Lastly, we presented a comprehensive redesign of AWG circuitry to better suit specific astronomical requirements for the next generation of IPS devices. Two particular designs were discussed, alongside their predicted performance modelled using beam propagation algorithms. Firstly, the free spectral range of the IPS was increased to encompass an entire NIR atmospheric window (H-band) while maintaining the same resolution as our previous chips. This design allows for the construction of an entirely-photonic platform with a small physical footprint, ideal for space applications, while maintaining broad wavelength coverage. Secondly, we presented a new AWG design with a resolving power of 60,000, which was designed specifically for high precision radial velocity studies of planets around M-dwarf stars. This high resolution AWG chip is to be used as part of the PANDORA instrument, collaboratively developed between Macquarie University, the Astrophysical Institute of Potsdam, the Australian Astronomical Observatory, and the Subaru telescope in Hawaii. We highlighted the overall instrument concept, with its projected performance, and highlight the advantages over a traditional spectrograph design.

7.1 Future work

The primary aim for future activities regarding IPS devices is to successfully complete fabrication of the high resolution AWG chip as part of PANDORA, and demonstrate the concept on-sky. The AWG outlined in the previous chapter would be the most advanced AWG (in terms of resolution and stability) fabricated to date. Further, a comprehensive study of SMF injection using new extreme AO systems has not yet been conducted, and is necessary to assess the long-term feasibility of interfacing SM photonic devices to telescopes. In 2014 we aim to complete the laboratory characterisation of the new AWG chips, as well as perform the initial testing of a SMF injection on the SCExAO system at Subaru. Depending on these results, we aim to perform initial testing of the IPS behind the AO system in late 2014, early 2015.

Another avenue of IPS development is to shift the technology to different wavelengths. In particular, an IPS performing at visible wavelengths can make use of the abundance of low noise, inexpensive, silicon detectors. While groups around the world are moving towards visible wavelength AWGs for bio-medical sensing applications, applying this kind of IPS to astronomy faces a few extra hurdles. Firstly, to maintain single mode performance, the waveguides in the AWG chip must be smaller in size than those for NIR, because the refractive indices involved a single mode at ~ 600 nm is ~ 3 μm in diameter. While this will decrease the AWG's footprint, alignment and coupling becomes more difficult. More importantly however, is that at visible wavelengths the number of modes in a seeing disk of an uncorrected ground-based telescope increases. Therefore, either the coupling to the SMF will decrease, or the instrument must scale using larger photonic lanterns. Having said that, as AO systems continue to improve at shorter wavelengths, this challenge may be overcome in the coming years.

The other wavelength region where IPS devices will see development is towards the Mid-IR, $3 - 4$ μm and perhaps out to 10 μm. This wavelength regime has seen development in recent years due in part to the overlap with molecular/environmental sensing and defence applications, which require integrated photonic devices. However, the materials used to fabricate devices at these wavelengths are substantially different from those used for NIR, with silica absorbing light beyond ~ 2.5 μm. Thus, Mid-IR AWGs are perhaps still a few years away from achieving the same performance as NIR devices. Nevertheless, AO correction at longer wavelengths is simpler to perform, and

the size advantage of an IPS compared to a classic spectrograph allows for less complex cryogenic systems to be implemented.

7.2 Final remarks

In this body of work we conducted the first study of the applicability of practical photonic spectrographs in astronomy, informed by initial on-sky tests. One of the important take away points is that the IPS chips themselves are very efficient, with a typical throughput of 75% from input fibre to output. This is also consistent across the higher and lower orders of the AWG, enabling efficient broadband performance when cross-dispersion is implemented. However, while the chip itself is efficient, the coupling from a seeing-limited telescope into the SM fibres required to feed the IPS chips had considerable losses. While the use of photonic lanterns improved the coupling, the large quantity of modes injected into a MMF by the telescope makes this type of telescope interface difficult to scale, and would not likely provide a considerable advantage over traditional spectrographs. There are however three regimes we identified where an IPS system can be advantageous.

If no forms of wavefront correction can be applied to the telescope, coupling light into the IPS at comparable values to traditional spectrographs will be difficult for large aperture telescopes. At these scales, as was demonstrated by our on-sky tests, the number of modes in the seeing disk (100's) requires a large number of photonic lantern outputs, and therefore a large number of AWG chips (even with multiple fibre injection). Thus, for the uncorrected case, little advantage is gained by going to telescopes with larger apertures. However, due to the mass-produced modular nature of the IPS devices, it makes them ideal for a farm of a number of small-aperture telescopes. Of particular advantage would be the high resolution AWG we are fabricating, which (if mass-produced) could bring the unit cost for a $R = 65,000$ spectrograph down to a few thousand dollars per unit. While this concept would have a substantial disadvantage in the light collected when compare to large research telescopes, if a large number of small telescopes are used with much more observing time dedicated to a single source, this method becomes viable.

For the case where the number of modes in the seeing disk are reduced by using some form of wavefront correction, or even deployment on a space platform, the IPS

provides clear advantages over bulk-optic designs. The rapid improvements in adaptive optics systems on observatories around the world makes this a promising prospect, particularly for the next generation of ELTs under construction. For basic AO correction, it becomes feasible to use low fibre-count photonic lanterns to maintain high coupling into the IPS. This is improved further with extreme AO systems with the capabilities of obtaining high Strehl ratios. Such systems could focus the light from a large aperture telescope directly into a SMF, or alternatively a few-mode MMF split by a photonic lantern. Such devices can perform by using a single AWG chip if necessary.

The impact of the inherent stability for small, on-chip, spectrographs should not be underestimated, and may prove to be the defining advantage of this technology. The drive of exoplanetary science has imposed stricter requirements for spectrograph stability and sensitivity with unprecedented RV precision likely required in the coming decades. The photonic approach, with its small footprint, no moving parts, and easy calibration, could prove to be the optimal way for constructing the next series of planet-hunting spectrographs.

While this technology is still in its infancy when compared to the centuries of use of bulk-optic spectrographs, we believe that much like how optical fibres revolutionised MOS instruments, the IPS will usher in a new wave of photonic device integration on telescopes around the world.

A

Appendix A: IPS Data Reduction Code

This appendix contains the Matlab script used to reduce on sky data obtained by the IPS prototype and outlined in Chapter 5.

```
%%%%%%%%  Data reduction Code

%% select file to import
[spectrumFlat]=datareduceFlats;
%[spectrumBe]=datareduceAlfara;
    rawdata = fitsread('pi01gru_rotate.fits');
    %rawdata = fitsread('arc_rotate.fits');

%% Plot Data
clims=[0 200];
%Sets the limit for the colour mapping that is then stretched to
%interpolate the colours

%% Seperate data into fibre spectra
%% Fiber #1
%Fibre #1 coordinates
x1=29;
x2=389;
y1=90;
y2=y1+5;
%Collapse Fibre #1
colapsedF1=sum(F1,1);
j=1;
while j<=size(colapsedF1,2)
    b=y1+(1.135*(j+x1));
```

```
    W=(0.0000173785*(b^2))+(0.1922552022*b)+1406.2115199113;
    colapsedF1(2,j)=W;
    j=j+1;
end
j=1;

%% Fiber #2
%Fiber #2 coordinates
x1=38;
x2=398;
y1=99;
y2=y1+4;
%Collapse Fibre #2
colapsedF2=sum(F2,1);
j=1;
while j<=size(colapsedF2,2)
    b=y1+(1.135*(j+x1));
    W=(0.0000173785*(b^2))+(0.1922552022*b)+1406.2115199113;
    colapsedF2(2,j)=W;
    j=j+1;
end
j=1;


% *** The code continues for all fibres


%% Fiber #60
%Fiber #60 coordinates
x1=664;
x2=1024;
y1=657;
y2=y1+2;
%Collapse Fibre #60
colapsedF60=sum(F60,1);
j=1;
while j<=size(colapsedF60,2)
    b=y1+(1.135*(j+x1));
    W=(0.0000173785*(b^2))+(0.1922552022*b)+1406.2115199113;
    colapsedF60(2,j)=W;
    j=j+1;
end
j=1;


%% Adding all the Fibres into one array
bigdata=NaN(65,1600);
bigdata(1,1:size(F1,2))=colapsedF1(2,:);
bigdata(2,1:size(F1,2))=colapsedF1(1,:);

%F2
[Row,Col]=find(bigdata(1,:)>=colapsedF2(2,1));
Col(1,1);
bigdata(3,Col(1):size(colapsedF2,2)+Col(1)-1)=colapsedF2(1,:);
```

```
%lodes the 2nd spectrum into third row
bigdata(1,size(colapsedF1,2)+1:size(colapsedF1,2)+Col(1)-1)=
colapsedF2(2,size(colapsedF2,2)-Col(1)+2:size(colapsedF2,2));
%Adds spillover spectrum into 1st row
endwavelength=size(colapsedF1,2)+Col(1)-1;
prevCol=Col(1);

%F3
[Row,Col]=find(bigdata(1,:)>=colapsedF3(2,1));
Col(1,1);
bigdata(4,Col(1):size(colapsedF3,2)+Col(1)-1)=colapsedF3(1,:);
bigdata(1,endwavelength+1:size(colapsedF1,2)+Col(1)-1)=
colapsedF3(2,size(colapsedF3,2)-Col(1)+prevCol+1:size(colapsedF3,2));
endwavelength=size(colapsedF1,2)+Col(1)-1;
prevCol=Col(1);

% Code continues for all fibres

%F60
[Row,Col]=find(bigdata(1,:)>=colapsedF60(2,1));
Col(1,1);
bigdata(61,Col(1):size(colapsedF60,2)+Col(1)-1)=colapsedF60(1,:);
bigdata(1,endwavelength+1:size(colapsedF1,2)+Col(1)-1)=colapsedF60(2,size(colapsed
endwavelength=size(colapsedF1,2)+Col(1)-1;
prevCol=Col(1);


%% Getting rid of cosmic rays/hot pixels

%Sigma Cut
sigma=6000
bigdata(15,501)=NaN;
j=1;k=1;
for j=2:size(bigdata,1)

    for k=1:size(bigdata,2)

        if bigdata(j,k)>=sigma

            bigdata(j,k)=NaN;
        end
    end
end

%Manual cosmic ray reduction
bigdata(45,863)=bigdata(45,864);
bigdata(29,561:562)=bigdata(29,563:564);
bigdata(15,364)=bigdata(15,365);
bigdata(59,1305)=bigdata(59,1306);
bigdata(48,1182)=bigdata(48,1183);
bigdata(54,1102)=bigdata(54,1103);
bigdata(57,1073)=bigdata(57,1074);
bigdata(11,503:504)=bigdata(11,505:506);
bigdata(15,349)=bigdata(15,350);
```

```
bigdata(53,1341)=bigdata(53,1342);
bigdata(55,1389)=bigdata(55,1390);
bigdata(20,582)=bigdata(20,583);

%% Colapsing into 1D Spectrum
spectrum=NaN(2,endwavelength);
spectrum(2,:)=nansum(bigdata(2:65,1:endwavelength));
spectrum(1,:)=bigdata(1,1:endwavelength);

%Adjust spectrum based on Arclamp missfit (see excel spreadsheet)
spectrum(1,:)=spectrum(1,:)-((0.000075764628810*(spectrum(1,:).^2))-
(0.246184415837800*spectrum(1,:))+201.926949737973000);

spectrum2(1,:)=spectrum2(1,:)-((0.000075764628810*(spectrum2(1,:).^2))-
(0.246184415837800*spectrum2(1,:))+201.926949737973000);
spectrum(2,:)=spectrum(2,:)./spectrumFlat(2,:);

%% Adding Known Spectral lines Values

%% C-O
j=1;
k=1;
spectrum(3,1:size(spectrum,2))=-1;
%  #1
for k=1:size(spectrum,2)
   if  spectrum(1,k)>=1558
       spectrum(3,k)=4E4;
   end
end
k=1;
% #2
for k=1:size(spectrum,2)
   if  spectrum(1,k)>=1578
       spectrum(3,k)=-1;
   end
end
k=1;
% #3
for k=1:size(spectrum,2)
   if  spectrum(1,k)>=1598
       spectrum(3,k)=4E4;
   end
end
k=1;
% #4
for k=1:size(spectrum,2)
   if  spectrum(1,k)>=1619
       spectrum(3,k)=-1;
   end
end
k=1;
% #5
for k=1:size(spectrum,2)
   if  spectrum(1,k)>=1640
```

```
        spectrum(3,k)=4E4;
    end
end
k=1;
% #6
for k=1:size(spectrum,2)
    if  spectrum(1,k)>=1661
        spectrum(3,k)=-1;
    end
end
k=1;
% #7
for k=1:size(spectrum,2)
    if  spectrum(1,k)>=1684
        spectrum(3,k)=4E4;
    end
end
k=1;
% #8
for k=1:size(spectrum,2)
    if  spectrum(1,k)>=1706
        spectrum(3,k)=-1;
    end
end
k=1;
% #9
for k=1:size(spectrum,2)
    if  spectrum(1,k)>=1730
        spectrum(3,k)=4E4;
    end
end
k=1;

%% O-H
k=1;
spectrum(4,1:size(spectrum,2))=-2;
%  #1
for k=1:size(spectrum,2)
    if  spectrum(1,k)>=1537
        spectrum(4,k)=4E4;
    end
end
k=1;
% #2
for k=1:size(spectrum,2)
    if  spectrum(1,k)>=1590
        spectrum(4,k)=-2;
    end
end
k=1;
% #3
for k=1:size(spectrum,2)
    if  spectrum(1,k)>=1625
        spectrum(4,k)=4E4;
```

```
   end
end
k=1;
% #4
for k=1:size(spectrum,2)
   if  spectrum(1,k)>=1650
       spectrum(4,k)=-2;
   end
end
k=1;
% #5
for k=1:size(spectrum,2)
   if  spectrum(1,k)>=1690
       spectrum(4,k)=4E4;
   end
end
k=1;

%% Si
k=1;
spectrum(5,1:size(spectrum,2))=-2;
%  #1
for k=1:size(spectrum,2)
   if  spectrum(1,k)>=1588.8
       spectrum(5,k)=4E4;
   end
end
k=1;
% #2
for k=1:size(spectrum,2)
   if  spectrum(1,k)>=1596
       spectrum(5,k)=-2;
   end
end
k=1;
% #3
for k=1:size(spectrum,2)
   if  spectrum(1,k)>=1638.2
       spectrum(5,k)=4E4;
   end
end
k=1;

%% Mg
k=1;
spectrum(6,1:size(spectrum,2))=-2;

%  #1
for k=1:size(spectrum,2)
   if  spectrum(1,k)>=1575
       spectrum(6,k)=4E4;
   end
end
k=1;
```

```
% #2
for k=1:size(spectrum,2)
   if  spectrum(1,k)>=1710
       spectrum(6,k)=-2;
   end
end
k=1;

%% Al
k=1;
spectrum(7,1:size(spectrum,2))=-2;
%  #1
for k=1:size(spectrum,2)
   if  spectrum(1,k)>=1670
       spectrum(7,k)=4E4;
   end
end
k=1;


%% Ca
k=1;
spectrum(8,1:size(spectrum,2))=-2;
%  #1
for k=1:size(spectrum,2)
   if  spectrum(1,k)>=1620.9
       spectrum(8,k)=4E4;
   end
end
k=1;
%% Fe
k=1;
spectrum(9,1:size(spectrum,2))=-2;
%  #1
for k=1:size(spectrum,2)
   if  spectrum(1,k)>=1582
       spectrum(9,k)=4E4;
   end
end
k=1;

%% Ploting the Spectrum
figure
plot (spectrum(1,:)',spectrum(2,:)','-r')
hold on
```

B

Appendix B: AWG Output Power & PSF Analysis Matlab Script

This appendix contains the Matlab script used to analyse the output PSF and throughput of the AWG chips, as outlined in Chapter 4.

```
%%%%%% Xenics Camera Reduction Code %%%%%%%
function powercalc
clc;

%% select file to import
[filename]=uigetfile('*.csv','Select a file to load');
% for the first field (*.csv) type in the file type.

%% Import data
    data=importdata(filename);
    [PATHSTR,NAME,EXT,VERSN] = fileparts(filename);
%splits the file parts , the location, the file name, the type of file,
%and the version.

[sizey,sizex]=size(data);
[xmax,centrex]=max(max(data));
[ymax,centrey]=max(max(data,[],2));

%% Plot Data
    %Plot WITHOUT Centering
        %Spatial
        imagesc([1:1:sizex],[1:1:sizey],data);
```

```
        %Spectral
        %imagesc([1/magx:1/magx:sizex/magx],[1/magy:1/magy:sizey/magy],data);
        %Plot WITH Centering
        %imagesc([(-centrex-0.5)/magx:sizex/magx:(sizex-centrex-0.5)/magx],
        [(-centrey-0.5)/magy:sizey/magy:(sizey-centrey-0.5)/magy],data);
        %plot with correct scales and zero
    shading interp;
    colormap(jet);
    %caxis([0 256]);%caxis([0 log10(256)]);

    %Plot Spatial
        axis square;set(gca, 'FontSize',11,'box','off','TickDir', 'out', 'TickLength',
        [0.015 0.01]); %set axis parameters
        xlabel('Position (Pix)','FontSize',14);
        ylabel('Position (Pix)','FontSize',14);title(NAME,'FontSize',14);

    %Croping the Image
        axisbeginx=0;
        axisendx=700;
        axisbeginy=0;
        axisendy=700;

%% Bacground Calc
[y1,x1]=ginput(1);
[y2,x2]=ginput(1);
x1=round(x1);
y1=round(y1);
x2=round(x2);
y2=round(y2);
totsumold=0;
x3=x2-x1
y3=y2-y1
for j=x1:x2-1
    for k=y1:y2-1
        totsumnew=data(j,k)+totsumold;
    totsumold=totsumnew;
    end
end
totsumnew
totsumold
totnumb=(y2-y1)*(x2-x1)
avebackgrnd=totsumold/totnumb
datanew=data-avebackgrnd;
%pause

[sizeynew,sizexnew]=size(datanew);
imagesc([1:1:sizexnew],[1:1:sizeynew],datanew);
shading interp;
colormap(jet);

axis square;set(gca, 'FontSize',11,'box','off','TickDir', 'out', 'TickLength',
[0.015 0.01]); %set axis parameters
xlabel('Position (Pix)','FontSize',14);ylabel('Position(Pix)','FontSize',14);
title(NAME,'FontSize',14); %% Total Area
```

```
        axisbeginx=0;
        axisendx=700;
        axisbeginy=0;
        axisendy=700;
        %crop=input('Do you want to crop the image? y/n : ', 's');
          crop='y';
            if crop=='y'
                cropdone='n';
                while cropdone=='n'
                axisbeginx=input('Enter the value where to BEGIN the x axis: ');
                axisendx=input('Enter the value where to END the x axis: ');
                axisbeginy=input('Enter the micron value where to BEGIN the y axis: ')
                axisendy=input('Enter the micron value where to END the y axis: ');
                axis([axisbeginx axisendx axisbeginy axisendy]);
                cropdone=input('Are you done croping? y/n : ', 's');
                end
            end

[newy1,newx1]=ginput(1);
[newy2,newx2]=ginput(1);
newx1=round(newx1);
newy1=round(newy1);
newx2=round(newx2);
newy2=round(newy2);
totsumold2=0;
for j=newx1:newx2-1

    for k=newy1:newy2-1

        totsumnew2=datanew(j,k)+totsumold2;
        totsumold2=totsumnew2;

    end
end

totsumold2
```

List of Publications

Peer-Reviewed Journal Publications

- **N. Cvetojevic**, J.S. Lawrence, S.C. Ellis, J. Bland-Hawthorn, R. Haynes, A. Horton *"Characterisation and on-sky demonstration of an integrated photonic spectrograph for astronomy"*. Optics Express **17**, 18643-18650 (2009)

- **Nick Cvetojevic**, Nemanja Jovanovic, Jon Lawrence, Michael Withford and Joss Bland-Hawthorn *"Developing arrayed waveguide grating spectrographs for multi-object astronomical spectroscopy"*. Optics Express **20**, 2062-2072 (2012)

- Geraldine Marien, Nemanja Jovanovic, **Nick Cvetojevic**, Robert Williams, Roger Haynes, Jon Lawrence, Quentin Parker and Michael J. Withford *"Fibre Bragg gratings for high spectral and temporal resolution astronomical observations"*. Monthly Notices of the Royal Astronomical Society **421**, 3641-3648 (2012)

- **N. Cvetojevic**, N. Jovanovic, C. Betters, J. S. Lawrence, S. C. Ellis, G. Robertson and J. Bland-Hawthorn *"First starlight spectrum captured using an integrated photonic micro-spectrograph"*. Astronomy & Astrophysics Letters **544**, L1-L4 (2012)

Conference Proceedings: Post-deadline papers

- **Nick Cvetojevic**, Nemanja Jovanovic, Chris Betters, Jon Lawrence, Simon Ellis, Gordon Robertson, Michael Withford and Joss Bland-Hawthorn, *"First Astronomical Spectra using an Integrated Photonic Spectrograp"*, Proceedings of FiO, San Jose, California, paper PDPA4, 2011.

Conference Proceedings: Proceedings of SPIE

- **Nick Cvetojevic**, Nemanja Jovanovic, Jon S. Lawrence, Michael J. Withford, and Joss Bland-Hawthorn, *"Redesign of the Integrated Photonic Spectrograph for Improved Astronomical Performance"*, Proceedings of SPIE, Amsterdam, paper 8446-130, 2012.

- J. Lawrence, J. Bland-Hawthorn, **N. Cvetojevic**, R. Haynes and N. Jovanovic and, *"Miniature astronomical spectrographs using arrayed waveguide gratings: Capabilities and limitations"*, Proceedings of SPIE, San Diego, California, paper 7739-92, 2010.

- **N. Cvetojevic**, J. B. Hawthorn, R. Haynes, N. Jovanovic and J. Lawrence, *"Experimental characterisation of arrayed waveguide gratings for astronomy"*, Proceedings of SPIE, San Diego, California, paper 7739-91, 2010.

- J. Bland-Hawthorn, J. Lawrence, G. Robertson, S. Campbell, B. Pope, C. Betters, S. Leon-Saval, T. Birks, R. Haynes, **N. Cvetojevic** and N. Jovanovic, *"PIMMS: Photonic integrated multimode microspectrograph"*, Proceedings of SPIE, San Diego, California, paper 7735-23, 2010. (2 Citations)

- G. Marien, **N. Cvetojevic**, J. Dawes, R. Haynes, N. Jovanovic, J. Lawrence, Q. Parker, and M. Withford, *"Fibre Bragg gratings for temporal spectral astronomy"*, Proceedings of SPIE, San Diego, California, paper 7739-81, 2010.

Conference Proceedings: Contributed papers

- **Nick Cvetojevic**, Nemanja Jovanovic, Jon Lawrence, Michael Withford, Joss Bland-Hawthorn *"Redesign of the Integrated Photonic Spectrograph for Improved Astronomical Performance"* Australian Institute of Physics (AIP) Congress, paper 818, Sydney, Australia, 2012.

- **Nick Cvetojevic**, Nemanja Jovanovic, Chris Betters, Jon Lawrence, Joss Bland-Hawthorn and Michael Withford, *"Technology for telescope integration of the integrated photonic spectrograph prototype"*, Proceedings of CLEO Pacific Rim, paper 4700-PO-29, pp 1922-1925, Sydney, Australia, 2011.

- Geraldine Marin, **Nick Cvetojevic**, Nemanja Jovanovic, Judith Dawes, Roger Haynes, Jon Lawrence, Quentin Parker and Michael Withford, *"The uses of fibre Bragg gratings for temporal spectral astronomy"*, Proceedings of CLEO Pacific Rim, paper 3700-PO-31, pp 1601-1603, Sydney, Australia, 2011.

- Geraldine Marin, **Nick Cvetojevic**, Nemanja Jovanovic, Judith Dawes, Roger Haynes, Jon Lawrence, Quentin Parker, Michael Withford, *"Fibre Bragg Grating Stopband Profile Trade-off for Temporal Spectral Astronomy"*, Proceedings of ECLEO, paper JSIII.P.4, Munich, Germany, 2011.

- **Nick Cvetojevic**, Nemanja Jovanovic, Joss Bland-Hawthorn, Roger Haynes, Jon Lawrence, *"Arrayed waveguide gratings for astronomy with multiple off-axis fibre launch"*, Proceedings of ECLEO, paper JSIII2.3, Munich, Germany, 2011.

- Jon Lawrence, Chris Betters, Joss Bland-Hawthorn, **Nick Cvetojevic**, Simon Ellis, Roger Haynes, Anthony Horton, Nemanja Jovanovic, Sergio Leon-Saval and Gordon Robertson, *"Development of an Array-Waveguide Grating Astronomical Spectrograph"*, Frontiers in Optics (FiO) 2010, paper FTuU4, Rochester, 2010.

- **Nick Cvetojevic**, Nemanja Jovanovic, Joss Bland-Hawthorn, Roger Haynes and Jon Lawrence, *"Miniature Photonic Spectrographs for Astronomical Applications"*, Australian Institute of Physics (AIP) Congress, paper 507, Melbourne, Australia, 2010.

- Geraldine Marin, **Nick Cvetojevic**, Nemanja Jovanovic, Judith Dawes, Joss Bland-Hawthorn, Roger Haynes, Jon Lawrence, Quentin Parker, Michael J. Withford, *"Profiles of Fibre Bragg Grating stopbands for Temporal Spectral Astronomy"*, Proceeding of ACOFT, Melbourne, Australia, 2010.

- G. Marien, **N. Cvetojevic**, N. Jovanovic, J. Dawes, R. Haynes, J. Lawrence, Q. Parker, and M. Withford, *"Fibre Bragg grating characteristics for temporal spectral astronomy"*, Proceedings of BGPP, Karlsruhe, Germany, paper JThA37, 2010.

- **N. Cvetojevic**, N. Jovanovic, J. Lawrence J. B. Hawthorn and R. Haynes, *"Arrayed waveguide gratings for astronomical applications"*, Proceedings of BGPP, Karlsruhe, Germany, paper JThA46, 2010.

Public articles

- *"The Integrated Photonic Spectrograph's First Look at the Heart of the Scorpion"*, AAO Observer - newsletter of the Australian Astronomical Observatory (AAO) (2011).
- *"Integrated Photonic Spectrograph: first on-sky results "*, AAO Observer (2010).
- *"Recent developments within the Consortium for Australian Astrophotonics"*, Optics and Photonics news/Australia Optical Society newsletter.

References

[1] I. Newton. *Opticks or, a treatise of the reflections, refractions, inflexions and colours of light: also two treatises of the species and magnitude of curvilinear figures.* (London, 1704), 1st ed. 1

[2] D. Brewster and I. Newton. *Memoirs of the life, writings and discoveries of Sir Isaac Newton*, vol. 1, p. 449 (Edinburgh: Edmonston and Duglas, 1855). 1

[3] D. Schroeder. *Astronomical Optics*, chap. 12 (Academic Press), 2nd ed. 10, 18, 137

[4] J. F. James. *Spectrograph Design Fundamentals* (Cambridge University Press, 2007).

[5] J. Hearnshaw. *Astronomical Spectrographs and Their History* (Cambridge University Press, 2009). 10

[6] J. Bland-Hawthorn, M. Englund, and G. Edvell. *New approach to atmospheric oh suppression using an aperiodic fibre bragg grating.* Opt. Express **12**(24), 5902 (2004). 23, 24

[7] A. P. G. Russell, T. G. Hawarden, E. Atad, S. K. Ramsay-Howat, A. Quirrenbach, R. Bacon, and M. Redfern. *Instrumentation studies for a european extremely large telescope: a strawman instrument suite and implications for telescope design.* Proc. SPIE 5382 p. 684 (2004). 23

[8] R. Haynes, J. Bland-Hawthorn, M. C. Large, K.-F. Klein, and G. W. Nelson. *New age fibers: the children of the photonic revolution* pp. 586–597 (2004). 24

[9] J. R. Allington-Smith, T. A. Birks, J. Bland-Hawthorn, C. R. Cunningham, S. Dagupta, R. Haynes, P. J. V. Garcia, A. K. Kar, A. Kelz, P. Y. Kern,

L. Labadie, J. S. Lawrence, E. P. Le Coarer, M. M. Roth, S. Minardi, R. M. Sharples, and R. R. Thomson. *Defining requirements and identifying relevant technologies in astrophotonics* pp. 773925–773925–13 (2010).

[10] J. Bland-Hawthorn and P. Kern. *Astrophotonics: a new era for astronomical instruments.* Opt. Express **17**(3), 1880 (2009).

[11] S. G. Leon-Saval, T. A. Birks, J. Bland-Hawthorn, and M. Englund. *Multimode fiber devices with single-mode performance.* Opt. Lett. **30**(19), 2545 (2005).

[12] J. Corbett and J. Allington-Smith. *Coupling starlight into single-mode photonic crystal fiber using a field lens.* Opt. Express **13**(17), 6527 (2005). 24

[13] F. G. Watson. *Multifiber waveguide spectrograph for astronomy.* In S. C. Barden, ed., *Society of Photo-Optical Instrumentation Engineers (SPIE) Conference Series*, vol. 2476 of *Society of Photo-Optical Instrumentation Engineers (SPIE) Conference Series*, pp. 68–74 (1995). 24

[14] F. G. Watson. *Waveguide spectrographs for astronomy?* In A. L. Ardeberg, ed., *Society of Photo-Optical Instrumentation Engineers (SPIE) Conference Series*, vol. 2871 of *Society of Photo-Optical Instrumentation Engineers (SPIE) Conference Series*, pp. 1373–1378 (1997). 24

[15] J. Bland-Hawthorn and A. Horton. *Instruments without optics: an integrated photonic spectrograph.* In *Society of Photo-Optical Instrumentation Engineers (SPIE) Conference Series*, vol. 6269 of *Society of Photo-Optical Instrumentation Engineers (SPIE) Conference Series* (2006). 24

[16] M. Smit. *Phasar-based wdm-devices: Principles, design and applications.* IEEE J. of Select. Topics in Quantum Elec. **2**, 236 (1996). 24, 30

[17] C. R. Doerr and K. Okamoto. *Advances in silica planar lightwave circuits.* Journal of Lightwave Technology **24**(12), 4763 (2006). 25, 26, 38

[18] H. Takahashi, S. Suzuki, K. Kato, and I. Nishi. *Arrayed-waveguide grating for wavelength division multi/demultiplexer with nanometer resolution.* Electronic Letters **26**(2), 87 (1990). 26

[19] K. Okamoto, K. Takiguchi, and Y. Ohmori. *Eight-channel flat spectral response arrayed-waveguide multiplexer with asymmetrical mach-zender filers.* Photonics Technology Letters **8**, 373 (1996). 27

[20] N. Cvetojevic, J. S. Lawrence, S. C. Ellis, J. Bland-Hawthorn, R. Haynes, and A. Horton. *Characterization and on-sky demonstration of an integrated photonic spectrograph for astronomy.* Optics Express **17**, 18643 (2009). 31, 52, 55, 88

[21] C. Dragone, C. H. Henry, I. P. Kaminow, and R. C. Kistler. *Efficient multichannel integrated optics star coupler on silicon.* IEEE Photonics Tech. Lett. **1**(8), 241 (1989). 32

[22] K. Okamoto, H. Takahashi, S. Suzuki, A. Sugita, and O. Y. *Design and fabrication of integrated-optic 8x8 star coupler.* Electron. Lett. **27**, 774 (1991). 32

[23] K. Okamoto. *Fundementals of Optical Waveguides*, chap. 9 (Academic Press, 1992). 32

[24] K. Okamoto and H. Yamada. *Arrayed-waveguide grating multiplexer with flat spectral response.* Opt. Lett. **20**, 43 (1995). 36

[25] K. Okamoto and A. Sugita. *Flat spectral response arrayed-waveguide grating multiplexer with parabolic waveguide horns.* Electron. Lett. **32**, 1661 (1996). 36

[26] M. R. Amersfoort, J. B. D. Soole, H. P. LeBlanc, N. C. Andreadakis, A. Rajhei, and C. Caneau. *Passband broadening of integrated arrayed waveguide filters using multimode interference couplers.* Electron. Lett. **32**, 449 (1996). 36

[27] D. Trouchet, A. Beguin, H. Boek, C. Prel, C. Lerminiaux, and R. O. Maschmeyer. *Passband flattening of phasar wdm using input and output star couplers designed with two focal points.* Proc. OFC 97 ThM7, Dallas, Texas. (1997). 36

[28] G. H. B. Thompson, R. Epworth, C. Rogers, S. Day, and S. Ojha. *An original low-loss and pass-band flattened sio2 on si planar wavelength demultiplexer.* Proc. OFC 98 TuN1, San Jose, CA. (1998). 36

[29] C. R. Doerr, L. W. Stulz, and R. Pafchek. *Compact and low-loss integrated box-like passband multiplexer.* IEEE Photonics Tech. Lett. **15**, 918 (2003). 36

[30] W. K. Burns, A. F. Milton, and A. B. Lee. *Optical waveguide parabolic coupling horns.* Appl. Phys. Lett. **30**, 28 (1997). 37

[31] T. Kitoh, Y. Inoue, M. Itoh, and Y. Hibino. *Low chromatic-dispersion flat-top arrayed waveguide grating filter.* Electron. Lett. **39**, 1116 (2003). 39

[32] C. van Dam, A. A. M. Staring, E. J. Jansen, J. J. M. Binsma, T. Van Dongen, M. K. Smit, and B. H. Verbeek. *Loss reduction for phased array demultiplexers using a double etch technique.* Integrated Photonics Research 1996, Boston, MA, April 29May 2 pp. 52–55 (1996). 40

[33] A. Sugita, A. Kaneko, K. Okamoto, M. Itoh, A. Himeno, and Y. Ohmori. *Very low insertion loss arrayed-waveguide grating with vertically tapered waveguides.* IEEE Photonics Tech. Lett. **12**, 1180 (2000). 40

[34] C. R. Doerr. *Optical add/drops and cross connects in planar waveguides.* Proc. ECOC 2003 Th1.3, Rimini, Italy (2003).

[35] K. Maru, T. Chiba, M. Okawa, H. Ishikawa, K. Ohira, S. Sato, and H. Uetsuka. *Low-loss arrayed-waveguide grating with high index regions at slab-to-array interface.* Electron. Lett. **37**, 1287 (2001). 40

[36] Y. P. Li. *Optical device having low insertion loss.* U. S. Patent 5 745 618 (1998). 40

[37] C. Mack. *Fundemental Principals of Optical Lithography* (John Wiley & Sons, 2008). 41

[38] E. le Coarer, S. Blaize, P. Benech, I. Stefanon, A. Morand, G. Lerondel, G. Leblond, P. Kern, J. M. Fedeli, and P. Royer. *Wavelength-scale stationary-wave integrated fourier-transform spectrometry.* Nat Photon (1), 473 (2007). 45, 46, 47

[39] H. Ives. *Standing light waves, repetition of an experiment by wiener, using a photoelectric probe surface.* JOSA **23**, 73 (1933). 46

[40] L. C. E. Connes, P. *3-d spectroscopy: The historical and logical viewpoint.* IAU Colloquium pp. 38–49 (1994). 46

[41] e. a. Knipp, D. *Silicon-based micro-fourier spectrometer.* IEEE Trans. on Electron Devices **53**(3), 419 (2005). 46

[42] D. L. FRIED. *Statistics of a geometric representation of wavefront distortion.* J. Opt. Soc. Am. **55**(11), 1427 (1965). 49

[43] R. J. Noll. *Zernike polynomials and atmospheric turbulence.* J. Opt. Soc. Am. **66**(3), 207 (1976). 49

[44] S. Lu, W. H. Wong, E. Y. B. Pun, Y. Yan, D. Wang, and D. Y. G. Jin. *Design of flat-field arrayed waveguide grating with three stigmatic points.* Opt. Quantum Electron **35**(8), 783 (2003). 52

[45] Y. L. D. Wang, W. Zeng and W. Tsay. *Novel arrayed waveguide grating designs for optical monitoring.* Opt. Fiber Commun. Conf **1**, 32 (2003). 53

[46] *Xenics xeva 1.7 datasheet.* `www.adept.net.au/cameras/XenICs/PDF/Xeva-1.7-320_scientific.pdf`. 59

[47] D. B. Murphy. *Fundamentals of Light Microscopy and Electronic Imaging*, chap. 10 (Wiley-Liss, 2001), 1st ed. 67

[48] K. I. White. *Practical application of the refracted near-field technique for the measurement of optical fibre refractive index profiles.* Optical and Quantum Electronics **11**(2), 185 (1979). 68

[49] R. Goring and M. Rothhardt. *Application of the refracted near-field technique to multimode planar and channel waveguides in glass.* Journal of Optical Communications **7**(3), 82 (1986). 69

[50] N. Gisin, J. P. Pellaux, P. Stamp, N. Hori, and M. Masuyama. *Alternative confguration for refracted near-feld measurements of refractive index on glassintegrated-optics waveguides.* Applied Optics **31**(33), 7108 (1992). 69

[51] N. Gisin, R. Passy, P. Stamp, N. Hori, and S. Nagano. *New optical confguration for nondestructive measurements of refractive index profles of linbo(3) waveguides.* Applied Optics **33**(9), 1726 (1994).

[52] P. Oberson, B. Gisin, B. Huttner, and N. Gisin. *Refracted near-field measurements of refractive index and geometry of silica-on-silicon integrated optical waveguides.* Applied Optics **37**(31), 7268 (1998). 69

[53] URL http://www.jdsu.com/en-us/Optical-Communications/Products/a-z-product-list/Pages/arrayed-waveguide-grating-100-ghz-narrowband-gaussian.aspx. 78

[54] S. Shaklan and F. Roddier. *Coupling starlight into single-mode fiber optics.* Appl. Opt. **27**(11), 23342338 (1988). 78

[55] V. C. du Foresto, M. Faucherre, N. Hubin, and P. Gitton. *Using single-mode fibers to monitor fast strehl ratio fluctuations. application to a 3.6 m telescope corrected by adaptive optics.* A and A **145**, 305310 (2000). 78

[56] C. G. Tinney, S. D. Ryder, S. C. Ellis, V. Churilov, J. Dawson, G. Smith, L. Waller, J. Whittard, R. Haynes, A. Lankshear, J. R. Barton, C. J. Evans, K. Shortridge, T. Farrell, and J. Bailey. *IRIS2: a working infrared multiobject-spectrograph and camera.* In *Society of Photo-Optical Instrumentation Engineers (SPIE) Conference Series*, vol. 5492 of *Society of Photo-Optical Instrumentation Engineers (SPIE) Conference Series*, p. 998 (2004). 88

[57] S. C. Ellis and J. Bland-Hawthorn. *The case for oh suppression at near-infrared wavelengths.* Monthly Notices of the Royal Astronomical Society **386**(1), 47 (2008). 89

[58] C. Q. Trinh, S. C. Ellis, J. Bland-Hawthorn, J. S. Lawrence, A. J. Horton, S. G. Leon-Saval, K. Shortridge, J. Bryant, S. Case, M. Colless, W. Couch, K. Freeman, H.-G. Lhmannsrben, L. Gers, K. Glazebrook, R. Haynes, S. Lee, J. OByrne, S. Miziarski, M. M. Roth, B. Schmidt, C. G. Tinney, and J. Zheng. *Gnosis the first instrument to use fiber bragg gratings for oh suppression.* The Astronomical Journal **145**(2), 51 (2013). 92

[59] D. Noordegraaf, P. M. Skovgaard, M. D. Nielsen, and J. Bland-Hawthorn. *Efficient multi-mode to single-mode coupling in a photonic lantern.* Opt. Express **17**(3), 1988 (2009). 95, 96

[60] S. G. Leon-Saval, T. A. Birks, J. Bland-Hawthorn, and M. Englund. *Multimode fiber devices with single-mode performance.* Opt. Lett. **30**(19), 2545 (2005). 95, 96

[61] S. G. Leon-Saval, A. Argyros, and J. Bland-Hawthorn. *Photonic lanterns: a study of light propagation in multimode to single-mode converters.* Opt. Express **18**(8), 8430 (2010). 96

[62] S. G. Leon-Saval, T. A. Birks, N. Y. Joly, A. K. George, W. J. Wadsworth, G. Kakarantzas, and P. S. J. Russell. *Splice-free interfacing of photonic crystal fibers.* Opt. Lett. **30**(13), 1629 (2005). 96

[63] C. G. Tinney, S. D. Ryder, S. C. Ellis, V. Churilov, J. Dawson, G. A. Smith, L. Waller, J. D. Whittard, R. Haynes, A. Lankshear, J. R. Barton, C. J. Evans, K. Shortridge, T. Farrell, and J. Bailey. *IRIS2: a working infrared multi-object spectrograph and camera.* In A. F. M. Moorwood and M. Iye, eds., *Society of Photo-Optical Instrumentation Engineers (SPIE) Conference Series*, vol. 5492 of *Society of Photo-Optical Instrumentation Engineers (SPIE) Conference Series*, pp. 998–1009 (2004). 99, 132

[64] L. Origlia, A. F. M. Moorwood, and E. Oliva. *The 1.5-1.7 micrometer spectrum of cool stars: Line identifications, indices for spectral classification and the stellar content of the Seyfert galaxy NGC 1068.* A & A **280**, 536 (1993). 102, 111, 112

[65] *Iris2 user guide - australian astronomical observatory.* `www.aao.gov.au/AAO/iris2/iris2_wave.html/calibrate_arc`. 105

[66] De Beck, E., Decin, L., de Koter, A., Justtanont, K., Verhoelst, T., Kemper, F., and Menten, K. M. *Probing the mass-loss history of agb and red supergiant stars from co rotational line profiles.* A & A **523**, A18 (2010). 111

[67] A. Lancon and P. R. Wood. *A library of 0.5 to 2.5 mu m spectra of luminous cool stars.* A & A **146**, 217 (2000). 112

[68] R. Scarmozzino, A. Gopinath, R. Pregla, and S. Helfert. *Numerical techniques for modeling guided-wave photonic devices.* Selected Topics in Quantum Electronics, IEEE Journal of **6**(1), 150 (2000). 117, 118

[69] L. Eldada, M. N. Ruberto, R. Scarmozzino, M. Levy, and R. Osgood. *Laser-fabricated low-loss single-mode waveguiding devices in gaas.* Lightwave Technology, Journal of **10**(11), 1610 (1992).

[70] M. Levy, L. Eldada, R. Scarmozzino, J. Osgood, R.M., P. Lin, and F. Tong. *Fabrication of narrow-band channel-dropping filters.* Photonics Technology Letters, IEEE **4**(12), 1378 (1992).

[71] L. Eldada, N. Zhu, M. N. Ruberto, M. Levy, R. Scarmozzino, and R. Osgood. *Rapid direct fabrication of active electro-optic modulators in gaas.* Lightwave Technology, Journal of **12**(9), 1588 (1994).

[72] I. Ilic, R. Scarmozzino, R. Osgood, J. T. Yardley, K. W. Beeson, and M. McFarland. *Modeling multimode-input star couplers in polymers.* Lightwave Technology, Journal of **12**(6), 996 (1994).

[73] R. O. J. J. Y. K. B. I. Ilic, R. Scarmozzino, M. McFarland, and J. Schweyen. *Photopatterned Polymer Multimode 8x8 Star Couplers: Comparative Design Methodologies and Device Measurements.* IEICE Trans. Commun. (1997).

[74] M. C. Shih, M. H. Hu, M. B. Freiler, M. Levy, R. Scarmozzino, J. Osgood, R.M., I. W. Tao, and W. Wang. *Fabrication of an ingaas single quantum well circular ring laser by direct laser patterning.* Applied Physics Letters **66**(20), 2608 (1995).

[75] L. Eldada, R. Scarmozzino, R. Osgood, D. Scott, Y. Chang, and H. R. Fetterman. *Laser-fabricated delay lines in gaas for optically steered phased-array radar.* Lightwave Technology, Journal of **13**(10), 2034 (1995).

[76] M. H. Hu, Z. Huang, K. Hall, R. Scarmozzino, and R. Osgood. *An integrated two-stage cascaded mach-zehnder device in gaas.* Lightwave Technology, Journal of **16**(8), 1447 (1998).

[77] M. H. Hu, J. Z. Huang, R. Scarmozzino, M. Levy, and J. Osgood, R.M. *A low-loss and compact waveguide y-branch using refractive-index tapering.* Photonics Technology Letters, IEEE **9**(2), 203 (1997).

[78] M. H. Hu, J. Z. Huang, R. Scarmozzino, M. Levy, and J. Osgood, R.M. *Tunable mach-zehnder polarization splitter using height-tapered y-branches.* Photonics Technology Letters, IEEE **9**(6), 773 (1997).

[79] D. Levy, Y. Li, R. Scarmozzino, and R. Osgood. *A multimode interference-based variable power splitter in gaas-algaas.* Photonics Technology Letters, IEEE **9**(10), 1373 (1997).

[80] D. Levy, R. Scarmozzino, Y. Li, and R. Osgood. *A new design for ultracompact multimode interference-based 2 times;2 couplers.* In *Lasers and Electro-Optics Society Annual Meeting, 1997. LEOS '97 10th Annual Meeting. Conference Proceedings., IEEE*, vol. 1, pp. 399–400 vol.1 (1997).

[81] J. Z. Huang, M. H. Hu, J. Fujita, R. Scarmozzino, and J. Osgood, R.M. *High-performance metal-clad multimode interference devices for low-index-contrast material systems.* Photonics Technology Letters, IEEE **10**(4), 561 (1998).

[82] J. Z. Huang, R. Scarmozzino, and J. Osgood, R.M. *A new design approach to large input/output number multimode interference couplers and its application to low-crosstalk wdm routers.* Photonics Technology Letters, IEEE **10**(9), 1292 (1998).

[83] T. Ramadan, R. Scarmozzino, and R. Osgood. *Adiabatic couplers: design rules and optimization.* Lightwave Technology, Journal of **16**(2), 277 (1998).

[84] J. Fujita, M. Levy, R. Scarmozzino, R. Osgood, L. Eldada, and J. T. Yardley. *Integrated multistack waveguide polarizer.* Photonics Technology Letters, IEEE **10**(1), 93 (1998).

[85] Z. Huan, R. Scarmozzino, G. Nagy, M. Steel, and J. Osgood, R.M. *Realization of a compact and single-mode optical passive polarization converter.* Photonics Technology Letters, IEEE **12**(3), 317 (2000).

[86] D. Yevick and B. Hermansson. *Efficient beam propagation techniques.* Quantum Electronics, IEEE Journal of **26**(1), 109 (1990). 121

[87] Y. Chung and N. Dagli. *An assessment of finite difference beam propagation method.* Quantum Electronics, IEEE Journal of **26**(8), 1335 (1990).

[88] R. Scarmozzino and J. R. M. Osgood. *Comparison of finite-difference and fourier-transform solutions of the parabolic wave equation with emphasis on integrated-optics applications.* J. Opt. Soc. Am. A **8**(5), 724 (1991). 117, 121, 122

[89] G. R. Hadley. *Wide-angle beam propagation using pad approximant operators.* Opt. Lett. **17**(20), 1426 (1992). 117

[90] H. Rao, R. Scarmozzino, and R. Osgood. *A bidirectional beam propagation method for multiple dielectric interfaces.* Photonics Technology Letters, IEEE **11**(7), 830 (1999). 117

[91] M. D. Feit and J. J. A. Fleck. *Light propagation in graded-index optical fibers.* Appl. Opt. **17**(24), 3990 (1978). 118, 121

[92] D. Yevick. *A guide to electric field propagation techniques for guided-wave optics.* Optical and Quantum Electronics **26**(3), S185 (1994). 118

[93] I. Newton. *BeamPROP 8.1 User Guide* (Rsoft, 2008). 121

[94] G. Hadley. *Transparent boundary condition for the beam propagation method.* Quantum Electronics, IEEE Journal of **28**(1), 363 (1992). 122

[95] A. W. Snyder and L. Love. *Optical Waveguide Theory* (Springer, 1983). 127

[96] M. Colless, G. Dalton, S. Maddox, W. Sutherland, P. Norberg, S. Cole, J. Bland-Hawthorn, T. Bridges, R. Cannon, C. Collins, W. Couch, N. Cross, K. Deeley, R. De Propris, S. P. Driver, G. Efstathiou, R. S. Ellis, C. S. Frenk, K. Glazebrook, C. Jackson, O. Lahav, I. Lewis, S. Lumsden, D. Madgwick, J. A. Peacock, B. A. Peterson, I. Price, M. Seaborne, and K. Taylor. *The 2dF Galaxy Redshift Survey spectra and redshifts.* MNRAS **328**, 1039 (2001). 130, 131

[97] C. Evans, M. Puech, B. Barbuy, N. Bastian, P. Bonifacio, E. Caffau, J.-G. Cuby, G. Dalton, B. Davies, J. Dunlop, H. Flores, F. Hammer, L. Kaper, B. Lemasle, S. Morris, L. Pentericci, P. Petitjean, D. Schaerer, E. Telles, N. Welikala, and B. Ziegler. *ELT MOS White Paper Science Overview Requirements.* ArXiv e-prints (2013). 130

[98] W. Saunders, M. Colless, I. Saunders, A. Hopkins, M. Goodwin, J. Heijmans, J. Brzeski, and T. Farrell. *Manifest: a many-instrument fiber-positioning system for gmt* (2010). URL http://dx.doi.org/10.1117/12.856353. 131

[99] R. R. Thomson, T. A. Birks, S. G. Leon-Saval, A. K. Kar, and J. Bland-Hawthorn. *Ultrafast laser inscription of an integrated photonic lantern.* Opt. Express **19**(6), 5698 (2011). 132

[100] I. Spaleniak, S. Gross, N. Jovanovic, R. J. Williams, J. S. Lawrence, M. J. Ireland, and M. J. Withford. *Multiband processing of multimode light combining 3d photonic lanterns with waveguide bragg gratings.* Laser and Photonics Reviews (2013). 133

[101] I. Spaleniak, N. Jovanovic, S. Gross, M. J. Ireland, J. S. Lawrence, and M. J. Withford. *Integrated photonic building blocks for next-generation astronomical instrumentation ii: the multimode to single mode transition.* Opt. Express **21**(22), 27197 (2013). 133

[102] F. Hammer, F. Sayède, E. Gendron, T. Fusco, D. Burgarella, V. Cayatte, J.-M. Conan, F. Courbin, H. Flores, I. Guinouard, L. Jocou, A. Lancon, G. Monnet, M. Mouhcine, F. Rigaud, D. Rouan, G. Rousset, V. Buat, and F. Zamkotsian. *The FALCON Concept: Multi-Object Spectroscopy Combined with MCAO in Near-IR.* In J. Bergeron and G. Monnet, eds., *Scientific Drivers for ESO Future VLT/VLTI Instrumentation*, p. 139 (2002). 136

[103] J. Odori, T. Yoshida, K. Sorimoto, H. Iitsuka, H. Kawashima, and T. Hiroyuki. *Low cross-talk silica arrayed-waveguide grating for visible light spectroscopy.* In *Advanced Photonics Congress*, p. ITu3B.5 (Optical Society of America, 2012). 137

[104] D. Kopon, J. R. Males, L. M. Close, and V. Gasho. *Enabling Technologies for Visible Adaptive Optics: The Magellan Adaptive Secondary VisAO Camera.* ArXiv e-prints (2010). 137

[105] S. Shaklan and F. Roddier. *Coupling starlight into single-mode fiber optics.* Appl. Opt. **27**(11), 2334 (1988). 138

[106] O. Guyon. *Phase induced amplitude apodization of telescope pupils for extrasolar terrestrial planet imaging.* Astronomy and Astrophysics **404**, 379 (2003). 138

[107] C. Lovis, F. Pepe, F. Bouchy, G. Lo Curto, M. Mayor, L. Pasquini, D. Queloz, G. Rupprecht, S. Udry, and S. Zucker. *The exoplanet hunter HARPS: unequalled accuracy and perspectives toward 1 cm s^{-1} precision.* In *Society of Photo-Optical Instrumentation Engineers (SPIE) Conference Series*, vol. 6269 of *Society of Photo-Optical Instrumentation Engineers (SPIE) Conference Series* (2006). 144, 145

[108] N. M. Batalha, J. F. Rowe, S. T. Bryson, T. Barclay, C. J. Burke, D. A. Caldwell, J. L. Christiansen, F. Mullally, S. E. Thompson, T. M. Brown, A. K. Dupree, D. C. Fabrycky, E. B. Ford, J. J. Fortney, R. L. Gilliland, H. Isaacson, D. W. Latham, G. W. Marcy, S. N. Quinn, D. Ragozzine, A. Shporer, W. J. Borucki, D. R. Ciardi, T. N. Gautier, III, M. R. Haas, J. M. Jenkins, D. G. Koch, J. J. Lissauer, W. Rapin, G. S. Basri, A. P. Boss, L. A. Buchhave, J. A. Carter, D. Charbonneau, J. Christensen-Dalsgaard, B. D. Clarke, W. D. Cochran, B.-O. Demory, J.-M. Desert, E. Devore, L. R. Doyle, G. A. Esquerdo, M. Everett, F. Fressin, J. C. Geary, F. R. Girouard, A. Gould, J. R. Hall, M. J. Holman, A. W. Howard, S. B. Howell, K. A. Ibrahim, K. Kinemuchi, H. Kjeldsen, T. C. Klaus, J. Li, P. W. Lucas, S. Meibom, R. L. Morris, A. Prša, E. Quintana, D. T. Sanderfer, D. Sasselov, S. E. Seader, J. C. Smith, J. H. Steffen, M. Still, M. C. Stumpe, J. C. Tarter, P. Tenenbaum, G. Torres, J. D. Twicken, K. Uddin, J. Van Cleve, L. Walkowicz, and W. F. Welsh. *Planetary Candidates Observed by Kepler Analysis of the First 16 Months of Data.* APJ **204**, 24 (2013). 145, 149, 150

[109] M. Mayor and D. Queloz. *A jupiter-mass companion to a solar-type star.* Nature **378**, 355 (1995). 146

[110] J. C. Tarter, P. R. Backus, R. L. Mancinelli, J. M. Aurnou, D. E. Backman, G. S. Basri, A. P. Boss, A. Clarke, D. Deming, L. R. Doyle, E. D. Feigelson, F. Freund, D. H. Grinspoon, R. M. Haberle, S. A. Hauck, II, M. J. Heath, T. J. Henry, J. L. Hollingsworth, M. M. Joshi, S. Kilston, M. C. Liu, E. Meikle, I. N. Reid, L. J. Rothschild, J. Scalo, A. Segura, C. M. Tang, J. M. Tiedje, M. C. Turnbull, L. M.

Walkowicz, A. L. Weber, and R. E. Young. *A Reappraisal of The Habitability of Planets around M Dwarf Stars.* Astrobiology **7**, 30 (2007). 149

[111] J. Scalo, L. Kaltenegger, A. G. Segura, M. Fridlund, I. Ribas, Y. N. Kulikov, J. L. Grenfell, H. Rauer, P. Odert, M. Leitzinger, F. Selsis, M. L. Khodachenko, C. Eiroa, J. Kasting, and H. Lammer. *M Stars as Targets for Terrestrial Exoplanet Searches And Biosignature Detection.* Astrobiology **7**, 85 (2007). 149

[112] G. W. Marcy and R. P. Butler. *Detection of Extrasolar Giant Planets.* Annual Review of Astronomy and Astrophysics **36**, 57 (1998). 149

[113] S. Udry, X. Bonfils, X. Delfosse, T. Forveille, M. Mayor, C. Perrier, F. Bouchy, C. Lovis, F. Pepe, D. Queloz, and J.-L. Bertaux. *The HARPS search for southern extra-solar planets. XI. Super-Earths (5 and 8M) in a 3-planet system.* Astronomy and Astrophysics **469**, L43 (2007). 149

[114] F. Allard and P. H. Hauschildt. *Model atmospheres for M (sub)dwarf stars. 1: The base model grid.* The Astrophysical Journal **445**, 433 (1995). 149

[115] M. Tamura, H. Suto, J. Nishikawa, T. Kotani, B. Sato, W. Aoki, T. Usuda, T. Kurokawa, K. Kashiwagi, S. Nishiyama, Y. Ikeda, D. Hall, K. Hodapp, J. Hashimoto, J. Morino, S. Inoue, Y. Mizuno, Y. Washizaki, Y. Tanaka, S. Suzuki, J. Kwon, T. Suenaga, D. Oh, N. Narita, E. Kokubo, Y. Hayano, H. Izumiura, E. Kambe, T. Kudo, N. Kusakabe, M. Ikoma, Y. Hori, M. Omiya, H. Genda, A. Fukui, Y. Fujii, O. Guyon, H. Harakawa, M. Hayashi, M. Hidai, T. Hirano, M. Kuzuhara, M. Machida, T. Matsuo, T. Nagata, H. Ohnuki, M. Ogihara, S. Oshino, R. Suzuki, H. Takami, N. Takato, Y. Takahashi, C. Tachinami, and H. Terada. *Infrared doppler instrument for the subaru telescope (ird)* (2012). 150, 151

[116] J. Lozi, F. Martinache, and O. Guyon. *Phase-Induced Amplitude Apodization on Centrally Obscured Pupils: Design and First Laboratory Demonstration for the Subaru Telescope Pupil.* PASP **121**, 1232 (2009). 152

[117] *Fiber fabry-perot tunable filter technical reference.* `http://www.micronoptics.com/uploads/library/documents/filters_docs/TF2_Technical_Reference.pdf`. 153